Self-starting of a small urban Darrieus rotor

Strategies to boost performance in low-Reynolds-number flows

René Bos

Master of Science Thesis

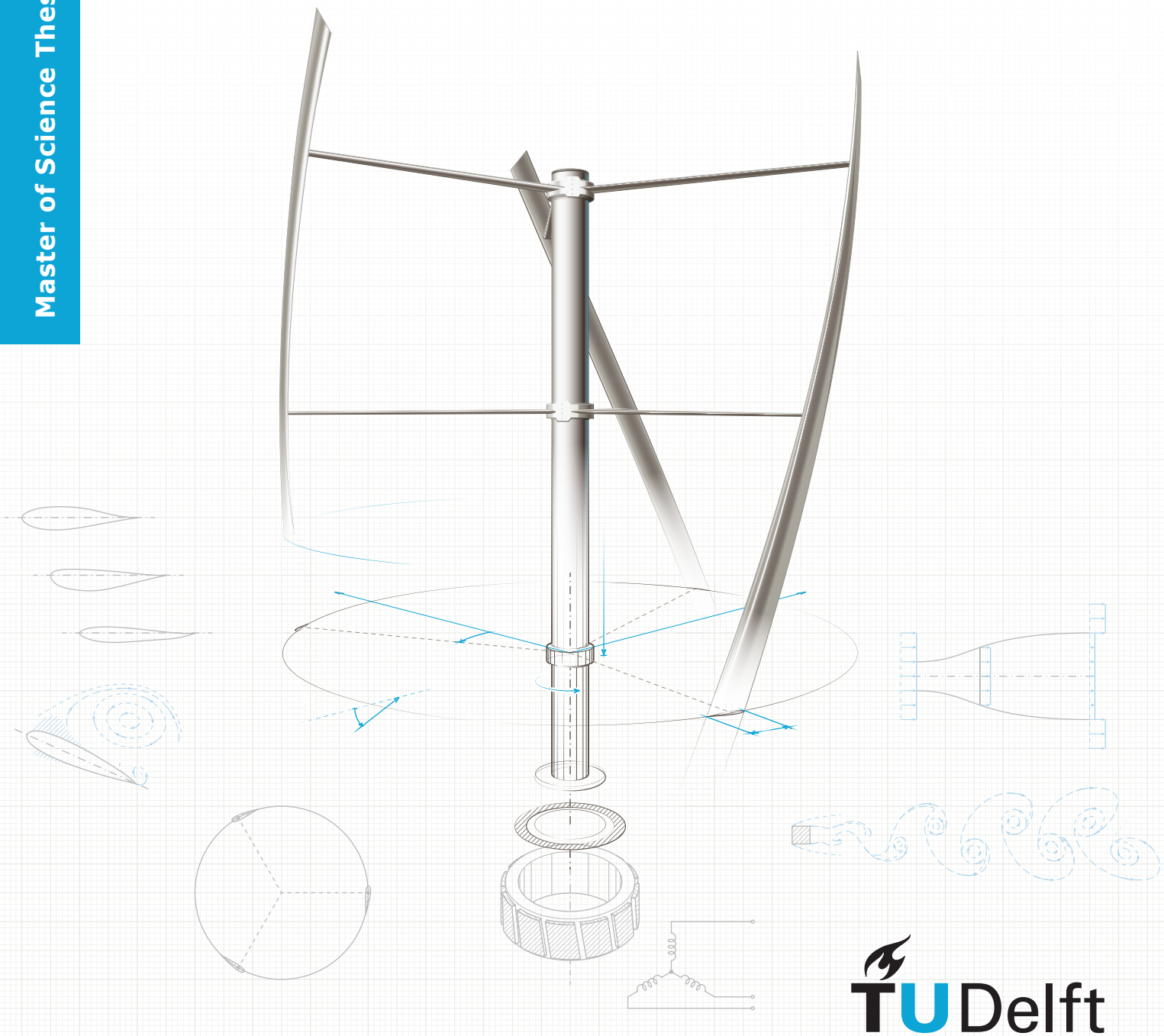

TU Delft

Delft University of Technology

Self-starting of a small urban Darrieus rotor

Strategies to boost performance in low-Reynolds-number flows

Master of Science Thesis

For the degree of Master of Science in Sustainable Energy Technology
at Delft University of Technology

R. Bos

20th November, 2012

Faculty of Aerospace Engineering · Delft University of Technology

Delft University of Technology
Department of Wind Energy

The undersigned hereby certify that they have read and recommend to the Faculty of Aerospace Engineering for acceptance the thesis entitled **"Self-starting of a small urban Darrieus rotor"** by **R. Bos** in partial fulfillment of the requirements for the degree of **Master of Science**.

Dated: 20th November, 2012

Supervisors:

Prof.dr. G.J.W. van Bussel

ir. W.A. Timmer

ir. B.M. Geurts

Reader:

dr.ir. L.L.M. Veldhuis

Preface

This report contains the graduation work I carried out at the department of Wind Energy at Aerospace Engineering. It marks the end of a year in which I studied the performance of vertical-axis wind turbines in start-up conditions. During this period, I extended my knowledge on various topics of aerodynamics, learned all about doing intensive research and grew a strong love-hate relationship with my computer.

Of course, I want to thank my supervisors Nando Timmer and Ben Geurts for their time, knowledge and wisdom. Further thanks go to Dick Sidler for the helpful e-mail conversations and for kindly providing me with data of Turby. Also, I would like to thank Carlos Simão Ferreira for helping me out with the genetic algorithm and for the inspiring lectures on rotor aerodynamics. Finally, some special thanks go out to my girlfriend, Esther, for listening to my exciting stories about separation bubbles, airfoil design and what else.

Summary

Like many vertical-axis wind turbines (VAWTs) of the Darrieus type, Turby fails to achieve a fully passive start-up. Experiments indicate that there is a band of negative torque—often referred to as *dead band* in literature—somewhere in the tip speed range $0.5 \leq \lambda \leq 1.6$. The reason behind this is that, unfortunately, the power coefficient obtained at the rated wind speed is all but constant. The combination of low wind speeds and the small scale of the device leads to very low Reynolds numbers; well in the order of $< 10^5$. The lift production and stall behavior of the airfoils aggravates in these conditions, with low starting torque as a result.

The design case revolved around Turby – a small 1.6 kW, 2.20 m diameter VAWT with a projected cut-in wind speed of 3 m/s. The purpose of this master thesis is to investigate the cause of the poor start-up performance and to find possible solutions for the problem. This eventually led to a design proposal.

The start-up problem has to do with the large angle of attack variations encountered at low tip speed ratios. Here, the rotor blades are stalled during most of their trajectories and operate primarily on flat plate behavior. In this case, the resulting tangential force, C_t, is predominantly negative for $\alpha \leq 45°$ (depending primarily on leading-edge geometry) and positive for $\alpha > 45°$. The range of angles spanning from the airfoil's deep stall angle to 45° marks a *post-stall region* where the drag of the stalled airfoils produces a considerable braking torque, preventing the rotor from advancing to higher tip speed ratios. This manifests itself as a band of negative torque in the performance curves – often called a *dead band* in literature (see figure 1). Moreover, combinations of small chords lengths and low apparent wind speeds will lead to low Reynolds numbers, well below 10^5. Performance degradation at these conditions will decrease C_l/C_d, lower the deep stall angle and widen the post-stall region, resulting in a more severe dead band (see figure 2).

Despite the presence of the dead band, a rotor can still possess sufficient angular momentum to pass through it. Furthermore, in gusty conditions, a drop in wind speed can briefly increase the tip speed ratio to a value of positive C_P that allows the rotor to advance to higher tip speed ratios.

A common approach to model a vertical-axis rotor is to use air-

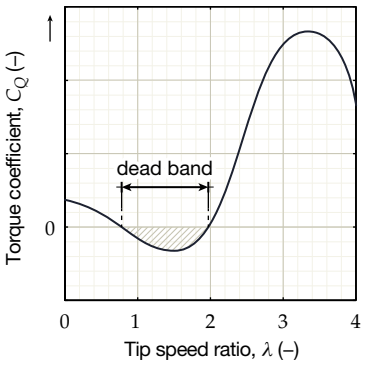

Figure 1: Hypothetical $C_Q - \lambda$ curve, showing the presence of a *dead band*.

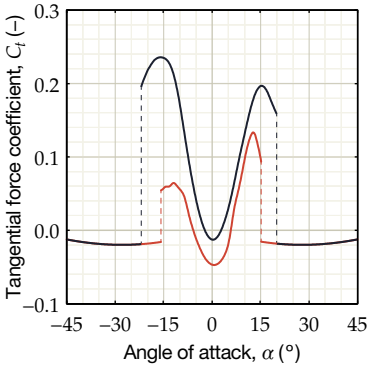

Figure 2: Predicted tangential force of DU 06-W-200 at $\mathrm{Re} = 40,000$ (—) and $\mathrm{Re} = 350,000$ (—).

foil data for an average Reynolds number or to assume completely inviscid flow conditions. Usually, the induced errors are acceptable for high tip speed ratios or high Reynolds numbers. A start-up of a small turbine like Turby is the complete opposite, however. The static stall angle is encountered regularly and—especially at low tip speed ratios—the variations in Reynolds number become increasingly important. Furthermore, modeling is a complex endeavor since the flow is governed by separation, unsteady aerodynamics and rotational effects.

In the present work, modeling was done by making a cross-section of the rotor and predicting the induced velocities by a vortex panel method. Viscous airfoil data was generated using RFOIL and, where applicable, then fed into an empirical dynamic stall model. This was evaluated using Strickland's adaptation of the Gormont model, accompanied by the Massé-Berg modification (see Gormont, 1973; Strickland, 1975; Massé, 1981). This approach has several important weaknesses – e.g. no feedback on the wake, absence of rotational effects on the boundary layer, etc. Modeling this dead band means that a lot of these inaccuracies come into play, which cannot be verified until they are compared with a real-life experimental set-up.

Facilitating a passive start-up for a small Darrieus turbine implies switching to low-Reynolds-number airfoils or finding other means of adding extra torque. An extensive literature study was conducted to put together a collection of solutions to the problem. From this list of strategies, the choice fell on a new low-Reynolds-number airfoil, a new strut geometry and the addition of strut joint fairings.

The current struts are shaped like NACA 0018 sections with a chord length of 12 cm at the root to 8 cm at the blades. However, at the Reynolds numbers encountered by Turby, struts of a NACA 0012 cross-section will have lower drag than when using a NACA 0018 profile, even when it means increasing the chord length to compromise for the lower bending stiffness. Therefore, struts of a constant 12 cm chord were designed that were shaped like a NACA 0018 at the hub and linearly decreased in thickness to a NACA 0010 at the blades. This is expected to result in a reduction in strut drag in the order of 30% at start-up – but of course depending mainly on Reynolds number.

New airfoils were generated under turbulent conditions using a genetic algorithm, which is a suitable tool to design geometries that have to satisfy many different requirements or have to operate in a wide range of conditions. Here, a distinction was made between start-up ($\lambda \approx 1.5$, $U_\infty = 3$ m/s, Re $\approx 40{,}000$) and nominal operation ($\lambda \approx 4.0$, $U_\infty = 11$ m/s, Re $\approx 350{,}000$). This yielded two new airfoil concepts to compete with the original DU 06-W-200 in the two cases (see figure 3), with the eye on the development of multiple set-ups.

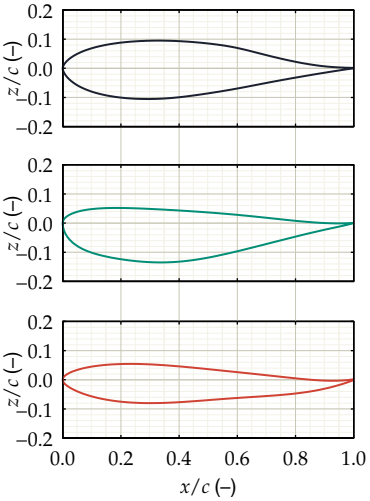

Figure 3: Two airfoil geometries, concepts 1 (—) and 2 (—), to outperform the flipped DU 06-W-200 (—) during nominal operation and start-up, respectively.

- The first configuration was optimized for start-up (see figure 4). It uses the flipped DU 06-W-200 airfoil, tripped at $x = 30\%c$ and $x = 50\%c$ on the inboard and outboard side, respectively. For self-

starting to become feasible, it required a high solidity of $\sigma = 0.22$ and a zero pitch angle. Therefore, it suffered greatly from stall, which limited the power coefficient to 0.20.

- The second configuration was designed to find a balance between start-up and nominal operation (see figure 5). It uses the flipped DU 06-W-200 airfoil, tripped at $x = 30\%c$ and $x = 50\%c$ on the inboard and outboard side, respectively. It relied on a somewhat higher solidity than the baseline case ($\sigma = 0.19$), but has a fixed pitch angle of $\gamma = 4°$ to avoid stall at high λ. It reached a peak power coefficient of 0.35.
- The third configuration was optimized for maximum power (see figure 6), using the replacement airfoil from the genetic algorithm. It has a lower solidity of $\sigma = 0.16$ and a pitch angle of $\gamma = 4°$. The peak power coefficient was estimated at $C_{P_{\max}} = 0.37$, but also showed good improvement around the rated tip speed ratio.

Unfortunately, no configuration succeeded in facilitating a passive start-up without causing a large drop in the peak power coefficient.

The design process showed some important things that should be taken into account when designing for small VAWTs. First, airfoil performance at start-up is strongly dominated by laminar separation bubbles, and a well-placed boundary layer trip can often accomplish more than switching to a thinner airfoil. The locations for fixed transition should therefore be included in the airfoil design process. In addition, for airfoils that operate on the verge of dynamic stall, parameters like solidity and pitch angle have a big impact on airfoil design. Together they set the range of Reynolds numbers, angles of attack and apparent wind speeds in which the blades have to perform, and not including them in the process will favor certain airfoils over other promising designs.

Future studies on this topic should focus on quantifying the impact of the viscous effects inside the dead band. Furthermore, some more attention could go out to perfecting automated methods used to generate airfoils at low Reynolds numbers. Shapes that are designed through a more thorough process might still achieve a good balance between start-up and nominal operation. Including parameters such as solidity, pitch angle and trip location seems vital to achieve good results.

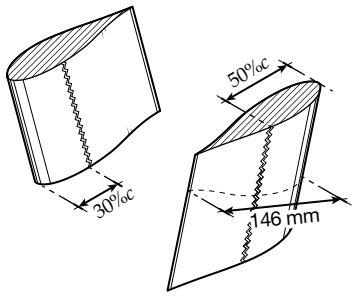

Figure 4: Geometry of the configuration optimized for start-up.

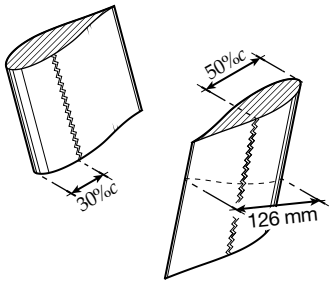

Figure 5: Geometry of the balanced configuration.

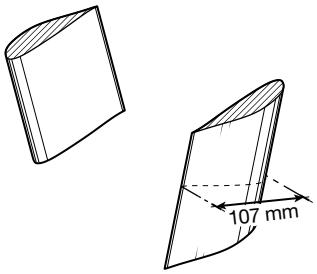

Figure 6: Geometry of the configuration optimized for maximum power.

Contents

Nomenclature

Symbols

A	Area	(m^2)
AR	Blade aspect ratio	(–)
a	Induction factor	(–)
b	Blade span	(m)
$C_{(\,)}$	Dimensionless force component	(–)
C_D	Drag coefficient (3D)	(–)
C_d	Drag coefficient (2D)	(–)
C_f	Skin friction coefficient	(–)
C_L	Lift coefficient (3D)	(–)
C_l	Lift coefficient (2D)	(–)
C_m	Pitching moment coefficient (2D)	(–)
C_n	Normal force coefficient (2D)	(–)
C_P	Power coefficient	(–)
C_p	Pressure coefficient	(–)
C_Q	Torque coefficient	(–)
C_T	Rotor thrust coefficient	(–)
C_t	Tangential force coefficient (2D)	(–)
c	Chord length	(m)
$\mathbf{D}$	Drag force	(N)
d	Diameter	(m)
E	Modulus of elasticity	(Pa)
e	Oswald efficiency factor	(–)
$\hat{\mathbf{e}}$	Unit vector	(–)
$\mathbf{F}$	Body force	(N)
f	Frequency	(Hz)
$\mathbf{g}$	Acceleration due to gravity	($m\ s^{-2}$)
H	Kinematic shape parameter	(–)
h	Rotor height	(m)
I	Second moment of area	(m^4)
J	Mass moment of inertia	($kg\ m^2$)
k	Reduced frequency	(–)

k_i	Induction factor exponent	(–)
$\mathbf{L}$	Lift force	(N)
l	Length	(m)
$\mathbf{M}$	Pitching moment	(N m)
M	Mach number	(–)
m	Blade mass	(kg)
$\mathbf{N}$	Normal force	(N)
N	Amplification ratio	(–)
n	Number of blades	(–)
P	Power	(W)
p	Pressure	(N m^{-2})
$\mathbf{Q}$	Torque	(N m)
q	Dynamic pressure	(N m^{-2})
R	Radius	(m)
Re	Reynolds number	(–)
$\mathbf{r}$	Radial coordinate	(m)
s	Stress	(Pa)
$\mathbf{T}$	Tangential force	(N)
$\mathbf{U}$	Wind speed	(m s^{-1})
u	Local velocity	(m s^{-1})
$\mathbf{V}$	Apparent wind speed	(m s^{-1})
$\mathbf{v}$	Induced velocity	(m s^{-1})
α	Angle of attack	(rad)
β	Flow skew angle	(rad)
Γ	Circulation	(m^2 s)
γ	Blade pitch angle	(rad)
δ	Boundary layer thickness	(m)
θ	Blade azimuth angle	(rad)
ϑ	Momentum thickness	(m)
κ	Von Kármán constant	(–)
Λ	Sweep angle	(rad)
λ	Tip speed ratio	(–)
μ	Dynamic viscosity	(Pa s)
ν	Kinematic viscosity	(m^2 s^{-1})
ξ	Arc of a helical blade	(rad)
ρ	Fluid density	(kg m^{-3})
σ	Rotor solidity	(–)
τ	Skin thickness	(m)
ϕ	Inflow angle	(rad)
χ	Wake skew angle	(rad)
$\mathbf{\Omega}$	Rotor speed	(rad s^{-1})
ω	Frequency	(rad s^{-1})

Subscripts

∞	Free stream
$\parallel$	Parallel to the leading-edge
$\perp$	Normal to the leading-edge
ac	Aerodynamic center
c	Camber
dyn	Dynamic
e	At the edge of the boundary layer
eff	Effective value
f	Friction
fict	Fictitious
gen	Generator
i	Inlet
mod	Modified
n	Natural frequency
o	Outlet
og	Ogive
r	In radial direction
ref	Reference value
ss	Static stall
z	In vertical direction
θ	In tangential direction

Abbreviations

BEM	Blade element momentum
CFD	Computational fluid dynamics
HAWT	Horizontal-axis wind turbine
HVAC	High voltage alternating current
HVDC	High voltage direct current
NACA	National Advisory Committee on Aeronautics
VAWT	Vertical-axis wind turbine
VG	Vortex generator

1 Introduction

The rising energy prices and the debate on sustainability has resulted in an increasing demand for decentralized energy production. Famous examples of this are roof-mounted photovoltaic arrays and small urban wind turbines, or *micro-turbines*. These devices are readily available on the market and, although often rated only a few kW, can help build a 'green image', save power costs and improve a building's energy efficiency[1].

Although the market for solar energy is booming, small wind turbines seem to be considerably less popular. Reasons for this include lack of policy, high initial investment costs and the public attitude towards wind energy. This is while the production of wind energy is often complementary with that of solar; periods of wind are frequently paired with bad weather, and vice versa. Still, it is often hard to receive a building permit to install a micro-turbine because of concerns for noise emissions and visual appearance. In the Netherlands, for instance, it is the position of the Dutch government that small windmills are too expensive and offer no serious potential for energy production (Cace and ter Horst, 2007, pp. 24–25). However, many of these concerns are, in fact, based on technological hurdles and can be overcome as the technology reaches maturity. This is why research and development is a key aspect in achieving market penetration.

In urban environments, vertical-axis wind turbines (VAWTs) perform exceptionally well due to their indifference to wind direction. However, they are plagued by poor start-up performance and generally require external power sources to accelerate from rest; for example by using an electric motor. Even though the amount of energy consumed during a start-up may be low, it involves extra complexity and is detrimental to the image of the device. The drawbacks that come with an active start-up are reason to investigate the self-starting capability of VAWTs and, in particular, the Turby MkIa. Turby is an urban VAWT of a Darrieus type and is rated at 1.6 kW. Currently, the device is started by relying on the generator's motor operation. Such a layout poses additional requirements on the electrical drive train; for instance the need for a bi-directional power converter. When the

[1] **In an attempt to cut CO_2 emissions, in 2003 the European Parliament and Council launched the *Directive on the energy performance of buildings* (EPBD), which required building owners to have an *Energy Performance Certificate* (EPC) at the moment of transaction. This label is a representation of a building's energy efficiency and helps to raise awareness and stimulate energy-saving measures (Haydock and Arbon, 2009, pp. i–iv).**

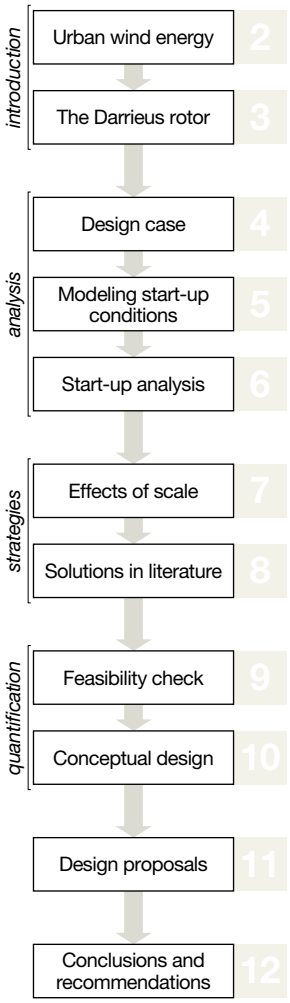

Figure 1.1: Report outline.

turbine is able to start up without external help, the whole configuration can reduce in complexity and costs.

This master project focuses on identifying strategies that could be used to boost the performance of small Darrieus turbines in start-up conditions. A collection of feasible solutions will then eventually form a design proposal for Turby. This process is shown in figure 1.1, which illustrates the coherent structure of the following chapters. First, chapter 2 gives a general introduction to urban wind energy and starts to introduce the Darrieus-type VAWT. Subsequently, several aspects of the Darrieus rotor are explored in chapter 3. Chapter 4 then discusses the design case and the research assignment in preparation for analysis. Next, chapter 5 treats the numerical tools at hand to predict the performance of VAWTs. These are then used in chapter 6 to help finalize the start-up analysis. Furthermore, a collection of different strategies to improve passive starting behavior is presented in chapters 7 and 8. From these solutions, several deserved special attention but need a prior feasibility check. These are treated separately in chapter 9. The remaining promising options are included in the conceptual design process in chapter 10 which will lead to the proposals presented in chapter 11. In conclusion, chapter 12 will summarize the important findings and will hand out some recommendations for future study.

2 Urban wind energy

Small urban wind turbines are safe, silent and aesthetic devices which, like photovoltaics, are a form of decentralized power generation. The motivation behind these kinds of building-integrated energy sources can be quite diverse; for instance to cut emissions, to be more independent from the volatile fossil fuel prices or to offer means to certify a building as energy-efficient. The development and integration, however, requires some technological and socio-economic hurdles to be overcome.

This introductory chapter will start off by briefly describing the nature of decentralized energy production in section 2.1. Next, section 2.2 describes how the wind is affected by the presence of buildings. Section 2.3 will then introduce the Darrieus-type rotor by comparing it to several of the many examples of wind energy conversion that have been proposed throughout history.

2.1 Decentralized energy production

The power grid as of today has emerged throughout the 20th century with the purpose of dividing and distributing the electrical energy generated by large central power plants. These production facilities rely on the efficiency and economy of scale: the bigger the conversion process, the less costs per kW[1]. Central locations are also convenient to set up supply lines of new fuel, but the choice for a site is also driven by several other factors. For example, pollution may force a coal-fired power plant to be set up far from inhabited regions; nuclear reactors will favor the availability of cooling water; a hydroelectric power plant will require a suitable spot to build a dam; etc. As a result, energy has to be transported from the producer to the customer, leading to transmission losses in the lines and transformers. This also means that it is difficult to reach remote sites. But what has been underestimated in the past, is that the large comprehensive network needed to distribute power has become more expensive than what is gained by the efficiency of scale (Lovins, 2002, pp. xii–xv).

[1] **Fossil fuels, for instance, burn more efficiently in a high volume combustion chamber.**

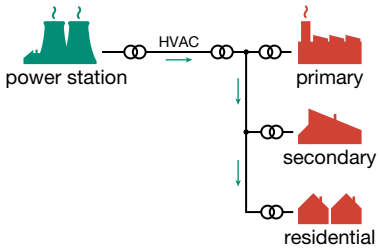

Figure 2.1: Conventional power grid where power from a central plant is distributed among different loads.

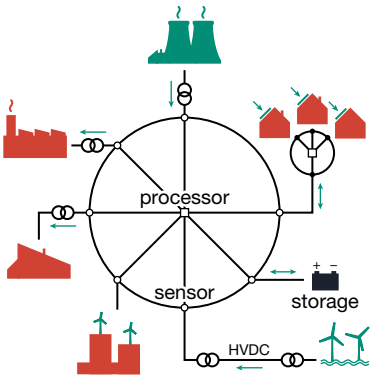

Figure 2.2: *Smart grids* can nurture decentralized power systems. Central processing units can react to faults picked up by sensors within microseconds.

A schematic of the conventional grid is shown in figure 2.1. After being produced in a power plant, electricity is transformed to 10 – 100 kV and fed to high voltage alternating current (HVAC) lines for transport. It is then transformed down in large substations to a medium voltage level. Subsequently, it is distributed to primary and secondary three-phase loads and ultimately to the low voltage grid. In the Netherlands, these voltage levels are 690 V, 400 V and 230 V, respectively.

The current rising need for (sustainable) energy require new ways of configuring the energy infrastructure. One of these aspects is *decentralized energy production*, which encompasses the generation of electricity from many small sources instead of one large central plant. This has several advantages. First—and most important—it allows the use of small-scale renewables, which can be mass-produced at a relatively low cost without the price volatility or negative externalities associated with fossil fuels. Second, there is a greater assurance of power since one large plant is more likely to fail than many smaller plants. And third, the development of micro power plants is especially useful for rural areas, which often rely on gasoline or diesel generators to charge batteries.

The connection between the many small generators can be made by a *smart grid* (see figure 2.2). These smart grids make use of ICT to be able to better match supply and demand while upholding the power quality. The demand can be controlled by shifting part of the automated loads to off-peak times. Also energy storage in large-scale systems (e.g. NaS batteries, compressed air energy storage, etc.) can be managed efficiently and faults in the grid can be better anticipated to. This relies on central processors to carry out procedures in order to maintain a set frequency, for instance by isolating areas from the main grid.

Popular examples of decentralized energy sources are solar panels and small wind turbines. These devices invite people to produce their own energy or even feeding it back to the grid. In urban areas, both solar panels and windmills can be mounted to buildings or even completely integrated, thereby producing electricity right where it is needed.

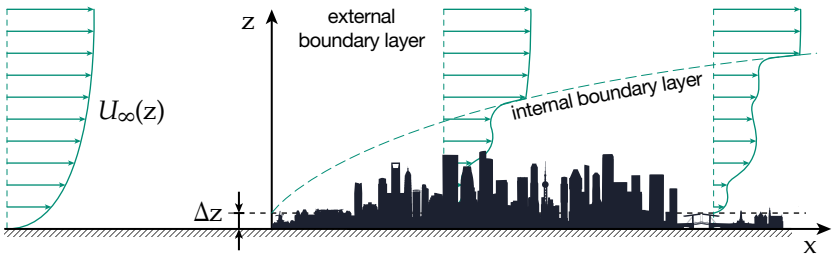

Figure 2.3: Development of an internal boundary layer (adapted from Mertens, 2006, p. 22).

Terrain description	z_0
Open sea; fetch at least 5 km	0.0002
Mud flats, snow; no vegetation, no obstacles	0.005
Open flat terrain; grass, few isolated obstacles	0.03
Low crops; occasional large obstacles ($x/h \geq 20$)	0.10
High crops; scattered obstacles ($15 \leq x/h \leq 20$)	0.25
Parkland, bushes; numerous obstacles, ($x/h \approx 10$)	0.5
Regular large obstacle coverage (e.g. suburb, forest)	1.0
City center with high- and low-rise buildings	≥ 2

Table 2.1: Examples of roughness lengths used by Wieringa (1980; adapted from Davenport, 1960). Here x/h refers to the spacing of obstacles with respect to their height.

2.2 FLOW AROUND BUILDINGS

Close to the ground, the horizontal wind speed, U_∞, is strongly determined by surface roughness. An elementary model to account for this is the log law, stated as

$$U_\infty(z) = \frac{u_f}{\kappa} \ln\left(\frac{z - \Delta z}{z_0}\right), \tag{2.1}$$

where z is the vertical coordinate, u_f the friction velocity, κ the von Kármán constant (≈ 0.41), Δz the zero plane displacement and z_0 the roughness height. The zero plane displacement is the height at which the wind speed is approximately zero due to tall objects such as buildings. The roughness height is a measure to account for the degree of roughness of the terrain. Table 2.1 shows some examples of terrain roughness heights.

When the wind approaches an urban area, there is a step in roughness height leading to the development of a new internal boundary layer (see figure 2.3). Outside of this boundary layer, the flow behaves according to the original upwind conditions. Inside, however, the flow is influenced by the local roughness and can vary strongly depending on the location. Especially flow separated from bluff bodies can lead to powerful eddies being shed. Under certain conditions, flow patterns such as the *von Kármán vortex street* can occur, caused by the interaction between vortices shed from the opposite sides of a body (see figure 2.4b).

At the upwind edge of a building's roof, flow will separate and cause regions of turbulence and recirculation, shown in figure 2.4a. This separation point will cause the flow close to the building to accelerate. Also it causes the velocity vectors to be skewed with respect to the horizontal plane. The skew angle tends to depend on the position of the roof, the upwind roughness height, the size of the building, the rounding of the upwind edge and the yaw angle of

Figure 2.4: Sketches of separated flow streamlines behind bluff bodies.

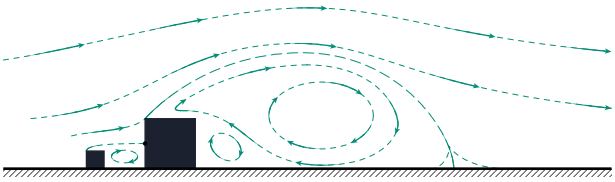

(a): Region of separated flow and reattachment. A high pressure stagnation point will exist on the facade of a building.

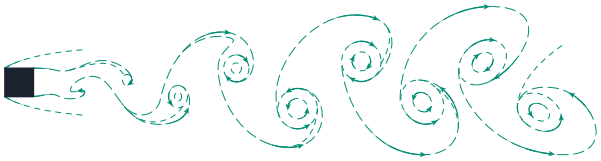

(b): A *von Kármán vortex street* caused by the interaction between pairs of vortices.

the free stream wind (i.e. the angle to the xz-plane) (Mertens, 2006, pp. 33–34).

For any wind turbine, the total energy yield increases when it is able to reach the higher wind speeds at high altitudes. Although the wind speeds inside the built environment are generally lower than in open terrain, tall buildings are often good locations to harvest wind energy. The case of skewed flow can result in some complexities, but can also offer opportunities for some turbine types, as will become clear in subsection 3.4.5.

2.3 THE DIVERSITY OF WIND TURBINES

Throughout history, many configurations of machines have been proposed to harvest energy from wind. The most common example is the modern three-bladed *horizontal-axis wind turbine* (HAWT), shown in figure 2.5a. These models generate torque, Q, through lift, implying that their blades generally travel at a velocity of multiple times the wind speed. The designation horizontal axis means that the axis of rotation lies parallel to the incoming wind vector, U_∞. Other iconic examples of HAWTs are the traditional Dutch windmill and the American-style windpump, shown in figures 2.5b and c respectively. An addition to HAWTs commonly seen in small urban wind mills is a *diffuser* (see figure 2.5d). Such a shroud around the rotor improves the aesthetic quality and leads to a higher negative back pressure, although the extra costs generally exceed what is gained in power output.

A variation on the common HAWT is the barrel-blade rotor which, instead of rigid airfoils, uses Flettner rotors (see figure 2.5e). This relies on the *Magnus effect*, which describes how friction forces on the surface of a spinning object can create circulation and eventually the generation of lift. This design has several disadvantages that limit its output; namely that part of the generated energy is used to power the blades, and that the cylindrical shape of the blades themselves leads to relatively high drag.

Two rather unconventional designs are shown in figures 2.5f and g. The first shows the *Andreau-Enfield wind turbine*. This design has hollow blades where the centrifugal forces draw out the air, leaving behind a low pressure region inside the tower. Energy from the resulting airflow can then be harvested by a smaller turbine. The second example is the *augmented vortex tower* which consists of an open cylindrical shell where the air is drawn in by opening several shutters. The combination with the freestream wind flowing over the device would then lead to the creation of a strong vortex. The low pressure core of this vortex is then the source of updraft that subsequently powers a turbine.

Figures 2.5h, i and j respectively show the use of a wing, Flettner rotor or kite mounted to a rail vehicle to create a forward thrust force, F. By placing several of these cars on a closed track—where the work done is extracted by generators connected to the axles—

one essentially creates a merry-go-round that is the equivalent of one very large rotor.

Next, figures 2.5k, l and m show examples of Darrieus rotors; named after their inventor, the French aeronautical engineer Georges Jean Marie Darrieus (1888–1979). They consist of a set of vertically orientated airfoils connected to a rotating shaft. Unlike the common horizontal-axis wind turbine, they are cross-flow devices, implying

Figure 2.5: Examples of wind energy conversion systems.

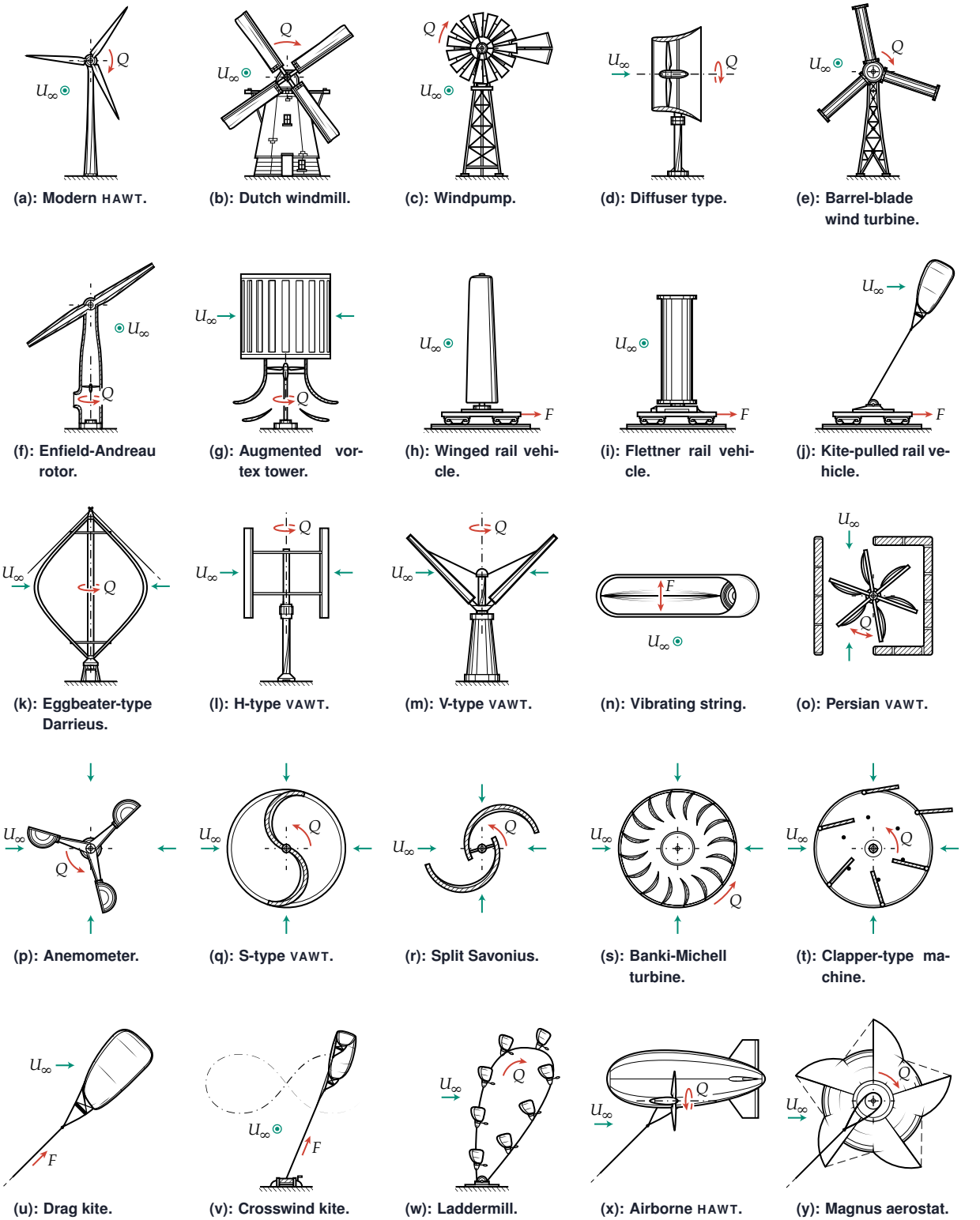

(a): Modern HAWT. (b): Dutch windmill. (c): Windpump. (d): Diffuser type. (e): Barrel-blade wind turbine.

(f): Enfield-Andreau rotor. (g): Augmented vortex tower. (h): Winged rail vehicle. (i): Flettner rail vehicle. (j): Kite-pulled rail vehicle.

(k): Eggbeater-type Darrieus. (l): H-type VAWT. (m): V-type VAWT. (n): Vibrating string. (o): Persian VAWT.

(p): Anemometer. (q): S-type VAWT. (r): Split Savonius. (s): Banki-Michell turbine. (t): Clapper-type machine.

(u): Drag kite. (v): Crosswind kite. (w): Laddermill. (x): Airborne HAWT. (y): Magnus aerostat.

that the direction of incoming flow is perpendicular to the axis of rotation instead of parallel. This allows the device to capture energy from every wind direction. These types of turbines are usually referred to as *vertical-axis wind turbines* (VAWT), although they could just as well operate horizontally. The Darrieus turbine has several advantages. First, the insensitivity to the wind direction makes a yaw mechanism unnecessary, which reduces complexity and costs. Second, the vertical shaft makes it possible to position the generator at the base of the tower, which avoids additional loads on the structure. Third, a Darrieus turbine might be more visually attractive, which is important when considering placement in urban environments. Also, a fourth point is that VAWTS can extract more energy from the turbulent flows shed by buildings, compared to propeller-types. However, the design is haunted by several problems, including its self-starting behavior, cyclic loads and protection from high wind speeds. In his original patent, Darrieus (1931) proposed several arrangements of straight and bent blades. The classic eggbeater design has long curved airfoils arched like a *troposkien*—after the Greek for *turning rope*)—preventing them from bending under centrifugal loads and leaving the stresses as pure tension. Additionally, this shape makes it easy for guy wires to support the tower. The downside is that these blades are also difficult to produce, transport and assemble. Other configurations include the H-type and V-type VAWTS.

The example in figure 2.5n is basically a string or belt that starts to vibrate as a result of aeroelastic flutter. The energy from this motion is then extracted by a linear actuator, much like magnetic pick-ups in an electric guitar. Although the yield from a single device is very low—in the order of milliwatts—it can compete with batteries to power small wireless devices. This technology is currently exploited by the American company Humdinger.

Although propeller-type rotors are considered to be the standard nowadays, many early windmill designs were in fact vertical-axis types. The most basic configuration of a VAWT is where the two halves of a rotor experience an unequal pressure force. For instance, in an ancient Persian design (see figure 2.5o) this differential resistance is provided by shielding part of the device by a wall. More commonly, however, a difference in drag is what generates the torque. Possibly the best known example is the *cup anemometer* shown in figure 2.5p. Other similar devices are the Savonius S-type and split S rotors, of which the latter one utilizes the airflow through its core to create additional pressure force. A *Banki-Michell turbine* is a drag device that is commonly used to extract energy from water flows, but is also widely seen in ventilation systems. Finally, a *clapper windmill* reduces the resistance of the upwind moving blades by allowing them to pivot like a weather vane. In downwind direction, the blades hit the stops to maximize their resistance again. Although drag-driven rotors can generate high torque, their efficiency is severely limited by the fact that their blades cannot travel faster than the wind itself.

The figures 2.5u, v and w show several ways to harvest energy at high altitudes by using kites. A *drag kite* is operated in an energy-yielding traction phase and an energy-consuming recovery phase. When power is produced, the kite is angled in such a way that the combination of the wind and the reel-out speed results in a maximum tether force (and vice versa during reel-in). This eventually results in a net power output. A *crosswind kite* operates in a similar fashion, but is steered in eight-figures in order to benefit from a higher lift force. The concept of a *laddermill* is a closed-loop pumping cycle built up from an array of kites where a central generator is powered continuously.

The final two examples, shown in figures 2.5x and y, are balloon systems. The first is essentially a HAWT mounted on a helium-filled aerostat. While this could greatly increase the available power, the fact that the generator is airborne means that electricity has to be transported to the ground and possible issues with safety might arise. The concept is worked out by the Canadian company LTA Windpower. The last example is a balloon that rotates because of the drag force generated by its vanes. A generator connected to its central axle then converts this motion into electricity, while an additional Magnus effect created by the rotation helps with stabilization. The device is patented by the American/Canadian company Magenn.

3 The Darrieus rotor

A Darrieus wind turbine is a vertical axis wind turbine (VAWT) invented by the French aeronautical engineer Georges Jean Marie Darrieus (1888–1979). It consists of a set of vertically orientated airfoils connected to a rotating shaft. Unlike the common horizontal-axis wind turbine (HAWT), it is a cross-flow device, implying that the direction of incoming flow is perpendicular to the axis of rotation instead of parallel. This allows the device to capture energy from every wind direction. However, the design is haunted by several problems, including its inability to self-start, cyclic loads and protection from high wind speeds. Also the aerodynamics are considered to be very complex, which make accurate performance predictions very difficult.

The purpose of this chapter is to analyze the working principle of this machine. First, a set of reference frames is defined in section 3.1, which will be used throughout this report. Then section 3.2 offers a concise and simplified approach to derive the governing equation of motion in 2D. A very important subject is the relation between the angle of attack and tip speed ratio and how it affects airfoil performance. This is dealt with in section 3.3. Next, a general discussion concerning the different subtopics of VAWT aerodynamics can be found in section 3.4. Finally, section 3.5 briefly treats some common ways to analyze the rotor numerically.

3.1 Frames of reference

First, it is convenient to set up a suitable set of reference frames. A stationary Cartesian system (x, y, z) can be fixed at the base of the

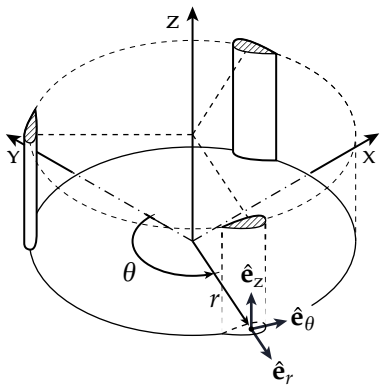

Figure 3.1: Cartesian and cylindrical coordinate systems with their origins fixed at the base of the rotor.

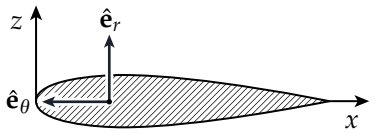

Figure 3.2: Coordinate system fixed to an airfoil's leading-edge.

rotor in a way that the x-axis points in the same direction as the incoming flow. In addition, a rotating cylindrical coordinate system (r, θ, z) can be defined containing the individual rotor blades, where the $0° \leq \theta \leq 180°$ describes the upwind half (see figure 3.1). Transformation between the two frames is done according to

$$\mathrm{x} = -r\sin\theta, \tag{3.1a}$$

$$\mathrm{y} = r\cos\theta, \tag{3.1b}$$

$$\mathrm{z} = \mathrm{z}. \tag{3.1c}$$

Attached to a rotating blade element, one can identify a set of unit vectors. The important ones are those defining the radial and tangential directions, given by

$$\hat{\mathbf{e}}_r = \begin{bmatrix} -\sin\theta \\ \cos\theta \\ 0 \end{bmatrix}, \tag{3.2a}$$

$$\hat{\mathbf{e}}_\theta = \begin{bmatrix} -\cos\theta \\ -\sin\theta \\ 0 \end{bmatrix}. \tag{3.2b}$$

A third reference frame is another Cartesian system (x, y, z) fixed to the leading-edge of an airfoil (see figure 3.2. This is especially useful when dealing with airfoil geometries.

3.2 TWO-DIMENSIONAL ROTOR DYNAMICS

Although the complicated rotor aerodynamics make the Darrieus turbine difficult to analyze, a simplified approach in 2D will help to understand its behavior and identify the governing parameters.

A blade element connected to the spinning rotor shown in figure 3.3) experiences a tangential velocity component due to rotation, $-\boldsymbol{\Omega} \times \mathbf{r}$, a local wind vector, $\mathbf{U}$, and an induced velocity, represented by $\mathbf{v}$. The latter term include the velocities induced by the wake and the interference between blades. The resulting component acting on the airfoil is the apparent wind velocity:

$$\mathbf{V} = \mathbf{U} + (-\boldsymbol{\Omega} \times \mathbf{r}) + \mathbf{v}. \tag{3.3}$$

This component hits the blade at a certain angle of attack with respect to the airfoil chord. This can be expressed as

$$\alpha = \arccos\left(\frac{\mathbf{V} \cdot -\hat{\mathbf{e}}_\theta}{\|\mathbf{V}\|}\right). \tag{3.4}$$

The angle of attack leads to the generation of lift, drag and a pitching moment; respectively given by

$$\mathbf{L} = C_l q c \left(\hat{\mathbf{e}}_\mathrm{z} \times \frac{\mathbf{V}}{\|\mathbf{V}\|}\right) dz, \tag{3.5a}$$

$$\mathbf{D} = C_d q c \frac{\mathbf{V}}{\|\mathbf{V}\|} dz, \tag{3.5b}$$

$$\mathbf{M} = C_m q c^2 \hat{\mathbf{e}}_\mathrm{z} dz, \tag{3.5c}$$

where c is the airfoil chord and q the upwind dynamic pressure, which is defined as

$$q \equiv \tfrac{1}{2}\rho\,(\mathbf{V} \cdot \mathbf{V})\,, \tag{3.6}$$

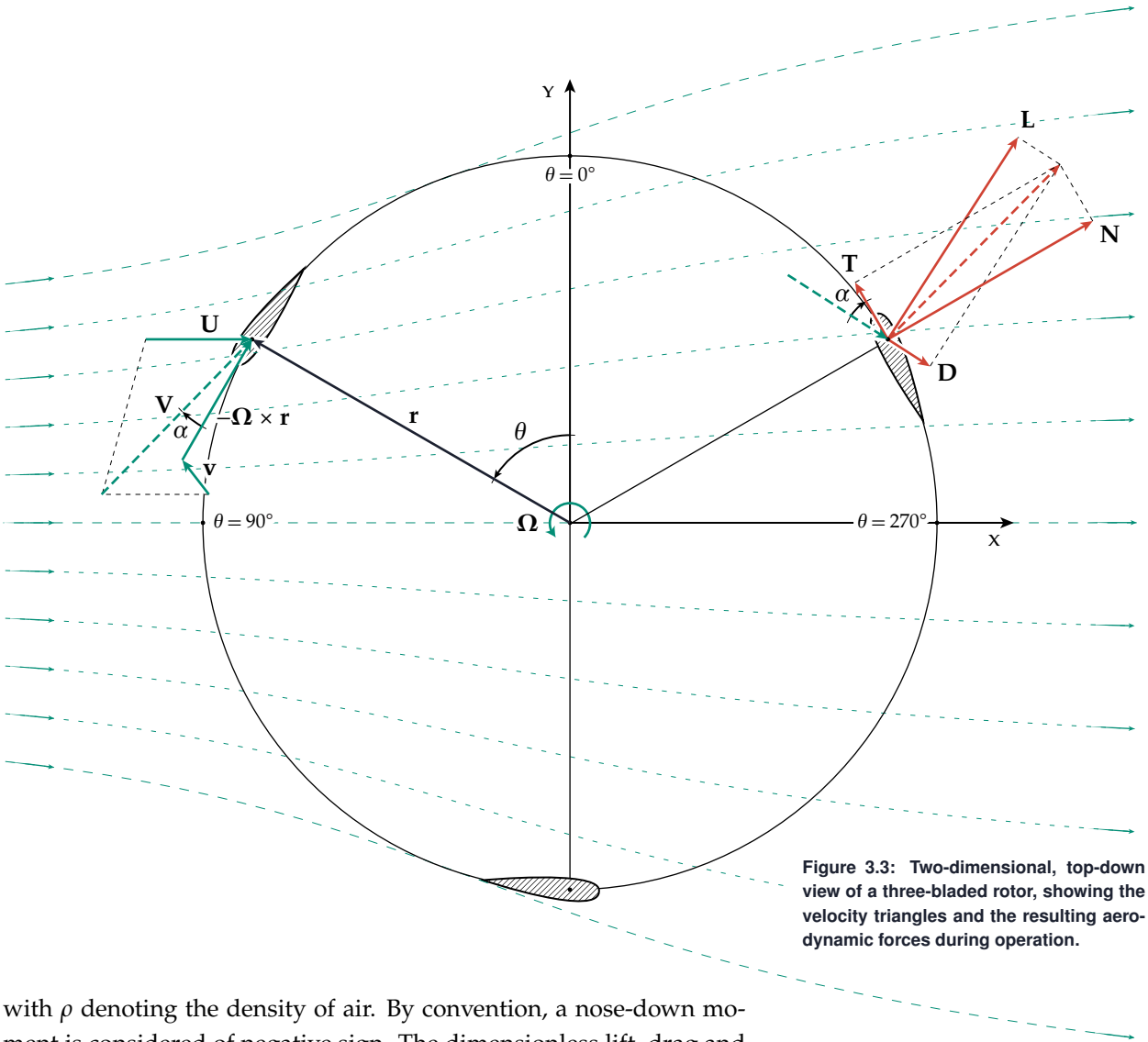

Figure 3.3: Two-dimensional, top-down view of a three-bladed rotor, showing the velocity triangles and the resulting aerodynamic forces during operation.

with ρ denoting the density of air. By convention, a nose-down moment is considered of negative sign. The dimensionless lift, drag and pitching moment coefficients (C_l, C_d and C_m) are further examined in figure 3.4. The contribution to the total torque can be expressed more explicitly by decomposing the lift and drag coefficients into tangential and normal force coefficients; corresponding to **T** and **N**:

$$C_n = C_l \cos\alpha + C_d \sin\alpha, \tag{3.7a}$$

$$C_t = C_l \sin\alpha - C_d \cos\alpha. \tag{3.7b}$$

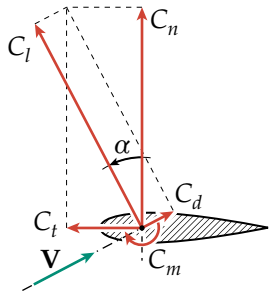

Figure 3.4: Lift, drag and pitching moment coefficients acting on the aerodynamic center of a blade cross-section.

Apart from pressure forces, additional fictitious forces may exist as a result of the rotating frame of reference. They are described by

$$\mathbf{F}_{\text{fict}} = -m\frac{dz}{h}\Big(\underbrace{\ddot{\mathbf{r}}_o}_{\substack{\text{acceleration}\\ \text{of the origin}}} + \overbrace{\dot{\boldsymbol{\Omega}} \times \mathbf{r}}^{\substack{\text{increment in}\\ \text{rotor speed}}} + \underbrace{\boldsymbol{\Omega} \times (\boldsymbol{\Omega} \times \mathbf{r})}_{\text{centripetal acceleration}} + \overbrace{2\boldsymbol{\Omega} \times \dot{\mathbf{r}}}^{\substack{\text{Coriolis}\\ \text{acceleration}}}\Big). \tag{3.8}$$

where m is a blade's mass and h the rotor height. Here, $\ddot{\mathbf{r}}_o$ refers to

the acceleration of the origin. This term is negligible when the axis of rotation is perfectly stationary, but may play a role when the tower is subject to, for instance, a swaying motion. The last term refers to the Coriolis effect and can be ignored when the rotation radius does not change with time, which is true for a rigid structure.

The primary equation of motion corresponds to the rotation around the z-axis. Using equations (3.5a), (3.5b), (3.5c) and (3.8), this can now be stated as

$$J\ddot{\theta} + Q_{\mathrm{f}} = -Q_{\mathrm{gen}} + \sum_{i=1}^{n} \mathbf{r}_i \times \left(\mathbf{L}_i - \mathbf{D}_i + \mathbf{F}_{\mathrm{fict},\,i}\right). \tag{3.9}$$

where J is the total moment of inertia of the rotor around the z-axis, Q_{f} the torque due to friction, Q_{gen} the generator torque[1] and n the number of blades.

[1] When $Q_{\mathrm{gen}} < 0$, the generator operates as a motor.

In many cases, it is convenient to use a dimensionless torque and power to make them independent from the operating conditions. The torque and power coefficients are then given by

$$C_Q \equiv \frac{Q}{\frac{1}{2}\rho U_\infty^2 A R}, \tag{3.10}$$

$$C_P \equiv \frac{P}{\frac{1}{2}\rho U_\infty^3 A}, \tag{3.11}$$

where A is the frontal rotor area ($A = 2Rh$ for a VAWT) and R the rotor radius. The subscript ∞ indicates free stream conditions.

3.3 AIRFOIL PERFORMANCE

In comparison to fixed-wing aircraft, the aerodynamics of rotor blades are much more complex. Especially for VAWTS in start-up, the flow conditions vary continuously.

3.3.1 Angle of attack and tip speed ratio

When assuming that the direction and magnitude of $\mathbf{U}$ remains constant throughout the rotor, the situation is reduced to its simplest form. This implies that

$$\mathbf{r} = \begin{bmatrix} -R\sin\theta \\ R\cos\theta \\ 0 \end{bmatrix}, \quad \boldsymbol{\Omega} = \begin{bmatrix} 0 \\ 0 \\ \dot{\theta} \end{bmatrix}, \quad \mathbf{U}(\mathrm{X},\mathrm{Y}) = \begin{bmatrix} U_\infty \\ 0 \\ 0 \end{bmatrix},$$

In this case, equation (3.4) can be rewritten to

$$\alpha = \arctan\left(\frac{\sin\theta}{\lambda + \cos\theta}\right), \tag{3.12}$$

where λ denotes the tip speed ratio defined as

$$\lambda \equiv \frac{\dot{\theta} R}{U_\infty}. \tag{3.13}$$

Apart from the great dependence on the angular position, θ, the angle of attack variation of a blade is strongly determined by the tip speed ratio, λ. This dependence can best be illustrated through a

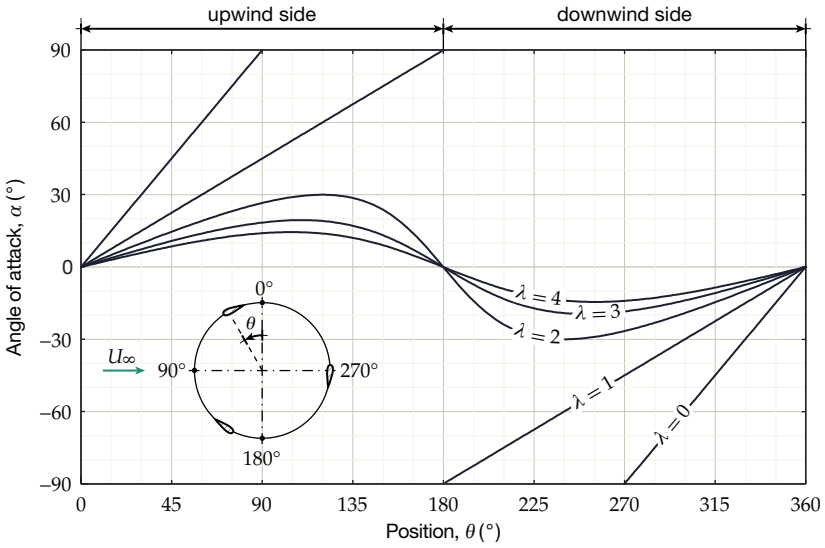

Figure 3.5: (*left*) Angle of attack experienced by a blade during a rotation cycle (without induction).

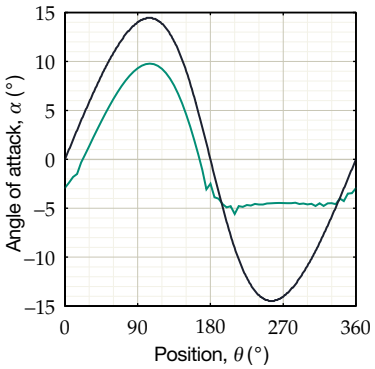

Figure 3.6: (*above*) Variation in angle of attack at $\lambda = 4$, as result of evaluating equation (3.12) (—) in comparison to a more realistic case (—) (Simão Ferreira, 2009, p. 35).

plot, shown in figure 3.5. At $\lambda = 0$, the blade experiences only the wind speed and its angle of attack simply varies linearly with its position. Consequently, when the rotor is at rest, it has to cope with a wide range of angles of attack ($-180° \leq \alpha \leq 180°$) and up to the point when $\lambda = 1$, the apparent wind speed can approach an airfoil from the rear. It is only when $\lambda > 1$ that a blade experiences a headwind at every position (allowing α to drop to zero at $\theta = 180°$).

The assumption made to derive equation (3.12) will never hold in practice. Nevertheless, the tip speed ratio remains a key parameter that governs the behavior of a VAWT. In reality, the downwind half of the rotor is strongly influenced by the vorticity shed by the upwind half and figure 3.5 would look more like figure 3.6. These complexities are discussed in the next section.

3.3.2 Laminar separation bubbles

At Reynolds numbers below 1,000,000, airfoil performance is predominantly determined by laminar separation bubbles. In these conditions, a boundary layer may still be laminar when it approaches the suction peak over an airfoil. Instead of entering the regular transition process, it separates from the surface right away. Transition will occur as the separated flow grows unstable and fluid can reconnect as a thick turbulent boundary layer which is able to withstand the higher pressure gradient and leaving behind a *laminar separation bubble*. This phenomenon leads to a loss in momentum—caused by the turbulent mixing inside the bubble and dissipation into heat—referred to as *bubble drag*. At $\mathrm{Re} < 150{,}000$, bubble drag often dominates the total drag (Drela, 1988).

The profile drag can be expressed as the momentum loss within the boundary layer, which can be expressed as

$$D'(x) = \rho \int_0^{\delta(x)} u\,(u_\mathrm{e} - u)\,dz, \tag{3.14}$$

where $\delta(x)$ is the boundary layer thickness at a point x and u_e is the

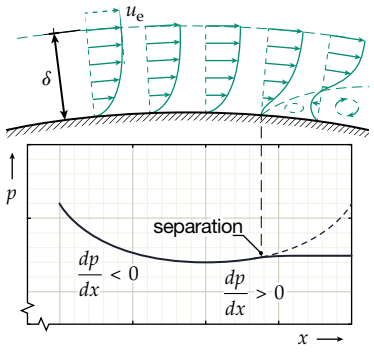

Figure 3.7: Sketch of a pressure gradient within a boundary layer (adapted from Leishman, 2006, p. 356).

velocity at the edge of the boundary layer (see figure 3.7). This can instead be given as a function of a momentum thickness, ϑ:

$$D'(x) = \rho u_e^2 \vartheta, \tag{3.15}$$

$$\vartheta = \int_0^\delta \frac{u}{u_e}\left(1 - \frac{u}{u_e}\right) dz. \tag{3.16}$$

The streamwise development of the momentum deficit is governed by the *von Kármán integral momentum equation*:

$$\tfrac{1}{2} C_f = \frac{d\vartheta}{dx} + (2 + H)\frac{\vartheta}{u_e}\frac{du_e}{dx}. \tag{3.17}$$

For the purpose of evaluating the drag of separation bubbles, Drela (1988) expresses the above as

$$\frac{1}{\rho u_e^2 \vartheta}\frac{d\left(\rho u_e^2 \vartheta\right)}{dx} = \frac{C_f}{2\vartheta} - \frac{H}{u_e}\frac{du_e}{dx}, \tag{3.18}$$

where H is the kinematic shape parameter and C_f is the skin friction coefficient. The shape factor is defined as

$$H = \frac{\delta^*}{\vartheta}. \tag{3.19}$$

Here, δ^* is the displacement thickness, which is used to describe the displacement of the outer streamlines in order to satisfy the principle of continuity. The shape parameter can be a useful measure to determine when separation is about to occur; high values of H denote strong adverse pressure gradients. Taken from White (2004, p. 471), separation can be expected at approximately

$$H \approx \begin{cases} 3.5 & \text{(laminar flow)} \\ 2.4 & \text{(turbulent flow)} \end{cases} \tag{3.20}$$

Inside the separation region, the skin friction coefficient can be assumed to be zero, leading to

$$\frac{\Delta\rho u_e^2 \vartheta}{\rho \bar{u}_e^2 \vartheta} \approx -H\frac{\Delta u_e}{\bar{u}_e},$$
$$\Delta\rho u_e^2 \vartheta \approx -\rho\Delta\rho\bar{u}_e\delta^*\Delta u_e. \tag{3.21}$$

From this, it can be concluded that the bubble drag is proportional to the average mass defect and the drop in edge velocity.

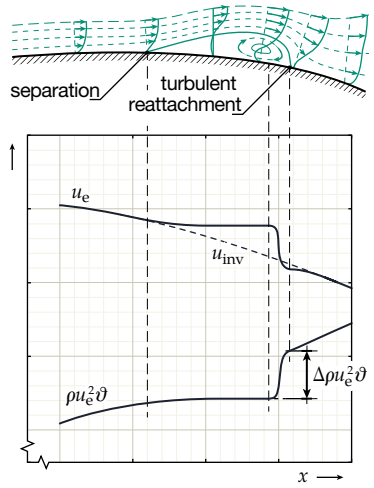

Figure 3.8: Sketch of momentum losses inside a laminar separation bubble (adapted from Drela, 1988).

Figure 3.8 shows how the terms u_e and $\rho u_e^2 \vartheta$ vary within a laminar separation bubble[2]. After the flow separates, the pressure distribution flattens out to a nearly constant value. During transition, the adverse pressure gradient increases to some peak value and the boundary layer may or may not attach as turbulent. Whether or not reattachment takes place will depend on the ability of the recovery pressure to re encounter the inviscid pressure distribution over the bubble. When the inviscid pressure gradient is too steep—for instance as result of a strong curvature or a high angle of attack—the two do not meet and the bubble will burst, leaving the airfoil in a stalled condition.

[2] **A negative du_e/dx implies a positive dp/dx, or an *adverse pressure gradient*.**

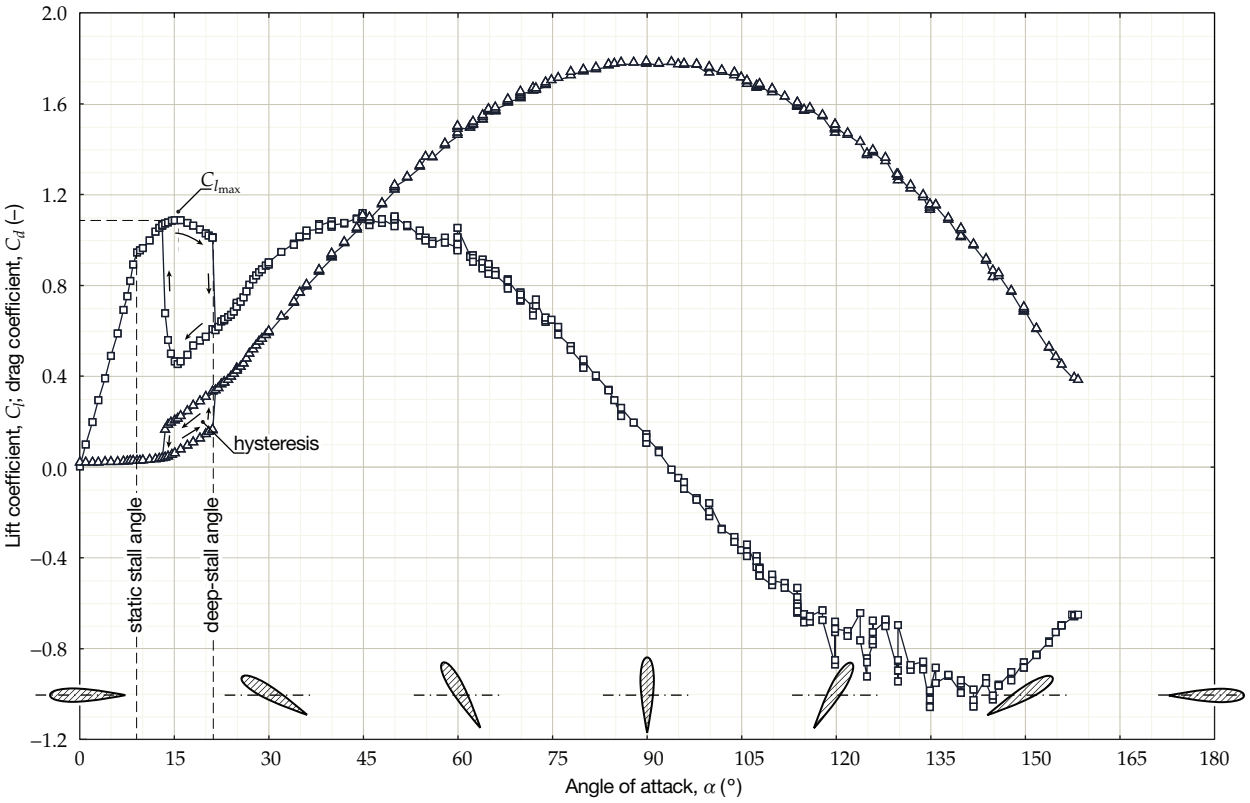

Figure 3.9: Lift (□) and drag (△) coefficients of a NACA0018 symmetric airfoil at $\mathrm{Re} = 500,000$, obtained from wind tunnel tests performed at Delft University of Technology.

3.3.3 Stall characteristics

At low Reynolds numbers, the stalling modes often fall into the three categories described by Gault (1957). The bursting of the laminar separation bubble at high angles of attack describes what is called *leading-edge stall*. Alternatively, a bubble can also be involved in *thin airfoil stall* generally found in airfoils with sharp noses. This is where the reattachment point keeps moving aft until the chord is completely enveloped by the separation bubble. The result is a fairly gentle stall behavior, in contrast to the sudden drop in lift that occurs with leading-edge stall. The third type of stall is *trailing-edge stall*, and happens when the point of boundary layer separation gradually travels forward from the trailing-edge. Trailing-edge stall is often exhibited by thicker airfoils and causes a round curve near $C_{l_{max}}$.

Since the airfoils of a VAWT often have to operate outside of the design conditions, the full lift and drag curves become relevant. An example is depicted in figure 3.9, showing data from a NACA 0018 symmetric airfoil over the full range of angles of attack[3]. At $\alpha \approx 9°$, the increase in lift becomes nonlinear as flow begins to separate from its top surface. Since this point marks the onset of dynamic stall (discussed in subsection 3.4.4), this is often referred to as the *static stall angle* when discussing unsteady aerodynamics. Past the point of maximum lift, the *deep stall angle* is reached. This causes massive separation from the leading-edge, resulting in a large sudden drop in lift accompanied by an equally abrupt increase in drag. When the angle of attack is decreased again, the airfoil has entered a hysteresis

[3] For a symmetrical airfoil, the data is identical for negative angles of attack

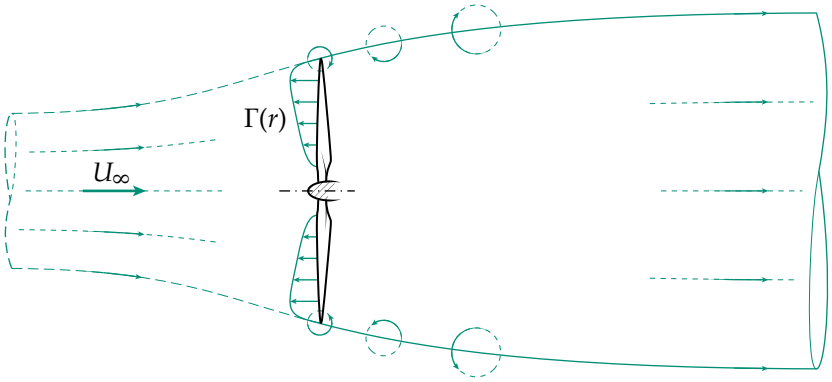

Figure 3.10: Streamtube containing a horizontal-axis wind turbine where bound circulation is steadily shed in radial direction.

loop, preventing flow to re-attach. In the high-angle-of-attack region, drag forces begin to dominate as the section starts to behave similar to a flat plate. The flow will also start to separate alternately from the leading-edge and trailing-edge, which is also the cause of the spread of measurement points in figure 3.9. At $\alpha > 90°$, flow comes up to the airfoil from behind and the lift force reverses in sign. When α approaches 180°, the flow tries to attach to the sharp corner of what is now the leading-edge, increasing the lift again.

3.4 ROTOR AERODYNAMICS

When compared to horizontal-axis wind turbines (HAWTS), the transverse rotor plane of the Darrieus machine lead to all sorts of complications. This section will discuss some of the principal aspects of the aerodynamics in more detail.

3.4.1 The near wake

For a HAWT, circulation across the blade span is shed in a continuous fashion, leaving behind a rotating vortex sheet. The strength of the trailing vorticity at a radial position r equals the change in bound circulation at the lifting line, reaching a maximum at the tips. The common approach to model a HAWT is to represent it by an infinitely thin actuator disc inside a streamtube, as depicted in figure 3.10.

The wake of a cross-flow device is fundamentally different (Simão Ferreira, 2009, pp. 11–16). Because the angles of attack are continuously changing, the lift forces vary significantly during a cycle. A change in circulation over a segment $d\theta$ is $d\Gamma = (d\Gamma/d\theta)d\theta$ and is compensated by the shedding of a vortex of an equal strength $-d\Gamma$ (see figure 3.11). This is the result of *Kelvin's theorem*, stating that the total circulation around a closed curve remains constant with time:

$$\frac{D\Gamma}{Dt} = 0. \tag{3.22}$$

Near $\theta = 0°$ and $\theta = 180°$, the angle of attack and the resulting lift force are zero, meaning that all vorticity is shed.

In the 3D case, the finite blade span causes circulation to be cast off at the tips. This is directly related to the aspect ratio, defined as

$$\mathrm{AR} \equiv \frac{b}{c}, \tag{3.23}$$

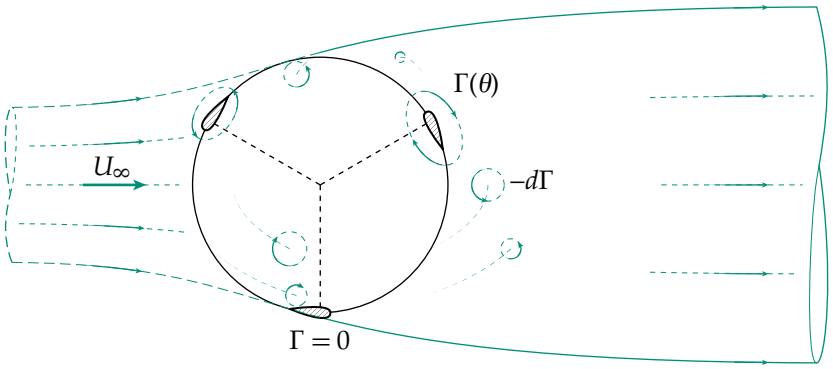

Figure 3.11: Streamtube containing a vertical-axis wind turbine. Here, circulation is cast off at different angular positions and at unequal rates.

where b is the blade span. The presence of a trailing vortex here is related to energy loss, represented by a loss in lift and an *induced drag* term:

$$C_L = C_l \left(1 + \frac{C_l}{\pi \mathrm{AR} e}\right)^{-1}, \tag{3.24a}$$

$$C_D = C_d + \frac{C_L^2}{\pi \mathrm{AR} e}, \tag{3.24b}$$

where e is the *Oswald efficiency factor*[4]. The capital subscripts here refers to the 3D, finite span configuration. Strong perturbations in angle of attack exist in the downwind half of the rotor as a consequence of the trailing vortex shed by the upwind trajectory. This is clear from CFD calculations by Scheurich et al. (2010) shown in figure 3.12. Near $\theta = 90°$ the bound circulation, Γ, reaches its peak value during the upwind blade passage. Large deviations in tangential force can therefore be expected downwind of that position near $\theta = 270°$.

[4] The *Oswald factor* incorporates the variation of the profile and parasitic drag elements with lift. This is due to the changes in the flow field caused by an angle of attack. It also indicates how close the ideal (elliptical) lift distribution is obtained.

3.4.2 Unsteady aerodynamics

The consequence of the ever-changing angle of attack is that the blades of a VAWT follow a pitching motion, $\dot{\alpha}$. A governing parameter in unsteady aerodynamics is the *reduced frequency*[5], k, which is the frequency of the pitching motion, ω, non-dimensionalized according to

$$k = \frac{\omega c}{2V}. \tag{3.25}$$

[5] This is, in fact, equivalent to the Strouhal number which is often used to describe oscillating flows.

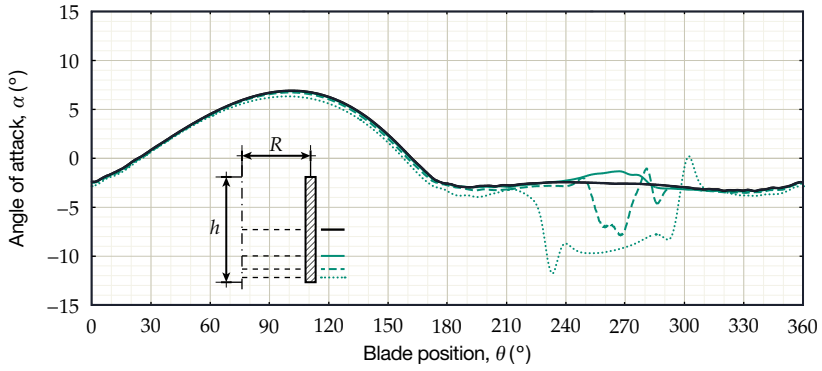

Figure 3.12: Angle of attack experienced by straight NACA 0015 blade elements at $z/h = 0.500$ (—), 0.250 (—), 0.125 (– –) and 0.045 (····) at $\lambda = 5$ (Scheurich et al., 2010).

In the case of a fixed-pitch turbine, the frequency experienced by the blades follow the rotor speed, such that $\omega = \dot{\theta}$.

According to Leishman (2006, p. 427), in a case where $0 \leq k \leq 0.05$, the flow can be regarded as quasi-steady and it is often justified to neglect the unsteady effects. Cases where $k \geq 0.05$ can be regarded as unsteady. Situations where $k \geq 0.2$ are considered highly unsteady and are often dominated by unsteady aerodynamics. Since the apparent wind, V, is so changeful, it is hard to determine the magnitude of k exactly. Even so, it can still give a useful ballpark figure on the degree of unsteadiness at various tip speed ratios. Nonzero values of k often lead to the presence of *virtual camber* and *dynamic stall*; topics which are addressed in the following two subsections.

3.4.3 Virtual camber

As a blade element moves along its circular path, its changing angle of attack causes the lift curve to deviate from the static case. Partially, this is a result of flow curvature effects. Because the flow is rotating, an airfoil experiences a vertical velocity perturbation along its chord. In an equivalent rectilinear flow, it behaves as having *virtual camber* (see figure 3.13) which inherently affects the generated lift.

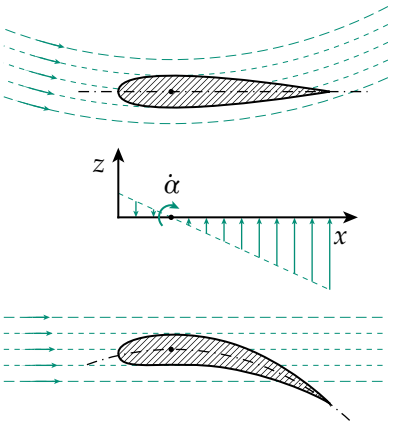

Figure 3.13: An airfoil in a rotating flow experiences *virtual camber* when compared to rectilinear flow (here strongly exaggerated.

Analogously, if one considers that the blades of a VAWT are not point masses but instead have a finite chord length, it is clear that the airfoil spans over a certain arc of its trajectory. Consequently the angle of attack varies along the chord according to the function $\alpha(\theta)$. The degree of induced camber scales with both c/R and λ. For larger diameter rotors, the blade chord is small compared to the total circumference and therefore the deviations of α become insignificant.

3.4.4 Dynamic stall

Past the static stall angle, the pitching motion causes an effect called *dynamic stall*. This phenomenon is inherent to oscillating wings and extends the lift curve past the point of stall under static conditions (see figure 3.14).

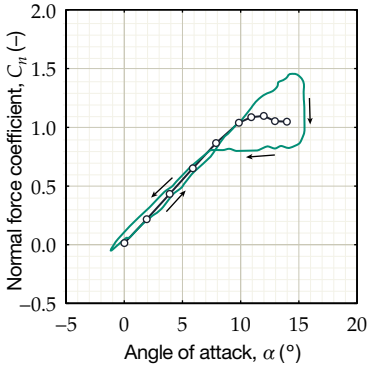

Figure 3.14: Example of a curve showing the normal force coefficient on a NACA 0012 airfoil under static (○) and dynamic stall conditions (—) for a pitching motion $\alpha(t) = 7.1° + 8.4° \sin \omega t$ at $k = 0.075$ (Leishman, 2006, p. 532).

When the airfoil moves past the static stall angle, flow separation is delayed by the effects of virtual camber, the influence of the shed wake and the unsteady response of the boundary layer (Leishman, 2006, pp. 528–529). At higher angles, flow which was separated due to leading-edge stall tends to roll up. This vortex then briefly grows in strength, detaches and travels in chordwise direction (see figure 3.15). Here it creates a strong suction effect, enhancing lift in a linear fashion and moving the center of pressure towards the rear of the airfoil. Meanwhile, a trailing-edge vortex of an opposite motion starts to build up as well. Finally, the leading-edge vortex separates at the trailing-edge, returning the airfoil normal stall conditions (Larsen, 2005, pp. 55–58). When the pitching motion is reversed to the point where the angle of attack is low enough again, it takes a while for the flow to be able to reattach again. In addition, there is a presence of virtual camber that affects the airfoil properties. This causes the airfoil to enter a hysteresis loop that also lowers the values for α at which full flow reattachment is achieved.

The intensity of dynamic stall strongly depends on the reduced frequency and therefore also on the tip speed ratio. Although the structure of the generated vortices remains more or less the same for different values of λ, the point of separation and the point of reattachment varies. Fujisawa and Shibuya (2001) visualized the flow field around a Darrieus rotor and noticed that actually two separate pairs of counter-rotating vortices develop in the wake. Their paths are illustrated in figure 3.16. The first pair contains vorticity that has been shed earlier when the linear growth of the leading-edge vortex came to a halt. The other pair is composed of the rolled-up vorticity and tends to move along with the airfoil, possibly leading to interaction when the blade passes downwind again (Simão Ferreira et al., 2009). But at high λ, the blades may not even reach their static stall angle.

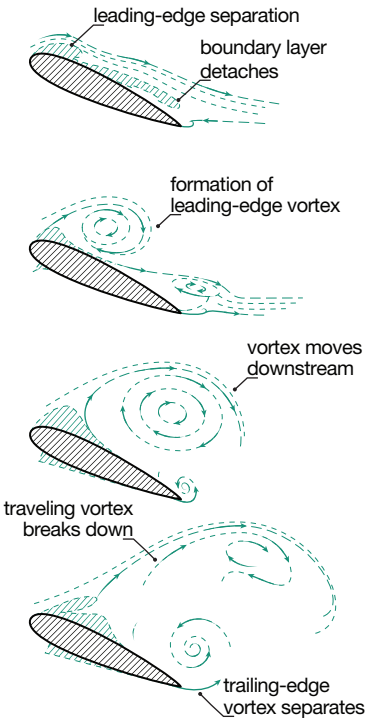

Figure 3.15: Flow over an airfoil during dynamic stall (adapted from Nørkær Sørensen, 1999, cited in Larsen, 2005, p. 58).

3.4.5 Skewed flow

Especially in urban areas the incoming wind is often not perfectly aligned in the XY-plane, but instead travels at a skew angle β. This is often the case on a roof, and it is here that the performance of a Darrieus rotor can truly excel over that of a propeller-type HAWT.

This is visualized in figures 3.17a and b, showing a horizontal disc and a cylinder of equal frontal area. In skewed flow, a single propeller disc essentially operates in yaw. Consequently, its power output is decreased since the rotor's thrust force is no longer aligned with the direction of the incoming flow. While this is also the case for a Darrieus rotor, they have the extra advantage that the skew angle causes part of the downwind blade passage to operate outside the wake of the upwind half. The result is that a larger rotor area is able interact with the undisturbed flow. This was verified experimentally by Mertens et al. (2003) and later by Simão Ferreira et al. (2009). The fraction of this area with respect to the total frontal area—based on the multiple streamtube model of Mertens et al. (2003)—is given by

$$\frac{A^*}{A} = \frac{1}{\pi}\int_0^{\pi} \frac{2R}{h}\tan\bar{\beta}\sin\theta d\theta; \quad \text{for } \bar{\beta} \leq \arctan\left(\frac{h}{2R}\right), \tag{3.26}$$

where $\bar{\beta}$ is the weighted average skew angle through the rotor vol-

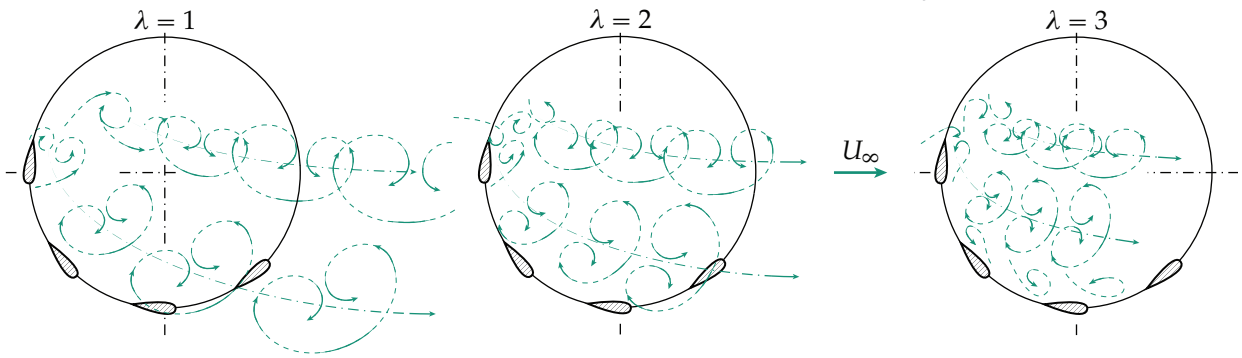

Figure 3.16: Paths taken by two pairs of separated vortices through a rotor during dynamic stall (adapted from Fujisawa and Shibuya, 2001).

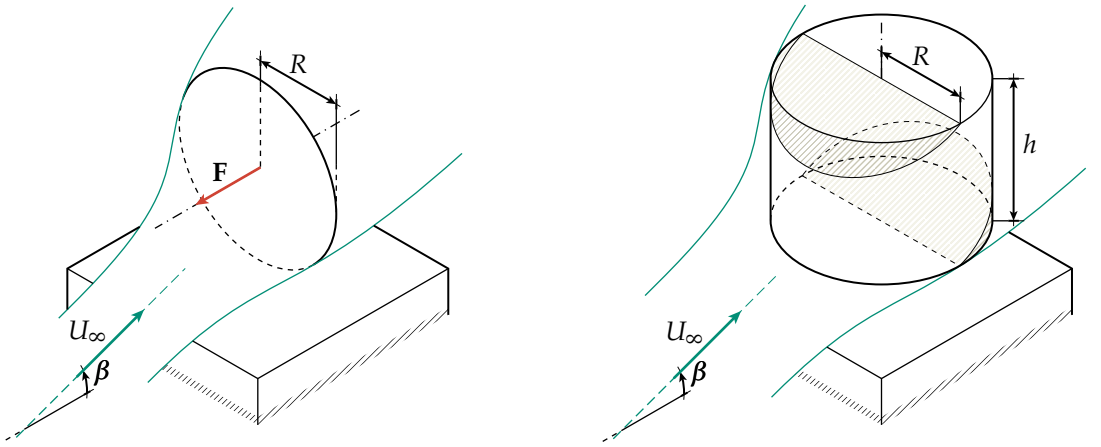

(a): Simplified sketch of a HAWT in the skewed flow over a roof.

(b): Sketch of a VAWT in skewed flow. The shaded areas represent the positions that only interact once with the flow.

Figure 3.17: While skewed flow can decrease performance for a propeller disc, it can increase the power output for a cylindrical rotor.

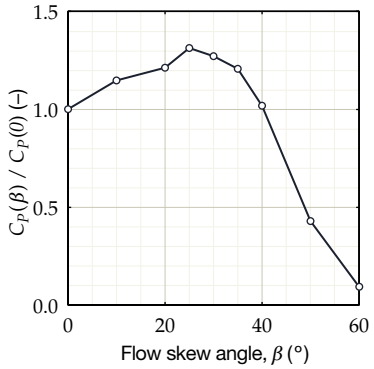

Figure 3.18: Gain in power for a straight-bladed VAWT (NACA 0018, $h/R = 1.3$, $c/R = 0.21$) as a function of the flow skew angle (Mertens et al., 2003).

ume. This evaluates to

$$\frac{A^*}{A} = \frac{4R}{\pi h} \tan \bar{\beta}. \tag{3.27}$$

Naturally, by increasing the rotor radius, R, relative to the height, h, the effect becomes even more notable. Vice versa, decreasing the ratio h/R will make the rotor more independent of the skew angle.

Another consequence treated by Scheurich and Brown (2011) is that, by ignoring the vertical component of the wind vector, the rotor finds its tip speed ratio increased by a factor $1/\cos\lambda$. The power coefficient is then

$$C_P(\lambda, \beta) = C_P\left(\frac{\lambda}{\cos\beta}, 0\right) \cos^3\beta. \tag{3.28}$$

For optimal performance, the rated tip speed ratio is therefore different than one would expect in the case of $\beta = 0°$. Equation (3.28) also shows that, at higher skew angles, the advantages disappear because of the dependence on $\cos^3\beta$. Wind tunnel measurements by Mertens et al. (2003) on a particular straight bladed Darrieus revealed that there is a positive gain for a considerable range β (see figure 3.18).

3.4.6 Helical blades

For a VAWT, the aerodynamic forces can vary strongly during a rotation cycle, resulting in strong time-dependent loads. Apart from the fact that these pulsating normal and tangential forces reduce the structure's fatigue life, they will also cause the turbine's output power to vary strongly with time.

A straightforward method to get rid of the pulsating torque is to use helical blades, as proposed by prof. Alexander Gorlov of Northeastern University in Boston, Massachusetts. A helical design ensures that there is always a blade section at each possible angle of attack. The resulting *Gorlov turbine* is claimed to have better efficiency than straight-bladed rotors, no torque fluctuation and self-starting capability in slow fluids (Gorlov, 1998, p. 7). The device, registered

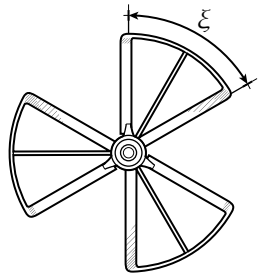

Figure 3.19: Plan view of a helical Darrieus rotor.

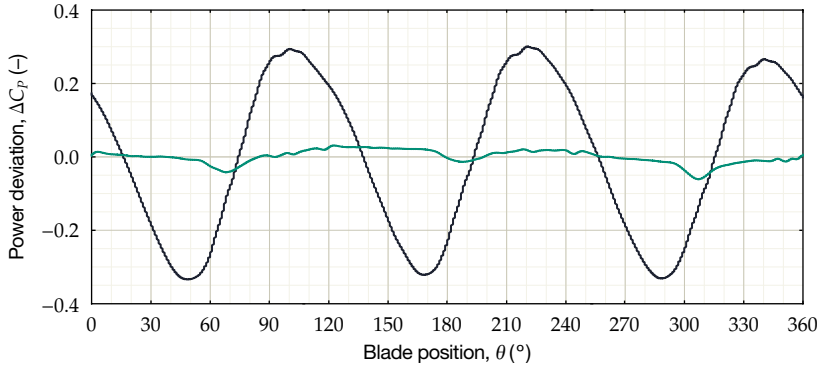

Figure 3.20: Deviations in power coefficient for a straight-bladed Darrieus (—) compared to a helical design with a $\xi = 120°$ blade arc (—) (Scheurich et al., 2010).

in a series of patents from 1995 onwards, now forms the basis for most modern Darrieus wind turbines.

The degree of twist of the blades can be expressed by the blade arc ξ, defined as the phase shift between the bottom ($z = 0$) and top blade element ($z = h$) (see figure 3.19). The effect of $\xi = 120°$ on the power output is well visible in the CFD simulations of Scheurich et al. (2010) (see figure 3.20). The output is not perfectly unsteady, however. This is because the helix induces an asymmetric wake. Moreover, the vorticity at the blade tips is still shed at different positions.

3.4.7 Sweep

When dealing with skewed flow, helical blades, or a combination of the two, a situation arises where the blade's leading-edge is not normal to the incoming flow. For helical turbines, the blades are inclined in the tangential plane and have a certain *sweep angle* that directly follows from the rotor geometry according to

$$\tan \Lambda = \frac{R\xi}{h}. \tag{3.29}$$

Compared to straight-blade geometry, the span of a helical blade increases to

$$b = \frac{h}{\cos \Lambda}. \tag{3.30}$$

Blade sweep leads to a fairly complex three-dimensional flow field and can affect performance in several ways. The classic rule of thumb is to assume that the airfoil only considers the flow normal to the leading-edge according to the *independence principle* (see figure 3.21). In practice this seems to apply fairly well for steady and unsteady flow up until stall (Leishman, 2006, pp. 548–551). For VAWTS this has two major consequences. Firstly, by ignoring the parallel velocity component, a swept blade inherently produces less lift. The effective lift coefficient is then given by

$$C_l = C_{l_\perp} \cos^2 \Lambda, \tag{3.31}$$

where $C_{l_\perp}$ is the lift coefficient of the airfoil section normal to the leading-edge. Secondly, the streamlines are deflected out of the XY-plane. The change in momentum is accompanied by an additional

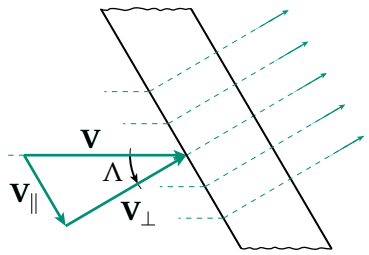

Figure 3.21: When dealing with swept geometries; matters can be simplified by assuming that a blade section is only affected by the velocity component normal to the leading-edge.

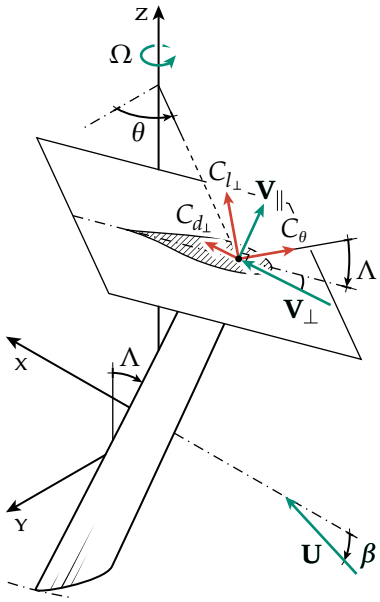

Figure 3.22: An element belonging to a blade inclined by an angle Λ.

force on the fluid in z-direction, which is at the expense of the tangential force. To visualize this, consider the blade depicted in figure 3.22 which leans forward by an angle Λ. The plane containing the relevant blade strip is now rotated by the same angle. By ignoring the parallel velocity component, $\mathbf{V}_\parallel$, the result is essentially the projection of the apparent wind on this plane. The lift and drag coefficients—as well as the tangential force—by definition lie in the same plane. The tangential force component is then

$$C_\theta = \left(C_{l_\perp} \sin\alpha_\perp - C_{d_\perp} \cos\alpha_\perp\right) \cos\Lambda. \tag{3.32}$$

When the incoming flow is skewed, sweep can also be used to decrease the angle of the incoming flow with respect to the leading-edge. The ideal sweep angle for this purpose would then depend on the nominal tip speed ratio and the mean skew angle, since those two parameters determine the direction of the apparent wind speed.

3.5 AERODYNAMIC MODELS

When trying to predict the performance of a VAWT, the challenge is to determine the apparent wind speeds, angles of attack and induced velocities per location. This involves incorporating all the aerodynamic effects discussed in the previous section. Since the 1970s, many numerical models have been developed to achieve this. Because the aerodynamics of a VAWT are so complex, these models often cope with severe limitations and low precision; although more elaborate calculation methods have been developed in recent studies with the help of computational fluid dynamics (CFD). An overview of aerodynamic models used to treat Darrieus turbines is presented by Islam et al. (2008).

3.5.1 Momentum models

The common approach to model a HAWT is to represent it by an infinitely thin actuator disc inside a streamtube, as depicted in figure 3.23. Here, the energy extracted by the rotor is represented by the change in the flow's axial momentum:

$$P_{\text{rot}} = \tfrac{1}{2}\rho A_0 U_0^3 - \tfrac{1}{2}\rho A_2 U_2^3, \tag{3.33}$$

where A_0 and A_2 are the cross-sections of the streamtube far upstream and far downstream of the rotor, respectively. These two parameters can be eliminated from the equation by applying the continuity equation and assuming a constant flow velocity through the rotor. This rotor velocity is reduced by an induction factor, a, according to

$$U_1 = (1-a)U_0. \tag{3.34}$$

In addition, it can be shown through *axial momentum theory* that

$$U_2 = (1-2a)U_0, \tag{3.35}$$

implying that

$$U_1 = \frac{U_0 + U_2}{2}. \tag{3.36}$$

This eventually leads to

$$\begin{aligned} P &= \tfrac{1}{2}\rho U_0^3 C_P A_1 \\ &= 2\rho A_1 U_0^3 a(1-a)^2. \end{aligned} \tag{3.37}$$

When solved for the maximum coefficient, this yields the Lanchester-Betz-Joukowsky limit, stating that $C_{P_{\max}} = \frac{16}{27}$ (59.3%).

A rather straightforward way to analyze the Darrieus rotor is therefore to also represent it by a *single actuator disc model*. Although equation (3.33) holds, the actual energy extraction plane is not one-dimensional and the rotor speed is not uniform. Using this model, the calculated rotor power is always higher than what is found in practice (Islam et al., 2008).

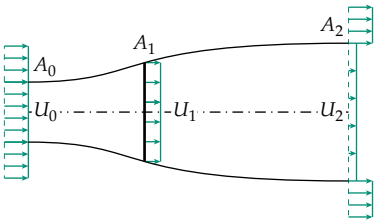

Figure 3.23: *Single disc model* where the rotor is modeled by one actuator disc.

Because most of the streamlines cross the blade trajectory twice, instead the rotor can be represented by two discs: each accounting for the upwind and downwind half of the rotor. This *double actuator disc model* splits the rotor speed up by including two induction factors (see figure 3.24):

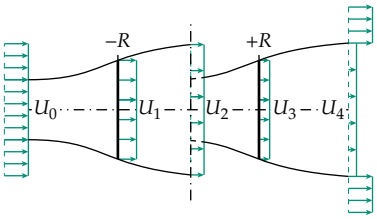

Figure 3.24: *Double disc model* where the upwind and downwind passages are represented by separate actuator discs.

$$U_1 = (1-a)U_0, \tag{3.38a}$$
$$U_2 = (1-2a)U_0, \tag{3.38b}$$
$$U_3 = (1-a')(1-2a)U_0, \tag{3.38c}$$
$$U_4 = (1-2a')(1-2a)U_0. \tag{3.38d}$$

In this model, the flow from the upwind half of the rotor is supposed to fully develop before passing through the second disc. This is a very gross assumption, since the unsteady aerodynamics inherent to the Darrieus rotor make it behave totally different than two HAWTS in series.

More sophisticated than using a single streamtube, is the *multiple streamtube model*. Here, the flow through the rotor is split up as several parallel streamtubes, each having a span corresponding to a fixed angle $\Delta\theta$ (see figure 3.25). This way, one can include a velocity distribution through the rotor or account for wind shear effects (Strickland, 1975, pp. 1–2).

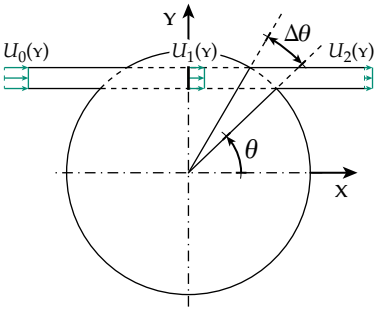

Figure 3.25: *Multiple streamtube model* where the flow is split up into several parallel tubes corresponding to an angle $\Delta\theta$.

A crossing between the latter two models is the *double-multiple streamtube model*, introduced by Paraschivoiu (1981). This again increases the accuracy by making a distinction between the upwind and downwind sides, as well as by allowing a velocity distribution between different streamtubes.

3.5.2 Vortex model

The vortex model was first used in VAWTS by Larsen (1975; cited in Islam et al., 2008), who applied it on a variable pitch machine and neglected stall effects by assuming small angles of attack. Over the years, the effects of dynamic stall, blade curvature, apparent mass[6] and tip losses have gradually been included.

Vortex models are based on potential flow and represent a lifting surface by a circulation of strength Γ (see subsection 3.4.1). The lift per unit span, L', generated by this bound vortex is given by the

[6] Under dynamic conditions, a blade has to accelerate the surrounding fluid with it. This causes the blade to behave as if it was heavier by an amount called the *apparent mass*.

Kutta-Joukowsky theorem:

$$L' = \rho V \Gamma. \tag{3.39}$$

Any changes in lift then result in the shedding of vorticity following Kelvin's theorem, stated in equation (3.22). The velocity induced by a vortex filament of a finite length $\mathbf{l}$ at a distance $\mathbf{r}$ is given by the Biot-Savart law:

$$d\mathbf{v} = \frac{\Gamma}{4\pi} \frac{d\mathbf{l} \times \mathbf{r}}{|\mathbf{r}|^3}. \tag{3.40}$$

With the induced velocity field known, the apparent wind speeds can be determined which are required to predict the pressure forces and, with it, the strength of circulation. The downside of vortex models is that they require a lot of computation time in general. Also it requires problems to be simplified by assuming potential flow throughout the domain.

3.5.3 Cascade model

The cascade model has been widely used to describe turbomachinery, but was first applied to VAWTs by Hirsch and Mandal (1987; cited in Islam et al., 2008). Here, the blade airfoils are lined up in a straight cascade of length $2\pi R$ normal to the rotor axis (see figure 3.26). The conditions for every section are assumed to equal that of the center reference blade. The wind speed just upstream of a blade is determined by two separate induction factors for the upwind and downwind halves:

$$\frac{U_\mathrm{u}}{U_0} = \left(\frac{U_1}{U_0}\right)^{k_\mathrm{i}}, \tag{3.41a}$$

$$\frac{U_\mathrm{d}}{U_0} = \frac{U_1}{U_0}\left(\frac{U_2}{U_1}\right)^{k_\mathrm{i}}, \tag{3.41b}$$

where k_i is an empirically determined constant which scales with the rotor solidity. The total torque is then found through the apparent wind speed and angle of attack at the cascade inlet (i) and outlet (o) according to

$$Q = \rho h R^2 \int_0^{2\pi} \left(V_\mathrm{o}^2 \sin\alpha_\mathrm{o} \cos\alpha_\mathrm{o} - V_\mathrm{i}^2 \sin\alpha_\mathrm{i} \cos\alpha_\mathrm{i}\right) d\theta. \tag{3.42}$$

According to Islam et al. (2008), the cascade model delivers quite accurate results while demanding reasonable computation time. It can be used for both low and high solidity rotors and even at high tip speed ratios.

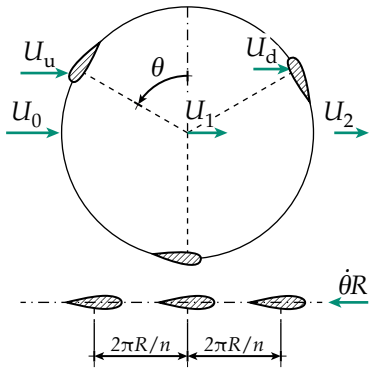

Figure 3.26: ***Cascade model*** **where the blades are lined up in a cascade configuration.**

4 Design case

The scope of this report is to improve the self-starting behavior of a VAWT. Here, the emphasis is on a particular rotor: the Turby, which has been developed in cooperation with Delft University of Technology.

The Turby project has been pioneered by Dick Sidler, who recognized the potential of urban wind energy and set out to find a suitable model for the purpose. At the time, the commercially available machines were inefficient and the choice fell on a completely new design. The aerodynamics was treated by dr. Sander Mertens, who was doing research on concentrator effects of buildings. The result was Turby: a Darrieus-type rotor able to efficiently extract energy from the skewed flow over tall buildings (Mols, 2005).

In this chapter, the case of the Turby is introduced in section 4.1. Next, section 4.2 shows a list with requirements that drove the original design, and which would naturally also apply to any solutions. Finally, the goal of this project is briefly stated in section 4.3.

4.1 Turby

The Turby MkIa, shown in figure 4.1, is a small wind turbine designed to operate within the urban boundary layer and in the skewed flow over the roofs of tall buildings. Placement in the urban environment means that the design is restricted by several requirements concerning noise emissions and vibrations. In order to guarantee low sound and vibration levels, the turbine is fit with three helical blades and operates at a relatively low tip speed ratio (van Bussel et al., 2004). The specifications of the Turby rotor are given in table 4.1.

Currently the device is started by relying on the generator's motor operation, which consumes around 1 kJ over 20 – 25 s. During operation, the electrical frequency is monitored and the rotor speed is regulated through a four-quadrant AC-DC-AC converter. Up to the rated wind speed the turbine operates at its maximum power point

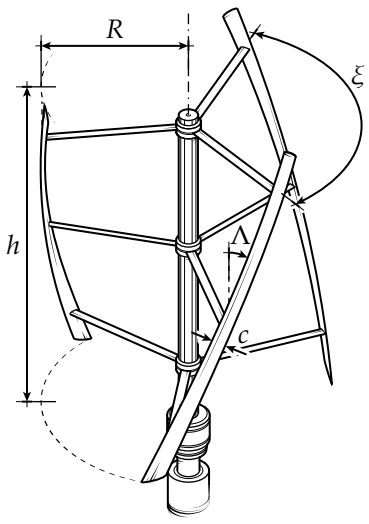

Figure 4.1: Sketch of the MkIa rotor, showing some of the geometry parameters tabulated in table 4.1.

Table 4.1: Specifications of the Turby Mkla rotor.

Operation		cut-in	rated	max	cut-out
Wind speed (m/s)	U	3	11	18	>25
Rotor speed (rpm)	Ω	–	378	378	378
Blade speed (m/s)	ΩR	–	44	44	44
Tip speed ratio (–)	λ	–	4.0	2.4	1.7
Power (kW)	P	–	1.3	2.5	–
Peak power coefficient (–)	$C_{P_{\max}}$	–	0.27	0.12	–

Geometry		
Airfoil		DU 06-W-200
Rotor height (m)	h	2.65
Rotor diameter (m)	$2R$	2.20
Number of blades	n	3
Blade chord (mm)	c	117.7
Blade aspect ratio (–)	AR	24.3
Rotor solidity (–)	σ	0.175
Blade arc (°)	ξ	60
Blade inclination angle (°)	Λ	23.5
Total mass (m)		150
Mass moment of inertia (kg m^2)	J	30

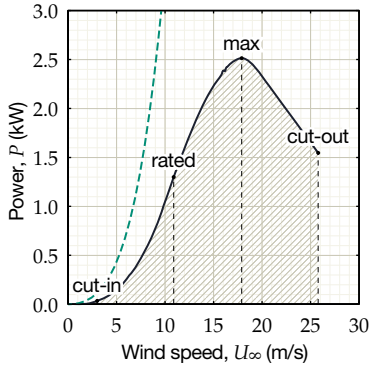

Figure 4.2: Power extracted by the Turby Mkla (—) compared to the available wind power (– –). Also indicated are the important wind speeds.

at $\lambda \approx 3.5 - 4.0$. When the rated wind speed is reached (see figure 4.2), the rotation speed is kept steady at 378 rpm. In extreme conditions, the control system is able to brake the rotor by short-circuiting. In reality, however, the optimal tip speed ratio is hard to determine without testing in controlled conditions, like in a wind tunnel. Actual wind speeds are highly variable and the rotor speed is never really steady. The tip speed ratios listed in table 4.1 are purely based on equation 3.13, using the fixed rotor speed maintained by the controller.

4.2 DESIGN REQUIREMENTS

For any modifications to the rotor to be successful, they have to comply with several requirements that drove the original design. They can be summed up as follows:

- *Performance*. The rotor has to perform well in the wide variety of wind speeds inherent to the urban environment. Preferably, the peak performance region in the C_P-λ curve should be as broad as possible. Also, a solution for self-starting should not compromise the total power output.
- *Noise emissions*. Especially in inhabited regions, the device has to be quiet. In the Netherlands, the noise emitted by wind turbines is limited by regulations. A weighted average of 47 dB is allowed, measured at the facade of a given building. During nighttime, there is a tight maximum of 41 dB (Agentschap NL, 2011).
- *Reliability*. The final design has to be structurally sound, simple and allow for easy maintenance.
- *Appearance*. Especially in inhabited regions, any additions to the rotor should not make it very unattractive. However, the aesthetic quality is very subjective and therefore hard to define[1].

[1] **Stankovic et al. (2009, pp. 88–89) give an example of an aesthetic turbine having a smooth, streamlined and modern-looking shape, while a turbine of low aesthetic quality appears crude and industrial.**

- *Vibration levels*. The structure's eigenmodes have to be avoided since mechanical vibrations can harm the device and the platform it is mounted on.
- *Capital costs*. Even when an addition to the rotor has the potential to earn itself back, it might scare away customers if it greatly raises the purchase price.
- *Safety*. During operation, no safety risks should occur.

4.3 RESEARCH ASSIGNMENT

The ultimate goal of this project can be summarized as a brief research assignment or mission statement:

> Revise the design of Turby to allow it to self-start from a point of rest to $C_{P_{\max}}$ at its cut-in wind speed of 3 m/s, while honoring the requirements that drove the original design and without compromising the total energy yield.

This encompasses the elimination of the regions of negative power from the $C_P - \lambda$ curve by improving low-speed performance. The next chapters discuss some of the possible strategies to achieve this.

5 Modeling start-up conditions

A common approach to model a vertical-axis rotor is to use airfoil data for an average Reynolds number or to assume completely inviscid flow conditions. Usually, the induced errors are acceptable for high tip speed ratios or high Reynolds numbers. A start-up of a small turbine like Turby is the complete opposite, however. The static stall angle is encountered regularly and—especially at low tip speed ratios—the variations in Reynolds number become increasingly important.

The purpose of this chapter is to discuss a modeling strategy to be used for the remaining work. First, section 5.1 treats the generation and processing of viscid airfoil data. The wake of the complete rotor is assessed in 2D, using a vortex panel method explained in section 5.2. Section 5.3 then summarizes the important assumptions and simplifications made throughout the process.

5.1 Viscid airfoil data

An important part of modeling start-up conditions is predicting how the blades behave under different Reynolds numbers. This is done in several steps, which are discussed in this section.

5.1.1 RFOIL

RFOIL is a model based on XFOIL that uses a panel method combined with boundary layer equations to predict the performance of 2D subsonic airfoils. This helps with performing quick design iterations without having to physically place specimens in a wind tunnel. The original XFOIL was first developed in the 1980s by Mark Drela at MIT. RFOIL is an extension of XFOIL, accomplished in a joint effort by

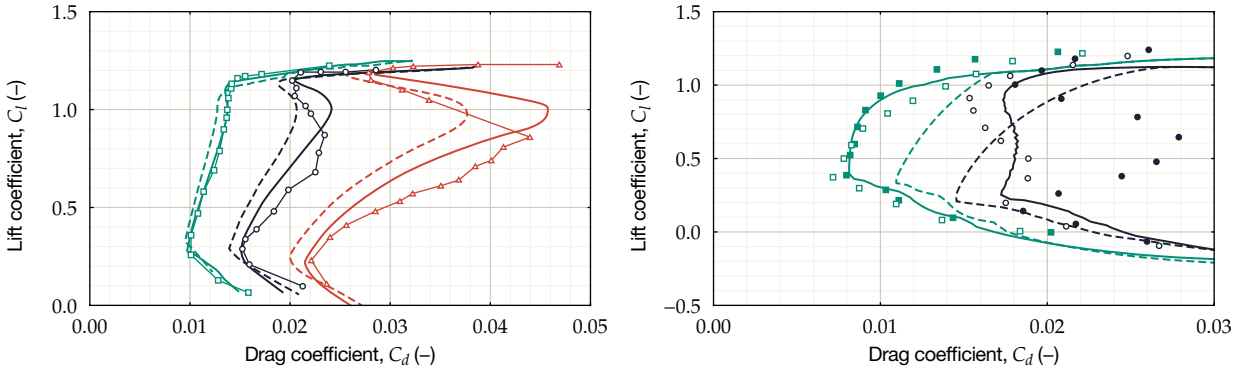

(a): Measurements of Eppler 387 at $\mathrm{Re} = 60,000$ (△), 100,000 (○) and $\mathrm{Re} = 200,000$ (□), compared to XFOIL predictions at $N_{\mathrm{crit}} = 9$ (– –) and 12 (—) (Drela, 1989).

(b): Measurements of SA7026 at $\mathrm{Re} = 100,000$ (●) and $\mathrm{Re} = 300,000$ (■), compared to RFOIL (—, —). Included is a boundary layer trip at 10%c (○, □, – –, – –) (Gopalarathnam et al., 2003).

Figure 5.1: Wind tunnel data compared to XFOIL and RFOIL predictions.

the Delft University of Technology, the Energy research Center of the Netherlands (ECN) and the National Aerospace Laboratory (NLR).

5.1.2 Validity of RFOIL predictions

A tool like XFOIL/RFOIL is, of course, merely a representation of real life. As figures 5.1a and b illustrate, accuracy tends to diminish at very low Reynolds numbers[1].

[1] Some more examples of this can be found in appendix A.

Laminar separation bubbles, for example, can be sources of error when they are present over parts of the airfoil modeled with a low panel resolution. Another issue is the uncertainty of predicting the free stream turbulence level and setting an appropriate amplification factor (see subsection 5.1.4). Furthermore, the drag coefficient in XFOIL is obtained by extrapolating the momentum thickness to the wake by using the Squire-Young formula (Drela, 1995). When trailing-edge separation is present, the assumption that justifies this method is violated and erroneous results can be expected. In any case, regions of separation—included those associated with separation bubbles—correspond to nonlinearities which will cause predictions to be off. Since this especially affects the low-Reynolds-number range, results at these conditions cannot be blindly trusted.

5.1.3 Large angles of attack

Although being a convenient tool for the design phase, RFOIL has troubles with convergence at lower Reynolds numbers ($< 10^5$) and close to separation. This limits the boundary of application to the range between plus and minus the static stall angle. For larger angles, an airfoil can be related to an ideal flat plate according to

$$C_l = \sin 2\alpha, \tag{5.1a}$$

$$C_d = 2\sin^2 \alpha. \tag{5.1b}$$

An airfoil is different from a flat plate in the sense that its thickness grants it more lift at the cost of a higher drag. It has been put forward that the maximum drag coefficient can be expressed as a function the leading-edge thickness (e.g. Gault, 1957). The reasoning behind this

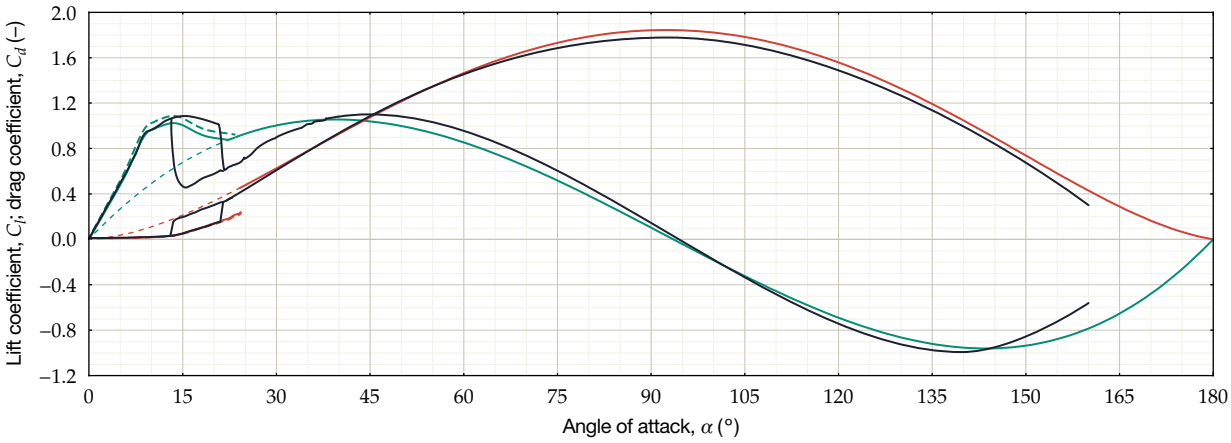

Figure 5.2: Approximated lift (—) and drag (—) coefficients of a NACA 0018 computed with RFOIL at $\mathrm{Re} = 500,000$ and $N_{\mathrm{crit}} = 11$; compared to smoothed wind tunnel data (—). The dashed lines (, – –) represent corrected values to better match the real-life case.

is that, at large angles of attack, the drag is dominated by pressure forces over the upper surface. Some examples from literature are given by Lindenburg (2003, pp. 11–16), where the normal force is related to several geometric parameters, such as the nose radius and the trailing-edge angle. A more straightforward relation is given by Timmer (2010):

$$C_{d_{\max}} = 1.994 - 5.4375 \frac{z_{1.25\%c}}{c}, \tag{5.2}$$

where the maximum drag coefficient is related to the upper surface thickness taken at $x = 1.25\%c$. Referring to Hoerner and Borst (1985, p. 21-1), Lindenburg (2003) argues that the normal force on a flat plate can be related to a maximum drag coefficient according to

$$C_n = C_{d_{\max}} \frac{\sin\alpha}{0.56 + 0.44\sin\alpha}. \tag{5.3}$$

Moreover, the tangential force of starting VAWTs can be approximated by

$$C_t = |C_n| \sqrt{\frac{r_0}{c}} \left(0.3 - 0.55\cos\alpha\right), \tag{5.4}$$

where r_0 is the airfoil nose radius.

In order to validate the above, the expressions are used to complement the RFOIL predictions of a NACA 0018 section at $\mathrm{Re} = 500,000$. They are plotted together with the wind tunnel data—shown earlier in figure 3.9—in figure 5.2. This again shows that RFOIL is able to predict the regions of fully attached flow fairly well. However, when separation starts to occur, larger errors start to show that can lead to false predictions. Even so, the data is definitely usable as long as the linear lift regime is represented correctly. In this range, RFOIL's predictions are about 5% off, and correction factors of $C_l^* = 0.95 C_l$ and $C_d^* = 1.05 C_d$ seem appropriate. The aerodynamic coefficients beyond this point are most likely dominated by the onset of dynamic stall anyway; as will be discussed in section 5.1.5. In the high α region, the lift curve seems inaccurate. This may be due to a bad fit, but can also be caused by the fact that unsteady vortex shedding makes it hard to obtain good quality static measurements. Even so, equations (5.3) and (5.4) are still convenient to use because it allows one to distinguish between airfoil geometries.

Table 5.1: (*left*) Typical values of N_{crit} for various situations as listed in the XFOIL manual (Drela, 1995).

Situation	N_{crit}	Turbulence level
Sailplane	12–14	0.009–0.020%
Motorglider	11–13	0.013–0.030%
Clean wind tunnel	10–12	0.020–0.046%
Average wind tunnel	9	0.070%
Dirty wind tunnel	4–8	0.106–0.563%

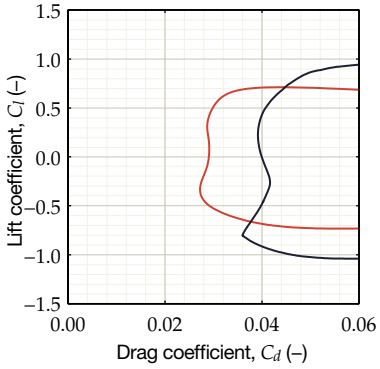

Figure 5.3: (*above*) Performance prediction of a DU 06-W-200 profile at a 0.07% (—) and a 1.97% turbulence level (—).

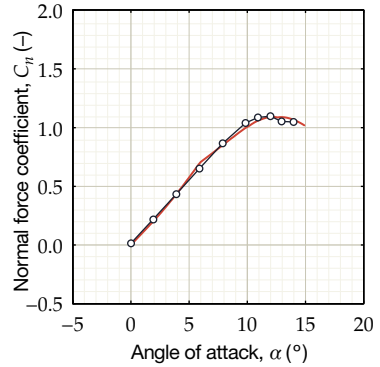

Figure 5.4: Static normal force coefficient of a NACA 0012 airfoil (○) compared to RFOIL predictions (—).

5.1.4 Turbulence levels

Especially in the downwind part of a vertical-axis wind turbine there exists quite a lot of turbulence. These perturbations could be of such a scale that they can affect the boundary layer and possibly stabilize it. This can be accounted for in RFOIL by setting an appropriate critical amplification factor for the e^n method, N_{crit}, which helps to predict free transition over the airfoil by Tollmien-Schlichting wave disturbances. Some examples of turbulence levels that follow from this parameter are given by the XFOIL manual (see table 5.1) and the effect on the lift curve is shown in figure 5.3.

Clearly, the effects can be quite significant. A similar notion has already been made by Paraschivoiu (2002) to limit the application of dynamic stall models to regions of low turbulence bound by $15° \leq \theta \leq 135°$ – the positions where all vorticity is shed at the extremes. Based on this, the rotor plane is split into an upwind region of relatively low turbulence ($N_{\text{crit}} = 9$), from 15° to 135°, and a downwind region of high turbulence ($N_{\text{crit}} = 4$) spanning the remaining angles.

Naturally, this only makes sense if transition occurs according to the mechanism adopted by RFOIL. Bypass transition or instabilities induced by crossflow—methods which can be imagined to occur in the downwind part of a Darrieus rotor—can lead to different situations. This has to be accounted for manually by setting trips at appropriate locations or using N_{crit} (Drela, 1995).

5.1.5 Dynamic stall models

Current dynamic stall models range from (semi-)empirical to complex CFD methods. Since the phenomenon features large separated flow structures, it can only be described properly by using the full Navier-Stokes equations along with a turbulence model. Clearly, this is out of the scope of this project. Instead, what are more convenient are correction factors to complement the viscid airfoil data. Such methods are well explicated in e.g. Masson et al. (1998), but are worth mentioning. The big drawback, however, is that such empirical relations are only really accurate for the airfoils and the conditions for which they were derived.

Instead of just repeating a heap of equations, the models in this subsection are evaluated for the case of a NACA 0012, excited at $k = 0.075$ and a Mach number of M = 0.4 according to $\alpha(t) = 7.1° + 8.4° \sin \omega t$ (see Leishman, 2006, p. 532). This should give a rough idea about how well the relations fit to the experimental data. First, figure 5.4 shows the static data as it follows from RFOIL.

An early empirical model has been proposed by Gormont (1973)

to deal with helicopter rotors, which is also commonly referred as the *Boeing-Vertol γ function method*. Here, the effect is represented by a reference angle

$$\alpha_{\text{ref}} = \alpha - K_1 \Delta\alpha, \tag{5.5}$$

where

$$K_1 = \begin{cases} 1, & \dot{\alpha} \geq 0, \\ -0.5 & \dot{\alpha} < 0, \end{cases} \tag{5.6}$$

$$\Delta\alpha = \begin{cases} \gamma_1 S, & S \leq S_C, \\ \gamma_1 S_C + \gamma_2 (S - S_C), & S > S_C, \end{cases} \tag{5.7}$$

$$S = \sqrt{\left| \frac{c\dot{\alpha}}{2V} \right|}, \tag{5.8}$$

$$S_C = 0.06 + 1.5 \left(0.06 - \frac{t}{c} \right), \tag{5.9}$$

$$\gamma_1 = \begin{cases} \gamma_2/2, & \text{(lift)} \\ 0, & \text{(drag)} \end{cases} \tag{5.10a}$$

$$\gamma_2 = \gamma_{\max} \max \left[0, \min \left(1, \frac{\mathrm{M} - \mathrm{M}_2}{\mathrm{M}_1 - \mathrm{M}_2} \right) \right], \tag{5.10b}$$

$$\gamma_{\max} = \begin{cases} 1.4 - 6.0\,(0.06 - t/c), & \text{(lift)} \\ 1.0 - 2.5\,(0.06 - t/c), & \text{(drag)} \end{cases} \tag{5.10c}$$

$$\mathrm{M}_1 = \begin{cases} 0.4 + 5.0\,(0.06 - t/c), & \text{(lift)} \\ 0.2, & \text{(drag)} \end{cases} \tag{5.11a}$$

$$\mathrm{M}_2 = \begin{cases} 0.9 + 2.5\,(0.06 - t/c), & \text{(lift)} \\ 0.7 + 2.5\,(0.06 - t/c). & \text{(drag)} \end{cases} \tag{5.11b}$$

This results in

$$C_{l_{\text{dyn}}} = C_l(\alpha_0) + m(\alpha + \alpha_0), \tag{5.12a}$$

$$C_{d_{\text{dyn}}} = C_d(\alpha_{\text{ref}}), \tag{5.12b}$$

where

$$m = \min \left[\frac{C_l(\alpha_{\text{ref}}) - C_l(\alpha_0)}{\alpha_{\text{ref}} - \alpha_0}, \frac{C_l(\alpha_{\text{ss}}) - C_l(\alpha_0)}{\alpha_{\text{ss}} - \alpha_0} \right]. \tag{5.13}$$

The parameter α_{ss} then represents the angle at which the lift slope leaves the linear regime. When the above is used to generate the normal force coefficient, the result is figure 5.5.

Specifically for the application in VAWTS, Strickland (1975) proposed modifications of Gormont's model (see figure 5.6). First, it was assumed that $S_C \approx 0$ since the airfoil thickness of VAWT blades usually exceed 12%c. Second, the flow is considered incompressible to eliminate the dependency on the Mach number, M. Furthermore, the dynamic coefficients were simplified for symmetrical airfoils, which limits the application to the region outside the linear lift regime ($a \geq a_{\text{ss}}$). The reference angle is then expressed as

$$\alpha_{\text{ref}} = \alpha_{\text{eff}} - \gamma K_1 \sqrt{\left| \frac{c\dot{\alpha}}{2V} \right|} S_{\dot{\alpha}}, \tag{5.14}$$

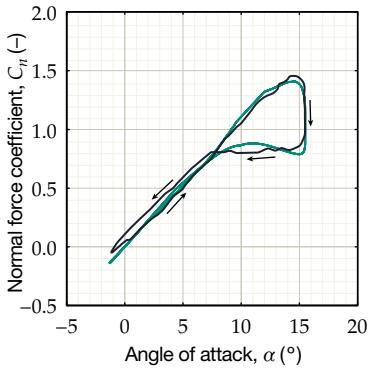

Figure 5.5: Dynamic normal force coefficient of a NACA 0012 airfoil (—) compared to an approximation by Gormont's model (—).

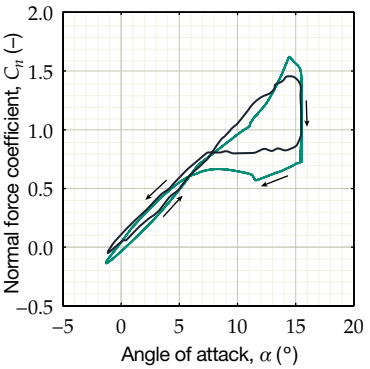

Figure 5.6: Dynamic normal force coefficient of a NACA 0012 airfoil (—) compared to the Strickland adaptation (—).

$$K_1 = 0.75 + 0.25 S_{\dot{\alpha}} \tag{5.15}$$

$$S_{\dot{\alpha}} = \begin{cases} -1, & \dot{\alpha} \geq 0, \\ 1, & \dot{\alpha} < 0, \end{cases} \tag{5.16}$$

$$\gamma = \begin{cases} 1.4 + 6.0\,(0.06 - t/c)\,, & \text{(lift)}, \\ 1.0 + 2.5\,(0.06 - t/c)\,, & \text{(drag)}, \end{cases} \tag{5.17}$$

The resulting aerodynamic force coefficients are then

$$C_{l_{\text{dyn}}} = \left(\frac{\alpha_{\text{eff}}}{\alpha_{\text{ref}} - \alpha_{\text{eff}_0}} \right) C_l\,(\alpha_{\text{ref}})\,, \tag{5.18a}$$

$$C_{d_{\text{dyn}}} = C_d\,(\alpha_{\text{ref}})\,, \tag{5.18b}$$

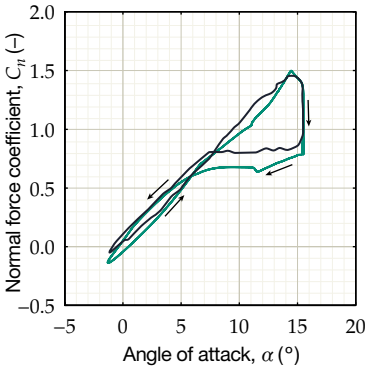

Figure 5.7: Dynamic normal force coefficient of a NACA 0012 airfoil (—) compared to the Strickland adaptation, taking into account the Massé-Berg modification (—).

Unlike helicopter blades for which the Gormont model was originally developed, VAWT blades encounter much higher angles of attack. To prevent overestimating the effect, Massé (1981) proposed a method to interpolate between the static and dynamic airfoil data:

$$C_{l_{\text{mod}}} = \begin{cases} C_l + \frac{A_M \alpha_{\text{ss}} - \alpha}{A_M \alpha_{\text{ss}} - \alpha_{\text{ss}}} \left(C_{l_{\text{dyn}}} - C_l \right), & \alpha \leq A_M \alpha_{\text{ss}}, \\ C_l, & \alpha > A_M \alpha_{\text{ss}}, \end{cases} \tag{5.19a}$$

$$C_{d_{\text{mod}}} = \begin{cases} C_d + \frac{A_M \alpha_{\text{ss}} - \alpha}{A_M \alpha_{\text{ss}} - \alpha_{\text{ss}}} \left(C_{d_{\text{dyn}}} - C_d \right), & \alpha \leq A_M \alpha_{\text{ss}}, \\ C_d, & \alpha > A_M \alpha_{\text{ss}}, \end{cases} \tag{5.19b}$$

where A_M is an empirical constant, of which Massé proposed a value of 1.8. Later, however, Berg (1983) instead adopted $A_M = 6$ to fit the measurements of the 17 m VAWT at Sandia. After applying this to Strickland's adaptation, the result is a reasonable fit of the experimental data (see figure 5.7), although the lift during the reattachment process seems to be a little undervalued.

5.2 2D VORTEX PANEL METHOD

A 2D configuration of a VAWT can be simulated using a vortex panel method. During this study, a model is used that was developed by dr. Carlos Simão Ferreira of Delft University of Technology.

5.2.1 Power and torque

A big drawback of this model is that it is based on potential flow. This means that turbulence and viscosity are neglected; things which obviously not hold in real life. One way to work around this is to use the viscid airfoil data from RFOIL in conjunction with the apparent wind speed as returned by the vortex panel model. Once the angles of attack and apparent wind speeds throughout a cycle are known, the 2D torque can be determined by the aerodynamic forces with respect to an aerodynamic center at 25%c:

$$\begin{aligned} Q &= \frac{1}{2\pi} \sum_{i=1}^{n} \int_0^{2\pi} RT_i(\theta) d\theta, \\ &= \frac{n}{2\pi} \int_0^{2\pi} RT d\theta. \end{aligned} \tag{5.20}$$

This can then be non-dimensionalized to find the torque coefficient:

$$\frac{Q}{\frac{1}{2}\rho U_\infty^2 AR} = \frac{n}{2\pi}\int_0^{2\pi} \frac{RT}{\frac{1}{2}\rho U_\infty^2 AR} d\theta,$$

$$C_Q = \frac{n}{2\pi}\int_0^{2\pi} \frac{\frac{1}{2}\rho V^2 C_t c R dz}{\frac{1}{2}\rho U_\infty^2 (2Rdz)R} d\theta,$$

finally leading to the expression

$$C_Q = \frac{nc}{4\pi R}\int_0^{2\pi} C_t \left(\frac{V}{U_\infty}\right)^2 d\theta. \tag{5.21}$$

In addition, by using equations (3.10) and (3.11), the power coefficient can be related to the torque coefficient by

$$P = Q\dot{\theta},$$
$$\frac{1}{2}\rho U_\infty^3 C_P A = \frac{1}{2}\rho U_\infty^2 C_Q AR\dot{\theta},$$
$$C_P = C_Q \frac{\dot{\theta}R}{U_\infty},$$

yielding

$$C_P = \lambda C_Q, \tag{5.22}$$

with λ being the tip speed ratio, given by equation (3.13). When inserting the expression for the tangential force coefficient and assuming $x^* = x_{\text{cp}}$, one arrives at an alternative expression also given by de Vries (1979, p. 4-22):

$$C_P = \frac{nc\lambda}{2\pi R}\int_0^{2\pi} \left(\frac{V}{U_\infty}\right)^2 C_l \sin\alpha \left(1 - \frac{C_d}{C_l}\cot\alpha\right) d\theta, \tag{5.23}$$

which, instead, is a more explicit function of the lift and drag coefficients.

5.2.2 Parasitic drag

The struts from Turby are composed of NACA 0018 sections of which the chord length varies linearly from 12 cm at the root to 8 cm near the point of attachment. The lifting effect is assumed to be negligible, but the variation of the profile drag coefficient with Reynolds number is taken into account. The resulting torque—for three struts per blade—is then

$$Q_s = \frac{9}{2\pi}\int_0^{2\pi}\int_0^{R} \frac{1}{2}\rho U_\infty^2 \left(\lambda\frac{r}{R} + \cos\theta\right) C_d c r dr d\theta. \tag{5.24}$$

Although this neglects the local induced velocity inside the rotor plane, it does give a rough estimation about the magnitude of the parasitic drag losses.

The friction of the bearings are taken into account by considering three reaction forces that counteract the weight of the rotor and the

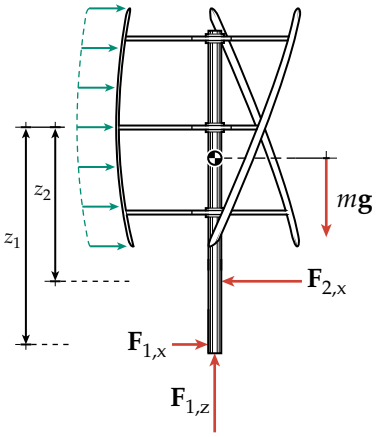

Figure 5.8: Free body diagram of the reaction forces acting on the rotor.

rotor's thrust force (see figure 5.8). This leads to the following force and moment equations:

$$\tfrac{1}{2}\rho U_\infty^2 C_T A = F_{2,x} - F_{1,x}, \tag{5.25}$$

$$mg = F_{1,y}, \tag{5.26}$$

$$0 = F_{1,x} z_1 - F_{2,x} z_2, \tag{5.27}$$

where C_T is the rotor thrust coefficient, m the mass of the rotor and $\mathbf{g}$ the acceleration due to gravity.

5.2.3 Skewed inflow

The vortex panel method still only accounts for a 2D situation and cannot account for sweep or skewed flow. The danger of this is that one might underestimate the power produced by the downwind blade path. To incorporate these 3D effects, the model will have to be stretched beyond its limits using several crude assumptions. The results that follow from such an approach cannot be blindly trusted. Therefore, for the remaining part of the report, the turbine is evaluated in unskewed conditions unless stated otherwise.

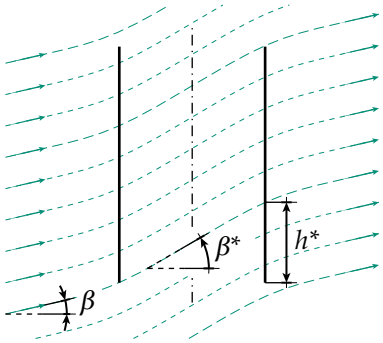

Figure 5.9: Skew angle after the flow passes the upwind blade trajectory.

The entire rotor in skewed flow can be modeled as a cylinder that contains single and double rotor parts (see figure 3.17b). Following the double actuator disc model by Mertens et al. (2003), the blade length in the downwind pass that only interacts once with the flow can be estimated as

$$h^* = 2R \tan\beta^* \sin\theta, \tag{5.28}$$

where β^* is the skew angle of the flow after it passes the upwind rotor half (see figure 5.9). By dividing the blade trajectory into multiple streamtubes[2], this skew angle can be related to the local induction factors of the upwind blade passage by

$$\beta^*(\theta) = \arctan\left(\frac{\sin\beta}{\cos\beta - a}\right); \quad \text{for } \pi \le \theta \le 2\pi. \tag{5.29}$$

[2] This relies on the assumption that the flow between the streamtubes does not mix.

The single downwind rotor part is then assumed to operate at the same apparent velocities as the upwind half, only at reversed angles of attack. The total power coefficient is then approximated as

$$C_P = \frac{1}{\pi}\int_0^{\pi} dC_P d\theta + \frac{1}{\pi}\int_{\pi}^{2\pi}\left(dC_P\frac{h-h^*}{h} + dC_P^*\frac{h^*}{h}\right)d\theta. \tag{5.30}$$

Then, the induction velocities returned by the vortex panel method, $\mathbf{v}(x, y)$, are rotated by the angle β^* according to

$$\mathbf{v}^* = \mathbb{R}_y(-\beta^*)\mathbf{v}(x, y), \tag{5.31}$$

where

$$\mathbb{R}_y(-\beta^*) = \begin{bmatrix} \cos\beta^* & 0 & -\sin\beta^* \\ 0 & 1 & 0 \\ \sin\beta^* & 0 & \cos\beta^* \end{bmatrix}. \tag{5.32}$$

The local apparent wind speed is then simply

$$\mathbf{V} = \mathbf{U} + (-\boldsymbol{\Omega} \times \mathbf{r}) + \mathbf{v}^*, \tag{5.33}$$

5.2.4 Swept blades

The effects of swept blades and skewed flow can involve large three-dimensional flow fields and are hard to model with just 2D data. Even so, sweep has an important effect on the lift coefficient and has to be taken into account somehow. For moderate sweep angles such as encountered with Turby, it is assumed that one can still get away with the independence principle.

First, consider the swept blade shown in figure 5.10. An additional set of unit vectors normal and Parallel to the leading-edge can be defined by rotating the unit vectors $\hat{\mathbf{e}}_\theta$ and $\hat{\mathbf{e}}_z$ around the r-axis:

$$\hat{\mathbf{e}}_\perp = \mathbb{R}_r(-\Lambda)\hat{\mathbf{e}}_\theta, \tag{5.34a}$$

$$\hat{\mathbf{e}}_\parallel = \mathbb{R}_r(-\Lambda)\hat{\mathbf{e}}_z, \tag{5.34b}$$

where $\mathbb{R}_r(-\Lambda)$ is the rotation matrix around the vector $\hat{\mathbf{e}}_r$, given by

$$\mathbb{R}_r(-\Lambda) = \begin{bmatrix} \cos\Lambda + \sin^2\theta(1-\cos\Lambda) & \cdots & \\ \sin\theta\cos\theta(\cos\Lambda - 1) & \cdots & \\ \cos\theta\sin\Lambda & \cdots & \\ \cdots & \sin\theta\cos\theta(\cos\Lambda-1) & -\cos\theta\sin\Lambda \\ \cdots & \cos\Lambda + \cos^2\theta(1-\cos\Lambda) & -\sin\theta\sin\Lambda \\ \cdots & \sin\theta\sin\Lambda & \cos\Lambda \end{bmatrix}. \tag{5.35}$$

The apparent velocity can then be projected onto the plane $\{\hat{\mathbf{e}}_r, \hat{\mathbf{e}}_\perp\}$ according to

$$\mathbf{V}' = (\mathbf{V}\cdot\hat{\mathbf{e}}_r)\hat{\mathbf{e}}_r + (\mathbf{V}\cdot\hat{\mathbf{e}}_\perp)\hat{\mathbf{e}}_\perp, \tag{5.36}$$

Now, the angle of attack is—similar to equation (3.4)—equal to the angle between the vectors $\mathbf{V}'$ and $-\hat{\mathbf{e}}_\perp$:

$$\alpha = \arccos\left(\frac{\mathbf{V}'\cdot -\hat{\mathbf{e}}_\perp}{\|\mathbf{V}'\|}\right), \tag{5.37}$$

Another consequence is that the tangential force points to the direction of the vector $\hat{\mathbf{e}}_\perp$, resulting in an additional force in z-direction.

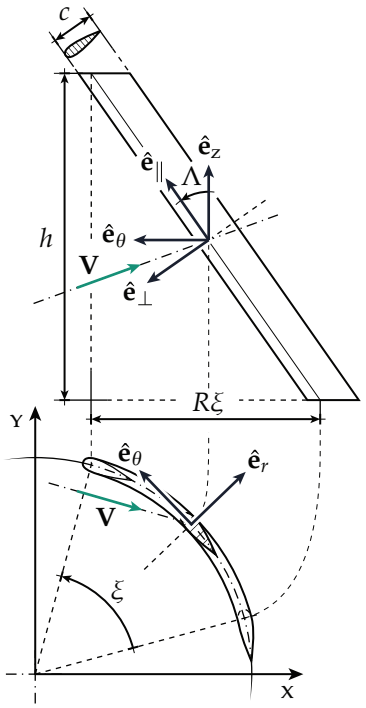

Figure 5.10: Flow as it hits a helical blade, locally swept by an angle Λ.

5.3 COMMENTS ON VALIDITY

Figure 5.11 shows a rough representation of the calculation sequence. To summarize, the following assumptions and simplifications were adopted:

- The airfoil performance is estimated using static data from RFOIL up to an approximate point of stall and is modeled by flat plate behavior for the remaining large angles. Especially the predictions for the post-stall region can be an important source of error for low λ. Furthermore, the results returned by RFOIL do not include the effects of unsteady flow on the airfoil's boundary layer.
- Downwind turbulence is taken into account by dividing the blade trajectory into different parts, where each part corresponds to a different critical amplification factor. Working with RFOIL also means that the transition mode is assumed to be natural transition and not other mechanisms.

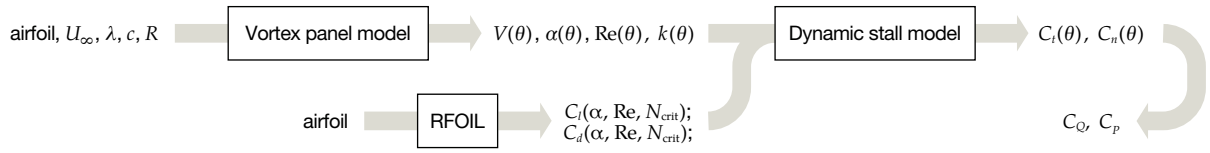

Figure 5.11: Modeling strategy to be able to assess the performance of a VAWT in low Reynolds number conditions.

- Dynamic stall is evaluated using Strickland's adaptation of the Gormont model, accompanied by the Massé-Berg modification (see Gormont, 1973; Strickland, 1975; Massé, 1981). This is a semi-empirical model, which means that the results obtained for other airfoils and different conditions are always questionable.
- The induction velocities are obtained from a 2D vortex panel method under the assumption of inviscid, incompressible flow. All 3D effects—including swept flow—are completely neglected during this process. This also implies that there is no feedback of the viscous airfoil data on the vortex wake.
- In the possible case of skewed inflow, the induced velocity vectors are skewed by an angle β^*. This angle is derived through multiple-streamtube theory (see Mertens et al., 2003).
- The apparent wind speeds are obtained by adopting the independence principle of swept wings. This implies that flow parallel to the blades is ignored; even past the point of stall which neglects any 3D effects that may arise.
- Tip losses are approximated by the equations (3.24a) and (3.24b).
- Of the struts, only the profile drag is taken into account. The velocities induced by the main blades are neglected at this point to prevent having to calculate the wake inside the entire rotor area.

Figure 5.12 shows the predicted aerodynamic power. This shows that, despite these simplifications, the model seems to return realistic values. The rated power at 11 m/s shows a good match, but one has to keep in mind that relative error can increase as one moves to lower wind speeds. Surely this has to do with the semi-empirical dynamic stall model, the poor predictions by RFOIL at low Reynolds numbers and the estimations for large α behavior. Still, although the model is not a completely accurate representation of the actual turbine, it does allow one to quantify some design considerations.

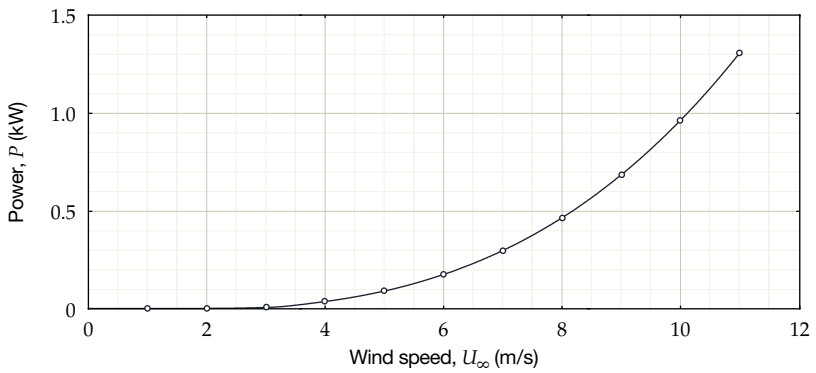

Figure 5.12: Predicted aerodynamic power of Turby MkIa.

6 Start-up analysis

In 1977, a 230 kW eggbeater-type Darrieus was installed on Magdalen Island, Quebec. After one successful year of operation, the turbine was stopped for inspection after a peculiar noise was heard coming from the gearbox. Assuming that it was not able to start-up by itself anyway, the brakes were removed during the process. Even so, on June 6, 1978, the turbine did start as a result of unusual gust conditions. With no load attached and no other way of stopping it, the rotor speed went well over the design speed of 38 rpm and eventually reached a disastrous 68 rpm. Ultimately, a guy wire broke and the turbine crashed to the ground (Johnson, 2001, p. 1-14). Even though the Darrieus was thought to be inherently not self-starting, it did happen under varying wind speeds.

The purpose of this chapter is to explore the issue of self-starting and, more specifically, the low speed performance of Turby. Section 6.1 first summarizes some observations of its start-up behavior in real life. Then, some possible explanations are given in section 6.2. To summarize, some general conclusions regarding Turby are drawn in section 6.3, which will form the basis for finding a suitable solution.

6.1 Start-up behavior of turby

Field tests with the Turby MkIa have revealed the following:

- The static (breakaway) torque is approximately 1 N m.
- The turbine is able to accelerate from rest to $\lambda \approx 0.5$ at $U_\infty = 3$ m/s, up to to $\lambda \approx 0.8$ at $U_\infty = 5$ m/s.
- A band of $C_P < 0$ is present up to $\lambda \approx 1.6$.
- Starting at $1.6 \lesssim \lambda \lesssim 2.0$, the power coefficient raises from zero to $C_{P_{\max}}$.

During these field tests, the turbine was left to operate with the intervention of the control system for periods up to 9 hours in wind

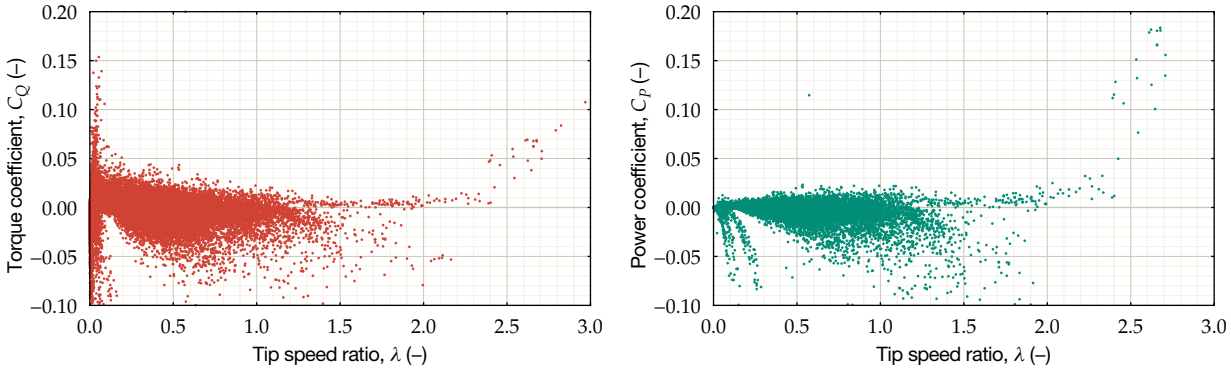

(a): Torque coefficients over a range of tip speed ratios.

(b): Power coefficients over a range of tip speed ratios.

Figure 6.1: Performance of Turby Mkla estimated from field tests.

speeds varying from 0 to ≈ 8 m/s. The data sets are composed of the wind speed and the measured generator frequency. Since the generator is known to have seven pole pairs, the latter parameter yields the rotor speed. The rotor torque can then be estimated by

$$Q \approx J \frac{\Delta \dot{\theta}}{\Delta t}. \tag{6.1}$$

The torque and power coefficients then naturally follow from equations (3.10) and (3.11).

Two representative data sets—each spanning a relatively wide range of tip speed ratios—have been plotted in figures 6.1a and b. To reduce the extreme peaks, the data has been smoothed over a 5 second window. Even so, the turbulence in the wind, the unsteady rotor speed and the motor operation cause these curves to be heavily scattered. However, a band of negative power is still visible at low tip speed ratios which can help estimate the amount of additional torque that is required for a passive start-up.

Figures 6.2c through d show two 4-hour extracts of the wind speeds measured in the field. The model treated in the previous chapter was then used to predict the torque necessary to evaluate the primary equation of motion. As an initial condition, the tip speed ratio was assumed to be higher than 0.5. The shaded areas correspond to $0.8 \leq \lambda \leq 1.6$; a range which is believed to cause a braking torque during experiments.

The results indicate that during periods of relatively low wind speed the rotor fails to accelerate through the shaded area. It is only when U_∞ is high enough that it is able to break through this band and advance to higher tip speed ratios. This is clearly depicted in figure 6.2d, where the wind is slowly gaining in strength. After passing some threshold, there is a sudden acceleration from $\lambda \approx 0.6$ to $\lambda \approx 4$.

Figure 6.2: The result of modeling the equation of motion for two 4 hour periods.

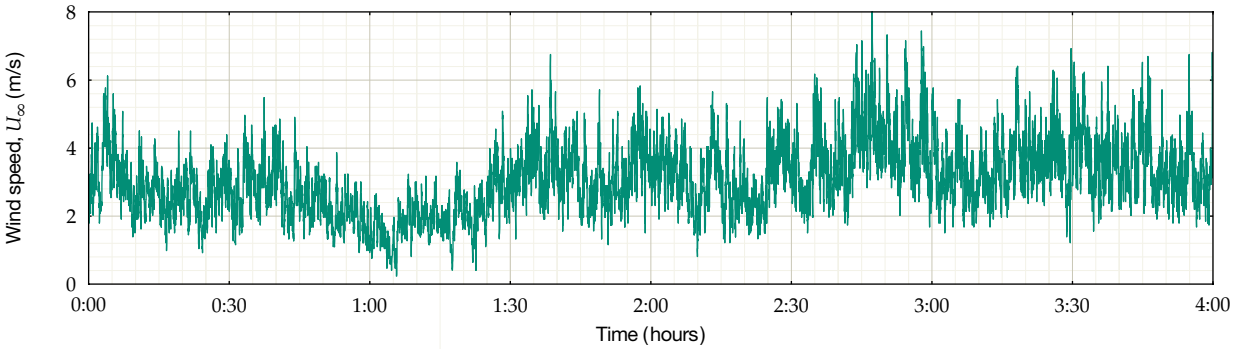

(a): Measured wind speeds during one 4 hour period in the open field.

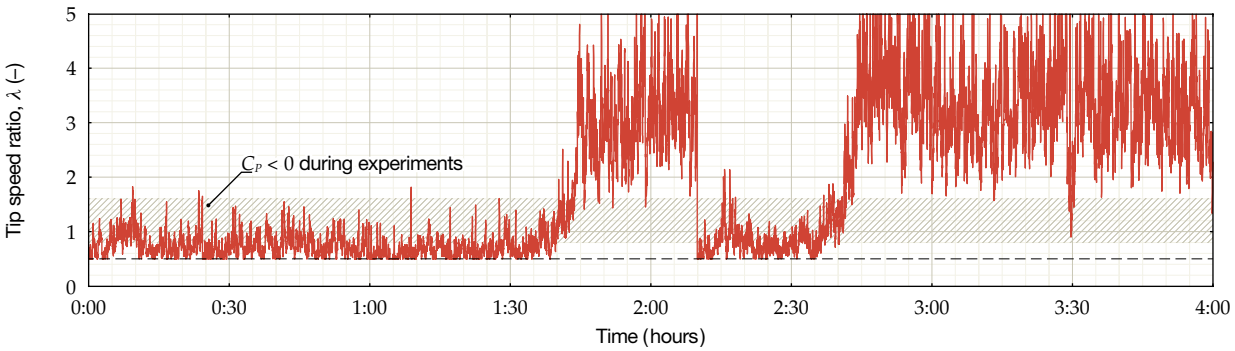

(b): Tip speed ratios calculated from the wind speed data above.

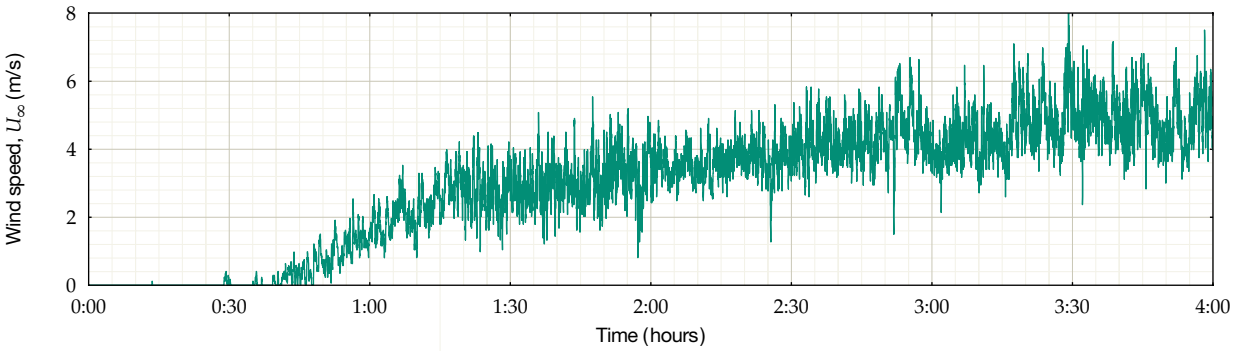

(c): Measured wind speeds during another 4 hour period in the open field.

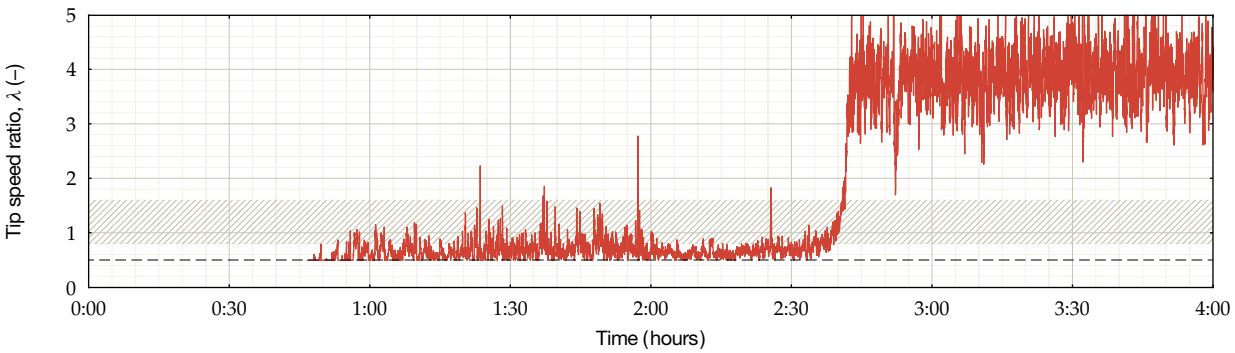

(d): Tip speed ratios calculated from the wind speed data above.

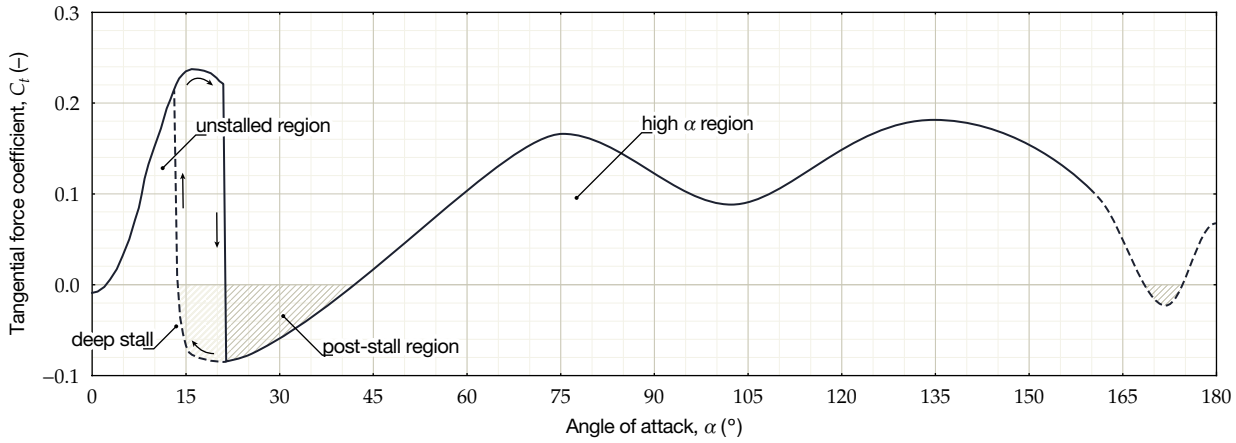

Figure 6.3: Smoothed static tangential force coefficient of a single NACA 0018 airfoil at rest ($\lambda = 0$), based on the data of figure 3.9 and completed with an estimate based on the result of Baker (1983).

6.2 FAILURE TO START

Darrieus turbines are notoriously bad starters, often relying on a start motor to increase the rotor speed. The exact definition of self-starting is inconsistent throughout literature, as pointed out by Hill et al. (2009). Usually, the device is said to have successfully started once the extraction of usable power is possible, or more specifically: when accelerated from a certain resting point. Alternatively, the definition of starting may involve accelerating from rest to $\lambda > 1$, requiring the blades to produce at least some lift. In this project, a start-up is considered successful if the rotor is able to rev up from rest to its nominal operating speed without external help.

6.2.1 Torque at rest

When the rotor is at rest, equation (3.12) reduces to $\alpha = \theta$, causing the blades to experience angles of attack from 0 to 360°. To illustrate the torque at rest, consider the case of a single two-dimensional NACA 0018 blade. Based on equation (3.7b) and the data from figure 3.9, the forward tangential force coefficient is drawn in figure 6.3. A large drop in C_t occurs at the point of leading-edge separation, caused by the sudden loss of lift and increase in drag. This results in a post-stall region of negative tangential force, followed by a high angle of attack region of positive C_t.

Still, although some regions of negative tangential force exist, the net torque over a complete cycle is definitely positive. This should allow this hypothetical layout to at least accelerate from rest.

6.2.2 The dead band

As the tip speed ratio increases, the angles of attack associated with the band of negative C_t just past static stall will eventually make out a larger part of the operating range. Past $\lambda = 1$, a blade may enter a region of reverse torque often called the *dead band* (Baker, 1983). The classic definition of this phenomenon can be visualized by comparing the angle of attack variation with a $C_t(\alpha)$ plot (see figure 6.4). At $\lambda = 1.5$, the amplitudes of the $\alpha(\lambda)$ curve are completely inside the post-stall region, and there are many situations imaginable

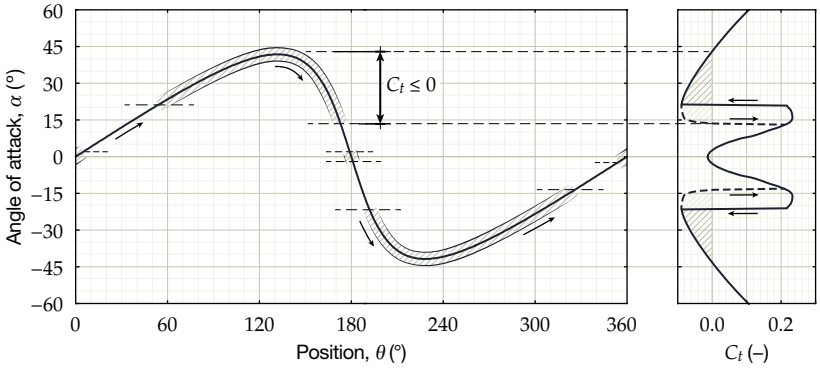

Figure 6.4: Regions of negative tangential force experienced by a NACA 0018 blade section at $\lambda = 1.5$ under static conditions (dynamic stall and wake effects are neglected).

where the sum of three blades will create a negative torque. This is again reflected by a dip in the torque curve of the rotor, shown in figure 6.5. The severity of this band will heavily depend on the airfoil characteristics, as well as other factors such as drive train friction and parasitic drag.

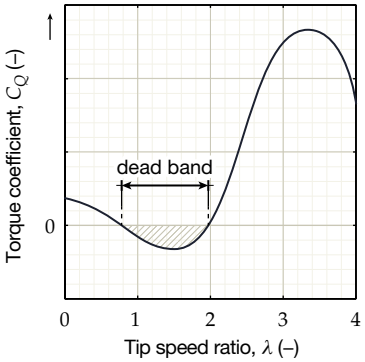

Figure 6.5: Hypothetical $C_Q - \lambda$ curve, showing the presence of a *dead band*.

However, it has been argued by Hill et al. (2009) that the presence of the dead band might be just a result of inaccurate modeling and is not necessarily inherent to Darrieus rotors. For instance, neglecting the effects of dynamic stall and wake interaction, as done in the previous example, will lead to false predictions. Also the Reynolds number of an airfoil can greatly fluctuate during a cycle and for different tip speed ratios. In addition, despite the presence of the dead band, a rotor can still possess sufficient angular momentum to pass through it and advance to higher tip speed ratios.

6.2.3 Reynolds number dependence

Airfoil performance tends to vary greatly with Reynolds number, which is a dimensionless number describing the ratio of inertial to viscous forces:

$$\mathrm{Re} \equiv \frac{cV}{\nu}, \tag{6.2}$$

where ν is kinematic viscosity of the fluid ($\nu = \mu/\rho$). The Reynolds number has two major implications on airfoils:

- *The location of the transition point* moves forward for increasing Reynolds numbers.
- *The boundary layer thickness* grows slower at higher Reynolds numbers according to $\delta^*/x \propto \mathrm{Re}_x^{-1/2}$; meaning that a boundary layer can persist in stronger adverse pressure gradients before separating (see equation (3.19)).

In general, performance tends to degrade at lower Reynolds numbers which—considering the dependence on V—is especially relevant for start-up. Hill et al. (2009) also notes that, since performance data is usually only available for a few operating conditions, accurate changes in Reynolds number are often not incorporated in models. This can lead to large errors and may lead to overestimating the performance at low speeds. Figure 6.3, which was created using airfoil

Table 6.1: Stall behavior of a DU 06-W-200 airfoil at different Reynolds numbers (Claessens, 2006; Worasinchai et al., 2011).

Re	$C_{l,\,\max}$	$\alpha_{\text{deep stall}}$
500,000	1.33	28°
300,000	1.33	22°
151,000	1.14	16°
91,000	1.07	16°
67,000	0.80	14°

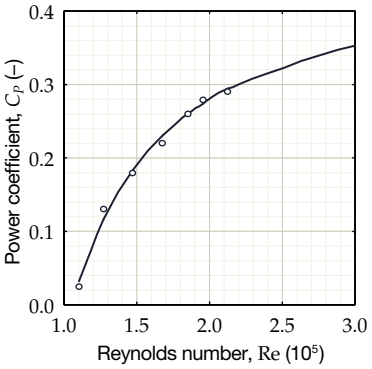

Figure 6.6: Measurements on the original Turby prototype (○) showing a trend (—) of a severe performance decrease for decreasing Reynolds numbers (Mertens, 2006, p. 12).

data at Re = 500,000, is therefore not representative for the start-up of a small turbine.

Because of this, Worasinchai et al. (2011) measured the performance of several sections, including Turby's DU 06-W-200, at Re = 67,000, 91,000 and 151,000. Table 6.1 shows that the airfoil is indeed very sensitive to changes in the operating conditions. The generation of lift can greatly drop at low Reynolds numbers which will obviously make starting more difficult. Such a dramatic case can be seen in figure 6.6, showing measurements performed with the original Turby prototype fitted with NACA 0018 blades.

From this, the obvious conclusion is that the failure to start is most likely due to the performance degradation of the airfoils at low Reynolds numbers. The post-stall region in the static $C_t - \alpha$ curve spans from the deep stall angle to approximately 40°. The poor performance characteristics at low Re can then force the rotor into a situation as depicted in figure 6.4, where a considerable portion of the blade trajectories reside in the post-stall region and generate a net negative torque.

6.3 CONCLUDING REMARKS

Like many VAWTS, Turby MkIa fails to achieve a fully passive start-up. Experiments indicate that there is a band of negative torque—often referred to as *dead band* in literature—somewhere in the range $0.5 \leq \lambda \leq 1.6$. The reason behind this is that, unfortunately, the power coefficient obtained at the rated wind speed is all but constant. The combination of low wind speeds and the small scale of the device leads to very low Reynolds numbers; often in the order of $< 10^5$. The lift production and stall behavior of the airfoils aggravates in these conditions, with low starting torque as a result.

How the power coefficient is affected by the wind speed is evaluated numerically and plotted in figures 6.7a and b. The simulations suggest that there is indeed a great dependence on wind speed. Especially near the point of cut-in, the predicted power coefficient is merely a fraction of what is achieved at 11 m/s or is even completely negative. To give an idea about the order of magnitude of the Reynolds numbers, the variation throughout one cycle is plotted for λ = 1.5 and λ = 4.0 in figures 6.7c and d, respectively. At the lower tip speed ratios encountered during start-up, the fluctuations in Re are especially violent, making it hard to design for a specific condition. In addition, a redesign of the airfoil cannot perform worse during nominal operation; estimated to be around Re = 300,000 to 400,000 at the rated wind speed[1].

In conclusion; a successful passive start-up will have to be achieved by either boosting the airfoil performance at Re $< 10^5$, raising the Reynolds numbers altogether or by finding other creative solutions. This is treated in the sequent chapters.

[1] **The current DU 06-W-200 airfoil was optimized by Claessens (2006) for the range $300,000 \leq \text{Re} \leq 700,000$.**

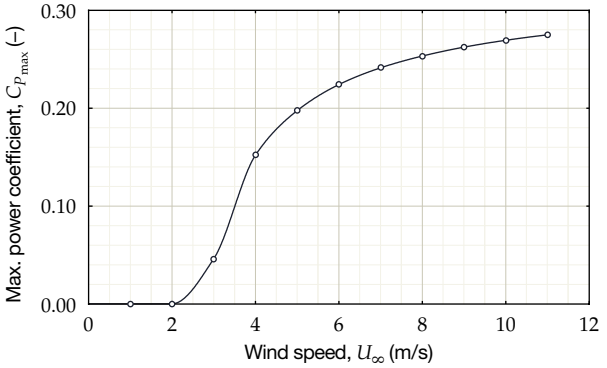

(a): Maximum power coefficient at different wind speeds.

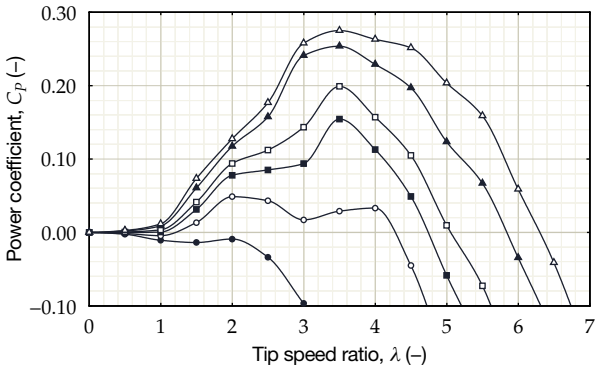

(b): $C_P - \lambda$ curves predicted at U_∞ = 2 m/s (●), 3 m/s (○), 4 m/s (■), 5 m/s (□), 8 m/s (▲) and 11 m/s (△).

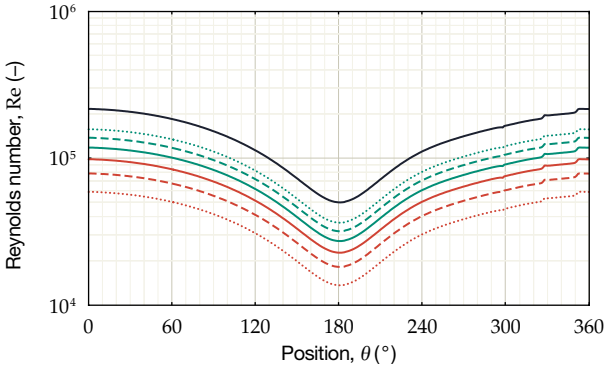

(c): Reynolds numbers encountered during a cycle at λ = 1.5 and U_∞ = 3 m/s (····), 4 m/s (– –), 5 m/s (——), 6 m/s (——), 7 m/s (– –), 8 m/s (····) and 11 m/s (——).

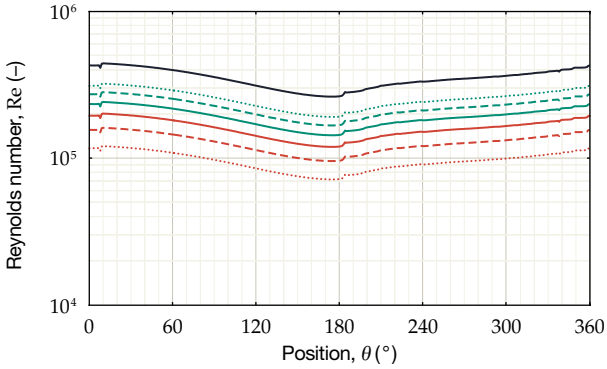

(d): Reynolds numbers encountered during a cycle at λ = 4.0 and U_∞ = 3 m/s (····), 4 m/s (– –), 5 m/s (——), 6 m/s (——), 7 m/s (– –), 8 m/s (····) and 11 m/s (——).

Figure 6.7: Predicted degradation of the power coefficient at $U_\infty \leq U_{\text{rated}}$.

7 Effects of scale

In chapter 6, it was concluded that the failure to start at low wind speeds is mainly due to the low Reynolds numbers. Partially, this is caused by the small scale of the device and it is interesting to look briefly into what happens when dimensions increase.

In this small chapter, the effects of upscaling are treated. Section 7.1 starts off with quantifying the raise in Reynolds numbers. The impact on the performance on the device is subsequently discussed in section 7.2.

7.1 Increasing Reynolds numbers

As the scale of the device increases, so do the Reynolds numbers. At an equal λ, the blade speed at the cut-in wind speed remains constant. This means that $\mathrm{Re} \propto c$, which is also reflected by figure 7.1. Here, all dimensions of the rotor are scaled linearly, implying that $c \propto R$ and $A \propto R^2$.

At a tip speed ratio of 1.5, the blades of the baseline model experience a mean Reynolds number of 38,000. Scaling up by a factor 2 and 4 increases it to respectively 76,000 and 152,000.

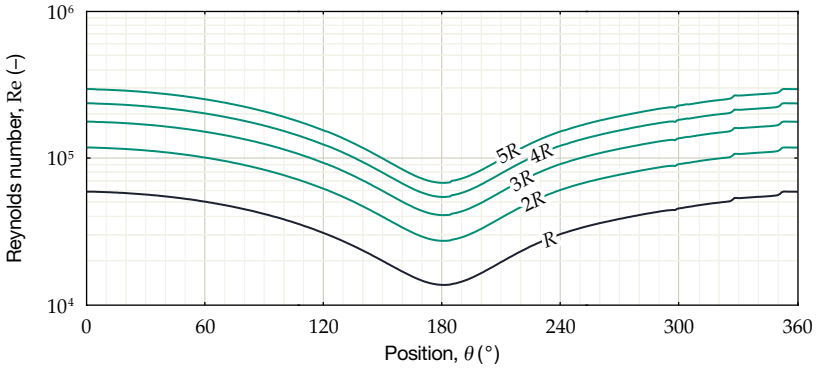

Figure 7.1: Reynolds numbers during a cycle at $\lambda = 1.5$, $U_\infty = 3$ m/s.

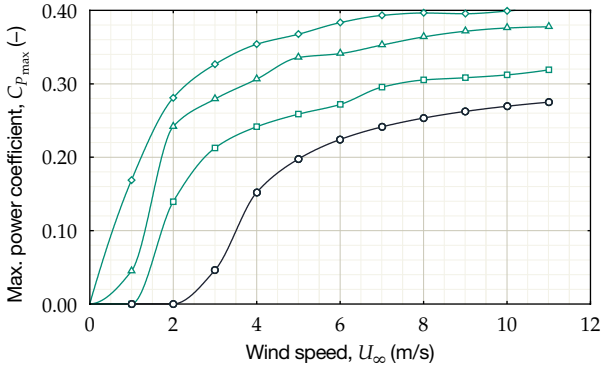

(a): Maximum power coefficients for the baseline case (○), $2R$ (□), $3R$ (△) and $4R$ (◇).

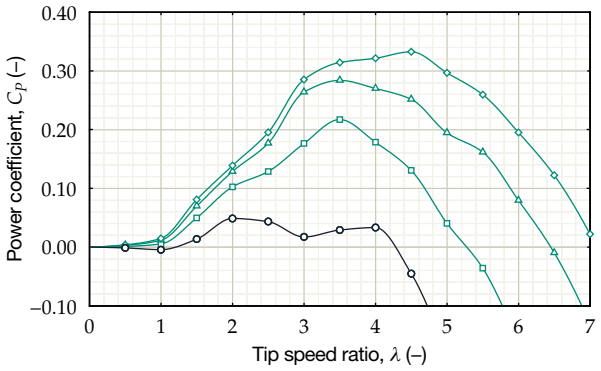

(b): Power coefficients for the baseline case (○), $2R$ (□), $3R$ (△) and $4R$ (◇) at U_∞ = 3 m/s.

Figure 7.2: Effects of scale on the performance of Turby.

7.2 EFFECT ON PERFORMANCE

The raise in Reynolds numbers is especially helpful around $\lambda = 1$; the point where the blades have to rely purely on lift in order to advance to higher tip speed ratios. In addition, a larger rotor can extract more power from lower wind speeds. This is clearly shown by figures 7.2a and b.

For each case, the gain eventually levels out when the wind speed approaches U_{rated}. Still, there are significant differences among the curves near the cut-in wind speed. Increasing the scale helps to escape the very low Reynolds number regime where the airfoils greatly suffer from performance degradation. This should make it easier for a rotor to progress from rest to the rated tip speed ratio and would also effectively decreases the cut-in wind speed.

Large-scale devices should therefore suffer significantly less from start-up problems. Increasing scale basically means increasing chord lengths without changing solidity. However, simply upscaling the turbine is not always a fitting solution, especially when considering placement in the urban environment where space is limited. The remaining chapters will therefore focus on other solutions where the outer dimensions of the rotor are kept fixed.

8

Solutions in literature

Over the years, several attempts have been made to develop a fully self-starting Darrieus turbine. In this chapter, several of these strategies are discussed in order to give a qualitative overview of possible solutions. Each section is concluded with a list of pros and cons, together with a sketch of the layout to give an idea about the impact on the design and its aesthetics. The next chapter will then treat a number of promising solutions in a more quantitative manner.

First, sections 8.1 and 8.2 explain the effect of rotor solidity and helical blades on self-starting. Next, sections 8.3 through 8.10 discuss several common and uncommon airfoil geometries. Several hybrid designs are then treated in sections 8.11 through 8.13. Also, some existing concepts using active and passive variable pitch systems are briefly discussed in section 8.14. Sections 8.15 and 8.16 respectively deal with the application of fairings and the implementation of magnetic bearings. In conclusion, section 8.17 makes a distinction between the feasible solutions and the ones that are not applicable to the design of Turby.

8.1 ROTOR SOLIDITY

A well-known strategy to increase the output torque of a turbine is to increase *solidity*.

8.1.1 Effect of solidity on performance

For a rotor with n blades, rotor solidity can be defined as

$$\sigma = \frac{nc}{2R\cos\Lambda}. \tag{8.1}$$

The rotor solidity, σ, basically describes what fraction of the swept area is solid and is something which affects the optimal tip speed ratio. A low σ rotor has less blade area interacting with the wind and has to rely on a high λ to cover the same swept area, yielding less torque. Vice versa, a high σ rotor operates at a much lower λ and delivers more torque. Therefore applications such as pumps, requiring a high starting torque, are usually connected to a high solidity rotor. For power generation a lower solidity is often preferred since a higher λ decreases the difference between the rotor speed and the electrical frequency[1].

[1] For example, consider the windmill types shown in figure 2.5a and c.

So purely to increase the starting torque, using a higher σ can be an option. According to equation (8.1), the solidity of a rotor with a radius R can be increased by either attaching more blades or by increasing the chord length. However, departing from a three-bladed design can be disadvantageous due to a number of reasons. First, more blades will obviously increase costs, weight and inertia. Sec-

ond, three-bladed rotors are generally considered more aesthetically pleasing (Stankovic et al., 2009, p. 88). And third, an even number of blades can lead to vibrations, because the forces generated by an opposing set of blades will tend to peak in the same direction and phase.

Increasing the chord length will, of course, also increase the blade weight. Another negative effect is that the tip losses are increased because the blade aspect ratio is decreased. However it also affects the ratio c/R, thereby increasing the presence of virtual camber (see subsection 3.4.3), which has an impact on the lift production and may increase the risk of encountering (dynamic) stall.

Additionally, the Reynolds number increases with increasing c, improving airfoil performance in general. However at a higher λ, what is gained in Reynolds number by a larger chord can easily be lost when the blades operate at a lower tip speed.

8.1.2 Pros and cons of increasing solidity

Pros

- A higher solidity will decrease the optimal tip speed ratio, meaning lower centrifugal forces and less noise output.
- A larger blade area will generate more torque.
- Lowering the nominal rpm will decrease the risk of eigenfrequencies coming into contact with the rotor speed.
- Longer chord lengths can maybe increase Reynolds numbers.

Cons

- A lower nominal rotor speed will increase the size of the direct-drive generator.
- High solidity rotors require more material and are heavier.
- Longer chord lengths will decrease the aspect ratio, thus increasing tip losses.
- A lower nominal λ will raise angles of attack and increase the risk of the blades going into dynamic stall.

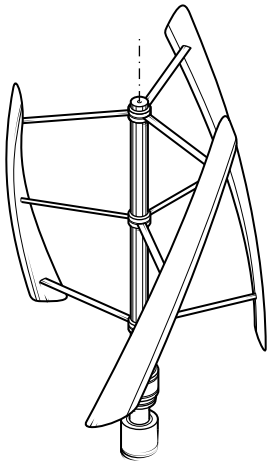

Figure 8.1: Sketch of a high solidity rotor.

8.2 BLADE SWEEP

A turbine with helical blades, can address a wide range of angles of attack. When a set of n blades are each twisted along the rotor axis according to an angle of $\frac{1}{n}360°$, every possible blade position should be occupied (see section 3.4.6). This should reduce torque fluctuations during normal operation.

8.2.1 Swept flows and stall

But as discussed in section 3.4.7, blade sweep reduces the lift by ignoring the parallel velocity component and would therefore seem to have a negative impact on the energy yield. Although the flow adheres to this independence principle for attached flow, the 3D effects play a larger role near stall. Here, the spanwise component of the flow helps to keep the boundary layer attached and delays separation to higher angles of attack[2]. Having the blades lean forward has already been proposed by Baker (1983) to improve performance for a high α, low Re flow. Higher stall angles would then reduce the width of the post-stall region containing negative tangential force (see figure 6.3).

[2] **The same effect occurs with delta-wing aircraft flying at extremely high angles of attack during take-off and landing. They rely on a large leading-edge vortex to energize the flow during subsonic flight.**

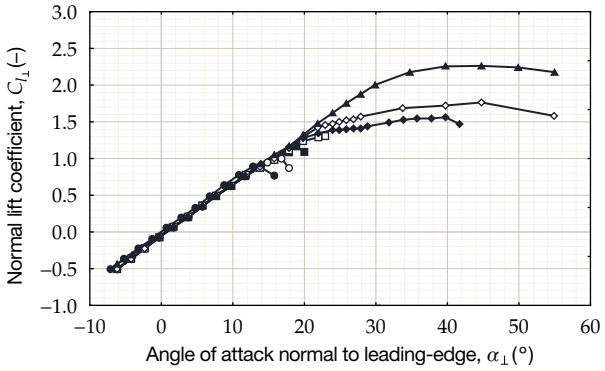

(a): Lift coefficient normal to the leading-edge of an airfoil for sweep angles $\Lambda = 0°$ (●), 15° (○), 30° (■), 35° (□), 40° (◆), 45° (◇), 60° (▲) (Purser and Spearman, 1951; cited in Leishman, 2006, p. 549).

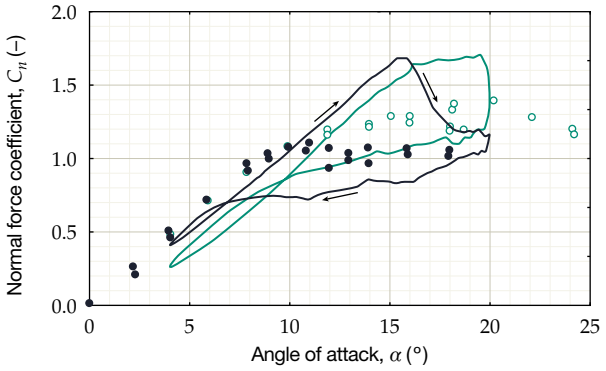

(b): Steady (●, ○) and dynamic lift for a NACA 0012 airfoil swept $\Lambda = 0°$ (—) and $\Lambda = 30°$ (—) for a pitching motion $\alpha(t) = 15° + 8° \sin \omega t$ at $k = 0.075$ (St. Hilaire and Carta, 1979; cited in Leishman, 2006, p. 550).

Figure 8.2: Effect of the sweep angle on performance.

The subject is treated by Leishman (2006) who illustrates the effect through the outcome of a series of measurements performed by Purser and Spearman (1951), showing the static performance of an airfoil normal to the leading-edge (see figure 8.2a). This shows that sweeping a blade by $\Lambda = 30°$ increases the stall angle from 16° to 20°, accompanied by an increase of $C_{l_{\max}}$ from ≈ 0.90 to ≈ 1.15. Increasing it further to $\Lambda = 60°$ even yields a stall angle of 55° and $C_{l_{\max}} \approx 2.25$. In the cases where the nature of stall is dynamic rather than static, the maximum lift coefficient stays roughly the same but is shifted towards higher values of α (see figure 8.2b). Yet the mean lift is raised as a result of a narrower hysteresis loop.

8.2.2 Pros and cons of decreasing blade sweep

Pros

- Decreasing the inclination angle will increase the lift according to $\cos^2 \Lambda$.
- Less sweep will reduce the angles of attack.
- Straight blades are easier to manufacture.

Cons

- Helical blades are indispensable for vibration-free operation.
- No sweep will affect the aesthetics.

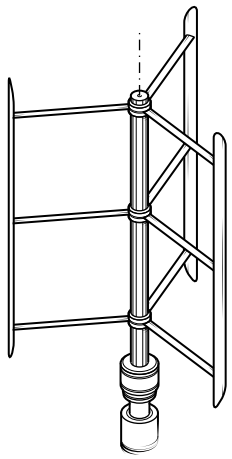

Figure 8.3: Sketch of a rotor with straight blades ($\Lambda = 0°$).

8.3 BLADE THICKNESS

The choice of a suitable airfoil is a critical factor for both start-up and peak performance.

8.3.1 Consequences of adding thickness

Thick airfoils have several advantages compared to thin sections. First, they are more resistant to bending and can offer the strength to operate at higher wind speeds. Alternatively, they can allow a lighter and cheaper structure with a lower moment of inertia. Second, thicker airfoils tend to stall less abrupt, which allows them to generate torque over a wider range of angles and will also lower

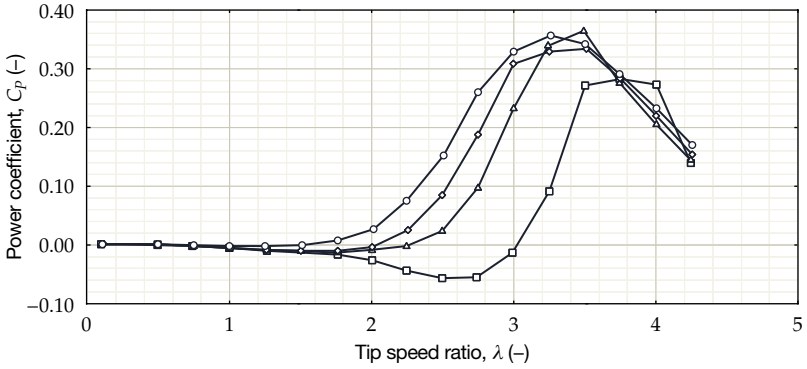

Figure 8.4: Effect of airfoil thickness on the $C_P - \lambda$ curve showing a NACA 0012 (□), NACA 0015 (△), NACA 0018 (◇) and NACA 0021 profile (○) at $\mathrm{Re} = 200,000$ (Kirke and Lazauskas, 1991; cited in Claessens, 2006, p.54).

noise emissions. Overall, airfoils at least up to 18% thickness yield more lift at lower Reynolds numbers (Jacobs and Sherman, 1937). For increasing thickness, the drag bucket widens, which in turn increases the operating range of the device (Claessens, 2006, p. 46). Related to the thickness is the leading-edge radius. Airfoils with a well-rounded leading-edge are more resistant to roughness effects that eventually lead to performance degradation over time. Moreover, they usually have an increased deep stall angle, but at the cost of a longer hysteresis loop (Timmer and van Rooij, 2001). Although having a thick leading-edge has the disadvantage of causing high pressure peaks, which can reduce performance especially at lower Reynolds numbers.

The effects of thickness on the starting capability of a Darrieus rotor have been computed by (Kirke and Lazauskas, 1991), although at a constant Reynolds number of 200,000. As shown in figure 8.4, in the case of a NACA 00XX section, increasing the thickness leads to an increase in performance at lower tip speed ratios; though it is questionable whether the choice of Reynolds number is really appropriate for starting conditions.

The great disadvantage of thick airfoils is the increased profile drag, which is more dominant at lower angles of attack. Increasing the thickness beyond 18% is usually accompanied by a loss in efficiency. This leads to a trade-off: a thick airfoil may increase the operating range of angles of attack, enhancing the performance at low λ, but will lead to a higher zero-lift drag coefficient which will affect the output at high λ.

In addition, the thickness of the airfoil is an important parameter when it comes to the formation of laminar separation bubbles. A thick profile has a higher suction peak followed by a stronger adverse pressure gradient than what is found over a thin airfoil. This makes that thicker airfoils suffer more from bubble drag at low Reynolds numbers. At higher Reynolds numbers, however, thin airfoils are prone to leading-edge separation since the flow has to travel around a relatively sharper nose. Eventually, they are outperformed by thicker sections with a rounder leading-edge[3].

[3] **This fact became known to aerodynamicists after work by Ludwig Prandtl in 1917. At that time, primarily low Reynolds number wind tunnels were used and thin airfoils were considered the standard. The discovery lead to the development of several successful thick airfoil designs, including the Göttingen 298 (13%c) profile used in the Fokker Dr-1 triplane flown by the Red Baron (Anderson, 1997, pp. 308–310).**

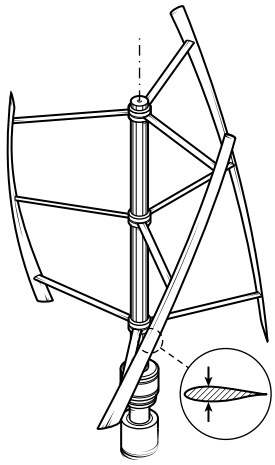

Figure 8.5: Sketch of a rotor with thicker blades.

8.3.2 Pros and cons of increasing blade thickness

Pros	Cons
• Thicker blades yield more lift. • Stiffness is increased. • Thick airfoils generally stall later than thin airfoils.	• The profile drag is increased. • Thicker noses have an increased risk of causing laminar separation bubbles.

8.4 CAMBERED AIRFOILS

Traditionally, Darrieus rotors make use of the NACA four digit symmetric airfoil series, such as the NACA 0012, NACA 0015 or NACA 0018 sections. Although this seems logical at first, cambered sections possess certain properties that could benefit a rotor's starting behavior.

8.4.1 Adding camber

Although cambered airfoils normally display higher lift-to-drag ratios, stall later, show higher pitching moments and are less sensitive to roughness, they perform poorly at negative angles of attack. Since a blade spends an equal amount of time at a positive angle as at a negative angle, the choice for a symmetric airfoil seems more logical at first. However, because of the induction velocities, the apparent wind speed is much higher when a blade is traveling upwind ($0° \leq \theta \leq 180°$). Since $P \propto V^3$, the higher performance of a cambered airfoil might outweigh the increased drag generated during its downwind pass.

At the low Reynolds numbers during start-up, the difference in performance between cambered and symmetrical sections is generally more pronounced and some sections, designed to operate at low Reynolds numbers, have the potential to completely self-start. This was computed by Kirke (1998, pp. 164–166), who compared a NACA 0015 blade to an S1210 blade[4]. However, this effect gradually decreases at higher Re and some airfoils can cause the peak performance of the turbine to drop significantly. This is shown by Islam et al. (2007a), who predicted the performance of five different sections at Re = 100,000 and Re = 300,000 (see figures 8.6a and b). Although some sections show increased torque and power at low λ, none of them are able to surpass the output of a symmetrical NACA 0015 airfoil. This would confirm that, although superior during start-up, the advantages of a thin and highly cambered section such as the S1210 completely disappear. At higher λ, drag becomes more of an issue[5], which gives the advantage to airfoils that are designed for higher Reynolds numbers.

Although simply increasing the blade camber opens the path to some interesting concepts already, there are some pitfalls when it comes to skewed flow. Adding positive camber means that one effectively downgrades the performance on the downwind side while enhancing it on the upwind side. In cases where the flow is skewed, however, the downwind passage may significantly contribute to the total energy yield (see subsection 3.4.5). The use of camber has some

[4] The S1210 airfoil was originally designed for model airplanes participating in a heavy lift/slow flight competition (Selig, 1995).

[5] This is evident when looking at equation (3.7b). At low tip speed ratios, the variations in angle of attack are large and the therm $C_l \sin\alpha$ is more pronounced. At high λ, values of α remain relatively low and $C_d \cos\alpha$ becomes important.

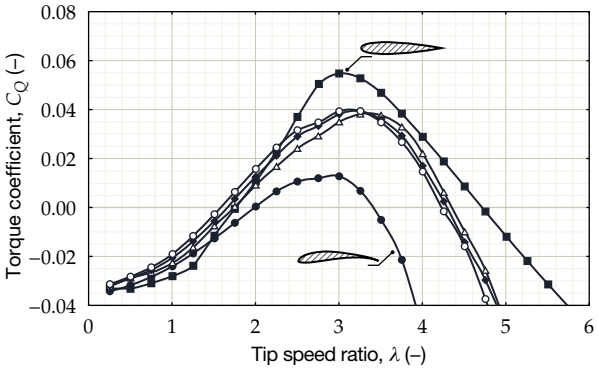

(a): Torque coefficients over a range of tip speed ratios at $\mathbf{Re = 100,000}$.

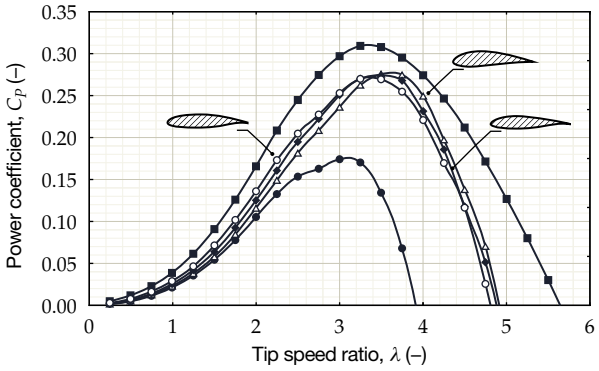

(b): Power coefficients over a range of tip speed ratios at $\mathbf{Re = 300,000}$.

Figure 8.6: Performance predictions for a NACA 0015 (■), NACA 4415 (△), NASA LS(1)-0417 (○), NASA NLF(1)-0416 (◆) and S1210 (●) profile (Islam et al., 2007a).

other disadvantages too. First, the generated forces will tend to fluctuate more during a cycle, which may cause unwanted vibrations. Second, since a cambered airfoil can produce positive lift at negative angles of attack, equation (3.7) indicates that the lift can start to produce a counteracting tangential force ($C_l \sin\alpha < 0$). To avoid this, it is possible to set the blade at a fixed negative pitch, but that will inherently lower the performance when $\alpha > 0$.

There are other ways of increasing camber, without affecting the airfoil performance too much. For instance, by adding a static extended trailing-edge (Liu et al., 2007), which is basically a thin surface attached to the rear of the airfoil (see figure 8.7). This is a feature derived from owl wings that typically have very thin trailing-edge feathers operating in the wake of the actual airfoil shape. Such an extension can effectively increase lift by relying on the same principle as a Gurney flap, but at a significantly smaller raise in drag. In addition, this can easily be combined with a serrated trailing-edge[6] as described by Howe (2007). However, the beneficial effect would only work for small variations in α, since the extension is prone to move outside of the wake. The extra chord length also means an increase in solidity with more interference effects as a result.

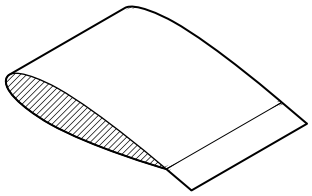

Figure 8.7: Example of a blade section with an extended trailing-edge.

[6] **This is used by owls to subdue the sound during flight. Their comb-like feathers break down the turbulent flow on the top side of the wing into smaller eddies. Smaller vortices create higher frequencies that are more effectively absorbed by the surrounding atmosphere (Roach, 2004).**

8.4.2 Pros and cons of increasing airfoil camber

Pros

- Asymmetrical airfoils will favor either positive or negative angles of attack. Positively cambered airfoils, for instance, yield more lift in the upwind half of the rotor ($\alpha > 0$), where there is generally more energy available. Negatively cambered airfoils perform well in the downwind part of the rotor where the angles of attack remain relatively stable.

Cons

- The tangential force at small angles of attack is decreased with respect to symmetric airfoils.
- Removing the energy contribution from the downwind half creates asymmetry and may not be a valid option when operating in skewed flow.

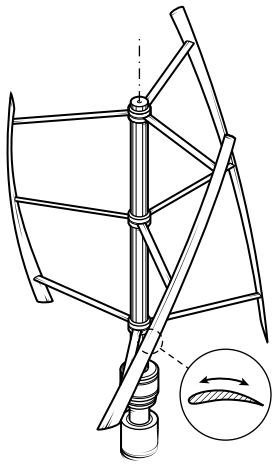

Figure 8.8: Sketch of a rotor with cambered blades.

8.5 BLUNT TRAILING-EDGE

Airfoils with blunt trailing-edges—also referred to as *flatback airfoils*—are sometimes used in the inboard sections of HAWT blades, where high lift and high structural strength are required.

8.5.1 Manufacturing constraints and performance

Blunt trailing-edges are generally created by driving a hypothetical wedge in the back of an airfoil, as shown in figure 8.9. The result is a larger sectional area with a higher bending stiffness. Such geometries are also convenient from a manufacturing point-of-view since the creation of sharp trailing-edges is often troublesome. This is especially true for very small chord lengths, where it becomes difficult to approach the exact airfoil shape.

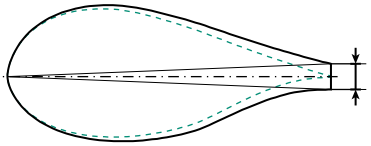

Figure 8.9: Creation of a trailing-edge gap.

Of course, there are effects on performance. Obviously, flatback airfoils leave a larger wake which can severely increase drag. Moreover, they suffer from bluff-body separation which can leave behind trailing vortices and cause noise emissions.

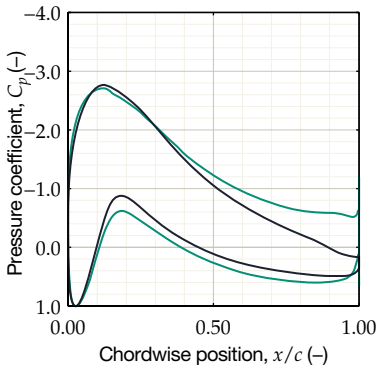

Figure 8.10: Pressure distributions of a TR-35 airfoil with a sharp trailing-edge (—) and with a 10%c trailing-edge gap (—) at $\alpha = 8°$ and $\mathrm{Re} = 4.5 \cdot 10^6$ (Standish and van Dam, 2003; cited in Baker et al., 2006).

Still, there are aerodynamic benefits. Most notably is the ability of the flatback airfoils to move part of the pressure recovery region into the wake. This means that the adverse pressure gradient is less steep and stall is delayed to higher angles of attack (see figure 8.10). Moreover, the sensitivity to roughness effects is reduced. Wind tunnel tests by Baker et al. (2006) on a 35% thick FB-3500 airfoil revealed that incorporating a trailing-edge gap of 8.75%c increased the maximum lift coefficient from 1.50 to 1.65 and also raised the lift-to-drag ratio from 35.5 to 44.0. A larger gap of 17.5%c further increased the lift to $C_{l_{\max}} = 2.16$, but reduced the airfoil's overall performance to $C_l/C_d = 18.6$, which hints that an optimum is to be found somewhere.

For VAWTS in start-up, flatback airfoils have several advantages. In cases of reversed flow ($\lambda \leq 1$), for instance, some extra torque can be generated hollowing out the trailing-edge. Furthermore, the weaker adverse pressure gradient can be utilized in the process of mitigating bubble losses and delaying the onset of (dynamic) stall, thereby decreasing the width of a dead band. However, the extra noise emissions can be a significant drawback, especially in urban areas. Also the increased baseline drag leads to a trade-off between decreasing performance at low angles of attack and enhancing performance at high α.

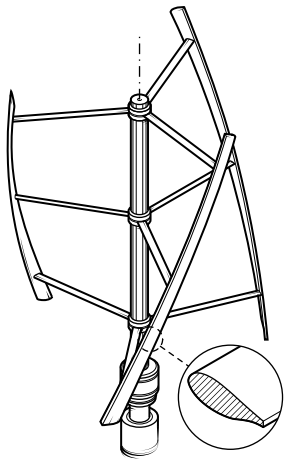

Figure 8.11: Sketch of a rotor with flatback airfoils.

8.5.2 Pros and cons of flatback airfoils

Pros

- Flatback airfoils yield more lift.
- The trailing-edge gap allows part of the pressure recovery process to occur in the wake, which can significantly reduce the adverse pressure gradient on the suction side and helps to postpone separation.
- Blunt trailing-edges are easier to manufacture.

Cons

- The baseline drag is increased.
- Bluff-body separation from the trailing-edge can increase noise emissions.

8.6 FLEXIBILITY

The performance of cambered blades can drop greatly under negative angles of attack, resulting in high drag. In accordance with figure 3.5, a blade mounted concave-in would perform better in the downwind half of the rotor, while a concave-out configuration would perform better upwind (see figures 8.12 and 8.13). One solution to get the best of both worlds is to use flexible blades that are able to bend inward and outward.

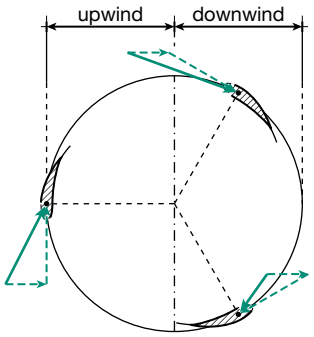

Figure 8.12: Blades that are flexed outward (concave-in) perform better downwind.

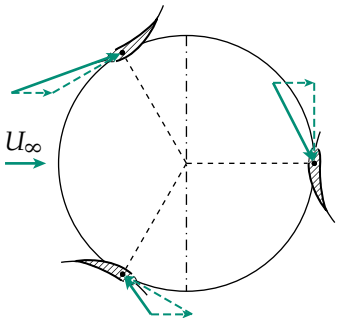

Figure 8.13: Blades that are flexed inward (concave-out) perform better upwind.

8.6.1 Flexible wings in biology and past experiments

Apart from being able to regulate camber, there are other advantages. For instance, flexible airfoils can be made up from fabric, sheet metal or by using a series of flaps, and can potentially be much lighter than rigid airfoils. Another important advantage is that a flexible lifting surface can passively change its shape to lower adverse pressure gradients and prevent flow separation (Shyy et al., 1999). These effects have been identified in flying squirrels that, although not displaying particularly high lift-to-drag ratios, are able to reach angles of attack up to 53.5° using a flexible membrane (Bishop, 2006). The same has been noticed with bats that continuously change the shape of their wings during the different phases of flapping flight. They rely on flexible bones and a highly anisotropically stressed skin to adapt to aerodynamic loadings (Swartz et al., 2007). Birds also possess this feature, but instead use several layers of interconnected feathers. It might therefore be promising to mimic the structure of biological wings, especially when considering the analogy between VAWTS and flapping flight.

At the rated wind speed, however, past experiments with sailwing and sheet metal blade VAWTS have not been able to surpass the performance of rigid cambered airfoils. Therefore, Kirke (1998) argues that it is probably not worthwhile it to investigate these designs further, quoting the outcomes of several studies including Robert and Newman (1979), Waltham (1984) and Pandey et al. (1988) (cited in Kirke, 1998, pp. 167–171). Also, there are other problems that arise from using these kinds of configurations. For instance, flexible sails are unable to handle a pitching moment and can twist spanwise. Furthermore, at low angles of attack, the membrane tension drops and the excess skin length can cause the sail to flap, an effect known as *luffing* (e.g. Newman and Païdoussis, 1991). Sheet metal blades on the other hand, clamped at the leading-edge and trailing-edge, are prone to fatigue. In both cases, the reversal of camber can create a flapping sound, possibly leading to noise pollution.

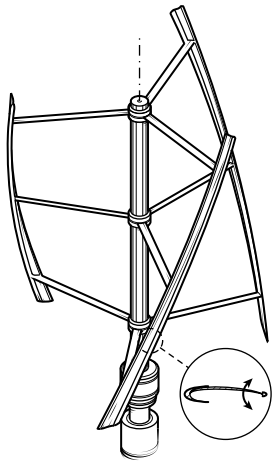

Figure 8.14: Sketch of a rotor with flexible blades.

8.6.2 Pros and cons of flexible blades

Pros

- Flexible airfoils can passively change camber.
- There is the ability of adapting to aerodynamic loadings to delay stall.

Cons

- Past experiments with sailwing or sheet-metal blades were not successful.
- Flexible blades are unable to handle pitching moments.
- Excess skin can flap at low angles of attack.

8.7 PASSIVE FLAPS

One effective way to increase the maximum lift and delay stall, is to use high-lift devices. Because of the strong variations in a blade's orientation, as well as the complexity of these systems, such solutions are often not applicable to Darrieus rotors. Although this might be the case for many active systems, it has been observed that many flying birds possess several passive high-lift devices. When noting the analogy between VAWTS and flapping flight, it is possible that these additions could aid in postponing stall.

8.7.1 The alula

When high lift is required, for instance during landing, flexible feathers will quickly deploy on the leading-edge and trailing-edge of the wing. This allows the bird to sense the degree of stall over its wings (Carruthers et al., 2007), but also helps to delay separation.

A bird's *alula* is a small extension from the leading-edge of the wing, representing the thumb, which is spread to prevent the wing from stalling. It is regarded as an important feature for low-speed flight. The alula is located near a suction peak on the bird's wing which, at high angles of attack, causes it to deploy (see figure 8.15). This creates an effect similar to leading-edge slats used on aircraft. They have the purpose of reducing the air velocity over the main wing, thereby lowering the pressure difference in the boundary layer to delay separation. The deployment of the alula occurs passively and is purely a result of the governing aerodynamic forces (Álvarez et al., 2001). Consecutive measurements by Meseguer et al. (2005) showed that deflecting the alula can enhance lift forces by 22% at higher angles of attack. Although being just a small attachment, the alula can affect the flow over 60% of a bird's wing area.

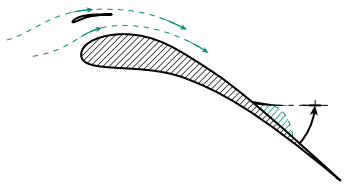

Figure 8.15: Cross-section of a bird wing near stall, showing the deflected alula and covert feathers.

8.7.2 Covert feathers

Covert feathers are located on the back of the wing and provide shape and thickness to the airfoil. At high angles of attack, reversed flow near the wing's surface will force these feathers to deflect, but cannot force them to enter the region of inviscid flow. It is hypothesized that, when lifted, the coverts will act as barriers that prevent flow separation from spreading over the entire wing. This eventually delays stall and can increase $C_{l,\,\max}$ by up to 18% (Bechert et al., 2000). In order to prevent premature deployment, the feathers are

slightly porous and tapered to level out the static pressure difference between both sides.

The effectiveness of these devices depends on both placement and flexibility since they have to deflect near the point of flow separation and at the right time. At very high angles of attack, the flaps have the danger of tipping over. In the experiments of Bechert et al. (2000) this was solved by connecting strings to the flap tips. Furthermore, when trailing-edge devices are placed too far downstream, there is not enough driving force for deflection. On the other hand, when placed too far upstream, flow separation is already allowed to spread over a considerable chord length. Also the appropriate length of the flaps would have to be determined. Longer devices further increase local lift but may have difficulties resetting to their original state.

8.7.3 Application to rotor blades

While both solutions seem promising in theory, the technology is very immature. Any serious applications on VAWTs will require an extensive period of testing and optimization. Adding an artificial alula is especially time-consuming because of the scarcely available information. Passive trailing-edge flaps have been applied to aircraft wings in the past by Bechert et al. (2000) which would be convenient to base a design on.

A following study by Schatz et al. (2004), however, revealed that the application is limited to unswept configurations. The reason behind this is that the radial boundary layer flow over swept wings makes it difficult to predict the deflection behavior. This makes the implementation of both types of feathers in helical VAWTs very troublesome.

8.7.4 Pros and cons of passive flaps

Pros	Cons
• Passive flaps are an elegant solution to delay separation.	• The technology is still at a very early stage of development. • Radial flow makes it difficult to predict deflection.

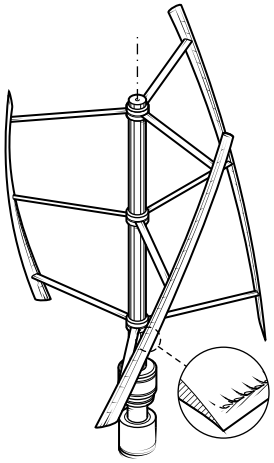

Figure 8.16: Sketch of a rotor with passive flaps.

8.8 BOUNDARY LAYER TRIP AND TRANSITION RAMP

In subsection 3.3.2, it was discussed how the formation of laminar separation bubbles lead to high drag at low Reynolds numbers. This section deals with additional ways to avoid this.

8.8.1 Control of boundary layer transition

There are two common strategies to reduce bubble drag. First, by tripping the boundary layer using a *turbulator*, it can be forced to turn turbulent before the expected point of separation. The mixing of momentum between the wall-region and the surrounding fluid then helps the air to stay attached. Although the resulting turbulent boundary layer leads to an increase in skin friction, the net effect is a decrease in total drag. The difficulty with applying trip is that the op-

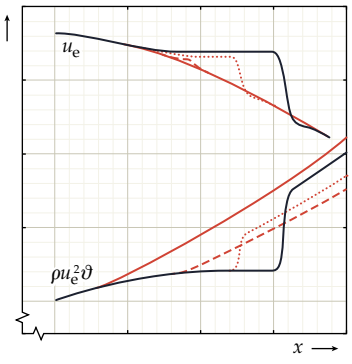

Figure 8.17: Sketch of momentum losses resulting from several transition locations (adapted from Drela, 1988).

timal location is very dependent on the angle of attack and Reynolds number (Gopalarathnam et al., 2003). The benefits of minimizing the effects of the bubble during start-up may be overshadowed by the penalties of a longer turbulent boundary layer at the rated wind speed (see figure 8.17). Adding turbulators is a relatively cheap and simple solution and can be as straightforward as applying zigzag tape at the right location, as is often done with sailplanes. The only complexity is making sure that the adhesive bond holds during the service life and in harsh weather conditions.

A second strategy is to shape the airfoil by including a *transition ramp*, referring to creating an instability in the pressure distribution. Natural transition on airfoils is caused by Tollmien-Schlichting waves that are amplified within the boundary layer until they reach critical amplitude. This growth rate is dependent on the local shape parameter, H, and therefore inversely proportional to the momentum thickness (see subsection 3.3.2). A favorable pressure gradient ($dp/dx < 0$) is stabilizing and an adverse pressure gradient ($dp/dx > 0$) is destabilizing. By careful design of the airfoil surface, transition can be promoted over the length of a weak adverse pressure gradient while

Figure 8.18: Effect of the transition ramp on airfoil performance(Selig, 2003).

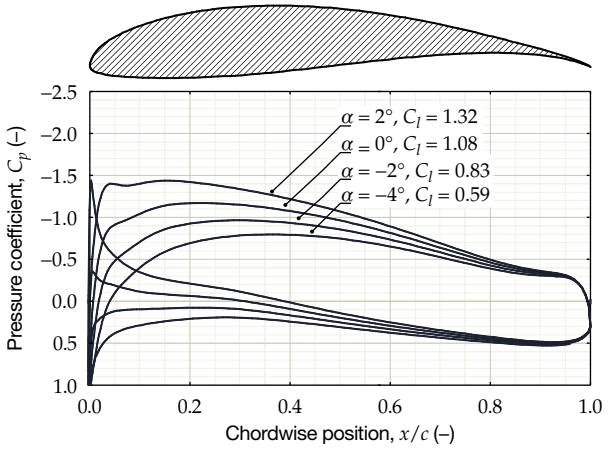

(a): Inviscid pressure distributions over an FX63-137 airfoil at $-4° \leq \alpha \leq 2°$.

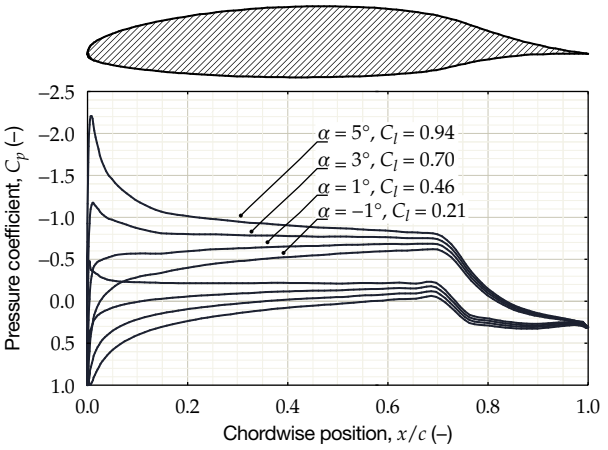

(b): Inviscid pressure distributions over a NASA NLF(1)-0414F airfoil at $-1° \leq \alpha \leq 5°$.

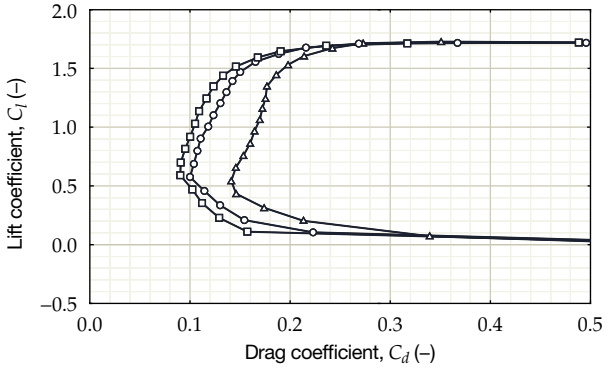

(c): Measurements of an FX63-137 airfoil at Re = 200,000 (△), Re = 350,000 (○) and Re = 500,000 (□).

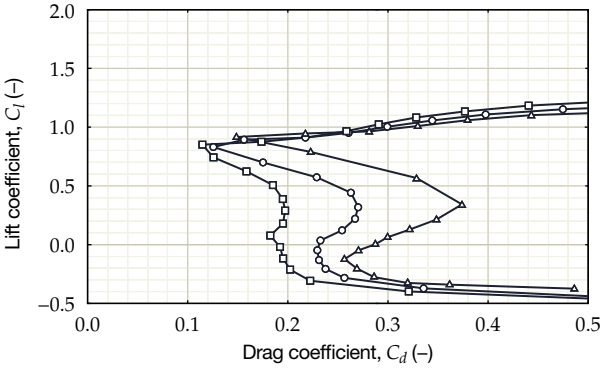

(d): Measurements of a NASA NLF(1)-0414F airfoil at Re = 200,000 (△), Re = 350,000 (○) and Re = 500,000 (□).

keeping the boundary layer attached. The optimal length of such a ramp is determined by the expected movement of the transition point over the operating range of angles of attack. An airfoil like the FX 63-137, designed to operate at low Re, has a smoothly curved upper surface which results in a gradual adverse pressure gradient and helps flow to recover at a wide range of α (see figure 8.18a). For a different airfoil such as the NASA NLF(1)-0414F, designed for high Re, this becomes less important. In this case a laminar boundary layer can be maintained by moving the point of maximum thickness more aft and transition can then be accounted for by implementing a much shorter ramp causing a rather abrupt rise in pressure (see figure 8.18b. At the design conditions, a laminar NLF profile would naturally have a low friction drag. However when operating in a low Re flow, the boundary layer can separate earlier and create a long separation bubble. The difference between the two configurations is reflected by the $C_l - C_d$ curves shown in figures 8.18c and d. The use of transition ramps in VAWTS has been treated by Saeed et al. (2008), who predicted the performance of a modified NACA 0018 profile and found a 15% increase in power and torque at $\lambda = 1.6$.

8.8.2 Pros and cons of turbulators

Pros

- A well-placed boundary layer trip can eliminate most of the problems caused by laminar separation bubbles.
- The resulting turbulent boundary layer can help to delay separation.
- Adding turbulators is a relatively cheap and simple solution and can be as straightforward as applying zigzag tape at the right location or creating patches of roughness.

Cons

- The turbulent boundary layer creates extra friction drag.
- An optimal position is hard to determine under strongly varying angles of attack.
- The adhesive bond has to hold the turbulator in place for at least 20 years and in harsh weather conditions.
- In real life, pollution can build up around the turbulator.

8.8.3 Pros and cons of transition ramps

Pros

- Performance at low Reynolds numbers is increased.

Cons

- An optimal geometry for low λ and low Re is most likely not an optimal geometry for the nominal λ and higher Re.
- The violent movement of the transition point with angle of attack makes it hard to establish a good curvature.

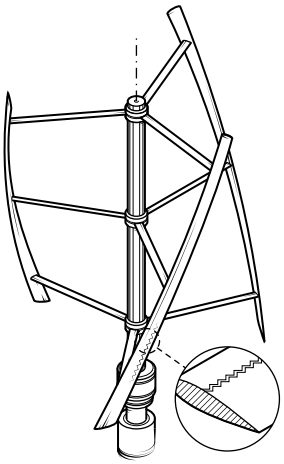

Figure 8.19: Sketch of a rotor with a zigzag strip.

8.9 VORTEX GENERATORS

Vortex generators (VG) are common additions to wings to delay separation. They are already widely used on stall-controlled wind turbines and on the control surfaces of regular aircraft in order to ensure good stability at large deflections.

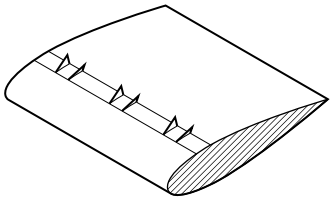

Figure 8.20: Example of a series of vortex generators on a blade section.

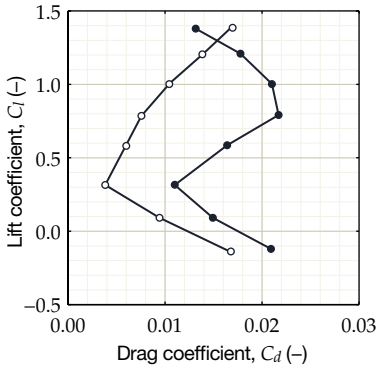

Figure 8.21: (*above*) Performance of an airfoil at $\mathrm{Re} = 235,000$ using wishbone-shaped vortex generators (○) placed at 22%—just upstream of the separation bubble—compared to the clean case (●) (Kerho et al., 1993; cited in Lin, 2002).

Figure 8.22: (*bottom*) Performance of an OA 209 rotorcraft airfoil in dynamic stall for a pitching motion $\alpha(t) = 13° + 7° \sin \omega t$ at $k = 0.1$ at $\mathrm{Re} = 1,150,000$ (Mai et al., 2008).

8.9.1 The effects of using vortex generators

Vortex generators are small rectangular or triangular devices that protrude from an aerodynamic surface and measure approximately half the height of the boundary layer (see figure 8.20). By generating a vortex, faster moving air over a surface is drawn to the boundary layer which can reenergize it through the exchange of momentum. Adding kinetic energy in the streamwise direction delays the point of flow reversal and can therefore postpone stall. This strategy is most efficient in case of a turbulent boundary layer, since it offers a more effective mixing of flow.

In the static case, VGs usually increase the maximum lift coefficient and are able to delay the stall angle. This is at the cost of an increased profile drag and a possible reduction of C_l/C_d. However, they might also help to reduce the size of the laminar separation bubble by promoting a more rapid reattachment. The result is then a thinner turbulent downstream boundary layer with considerably less friction drag. A striking example of this is shown in figure 8.21 where the VGs are able to mitigate most of the bubble over a wide operating range. At high C_l values, the bubble is too small for the effect to be noticeable.

There is also a distinction between co-rotating and counter-rotating VGs, depending on the direction of rotation of the generated vortex. In general, counter-rotating VGs seem to perform better in 2D flow, while co-rotating devices are more efficient in the 3D separation found on swept wings (Lin, 2002).

On oscillating airfoils, VGs still have a notable impact during dynamic stall. Although they do not increase the maximum lift and may even lower it, they tend to significantly reduce the depth of the hysteresis loop. This is because the mixing of flow is promoted which will speed up the reattachment process. The results of Mai et al. (2008), shown in figures 8.22a and b, show a 39% increase in lift during the downstroke at a cost of an 8% reduction in the peak lift coefficient. Furthermore, the drag was reduced by 25%. This was achieved with leading-edge VGs which are, unlike figure 8.20, shaped

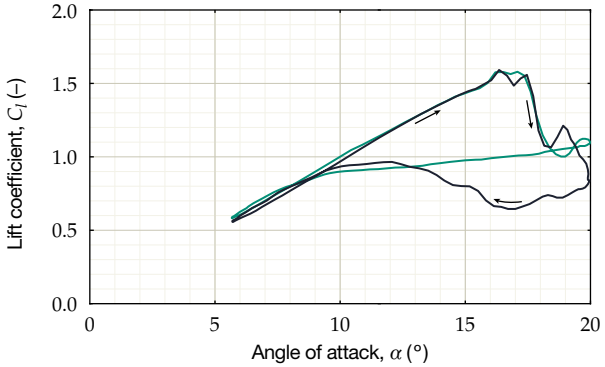

(a): Dynamic lift coefficient of a clean airfoil (—) and using leading-edge VGs (—).

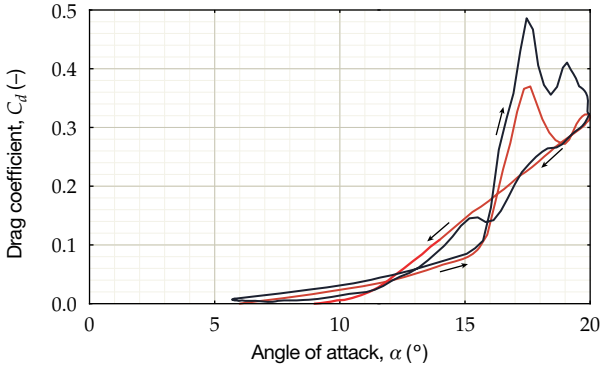

(b): Dynamic drag coefficient of a clean airfoil (—) and using leading-edge VGs (—).

like small cylinders and are placed on the nose of the airfoil.

The effect of vortex generators on the blades of an eggbeater-type Darrieus have been measured in the past. In a particular turbine, VGs increased the power output by 15 to 20%. However, the effect vanished for tip speed ratios higher than 4 (Paraschivoiu, 2002, p. 344) which immediately illustrates the major drawback. At the rated tip speed ratio, the blades will normally not approach the stall angle, rendering the VGs useless when it comes to postponing trailing-edge separation. Instead, the drag can increase substantially (e.g. Timmer and van Rooij, 2003) which is naturally reflected on the peak power coefficient. When bubble drag is concerned, it is therefore better to rely on turbulators.

8.9.2 Pros and cons of vortex generators

Pros

- Separation can be delayed by adding energy to the boundary layer.
- Bubble drag can be reduced in some cases by promoting reattachment.
- Flow reattachment after (dynamic) stall occurs earlier.

Cons

- The drag can increase substantially.

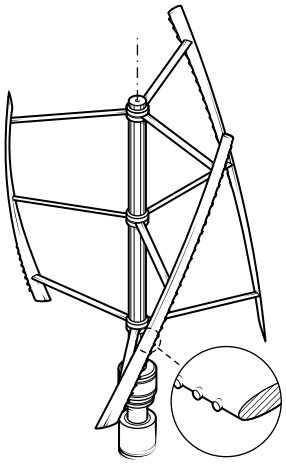

Figure 8.23: Sketch of a rotor with leading-edge vortex generators.

8.10 KLINE-FOGLEMAN AIRFOILS

The family of Kline-Fogleman airfoils (KFm) includes of a set of sections with one or multiple steps induced along the chord (see figure 8.24). The original patent[7] (Kline and Fogleman, 1972) describes a profile consisting of a sharp wedge-shaped leading-edge which abruptly changes to a thin trailing-edge.

8.10.1 Airfoils with steps or cavities

Although the idea enjoyed a lot of publicity in the 1970s, studies concluded that the Kline-Fogleman wing suffered from poor efficiency. One study by Lumsdaine et al. (1974) investigated the shape drawn in the original 1972 patent and concluded that the lift-to-drag ratio was actually lower than that of a flat plate. The high performance of the paper models was said to be the result of the strong leading-edge vortex that lifts delta wings. Therefore, the airfoil was claimed to be unfit for full-size aircraft and the concept was not pursued further. Nowadays, the concept is still very much alive among builders of model aircraft, who instead claim that step-induced airfoils offer superior performance and handling for something that can be easily constructed from foam.

A stepped airfoil supposedly operates by trapping a vortex in the open pocket, which should then make part of the total contour. One study by Finaish and Witherspoon (1998) investigated the effect of several geometries on the pressure distribution and the lift-to-drag ratio at Re = 500,000. Some promising results were obtained for

[7] In 1968, Richard Kline experimented with paper airplanes that he had been making for his son. In search of a model that would be able to climb well and continue in a steady gliding flight, he folded back the leading-edge of a delta wing in such a way that it left a slot in the bottom of the wing. The model then flew farther and steadier than any other paper airplane and with a great resistance to stall. He then teamed up with his friend Floyd Fogleman, a pilot, and decided to file a patent (Morris, 1984).

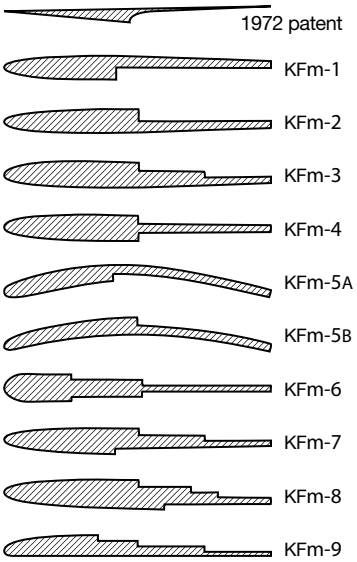

Figure 8.24: Kline-Fogleman family of airfoils, including the original 1972 patent (Kline and Fogleman, 1972; Kline, 2011).

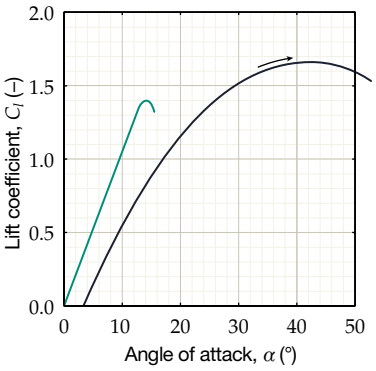

Figure 8.25: Sketch of the lift curve of a KFm airfoil (—) compared to a NACA 0009 section (—) (White, 2004, p. 498).

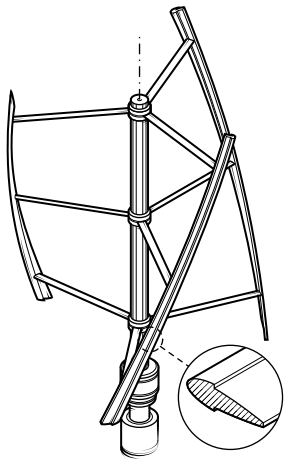

Figure 8.26: Sketch of a rotor with a stepped airfoil.

an upper surface cut-out, running from $0.5c$ to $0.625c$, and a lower surface step at 0.5, running towards the trailing-edge. Both features managed to enhance lift over a range of $0° \leq \alpha \leq 10°$. However, the reverse seems to be true when the steps are switched between the upper and lower surfaces and the same geometries actually lead to a decrease in lift. In addition, drag was increased in all cases. It was concluded that the effect on the lift-to-drag ratio would strongly depend on the local flight conditions. At higher angles of attack, flow visualization revealed that the reattachment process was not as stable as assumed and that vortex trapping within the cavity is probably not possible. This is in line with the outcomes of De Gregorio and Fraioli (2008), who computed the flow around an airfoil with a circular cavity. It was concluded that a trapped vortex would not be able to control flow separation without an active suction or blowing mechanism. A more recent paper about the subject revealed that such a geometry would lead to decreased lift and increased drag up to stall (Lasagna et al., 2011). With an active system, on the other hand, stall can be delayed and the performance near stall can be increased as result of a narrower wake and a higher lift-to-drag ratio (Olsman and Colonius, 2011).

Unfortunately, there is not a lot of definitive data available on the KFm family, especially performance curves. The effect of steps and cavities is still under study and a lot of aspects are open to speculation. Therefore, it is hard to draw a solid conclusion. If there is a source of truth and the actual performance looks in any way like the lift curve drawn by White (2004) (shown in figure 8.25), a smooth-stalling Kline-Fogleman airfoil would greatly enhance self-starting. But, at higher tip speed ratios, these benefits would gradually disappear when a much narrower range of angles of attack is addressed. As with many other solutions that aid self-starting, it will inevitably lower the peak performance.

8.10.2 Pros and cons of Kline-Fogleman airfoils

Pros	Cons
• The KFm family of airfoils is rumored to have interesting stall behavior.	• The amount of available data on these airfoils is very limited. • Airfoils with cavities are currently under investigation, but require active control.

8.11 SAVONIUS AUXILIARY ROTOR

Unlike Darrieus turbines, the drag-driven Savonius rotors have a low cut-in wind speed. Their maximum torque is obtained at $\lambda = 0$ where the apparent wind speed and the accompanying drag force is the highest. Therefore, one obvious way to improve the start-up is to construct a Darrieus-Savonius hybrid (see figure 8.27). By connecting the two rotors to a single shaft, the main rotor is given a boost at low speeds which decreases the cut-in wind speed.

8.11.1 Past experiments with secondary rotors

The combined Darrieus-Savonius rotors have been the subject of several studies. Gavaldà et al. (1990) connected a 13 cm diameter Savonius to a 40 cm diameter Darrieus rotor, both 20 cm in height. Their results are summarized in figures 8.28a and b. Figure 8.28a shows the torque of the two separate Savonius and Darrieus rotors at rest. The combined torque output of the hybrid machine can be smoothed by displacing the two individual devices by an angle $\Delta\theta_2$, to match the two functions. This way, one can get rid of the negative starting torque of the Darrieus. However, as figure 8.28b shows, the secondary device can lower the peak power coefficient. This is because the outmost section of the blades starts to produce an opposing torque when it is forced to operate at $\lambda_2 > 1$. In order to prevent this, one can either disconnect the Savonius rotor after start-up, or keep it from reaching a certain maximum. For maximum power production, the secondary rotor can be sized according to

$$R_2 \leq R_1 \frac{\lambda_{2,\,\text{rated}}}{\lambda_{1,\,\text{rated}}}, \tag{8.2}$$

where $\lambda_{1,\,\text{rated}}$ and $\lambda_{2,\,\text{rated}}$ are the rated tip speed ratios of the primary Darrieus and secondary Savonius rotor, respectively. Alternatively, the value for λ_2 can also be chosen as the instant the drag device begins to produce an opposing torque, which would allow a larger radius, R_2. Since equation (8.2) now limits the diameter of the secondary rotor, the torque output can only be improved by increasing the height. The consequence is a taller tower which demands more of the structure but also affects other aspects such as appearance. The upside is that an increased aspect ratio also diminishes the disadvantageous 3D effects.

Another study by Wakui et al. (2005) investigated two different hybrid configurations where a Savonius rotor, made of two parts separated by 90°, was connected to a troposkien-shaped Darrieus. One had its secondary rotor inside the primary, while the other type had the two rotors placed on top of each other. Furthermore, the radii of the individual machines were chosen with care to not violate equation (8.2). The two machines were analyzed using multiple

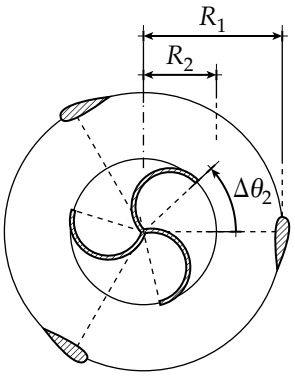

Figure 8.27: A Darrieus-Savonius hybrid where the two rotors have a phase difference $\Delta\theta_2$.

Figure 8.28: Results from the experiments by Gavaldà et al. (1990), showing a Savonius (△), Darrieus (□) and a combined Darrieus-Savonius hybrid (•).

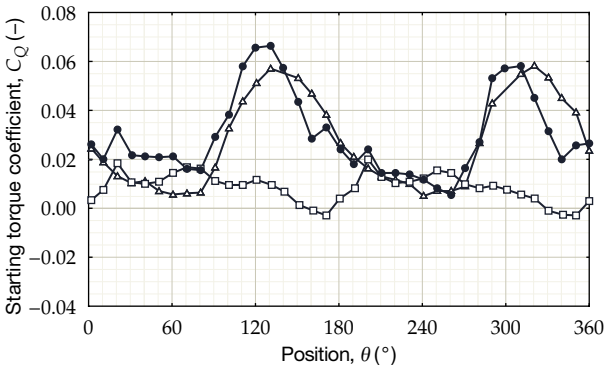

(a): Torque coefficients at rest ($\lambda_1 = 0$).

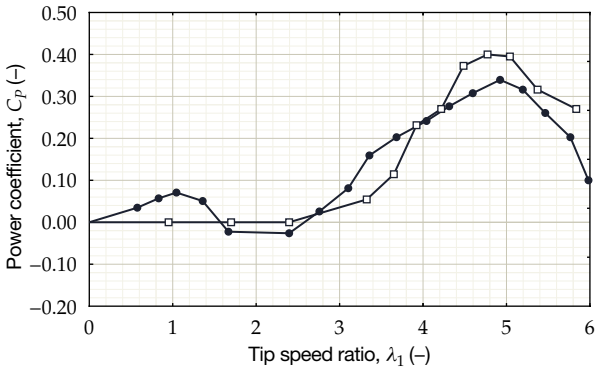

(b): Power coefficients over a range of tip speed ratios.

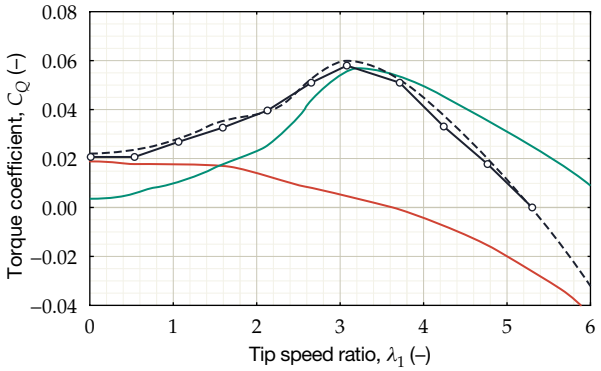

(a): Torque coefficients during operation for a combined Darrieus-Savonius hybrid with the secondary rotor *inside* the primary.

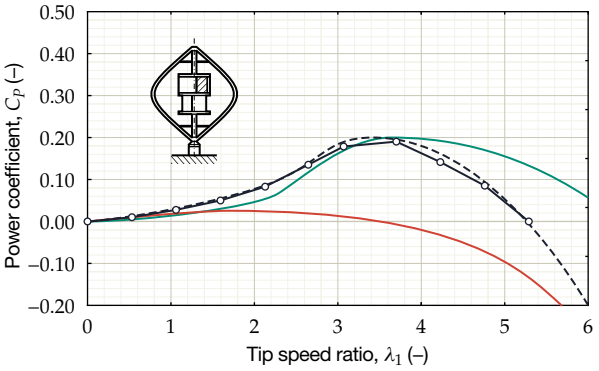

(b): Power coefficients during operation for a combined Darrieus-Savonius hybrid with the secondary rotor *inside* the primary.

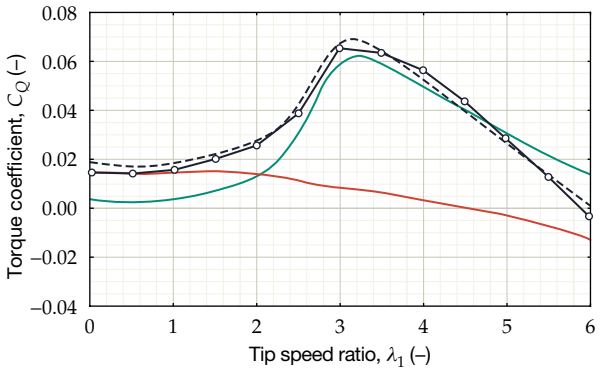

(c): Torque coefficients during operation for a combined Darrieus-Savonius hybrid with the secondary rotor *outside* of the primary.

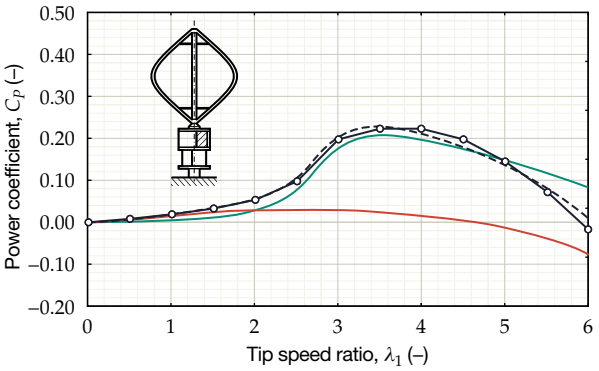

(d): Power coefficients during operation for a combined Darrieus-Savonius hybrid with the secondary rotor *outside* of the primary.

Figure 8.29: A combined Darrieus-Savonius hybrid during operation (○), compared to the computed values of the auxiliary Savonius rotor (—), primary Darrieus rotor (—) and the hybrid machine in total (– –) (Wakui et al., 2005).

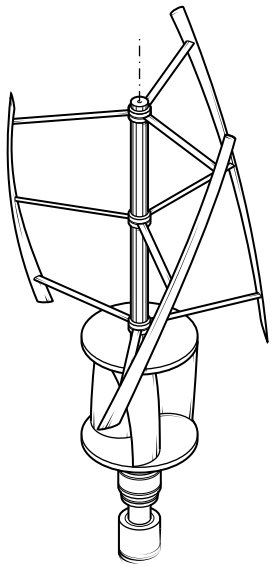

Figure 8.30: Sketch of a two-stage Darrieus-Savonius hybrid.

streamtube theory and tested in a wind tunnel. In the one case, where the secondary resides inside the primary (see figures 8.29a and b), the device is able to start well, but cannot perform optimally. This is because the Savonius is interfering with the Darrieus and vice versa and eventually, both devices find their peak power coefficients reduced. In the other case (see figures 8.29c and d), the two rotors are separated and are both able to contribute to the energy production. Unfortunately, the total configuration is now more complicated and needs a thicker shaft for support. This raises the moment of inertia, requiring more torque during start-up.

8.11.2 Pros and cons of auxiliary rotors

Pros

- A secondary Savonius turbine can add substantial amounts of torque at low speeds.
- It is possible to complement the torque variations of the main rotor.

Cons

- The support structure will have to be stronger.
- The moment of inertia will increase.
- Adding a second rotor is a relatively expensive solution.
- There is a huge impact on appearance.

8.12 RADIAL ARMS

The radial arms are used to transfer the torque and to increase the stiffness of the blades, but have the disadvantage of generating parasitic drag. In an aerodynamic sense, their presence is a necessary evil.

8.12.1 Drag-increasing struts

Though, by carefully shaping these struts, they can be allowed to contribute to the total torque instead. In this way, a Savonius device can be integrated into the existing structure (see figure 8.31). This should reduce the negative effects associated with the presence of a full-size secondary rotor.

But like the case of an auxiliary device, drag-increasing arms of a radius beyond the limit given by equation (8.2) will inevitably lower peak performance. Also when the starting torque requires a lot of surface area, the thickness of the struts would have to be increased up to the point where the result would eventually be similar to the configuration depicted in figure 8.29b. A well-shaped Savonius rotor is then probably a better option[8].

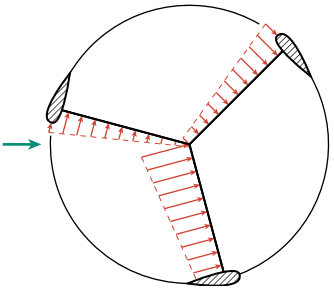

Figure 8.31: Darrieus-Savonius hybrid where the struts are shaped to act as a drag device.

[8] Since the arms still have to provide sufficient stiffness, shapes such as cups—although with a higher C_D—would be impractical.

8.12.2 Using the skewed flow

The case of skewed flow adds a vertical component to the wind vector, which makes it possible to draw an analogy to a propeller in yaw (see figure 8.32). This situation has been extensively studied for its occurrence in HAWTs and helicopters in forward flight. A strut shaped like an airfoil with some predetermined twist distribution should be able to generate a lift force and help the turbine to start. Such a configuration could in principle be combined with a drag-device near the rotor axis to offer some flexibility. Obviously, a propeller is only expected to perform well under high flow skew angles. Because the thrust of the actuator disc is deflected away from the flow, the power coefficient described in equation (3.11) reduces to

$$C_P = 4a(\sin\beta - a)^2, \tag{8.3}$$

which has a maximum at $C_{P_{\max}} = \frac{16}{27}\sin^3\beta$. For example, when a HAWT is yawed by an angle of 60° with respect to the incoming flow (the equivalent of a radial arm in a flow skewed by 30°), it is only able to extract $\frac{1}{8}$ of the Lanchester-Betz-Joukowsky limit.

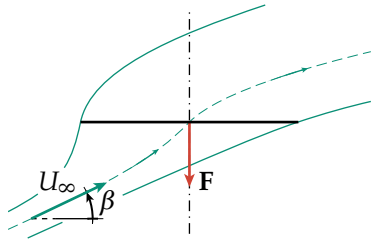

Figure 8.32: Horizontal actuator disc in a flow skewed by an angle β.

A big disadvantage of such a system therefore is the uncertainty about the skew angle β. In order for a turbine to self-start under a wide range of conditions, the struts should be able to provide sufficient torque even under small values of β. The same uncertainty makes it difficult to determine an optimum geometry, which is further complicated by the fact that the angle of attack changes for different skew angles, tip speed ratios and blade positions (see figure 8.33). A pitch system is most likely not worthwhile to install, so the twist angle of a strut element should be chosen carefully such that the airfoil does not stall at low λ and minimizes drag at high λ.

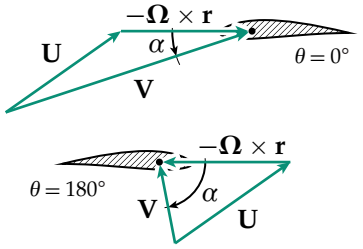

Figure 8.33: Angles of attack for an advancing (θ = 0°) and retreating (θ = 180°) radial arm section.

8.12.3 Pros and cons of hollow strut sections

Pros	Cons
• Hollow strut sections can give a purpose to something which would otherwise only cause parasitic drag.	• Creating enough surface area to provide torque for an advancing section is hard without causing too much drag when retreating. • At nominal tip speeds, the outer portions of the radial arms will no longer experience tailwind. Unfortunately, this is also where the most torque can be generated. • Thicker struts will cause disturbances in the heart of the rotor.

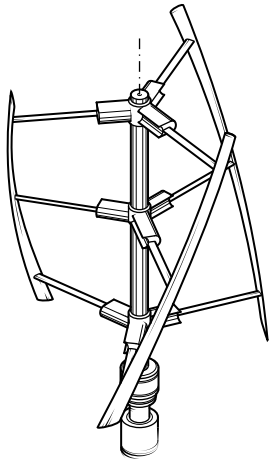

Figure 8.34: Sketch of a rotor with hollow strut sections extending to only part of the radius.

8.12.4 Pros and cons of lifting arms

Pros	Cons
• In skewed flow conditions, struts shaped as airfoils can provide a little extra lift without adding substantial amounts of drag.	• The exact skew angle is always uncertain, which means that it is hard to determine an optimal geometry. • The Reynolds numbers close to center of rotation are even lower than experienced by the main blades.

8.13 NESTED DARRIEUS ROTOR

Another design by Li et al. (1983; cited in Kirke, 1998, p. 41) consisted of a second Darrieus rotor nested inside the primary.

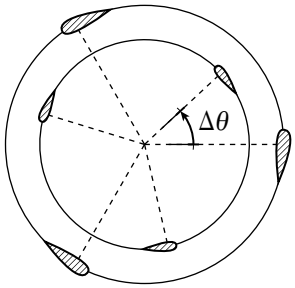

Figure 8.35: A nested Darrieus rotor could reduce the angles of attack on the main rotor blades (Li et al., 1983; cited in Kirke, 1998, p. 61).

8.13.1 Adding a second Darrieus

The secondary rotor is a smaller one and is displaced by some angle $\Delta\theta$ (see figure 8.35). This gives rise to a principle that also applies to sail ships, where an aft sail can operate in the flow deflected by a leading sail, thereby reducing the angle of attack (e.g. Doyle et al., 2002). The main function of the smaller rotor is therefore not to increase the total power output, but instead to lower the angle of attack of a trailing blade and decrease its tendency to stall.

Since the total blade area is increased, the generated aerodynamic forces are higher together with the interference between blades. It is improbable that such a configuration can be more efficient than simply increasing solidity, however. With the tip speed of the nested rotor being lower, the angles of attack are naturally higher, which leaves the airfoils in a stalled condition for most of the time. This would then lead to unwanted situations similar to when an aircraft's horizontal tail plane is moved into the turbulent wake of a stalled wing.

However, no real performance figures have been mentioned in the reference. Nonetheless it is still imaginable that adding a second Darrieus rotor would increase costs tremendously. Therefore, as already mentioned by Kirke (1998), it is improbable that such a system could be a feasible option.

8.13.2 Pros and cons of a nested rotor

Pros

- Reducing the angle of attack experienced by the main blades can be achieved in some cases.
- A second Darrieus rotor might yield some extra torque.

Cons

- The blades of the nested rotor are even more prone to stall, which creates exactly the opposite effect by ruining the flow.
- Adding a second Darrieus rotor is not cost-efficient.
- There is a large impact on aesthetics.

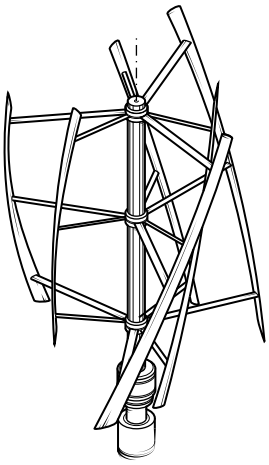

Figure 8.36: Sketch of a two-stage nested Darrieus rotor.

8.14 VARIABLE PITCH

Straight-bladed Darrieus turbines can be fitted with a blade pivot system to control the angle of attack during rotation. Although implementing such a system would be very difficult—although not entirely impossible—for a helical turbine, it is a common approach and worthwhile to mention, if only briefly.

8.14.1 Active pitch systems

Variable pitch VAWTs, also called *cycloturbines*, can be subdivided into active and passive systems. In active systems, the blades are continuously controlled by pushrods, cams or servomotors in order to avoid stall and to maintain favorable angles of attack (see figure 8.37). In addition, such a system can also provide an effective braking mechanism by pitching the blades at high wind speeds, similar to the control of a HAWT. Ideally, the pitch angle, γ, is varied in such a way that

$$\gamma(\theta) = \alpha_* - \arccos\left(\frac{\mathbf{V}\cdot -\hat{\mathbf{e}}_\theta}{\|\mathbf{V}\|}\right), \tag{8.4}$$

where α_* is some optimal angle of attack yielding the most torque. This is, however, hard to achieve since both the direction and magnitude of the apparent wind speed in the downwind region are hard to determine. In order to simplify this, the motion can be reduced to a sinusoidal variation in pitch:

$$\gamma(\theta) = \gamma_0 + \hat{\gamma}\sin\theta, \tag{8.5}$$

where γ_0 is some initial pitch angle and $\hat{\gamma}$ the pitch amplitude. A large amplitude tends to perform well at low λ, but lowers the output at high λ. Vice versa, a low pitch amplitude produces poor performance at low λ, but good performance at high λ (Lazauskas, 1992). The ideal pitch angle variation can be approximated more accurately by relying on aerodynamic models. Paraschivoiu et al. (2009) optimized the pitch control of an H-type Darrieus by applying a double actuator disc model. Their computations showed a performance increase for a narrow range around the rated wind speed, but also a clear decrease at low speeds. It was therefore concluded that pitch optimization is needed throughout the operating range. This means that the turbine has to continuously measure the local conditions[9] and translate them into pitch adjustments. By doing so, an increase

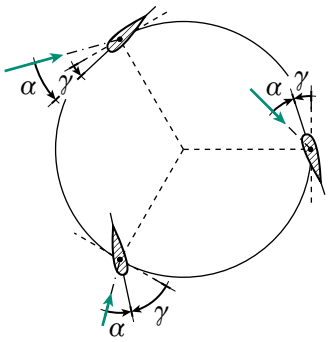

Figure 8.37: In variable pitch systems, the pitch angle, γ, is continuously adjusted to maintain an optimal angle of attack.

[9] Apart from the wind speed, the optimal pitch angle relies on θ and therefore also on the wind direction. This would actually affect the VAWT's indifference to yaw.

of almost 30% in the annual energy yield could be feasible. Whether this justifies the extra expenses for the control system naturally depends on the rotor and its output.

8.14.2 Passive pitch systems

Passive variable pitch systems eliminate the need for a complicated control system by allowing a blade to regulate its own pitch. It is based on the fact that an airfoil (or any other object), with its pivot point in front of the center of pressure, will resist rotation by inducing a pitching moment[10]. Therefore, a blade has a natural tendency to reduce the angle of attack and avoid stall. An automated stabilizer system would then provide an opposing moment to control the pitch amplitude. When the amplitude is not limited, the blades will align themselves with the wind when the turbine is at rest and aerodynamic forces are low, thus producing no starting torque. These stabilizer configurations can be quite diverse and may include springs, counterweights or cable systems.

[10] Basically, this is the same principle as a weather vane aligning itself with the wind

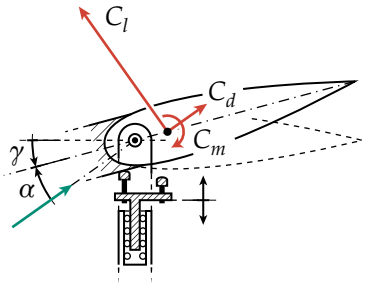

Figure 8.38: Passive pitch control mechanism where the pitch angle amplitude is controlled by a mass moving in radial direction. A counterweight arm balances the blade and, at the same time, serves to absorb energy when hit by the stops (Kirke, 1998, pp. 67, 229).

In one example by Kirke (1998), a set of stops is mounted on a mass able to move in and out the radial arm (see figure 8.38). Centrifugal force will move the stops in or outward to limit the pitching motion, depending on the rotor speed. The absence of springs conveniently relieves the system to allow larger deflections when the rotor is starting. Although the mechanism itself is quite promising and indeed seems to greatly improve the starting torque, the prototype rotor displayed a maximum C_P of less than a third of the predicted value (Kirke, 1998, pp. 268–277). Probably, this was due to several discrepancies between the original design and the actual real-life model. For example, the pitch amplitude was increased to improve the starting behavior in low wind speeds which, in hindsight, lowered peak performance.

8.14.3 Pros and cons of variable pitch systems

Pros

- Variable pitch gives complete control over the angles of attack.

Cons

- Pitch systems add a lot of complexity and moving parts.
- It is hard to integrate with swept blades.
- Determining the optimal pitch angle on-the-fly is hard, especially in conditions of strongly varying wind. This would remove the independence of wind direction.

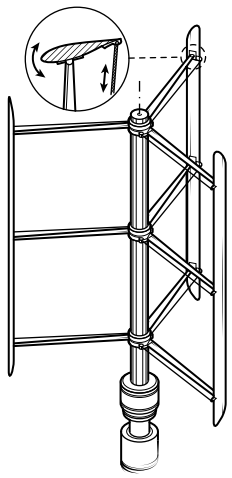

Figure 8.39: Sketch of a cycloturbine.

8.15 FAIRINGS

The parts where the support structure joins the blades can lead to additional sources of drag.

8.15.1 Interference drag

Two joined bodies will inevitably cause a higher drag than they would when separated, leading to *interference drag*. This can be due

to several reasons. First, when air is displaced by one surface it is accelerated and can lead to additional friction as it subsequently passes along the other surface. This is because air effectively flows through a narrower channel since there is less space available. As the air slows down again, there is the danger of separation if the deceleration process is not gradual enough. This is difficult if two lifting surfaces face each other with their suction sides, as can be the case with an aircraft's T-tail, for instance. Near the intersection, their minimum pressure peaks can coincide and be followed by a steep rise in pressure[11]. In the transonic regime, a shock can be expected to occur here, which is why reducing these effects is important for many airliners. For a geometry as depicted in figure 8.40, the pressure distribution over the main wing will be affected by a stagnation point existing at the nose of the second body. This will cause a strong adverse pressure gradient, leading to local separation and forces the boundary layer to roll up into a vortex. The presence of this vortex draws energy from the flow and results in additional friction drag by interacting with the corner.

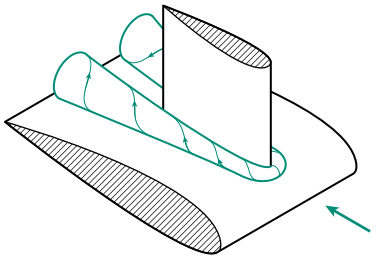

Figure 8.40: Seperation can be expected to occur locally at the intersection of two bodies due to a stagnation point (adapted from Greitzer et al., 2004, p. 117).

[11] The effect is drastic since both the fin and the horizontal stabilizer will act as end plates tending to mirror a 2D pressure distribution.

There are several ways to diminish interference drag. An easy and straightforward method is to add fairings at the intersection between the two surfaces (see figure 8.41). Rounding the edges will reduce the wetted area and therefore the friction drag. In aircraft, this is often applied at the wing root.

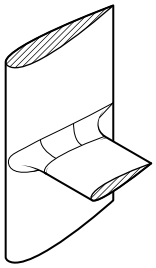

Figure 8.41: Smoothing out sharp corners at the intersection between the blade and strut will decrease the wetted area.

Another solution is to have the pressure distributions of the intersecting bodies complement each other. In the ideal case, a pressure side should meet a suction side in order to avoid large pressure peaks. For a Darrieus rotor this is not possible since the pressure sides of the airfoil are constantly alternating. Alternatively, by separating the locations of maximum thickness of the individual bodies, one can prevent the occurrence of narrowing channels and make sure that their pressure peaks do not meet. Also the additional stagnation point can be moved away from the lifting body. This is referred to as the *poor man's area rule* (Garrison, 2010). However, for parts such as T-tails, it often not done in practice because of structural reasons. The same applies to the turbine; moving the location of the strut away from the aerodynamic center will lead to large moments that have to be compensated by a heavier structure (see figure 8.42).

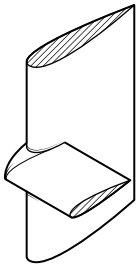

Figure 8.42: Large pressure peaks can be avoided by displacing the strut with respect to the blade.

A third strategy, which is often seen in aircraft T-tails, is the addition of a *bullet* or *acorn fairing*. Such a device, shown in figure 8.41, is used to separate the individual pressure fields and reduce interference. The result is an improved airflow at the intersection with a lower chance of separation. However, it is also accompanied by heavy material use and will generate additional drag because of its cross-sectional area. Therefore, it is probably only a good investment if large pressure forces over the strut are to be expected. The effects of applying a bullet fairing to the strut joint of a 19 m diameter eggbeater-type Darrieus has been estimated by Panek (1993, pp. 31–33) using a double-multiple streamtube model. It was predicted that the strut joints were responsible for a loss of 8% of the annual

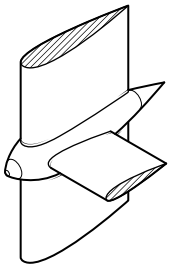

Figure 8.43: A *bullet fairing* can separate the two pressure fields to minimize interference.

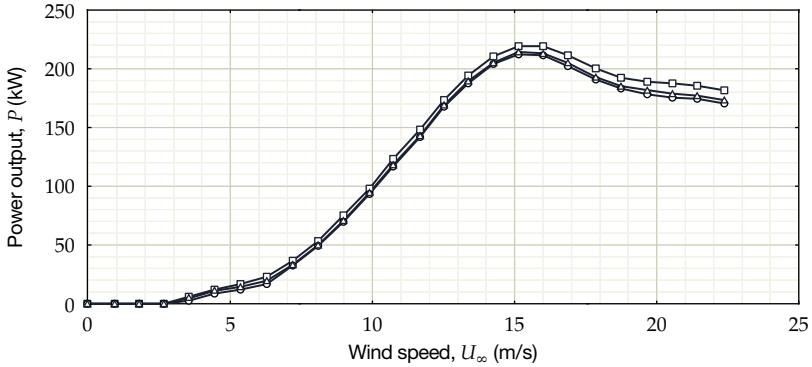

Figure 8.44: (*left*) Computed power output of a 19 m diameter eggbeater-type Darrieus without the drag caused by the strut joints (□), compared to the normal case (○) and to the use of faired strut joints (△) (Panek, 1993, p. 32).

energy output and the use of fairings recovered about 2%. As shown by the results in figure 8.44, the effect is only marginal, especially at low wind speeds. However, the costs of a set of bullet fairings does most likely not exceed that of 2% of the entire structure.

8.15.2 Pros and cons of fairings

Pros	Cons
• Fairings decrease the drag generated at the junction between the struts and the blades. • Boundary layer separation, as a result of strong low pressure peaks, is reduced.	• Smooth junctions will add to the total costs of the blades.

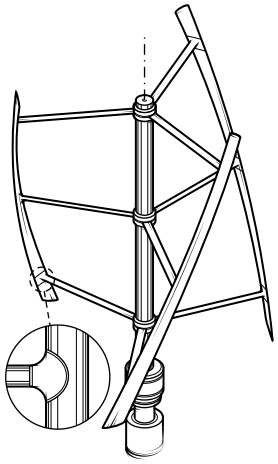

Figure 8.45: (*above*) Sketch of a rotor with faired strut joints.

8.16 MAGNETIC BEARINGS

Until now, the discussed strategies relied purely on aerodynamics. Though, a different solution would be to reduce mechanical friction.

8.16.1 Types of magnetic bearings

A very effective way to reduce friction losses is by the use of magnetic bearings. These bearings are able to support a rotating shaft without physical contact and have several other advantages including no wear, low noise output and no need for lubrication. Especially for VAWTS, with the generator and bearings located at the rotor base, this could be a very attractive option.

Magnetic bearings can be subdivided into several types (see figure 8.46). First, *passive magnetic bearings* (a) are built up from permanent magnets or superconductors. They are relatively simple and cheap to construct, but offer low stiffness and stability[12]. Second, *active magnetic bearings* (b) have a controllable magnetic field by using electromagnets. Displacements of the rotor can be measured using a sensor and corrected by varying the current through the windings. The big advantage is that damping and stiffness can be altered through electronics. However, electromagnets require a flow of current to operate which lowers the total yield of the turbine. Third, *hybrid magnetic bearings* (c) generate an electric field by a combination of permanent magnets and electromagnets. Their advantages and disadvantages

[12] **Earnshaw's theorem states that it is not possible for a collection of point charges to remain in a stable equilibrium. Two attracting or repelling magnets will keep attracting or repelling until they are attached or infinitely far away from each other. This means that there are no local minima or maxima in a magnetic field and that it is difficult for a magnetic bearing to keep a load stable. In addition, magnetism is a conservative force and cannot dampen vibrations.**

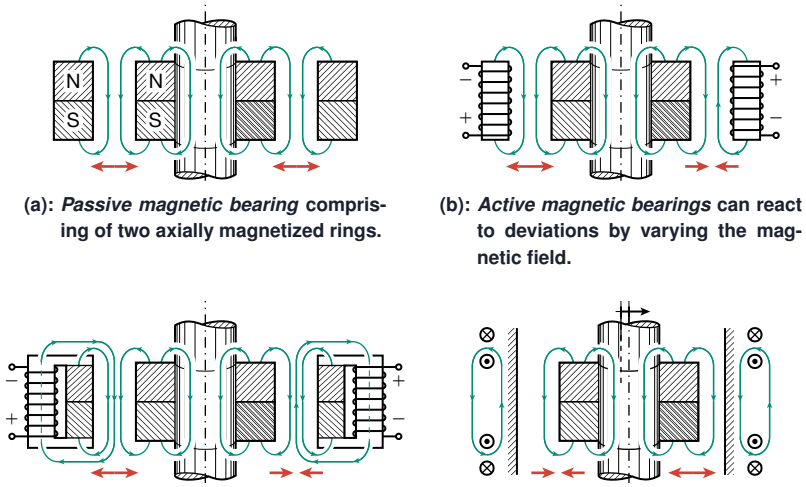

(a): ***Passive magnetic bearing*** comprising of two axially magnetized rings.

(b): ***Active magnetic bearings*** can react to deviations by varying the magnetic field.

(c): ***Hybrid magnetic bearings*** generate a magnetic field using both permanent magnets and electromagnets.

(d): ***Electrodynamic bearings*** can passively react to displacements of the rotor axis.

Figure 8.46: Several different configurations of radial magnetic bearings.

therefore lie somewhere between those of the two previous types. Finally, *electrodynamic bearings* (d) rely on Lenz' law, which states that a change in magnetic flux induces an opposing magnetic field. A displacement of the rotor axis is then countered by a magnetic field originating from eddy currents through a conductor. These types of bearings do not require a control system and can therefore be a lot cheaper and less complex than active systems.

8.16.2 Radial and axial bearings

The support system of a vertical shaft consists of a set of axial bearings and a set of radial bearings. The purpose of the axial bearings is to hold the weight of the rotor blades and part of the generator, causing a friction force that is present at all rotation speeds and wind speeds. Radial bearings are used to prevent the structure from wobbling by countering the rotor's thrust force. These radial loads are thus dependent on wind speed and less relevant when it comes to starting.

When only the axial bearings are replaced, the result would be similar to figure 8.47. Since magnetic bearings can only limit a single degree of freedom, the base has to be made up of both a radial and an axial bearing. It may also be convenient to keep the original bearings as a back-up in case the magnetic ones are unable to provide the required stiffness under extreme loads. A big disadvantage is that such a layout is not compatible with pretensioning; something which is done to reduce vibrations and noise. Instead, the whole system would have to be replaced by a magnetic set, meaning higher costs and complexity for a relatively low speed system.

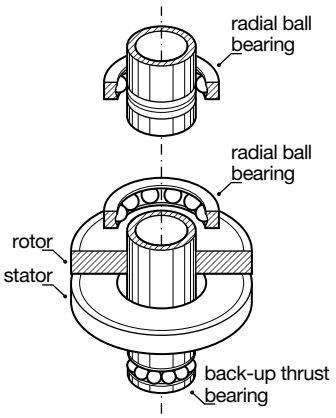

Figure 8.47: Sketch of a magnetic levitation system.

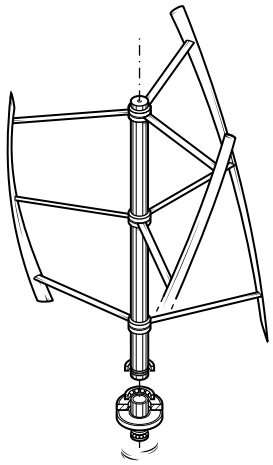

Figure 8.48: Sketch of a rotor with a magnetic thrust bearing.

8.16.3 Pros and cons of magnetic bearings

Pros	Cons
• The mechanical friction is reduced to zero.	• Magnetic bearings are less stiff than conventional ball bearings, which require the original sets to be used as a back-up in the case of extreme loads. • The configuration is relatively expensive, considering the current price of permanent magnets.

8.17 IDENTIFYING FEASIBLE SOLUTIONS

In conclusion, table 8.1 shows what strategies are considered simply unfeasible or not applicable to the Turby MkIa. Some may be an option but require a prior feasibility check. This is done in the next chapter.

The others are considered valid solutions and will be further treated in chapter 10. Almost all of these have an impact on blade geometry and the performance at low Reynolds numbers. So instead of analyzing all of these aspects separately, it makes sense to include them in the design of a low-Reynolds-number airfoil.

Table 8.1: Overview of the strategies discussed in this chapter.

Strategy	Not an option	Needs feasibility check (chapter 9)	Included in conceptual design (chapter 10)
8.1 Increasing rotor solidity			Is considered a powerful way to increase the torque during start-up. Though, determining the optimal chord length is best included in the airfoil design process (→ section 10.2).
8.2 Changing blade sweep		Has a notable effect on performance, but there is a trade-off with vibration levels which needs some further attention (→ section 9.1).	
8.3 Changing blade thickness			Has a large impact on the performance at low Reynolds numbers and is important to include in the airfoil design process; together with the structural requirements (→ section 10.2).
8.4 Changing blade camber			Should naturally be part of the airfoil design process (→ section 10.2).
8.5 Blunt trailing-edge	Is not really an option for urban VAWTs because of noise emissions.		
8.6 Flexible blades	Past experiments with flexible blades were unsuccessful, which is not inviting to look into this further.		
8.7 Passive flaps	Mimicking bird feathers is a time consuming process and good results are not at all guaranteed.		
8.8 Applying turbulators			Is an effective tool to enhance performance at low Re and should be included in the final design (→ section 10.2).
8.8 Transition ramp			Should be included in the airfoil design process (→ section 10.2).

Table 8.1: Overview of the strategies discussed in this chapter (*continued*).

Strategy	Not an option	Needs feasibility check (chapter 9)	Included in conceptual design (chapter 10)
8.9 Vortex generators	Might be very effective during start-up, but will inevitably decrease $C_{P_{\max}}$.		
8.10 Kline-Fogleman airfoils	There is no supporting evidence yet that the KFm family will perform better than regular airfoils.		
8.11 Auxiliary rotor		Delivers high torque but has a large impact on the design. The size of such a device must first be estimated in order to draw a valid conclusion (→ section 9.2).	
8.12 Drag-increasing arms		Might be an elegant solution, but requires an estimate of the effect on $C_{P_{\max}}$ (→ section 9.3).	
8.12 Lifting arms		Unsure if this will generate significant amounts of torque, but can be esimated along with the previous strategy (→ section 9.3).	
8.13 Nested Darrieus	The additional costs and the concerns regarding performance gives no reason to investigate this further.		
8.14 Variable pitch systems	Are not compatible with helical blades.		
8.15 Fairings			Will definitely improve the flow around the joint areas (→ section 10.2).
8.16 Magnetic bearings	Magnetic thrust bearings are not compatible with pretensioning and require the whole set of bearings to be replaced. This makes the solution not cost-effective.		

9 Feasibility check

The literature study in the previous chapter has resulted into several concepts that could possibly be implemented in the design of Turby. In this chapter, the aim is to quantify some of these solutions in order to learn more about their strengths and weaknesses. The approach remains purely computational, however. For this reason, the discussion is limited to the subjects that can be evaluated with the tools at hand.

First, the blade sweep angle is evaluated in section 9.1 and, second, the case of an external auxiliary Savonius rotor is treated in section 9.2. Finally, possible benefits of yawed propellers and drag devices, integrated into the support structure, are approximated in section 9.3.

9.1 Sweep angle

(*Continuing from section 8.2*)

Choosing the right blade sweep angle is a clear trade-off between increasing aerodynamic performance and decreasing torque pulsations. Figures 9.1a and a show the the results of evaluating the performance for various blade arcs. Since the predictions are purely based on extrapolating 2D airfoil data to 3D, it basically illustrates the independence principle for swept wings. Spanwise variations in lift—which would otherwise cause an additional torque ripple (see figure 3.20)—are not included, as well as any three-dimensional (dynamic) stall effects. The chord length is not equal for all cases, however, but is corrected in order to keep the solidity constant. As a result, the Reynolds numbers are somewhat higher for low sweep angles, while the aspect ratios are higher for high sweep angles.

The decrease in lift and the effect of distributing the torque production over the rotor height is well reflected in the two figures. The trade-off between the two aspects becomes even more clear in figure 9.2, which shows the relation between the performance sacrifice and

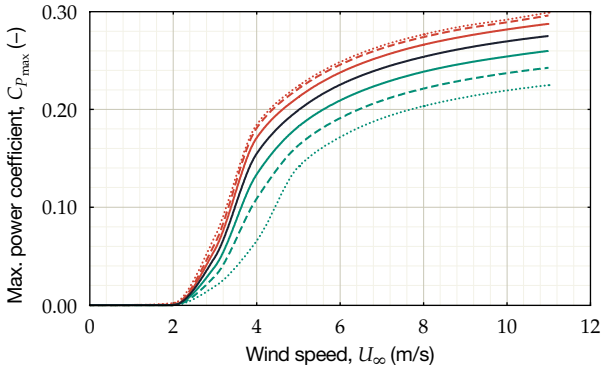

(a): Maximum power coefficient for $\xi = 0°$ (·····), 20° (– –), 40° (——), baseline 60° (——), 80° (——), 100° (– –) and 120° (·····).

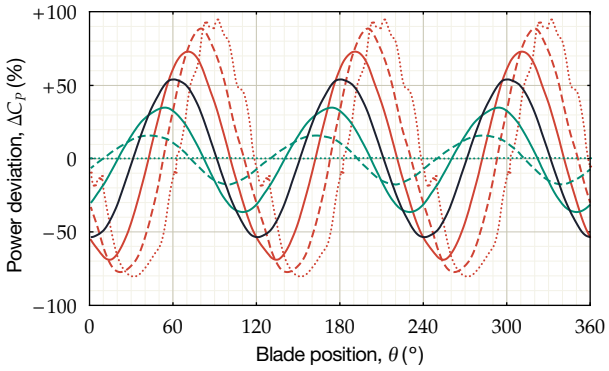

(b): Power pulsations at $\lambda = 4$ for $\xi = 0°$ (·····), 20° (– –), 40° (——), baseline 60° (——), 80° (——), 100° (– –) and 120° (·····).

Figure 9.1: Predicted performance for various blade arcs.

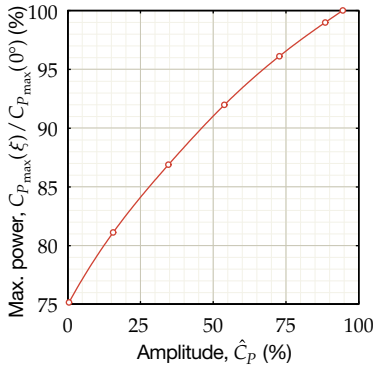

Figure 9.2: Maximum power coefficient with respect to a straight bladed geometry ($\xi = 0°$), as a function of the power amplitude during a cycle at $U_\infty = 11$ m/s.

the power amplitude. Currently, with a blade arc of $\xi = 60°$, about 8% of power is sacrificed to decrease the ripple by roughly 40%. It is possible to increase the power output by decreasing sweep, but this is clearly coupled with a high risk of fatigue damage. Decreasing the arc to $\xi = 40°$ will increase power by approximately 5% and allow the power amplitudes to grow by 35% – obviously not an interesting option.

9.2 AUXILIARY ROTOR

(*Continuing from section 8.11*)

In the past, many experiments have been conducted involving drag-based VAWTs. A distinction can be made between several types, shown in figures 9.3a, b and c. The simplest configuration is the traditional S shape which can be constructed from two half tubes. When the two halves overlap, air is able to flow from one side to the other. This increases the pressure on the concave side of the returning blade, which in turn improves the efficiency of the device (Fujisawa, 1991). According to Gupta et al. (2008), the best results are generally obtained using an *overlap ratio*[1] of $\frac{1}{6}$, although this would also strongly depend on the blade spacing (Akwa et al., 2012).

Like Darrieus turbines, the Savonius rotor can also be twisted into a helix to smooth out variations in torque. One can obtain the same effect by using different stages, each displaced by some angle (e.g. Kamoji et al., 2011), although that tends to decrease the maximum power coefficient. In addition, it is also possible to use three blades instead of two to ease starting. However, departing from a two-bladed design can also lower peak performance (Blackwell et al., 1977, p. 33).

Moreover, a further distinction can be made regarding the use of end plates, rotor aspect ratio, bucket shapes and numerous other geometrical parameters, which eventually leads to the great variety of devices reported in literature. End plates are a simple addition that reduce the tip losses and can greatly enhance the performance at high tip speed ratios. This is also true for the rotor aspect ratio.

[1] **The *overlap ratio* is defined as the ratio of the gap distance to the rotor diameter.**

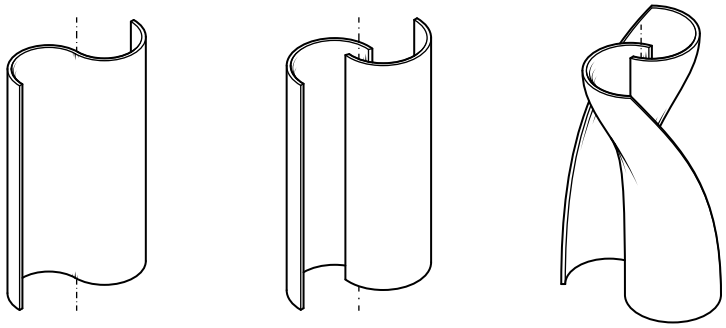

(a): Traditional S-shaped. (b): Split S design. (c): Helical Savonius.

Figure 9.3: Several different shapes of two-bladed Savonius machines.

Increasing aspect ratios will also reduce the moment of inertia, but can at the same time reduce the torque coefficient.

Though the Savonius rotor is extensively documented in scientific literature, there is a great variance in the reported performance. Mainly this is due to the differences in methodology between authors and primarily on the effects of wind tunnel blockage. For instance, Akwa et al. (2012) compared the outcomes of 17 different studies on the subject and found that the maximum power coefficient ranged from 0.14 to 0.32. Especially the upper bound is remarkable since the energy extraction of drag devices is generally believed to be limited by $C_P = \frac{4}{27} C_D$.

The results of Wakui et al. (2005), shown in figures 8.29c and d, nicely illustrate how the power output of an external Savonius rotor can be added to that of the main rotor. This allows the secondary device to be analyzed individually, which makes design considerably less complicated. Since the purpose of the auxiliary rotor is purely to aid with starting, a sensible option would be to look into a three-bladed helical design. This will ensure a high and smooth torque output while also maintaining part of the aesthetics. Going for three blades will also make it easier to match the starting torque of the two rotors.

A representative rotor is taken from Saha et al. (2008), which has an aspect ratio of 1.58, a projected area of $A = 0.0377$ m^2 and a maximum power coefficient of 0.16. However, no real $C_P - \lambda$ curves were reported. To still make a reasonable estimation, the literature study of Akwa et al. (2012) is consulted, which shows that Savonius rotors often have their peak C_P at $\lambda \approx 0.7 - 0.8$ and start to brake at $\lambda \gtrsim 1.5 - 1.6$. Furthermore, the $C_P - \lambda$ curves tend to have a characteristic parabolic shape, resulting in the approximation shown in figure 9.4.

The secondary rotor radius has to be chosen such that the auxiliary device starts to brake past the rated tip speed ratio ($\lambda \approx 3.5 - 4.0$).

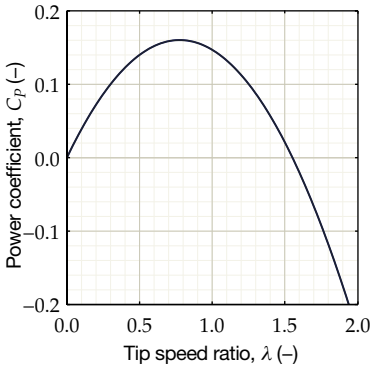

Figure 9.4: An approximated performance curve of a three-bladed helical Savonius rotor.

This means that

$$R_2 = \frac{\lambda_2}{\lambda_1} R_1,$$
$$= \frac{1.6}{4.0} \cdot 1.10 = 0.40 \text{ m}.$$

Purely based on figure 6.1a, a torque coefficient of $C_Q > 0.05$ is needed at $\lambda = 0.5$, which is about equal to a power coefficient of $C_P > 0.025$. For a radius of 0.40 m, the secondary rotor would be running at $\lambda = 0.18$ where it generates an estimated $C_P = 0.07$. Roughly speaking, the required area of the drag device would then be

$$A_2 = \frac{0.025}{0.07} A_1 \approx 0.36 A_1.$$

A frontal area of this size with a radius of 0.4 m, would mean that the Savonius would have to be about 2.6 m tall. Estimations by the model, however, would suggest that the dead band is less deep than what appears from the field test; since figures 6.1a and b also include wind speeds of 1 and 2 m/s. Even so, when assuming a value between $C_P \approx -0.005$ and ≈ -0.010, this would still mean a height of approximately 1 m. This is a considerable impact on aesthetics and overall complexity (see figure 9.5), which rules it out as a valid solution.

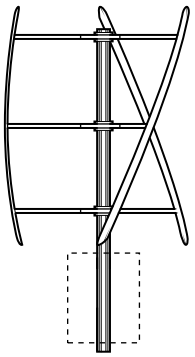

Figure 9.5: Projected size of an auxiliary rotor capable of supplying a power coefficient of $C_P = 0.01$ at $\lambda = 0.5$.

9.3 STRUT GEOMETRY

(*Continuing from section 8.12*)

The current struts are composed of 1 mm thick steel plates, folded as a NACA 0018 airfoil and following a chord distribution that varies linearly from 12 cm at the root to 8 cm at the blades. One blade—having a mass of 3.5 kg—is supported by three struts.

9.3.1 Blade element momentum theory for a yawed propeller

Since the operation of an airfoil-shaped radial arm has so much in common with a HAWT in yaw, it seems appropriate to rely on the blade element momentum (BEM) theory in steady yaw. However, a propeller in yaw experiences fluctuating angles of attack that may lead to unsteady aerodynamics; especially for small skew angles ($\beta \approx 20°$) that correspond to large yaw angles.

According to Burton et al. (2001, pp. 105–118), the relevant velocity components for a blade element[2] are

$$V_\theta(r) = U_\infty (\sin\beta - a) - U_\infty \lambda a' \frac{r}{R} \cos\theta \sin\chi (1 - \sin\theta \sin\chi), \quad (9.1a)$$

$$V_z(r) = U_\infty \lambda \frac{r}{R} \left[1 + a' \cos\chi (1 - \sin\theta \sin\chi)\right] - U_\infty \cos\theta \left(a \tan\tfrac{1}{2}\chi - \cos\beta\right). \quad (9.1b)$$

Here, χ is defined as the skew angle of the wake with respect to the rotor axis and is approximated by

$$\chi = (0.6a + 1)\left(\frac{\pi}{2} - \beta\right). \quad (9.2)$$

In equations (9.1a) and (9.1b), flow expansion terms have been excluded. The axial and tangential induction factors, a and a', follow

[2] The original equation has been slightly modified to have the variables θ and β correspond to the current frame of reference.

from

$$8\pi a\left(\sin\beta+\tan\tfrac{1}{2}\chi\cos\beta-a\sec^2\tfrac{1}{2}\chi\right)=\frac{nc}{2\pi r}\int_0^{2\pi}\frac{V^2}{U_\infty^2}C_z d\theta, \tag{9.3a}$$

$$4a'\left(\sin\beta-a\right)\lambda\pi\frac{r}{R}\left(1+\cos^2\chi\right) = \frac{nc}{2\pi r}\int_0^{2\pi}\frac{V^2}{U_\infty^2}(C_\theta\cos\chi-C_z\cos\theta\sin\chi)d\theta, \tag{9.3b}$$

where C_z and C_θ are the axial and tangential force coefficients[3], given by

$$C_z = C_l\cos\phi + C_d\sin\phi, \tag{9.4a}$$

$$C_\theta = C_l\sin\phi - C_d\cos\phi. \tag{9.4b}$$

Here, ϕ is the inflow angle; which produces the angle of attack together with a possible twist distribution, $\psi(r)$.

Apart from the unsteady aerodynamics and 3D effects that may occur, there are other things that affect the validity of this BEM method. One important aspect is that the induction factors are averaged for each rotor annulus, meaning that variations with the blade position, θ, cannot be accounted for. More important, however, is the vorticity shed by the main blades. This can be included by extracting the filaments of vorticity from the vortex panel method used earlier, and applying the Biot-Savart law at every position inside the rotor plane. These induced velocities are then skewed—following the method described in subsection 5.2.3—and used within the iterative process that determines the axial and tangential induction factors[4]. This causes the struts to be affected by the presence of the main blades, but not vice versa. Even so, with all these simplifications, the precision is deemed sufficient for a first-order estimate.

The predicted apparent wind speeds and angles of attack are plotted in figure 9.6. What is striking are the strong variations in both the radial and tangential direction, which indicates the presence of unsteadiness. Figures 9.6c and d also nicely illustrate how the area of tailwind decreases with increasing tip speed ratio.

[3] To avoid any confusion that could arise as a result of mixing the normal and tangential force coefficients of the propeller and VAWT blades, the choice is made to instead rely on the cylinderical coordinate system defined in section 3.1 and name the dimensionless force components accordingly.

[4] This adds a velocity component in the vertical direction and allows the skew angle to be included to some extent. However, the VAWT wake is still obtained without taking blade sweep into account; something which would also cause the streamlines to deviate upward.

9.3.2 Hollow arm sections

In section 9.2, it was already estimated that incorporating an additional drag device is most likely not worthwhile. Still, the struts are already present and, although probably not decisive for start-up, might still boost the torque a bit.

A good shape for a hollow strut section should be able to maximize drag when advancing, while minimizing drag when retreating. When considering high drag coefficients, the first that may come to mind is a flat plate or a half tube. Designing for low drag is a less straightforward process and focuses on finding a compromise between pressure and friction drag. In aerospace, there is a wide choice of nose shapes; i.e. depending on the Mach number and the ease of manufacturing. This can vary from sharp cones to half ellipses or parabolas. In nature, the body shape of many species of

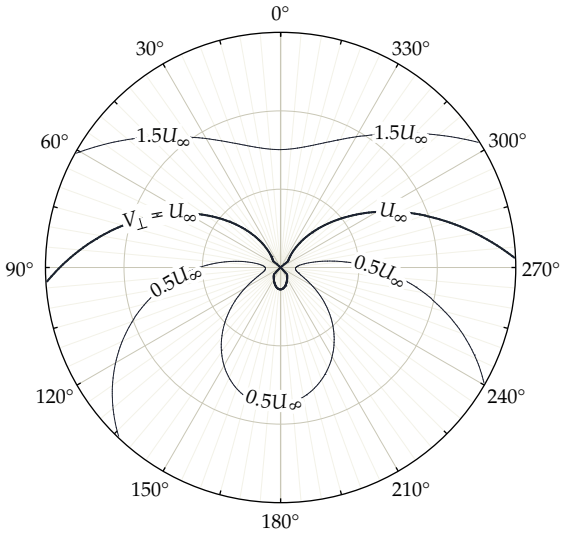

(a): Apparent wind speed, $V_\perp$, normal to the strut leading-edge, at $\lambda = 1$.

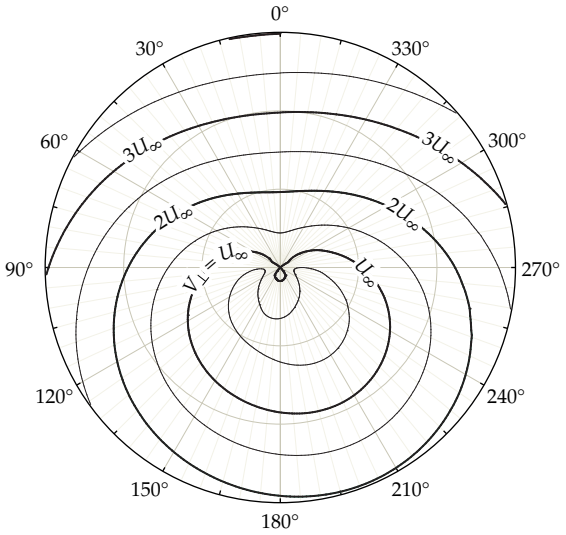

(b): Apparent wind speed, $V_\perp$, normal to the strut leading-edge at $\lambda = 3$.

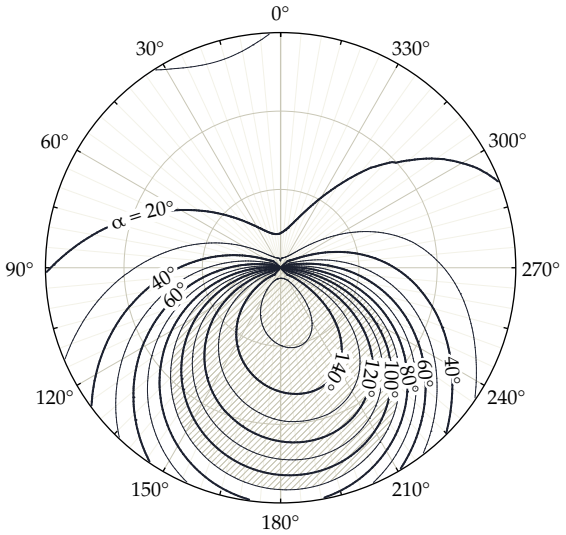

(c): Angle of attack perceived by a radial arm section at $\lambda = 1$. The shaded area refers to tailwind ($\alpha > 90°$).

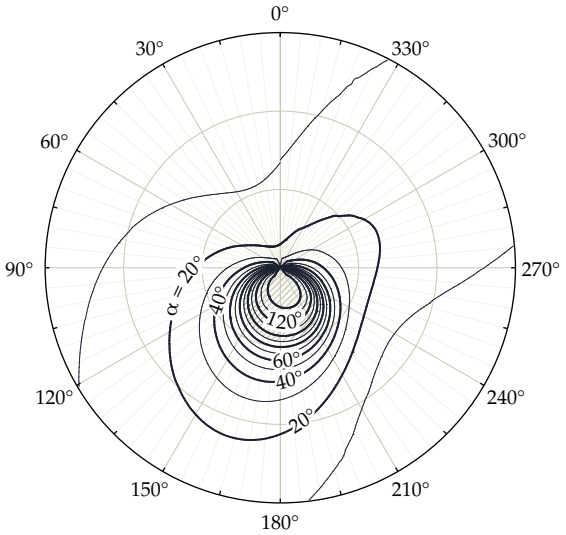

(d): Angle of attack perceived by a radial arm section at $\lambda = 3$.

Figure 9.6: Apparent wind speeds; predicted with a blade element method applied to a propeller in yaw ($\beta = 20°$), together with the induced velocities from a vortex panel method.

aquatic animals—especially those who migrate over long distances at high speeds—often describes a certain characteristic shape. Here, the diameter-to-length ratio, d/l, lies around $\frac{1}{4}$ with its maximum thickness at approximately $\frac{1}{3}l$; a shape that is also commonly used in airship hulls.

To create a hollow back, the streamlined shape will have to be cut somewhere. Where exactly is a design choice. As figure 9.7 illustrates, a cut close to the nose will create a large hollow surface, but results in a large turbulent wake in the case of headwind. Vice versa, a cut too far aft will yield a lower drag, but also leaves a much smaller tail surface. In addition, the struts also have an important structural function. This means that the profiles will have to provide sufficient stiffness or otherwise leave room to house a spar of some kind. Large struts, however, will lead to a lot of interference inside

the rotor. Naturally, the optimum lies somewhere in between.

As a starting point, a thick symmetric shape—made up from an elliptical nose and a tangent ogive—is drawn according to

$$z(x) = \pm \begin{cases} \frac{t_{\max}}{2}\sqrt{1-\left(\frac{x-x_{\hat{z}}}{x_{\hat{z}}}\right)^2}, & 0 \le x \le x_{\hat{z}}, \\ \sqrt{R_{\text{og}}^2 - (x_{\hat{z}}-x)^2} + \frac{t_{\max}}{2} - R_{\text{og}}, & x_{\hat{z}} \le x \le c, \end{cases} \tag{9.5}$$

where R_{og} is the radius of the rear ogive and $t_{\max}$ and $x_{\hat{z}}$ are respectively the value and location of the maximum thickness (see figure 9.8). In order for the two shapes to meet, the ogive radius is set to

$$R_{\text{og}} = \frac{(1-x_{\hat{z}})^2}{t} + \frac{t_{\max}}{4}. \tag{9.6}$$

A trailing-edge gap is then incorporated by cutting off the shape, by adding a term $t_{\text{gap}}x$ to act as a hypothetical wedge, or a combination of the two. Several combinations of this eventually yield a large number of possible profile shapes, which are evaluated in RFOIL and collected in the scatter plot shown in figure 9.9. The shape that shows the lowest frontal drag, relative to its trailing-edge gap size, corresponds to the tangent line. It has a gap size of 70%c and a frontal drag coefficient of 0.11[5].

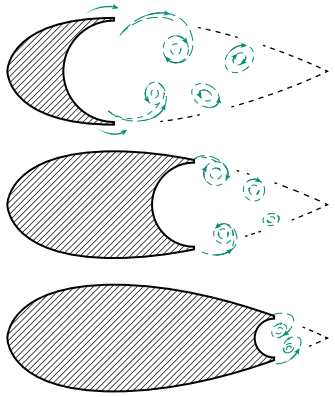

Figure 9.7: A streamlined shape with a hollow back at various positions.

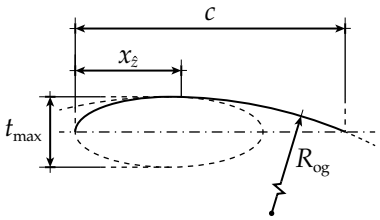

Figure 9.8: A streamlined shape composed of an ellipse and a tangent ogive.

[5] Still, it is the question whether this value approaches the real-life case, since the predictions involve calculating thick wakes containing bluff-body separation.

9.3.3 Performance of a strut in skewed flow

How well a profile performs is estimated by considering hollow sections that extend to a certain radius. The torque delivered by a strut, containing a hollow profile spanning from $r = 0$ to $r = R_{\text{s}}$, is then approximated by

$$Q = \frac{9}{2\pi}\int_0^{2\pi}\int_0^{R_{\text{s}}} \tfrac{1}{2}\rho V_\theta^2 \,(C_d c)^*\, r dr d\theta + \frac{9}{2\pi}\int_0^{2\pi}\int_{R_{\text{s}}}^{R} \tfrac{1}{2}\rho V^2 C_\theta c r dr d\theta. \tag{9.7}$$

The term $(C_d c)^*$ represents the drag coefficient times a characteristic length scale. For now, this is assumed to be either $-C_d c$ during headwind or $2.3t_{\text{gap}}$ during tailwind; the latter referring to the drag of a half tube based on its frontal area. The factor 9 in front of the integral refers to three sets of three struts. This relies on the assumption that there is no interference between the sets and that the torque

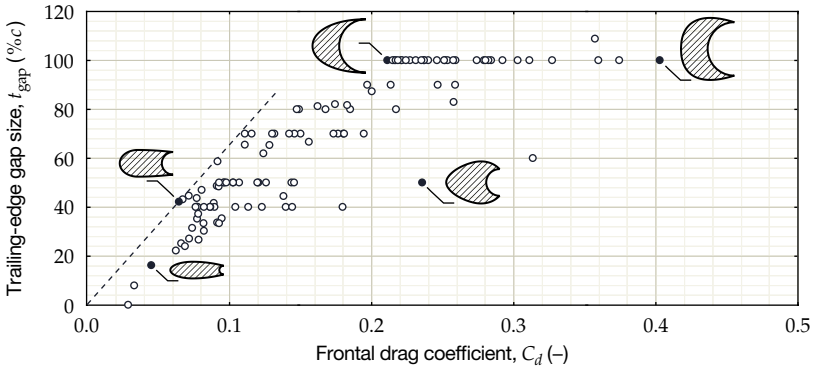

Figure 9.9: A variety of hollow profile shapes evaluated in RFOIL at $\text{Re} = 50,000$.

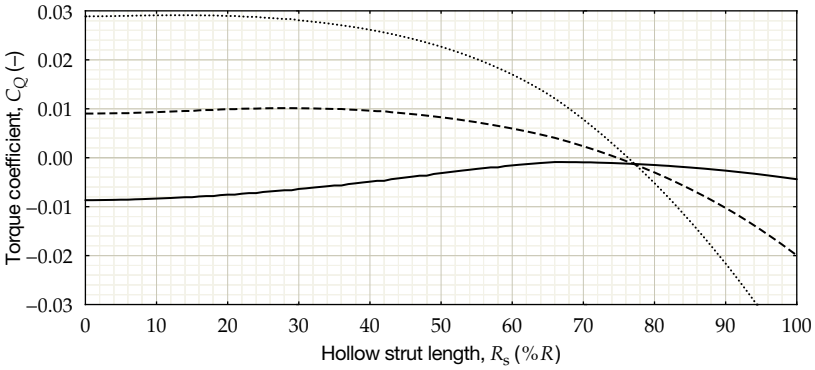

Figure 9.10: Torque predictions of 9 hollow strut sections spanning to various radii; evaluated at $\lambda = 1$ (——), $\lambda = 2$ (– –) and $\lambda = 3$ (·····).

contributions can be simply summed up, which seems reasonable considering the low skew angles.

The torque coefficient is determined by the frontal area of the main rotor, $2Rh$, and is plotted in figure 9.10. For $\lambda = 1$, there is an optimum at $R_s \approx \frac{2}{3}R$, which yields an increase in torque of about 0.008. However, this would decrease performance at $\lambda = 3$ by $\Delta C_Q = -0.017$. A position not affecting the performance at the nominal tip speed would be $R_s \approx \frac{1}{4}R$, yielding an increase of $\Delta C_Q = 0.002$. Although the gain is still positive, such a small torque increase is hardly worth the trouble of locally changing the cross-section and having the risk of disturbing the flow in the downwind part even more[6]. This again confirms the suspicion that it is hard to create a lot of surface inside the rotor without affecting the total output. The small areas of tailwind, shown in figures 9.6c and d, also indicate that there is not a lot of power available for a drag device to operate. Though the current prediction is still quite crude and only a wind tunnel test would be fully conclusive at this point, it would be wise to abondon the idea of having hollow strut sections.

However, the original NACA 0018 struts do show a positive contribution to torque because of the skew angle. This shows that alternative airfoils may help to decrease drag, but can also help to generate more torque, although not substantially. Either way, it is worthwhile to review the shape of the current sections.

[6] **The relation between power and torque is $C_P = \lambda C_Q$. This implies that at $\lambda = 1$, an increase of $\Delta C_Q = 0.002$ would correspond to an additional extraction of 0.2% of the total power in the wind: a negligible effect at low cut-in wind speeds.**

9.3.4 Finding a new airfoil

A new geometry for the radial arms should be chosen such that the arms provide high torque at moderate skew angles, but without affecting performance in the case of $\beta = 0°$. Even in the case of no skew, there is still flow in the vertical direction because of blade sweep, and a strut section will therefore always experience some angle of attack that could be used to generate torque. Unfortunately, this is not included in the procedure of subsection 9.3.1; but the assumption of a zero inflow angle ($\phi = 0°$) for zero skew would be a nice starting point. The range $0° \leq \beta \leq 20°$ therefore seems suitable for optimization; preventing high drag in the case of zero skew, without the risk of overestimating the torque production by assuming too high yaw angles.

The airfoils that will be considered are of the NACA 4-digit series[7],

[7] **The reason behind this is that NACA airfoils are easily generated, plus it keeps the amount of possible airfoils to a reasonable level.**

which are named by the first digit describing the maximum camber, $z_{\max}$, in $\%c$, the second digit describing the location of the maximum camber, $x_{\hat{z}}$, in tenths of the chord and the third and the fourth digit indicating the maximum thickness in $\%c$. The thickness is given by

$$t(x) = \frac{t_{\max}}{0.2} c \left[0.2969 \left(\frac{x}{c}\right)^{\frac{1}{2}} - 0.1260 \left(\frac{x}{c}\right) - 0.3516 \left(\frac{x}{c}\right)^2 + 0.2843 \left(\frac{x}{c}\right)^3 - 0.1015 \left(\frac{x}{c}\right)^4 \right]. \tag{9.8}$$

The mean camber line is given by

$$z(x) = \begin{cases} \frac{z_{\max}}{x_{\hat{z}}^2} \left(2x_{\hat{z}} x - x^2\right), & 0 \le x \le x_{\hat{z}}, \\ \frac{z_{\max}}{(1-x_{\hat{z}})^2} \left(1 - 2x_{\hat{z}} + 2x_{\hat{z}} x - x^2\right) & x_{\hat{z}} \le x \le c. \end{cases} \tag{9.9}$$

The upper and lower surface coordinates, (x', z), follow from the thickness distribution $t(x)$ according to

$$x' = x \pm t \sin\vartheta, \tag{9.10a}$$

$$z = z_c \pm t \cos\vartheta, \tag{9.10b}$$

where

$$\vartheta = \arctan\left(\frac{dz}{dx}\right). \tag{9.11}$$

Table 9.1: Aerodynamic performance and stiffness of several NACA 4-digit airfoils; evaluated with RFOIL at $\mathrm{Re} = 20,000$.

	Clean		$x_{tr} = 10\%c$				
NACA	C_{d_0} (–)	α_0 (°)	C_{d_0} (–)	α_0 (°)	I_{xx} (10^4 mm^4)	I_{zz} (10^6 mm^4)	I_{xz} (10^6 mm^4)
0012	0.030	0.0	0.025	0.0	0.322	1.845	-1.145
3312	0.036	-0.4	0.028	-2.5	0.399	1.901	-1.078
3412	0.037	-0.2	0.028	-2.6	0.404	1.880	-1.072
3512	0.037	0.1	0.028	-2.6	0.407	1.867	-1.070
6312	0.061	-2.8	0.055	-4.8	0.637	1.918	-1.013
6412	0.059	-2.7	0.047	-4.8	0.653	1.882	-1.007
6512	0.057	-2.5	0.041	-4.7	0.663	1.859	-1.004
9312	0.104	-4.5	0.108	-7.7	1.048	1.924	-0.953
9412	0.098	-4.2	0.097	-7.0	1.077	1.880	-0.945
9512	0.090	-3.9	0.074	-4.9	1.096	1.851	-0.945
0015	0.040	0.0	0.027	0.0	0.526	2.305	-1.678
3315	0.044	-1.0	0.029	-2.4	0.593	2.402	-1.602
3415	0.044	-0.7	0.029	-2.4	0.600	2.368	-1.593
3515	0.045	-0.2	0.029	-2.4	0.605	2.347	-1.588
6315	0.063	-3.0	0.046	-4.7	0.805	2.441	-1.516
6415	0.063	-2.7	0.041	-4.5	0.829	2.385	-1.515
6515	0.064	-2.4	0.039	-4.1	0.843	2.349	-1.509
9315	0.101	-4.8	0.097	-7.5	1.179	2.462	-1.455
9415	0.096	-4.4	0.079	-5.9	1.222	2.394	-1.442
9515	0.092	-3.9	0.062	-4.3	1.250	2.348	-1.439
0018	0.056	0.0	0.029	0.0	0.782	2.766	-2.198
3318	0.057	-1.8	0.031	-2.2	0.838	2.917	-2.115
3418	0.057	-1.0	0.031	-2.1	0.847	2.867	-2.106
3518	0.058	-0.3	0.031	-2.0	0.853	2.836	-2.097
6318	0.065	-2.8	0.041	-4.3	1.020	2.989	-1.954
6418	0.068	-2.4	0.040	-3.9	1.051	2.909	-1.983
6518	0.071	-2.0	0.039	-3.3	1.071	2.855	-2.005
9318	0.098	-4.8	0.078	-6.1	1.354	3.029	-1.799
9418	0.096	-4.2	0.065	-4.9	1.408	2.935	-1.872
9518	0.095	-3.7	0.061	-3.2	1.445	2.868	-1.923

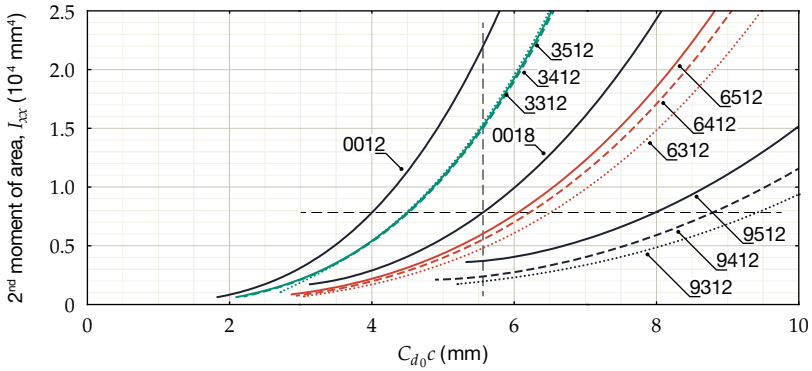

Figure 9.11: Drag of several NACA xx12 sections, compared to their structural stiffness; evaluated in RFOIL at Re = 20,000.

Limiting the search to $0 \leq z_{\max} \leq 9\%c$, $0.3c \leq x_{\hat{z}} \leq 0.5c$ and $12 \leq t_{\max} \leq 18\%c$ narrows the amount of candidates down to 30 airfoils. Table 9.1 shows the aerodynamic and structural characteristics corresponding to a chord length of 100 mm and a skin thickness of 1 mm. The second moments of area are obtained according to the method described in appendix B.

Picking the right strut profile can be done from multiple perspectives. In this case, it is either about minimizing the term $C_{d_0}c$ to achieve the lowest drag for a constant bending stiffness, or to maximize the term $C_l c$ to obtain an extra amount of torque in cases of skewed flow. Although, even in the second case, the profile drag cannot exceed that of the baseline NACA 0018 strut. A near-zero angle of attack is common in practice when the turbine is not placed on a roof, or when the low wind speeds are not able to generate high skew angles.

The design choice is visualized in figure 9.11, where the drag and stiffness of the NACA xx12 sections are evaluated at a range of chord lengths. This shows that the increased stiffness of the highly cambered sections do not make up for their higher profile drag. However, the symmetrical NACA 0012 and the cambered 3x12 sections do

Figure 9.12: Comparison of two possible strut profiles to the baseline NACA 0018 section, taking into account the differences in chord length.

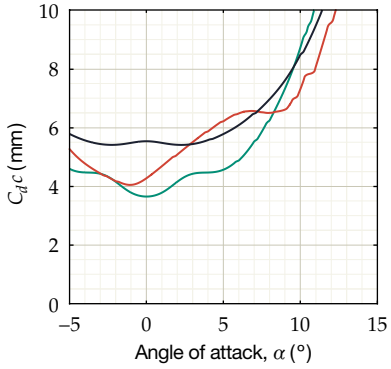

(a): Variation of $C_d c$ with angle of attack for NACA 0018 at Re = 20,000 (—), NACA 0012 at Re = 26,700 (—), and NACA 3512 at Re = 24,300 (—).

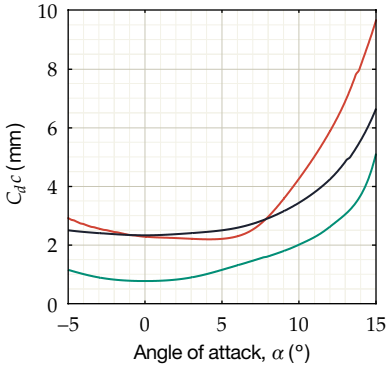

(b): Variation of $C_d c$ with angle of attack for NACA 0018 at Re = 75,000 (—), NACA 0012 at Re = 100,000 (—), and NACA 3512 at Re = 91,200 (—).

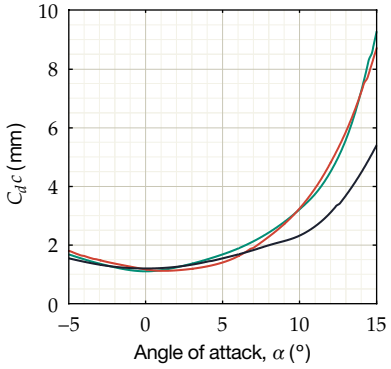

(c): Variation of $C_d c$ with angle of attack for NACA 0018 at Re = 200,000 (—), NACA 0012 at Re = 267,000 (—), and NACA 3512 at Re = 243,000 (—).

have a window in which they generate less drag and can offer higher stiffness.

Keeping the same stiffness with respect to the x-axis means that a NACA 0012 and a NACA 3512 section require a 33% and 22% longer chord length, respectively. Although this increases the weight and raises skin friction drag, the Reynolds numbers also increase significantly. Figures 9.12a, b and c clearly show what can be gained by the extra slenderness and a longer chord. At very low Reynolds numbers, for instance, a NACA 0012 section with a length of 133 mm has a lot less drag than a NACA 0018 of 100 mm, at least up to $\alpha \approx 10°$. The thicker airfoils may have less drag in conditions of skewed flow, but the additional lift generated by longer chords may compensate for this. Still, the NACA 0012 airfoil is the better option for the Reynolds numbers encountered by the struts.

10 Conceptual design

The previous chapters have led to the selection of a handful of strategies that could be used to design a self-starting variant of Turby. Many of these design aspects can be bundled into a new blade geometry. In addition, a new strut will be derived to minimize parasitic drag. The purpose of this chapter is to substantiate the design choices leading to one or multiple design proposals, which are summarized and presented in the next chapter.

First, this chapter will start off with some points to take into account while designing. These are discussed in section 10.1. Then, sections 10.2 and 10.3 will deal with finding new shapes for the blades and struts.

10.1 Considerations for design

As a starting point, it is convenient to lay out several aspects that have to be taking into account before designing. Most important perhaps are the angle of attack and Reynolds number ranges in which the blades have to operate.

10.1.1 Design conditions

Operating at low tip speed ratios and low wind speeds mean strong variations in α and Re. The difficult thing is that there is no exact design point. Instead, there is a wide range of conditions at which the design has to perform well. There is a particular trade-off between start-up performance and nominal operation. A configuration that is optimal for $\lambda = 1.5$ and $U_\infty = 3$ m/s is most likely non-optimal at $\lambda = 3.5$ and $U_\infty = 11$ m/s. Maximizing start-up performance focuses on increasing lift at high angles of attack (maximizing the term

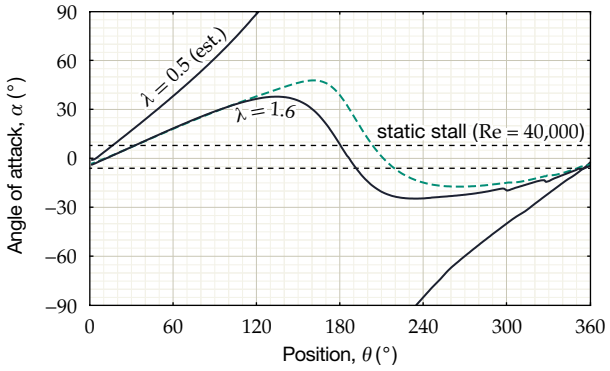

(a): Predicted geometrical (—) and effective (– –) angle of attack variation at $\lambda = 0.5 - 1.6$ ($U_\infty = 3$ m/s).

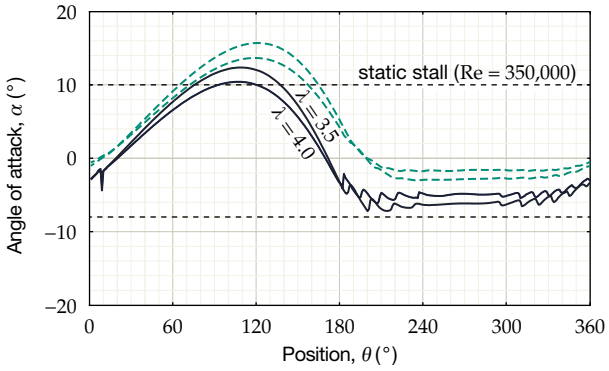

(b): Predicted geometrical (—) and effective (– –) angle of attack variation at $\lambda = 3.5 - 4.0$ ($U_\infty = 11$ m/s).

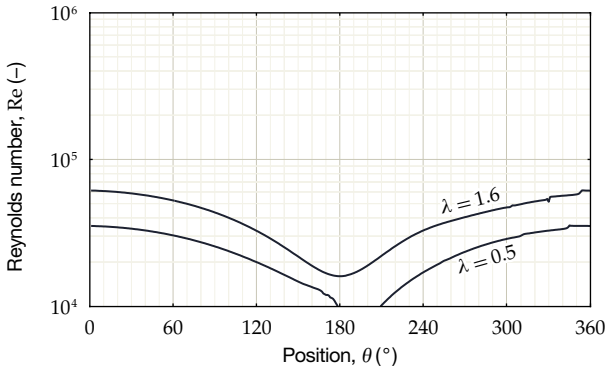

(c): Predicted Reynolds number variation at $\lambda = 0.5 - 1.6$ ($U_\infty = 3$ m/s).

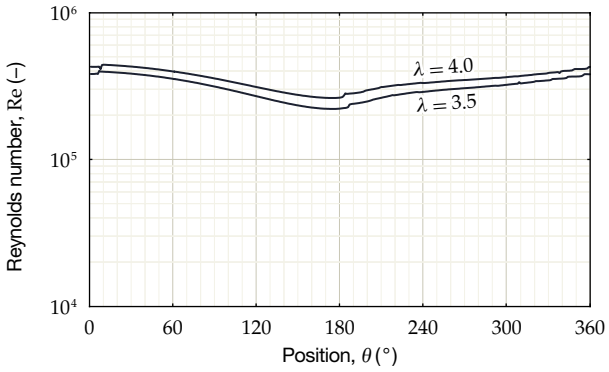

(d): Predicted Reynolds number variation at $\lambda = 3.5 - 4.0$ ($U_\infty = 11$ m/s).

Figure 10.1: Predicted operating conditions during start-up and nominal operation. Since the vortex panel model can only calculate the wake for $\lambda \geq 1$, the predictions at $\lambda = 0.5$ are merely speculation.

$C_l \sin\alpha$), narrowing the post-stall region, decreasing bubble drag, etc. Maximizing $C_{P_{\max}}$ at the rated wind speed, however, is more about decreasing profile drag (minimizing the term $C_d \cos\alpha$) and avoiding (dynamic) stall. Although dynamic stall can definitely help with starting up, one would rather avoid the hysteresis losses at high λ.

Two important design points can be identified, shown in figures 10.1a through d. First is the region of negative C_P at the cut-in wind speed of $U_\infty = 3$ m/s between $\lambda = 0.5$ and 1.6. Second is the maximum power point at the rated wind speed of $U_\infty = 11$ m/s at $\lambda \approx 3.5 - 4.0$. To reduce the amount of simulations in RFOIL to a more managable number, the profile characteristics are best evaluated based on a fixed *root-mean-square* (RMS) Reynolds number, which gives a good weighted average based on dynamic pressure:

$$\mathrm{Re}_{\mathrm{RMS}} = \frac{c}{\nu}\sqrt{\frac{1}{2\pi}\int_0^{2\pi} V^2 d\theta}. \tag{10.1}$$

The conditions shown in figures 10.1c and d correspond to $\mathrm{Re}_{\mathrm{RMS}} \approx 40,000$ and $\mathrm{Re}_{\mathrm{RMS}} \approx 350,000$, respectively.

10.1.2 Airfoil features

Any changes to the airfoils to improve starting should preferably not compromise performance at higher wind speeds. The optimal profile has an extensive list of desirable features, conveniently summarized by Islam et al. (2007b):

- *Performance*. Obviously, the blade has to display high lift-to-drag ratios over a wide range of angles and over a wide range of operating conditions. This also means that the drag bucket should be wide and that the profile drag, C_{d_0}, should be low.
- *Stall behavior*. Stall should be delayed to high angles of attack, particularly for low tip speed ratios. A high stall angle, in combination with a high $C_{l_{\max}}$, allows the blades to generate more useful torque during a cycle. For start-up, it is therefore especially important to evaluate an airfoil at low Reynolds numbers where performance of airfoils usually worsens.
- *Deep stall behavior*. Deep stall should be postponed to extend the range of angles at which usable lift can be produced. Also the hysteresis losses should preferably be low.
- *Pitching moment*. Preferably, the pitching moment should be strong positive so that it can contribute to the total torque[1].
- *Strength*. To keep the weight low, the blades should be thick enough to provide high stiffness.
- *Roughness sensitivity*. The airfoil should be insensitive to roughness to minimize the performance degradation over time. Leading-edge roughness causes a drop in $C_{l_{\max}}$ and raises C_{d_0}; thereby making start-up more difficult.
- *Noise generation*. The noise emitted by the trailing-edge should be low which also underlines the need for smooth stall characteristics[2].

[1] The exact role of the pitching moment is a bit unclear at the moment. At the moment of writing this report, there are indications that the resultant normal force does not play a significant role in the generation of torque. Because of this, the emphasis is put on the tangential force instead.

[2] When a downstream boundary layer becomes turbulent, fluctuations in velocity caused by eddies will produce audible sound at the trailing-edge. The frequencies will then correspond to the rate of change in airflow, proportional to variations in bound circulation. Moreover, at higher angles of attack, the performance of a blade will decrease and the energy lost with drag will be converted into acoustics. This trailing-edge sound is characterized by its relatively high frequency of 500-1,000 Hz at maximum and is regarded the most dominant source of noise (van den Berg, 2006, p. 33).

In the following analysis, Islam et al. (2007b) concluded that the optimal airfoil should have

- *Camber*. Airfoils with camber generally provide more lift at low Reynolds numbers, are less sensitive to roughness, stall later, and can show strong pitching moments.
- *High thickness*. A thickness of at least 18% should offer better performance in the range $200,000 \leq \mathrm{Re} \leq 300,000$ (Healy, 1978; cited in Islam et al., 2007b). Even thicknesses of 20 – 25% are mentioned solely for the benefit of self-starting, based on on the patent of Seki (2005). Furthermore, an increased width of the drag bucket, lower noise emissions and improvements in strength are reasons to go for high thickness.
- *Large leading-edge radius*. This helps to reduce the roughness sensitivity and delay the deep stall angle, although at the cost of a longer hysteresis loop.

- *Sharp trailing-edge*. While this raises the lift-to-drag ratio, manufacturing sharp edges can be problematic when it comes to small chord lengths.

10.1.3 Structural requirements

From the viewpoint of aerodynamics, thinner is often better in terms of drag. On the other hand, having sufficient thickness is important to ensure a strong and stable structure. An important parameter in this trade-off is the bending stiffness, which is the product of the modulus of elasticity, E, and the second moment of area, I. Where E is dependent on the material used to construct the blades, I is determined by the shape of the cross-section according to

$$I_{xx} = \iint_A z^2 \, dx \, dy, \tag{10.2a}$$

$$I_{zz} = \iint_A x^2 \, dx \, dy, \tag{10.2b}$$

$$I_{xz} = \iint_A xz \, dx \, dy, \tag{10.2c}$$

where the indices x and z refer to the airfoil frame of reference. Naturally, this favors thick airfoils and long chord lengths. Table 10.1 shows the second moments of area for the DU 06-W-200 profile in a range $15 \leq t \leq 25\%c$, using a polygon method explained in appendix B. Here, a spar is assumed to be located at its maximum thickness, with a width equal to a 3 mm skin thickness. It is clear that the differences in thickness produce great variations in bending stiffness. A thinner airfoil that produces a few percent more power might easily result in 10-20% less strength.

For example, the stress in the skin in spanwise direction, s_y – which is critical because of the high loads and the relatively low second moment of area – is given by

$$s_y = \frac{Mz}{I_{xx}}, \tag{10.3}$$

where M is an applied moment. Of course, the stress is highest when $z \approx \frac{1}{2}t$. And even though the aerodynamic normal force has a significant contribution, the highest loads on the blades during nominal operation come from centrifugal forces which scale linearly with blade mass. Therefore, one can say that

$$s_{y_{\max}} \propto \frac{At}{I_{xx}}. \tag{10.4}$$

Apart from static strength, there is also mechanical resonance. To illustrate: the natural frequency of a simple beam is

$$f_{\mathrm{n}} = \frac{1}{2\pi}\sqrt{\frac{EI}{m}}, \tag{10.5}$$

where the mass, m, scales linearly with the cross-sectional area. In the same manner, it can be said that

$$f_{\mathrm{n}} \propto \sqrt{\frac{I_{xx}}{A}}. \tag{10.6}$$

t (%c)	t (mm)	A (mm^2)	I_{xx} (10^4 mm^4)	I_{zz} (10^6 mm^4)	I_{xz} (10^6 mm^4)
15	17.7	642	180	361	−143
16	18.8	659	212	391	−162
17	20.0	660	246	409	−182
18	21.2	669	283	433	−202
19	22.4	678	322	457	−222
20	23.5	686	365	481	−242
21	24.7	695	411	505	−262
22	25.9	703	459	529	−283
23	27.1	711	511	553	−304
24	28.2	719	565	578	−325
25	29.4	727	623	602	−346

Table 10.1: Structural parameters of a DU 06-W-200 airfoil of a 117.7 mm chord length with a skin thickness of 3 mm. A spar is placed at its maximum thickness.

Because it is of the utmost importance that the system eigenmodes do not come near the operating range of the turbine, the parameter f_n should preferably be of high frequency. Both cases, in fact, state that the ratio A/I_{xx} should be as low as possible, which underlines the importance of having low mass and high stiffness.

10.1.4 Design philosophy

In order to boost the torque at start-up, there are a number of things to consider. Most important, perhaps, is delaying the point of leading-edge separation. This is convenient at start-up, because it decreases the width of the post-stall region (e.g. see figure 6.3). But also at higher tip speed ratios, the airfoils also move regularly in and out the dynamic stall region and a wide linear lift regime is desirable to reduce hysteresis effects. Comparing a NACA 0012 and the HH-02 and SC1095 rotorcraft airfoils, Leishman (2006, pp. 551–553) concluded that much of the static behavior also applies to the dynamic range. Designing for a high static lift capability would therefore also mean that dynamic stall is postponed to higher angles of attack.

Another point is the violent movement of laminar separation bubbles. It is possible to attempt a transition ramp, but the question is whether natural transition would occur at all during start-up. Because of the dependence of the Tollmien-Schlichting wave growth on the shape parameter, H, it is proportional to $\sqrt{\mathrm{Re}}$ and critical amplitudes may not be reached before the trailing-edge is reached. For the bottom side of the airfoil, the lower critical amplification factors, N_crit, encountered in the turbulent downwind rotor half will mean that instabilities grow much faster. Therefore, different approaches are required for both sides of the profile.

Then there is the stiffness requirement. The current DU 06-W-200 airfoil was designed by Claessens (2006) for the purpose of finding a profile that performed better than a NACA 0018; both aerodynamically and structurally. A thickness of 20%c was adopted as a result which, evidently, is a major gain over t = 18%c. Further increasing this thickness will result in a lighter rotor with a lower moment of inertia that is able to respond faster to changes in wind speed. Moreover, a thick nose can also improve performance in the high-angle-of-attack region which, at low λ, comprises such a large part of the operating range.

There are several design methods available for airfoils. The most straightforward one is simply tweaking the current airfoil—one aspect at a time—until favorable properties emerge. Obviously, this is very time-consuming and would only limit the search to designs that lie very close to the original. A more advanced method is the *surface speed design routine* of X/RFOIL. This revolves around modifying the distribution of the inviscid edge velocity, u_e, and can be an effective way of decreasing bubble drag. However, it becomes a tedious process when the design concerns a wide variation of angles of attack and Reynolds numbers instead of a narrow range of operating conditions. Instead, it becomes more attractive to rely on purely numerical methods of optimization. Therefore, the choice was made to work with the *OptiFlow airfoil optimization suite*, devised by de Oliveira (2011). This airfoil optimizer makes use of MATLAB's Genetic Algorithm Solver to find the trade-offs between two design criteria, which are represented by fitness functions. These functions determine how close the solution lies to the optimum, and combinations of the two will yield a *Pareto front*. What functions to use will, of course, depend on what the designer wants to achieve. In this case, the trade-off is between stiffness and aerodynamic performance.

10.2 AIRFOIL DESIGN

A wide variety of airfoils were generated with fitness functions that maximized the weighted C_l/C_d ratio or tangential force during a cycle at a variety of Reynolds numbers. The fitness of the airfoils was evaluated in XFOIL in turbulent conditions—transition is fixed at $x = 5\%c$ (upper surface) and $x = 10\%c$ (lower surface)—and with respect to a rotor with a solidity of $\sigma = 0.175$.

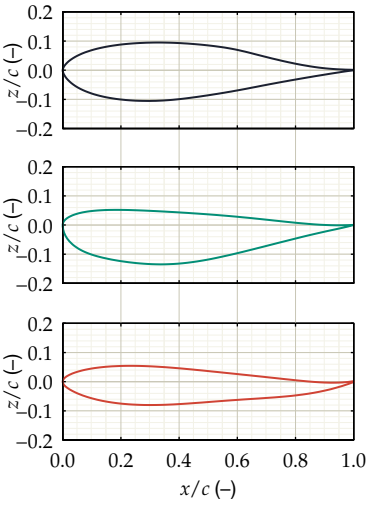

Figure 10.2: Two airfoil geometries, concepts 1 (—) and 2 (—), to outperform the flipped DU 06-W-200 (—) during nominal operation and start-up, respectively.

10.2.1 Results from the genetic algorithm

From the collection of generated airfoils, the two most promising ones were selected for further evaluation. These geometries, dubbed concepts 1 and 2, are shown in figure 10.2 and are candidates to surpass the original airfoil in nominal operation and in start-up conditions. Additionally, the DU 06-W-200 airfoil is flipped since, judging on the performance curves in appendix C, this seems to yield better performance at positive angles of attack.

The profile characteristics in comparison to the flipped DU 06-W-200 airfoil can be found in figures C.1 and C.2 in appendix C. These plots show that concept 1 has higher drag, but also has a much wider operating range – crucial in order to avoid stalling. This translates itself to greater power extraction in the upwind rotor half. Concept 2, on the other hand, shows a great improvement in C_l/C_d at Re = 40,000. This indicates an efficient managing of the separation bubbles that dominate the aerodynamics at start-up.

10.2.2 Thickness

The issue of either increasing or decreasing the airfoil thickness has been already discussed in section 8.3. From the viewpoint of low-

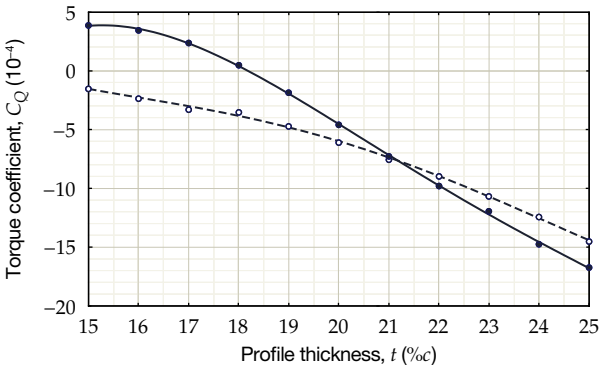

(a): Performance estimated for DU 06-W-200 (flipped) for normal (●) and turbulent flow (○) at start-up ($\mathrm{Re} = 40,000$, $\lambda = 1.5$, $U_\infty = 3$ m/s).

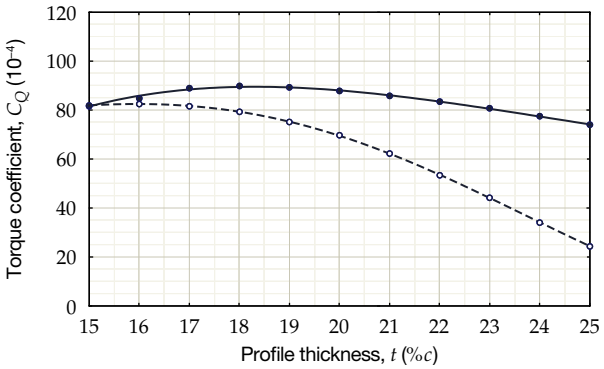

(b): Performance estimated for DU 06-W-200 (flipped) for normal (●) and turbulent flow (○) during nominal operation ($\mathrm{Re} = 350,000$, $\lambda = 4.0$, $U_\infty = 11$ m/s).

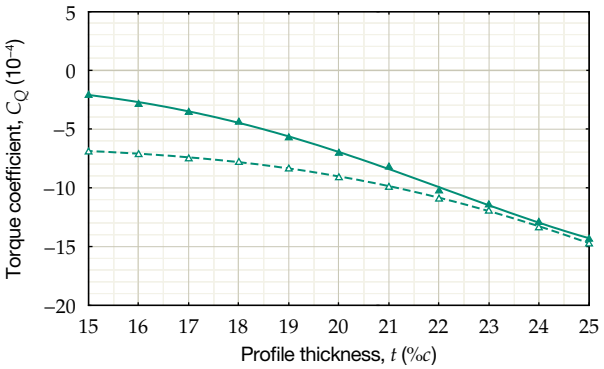

(c): Performance estimated for concept 1 for normal (▲) and turbulent flow (△) at start-up ($\mathrm{Re} = 40,000$, $\lambda = 1.5$, $U_\infty = 3$ m/s).

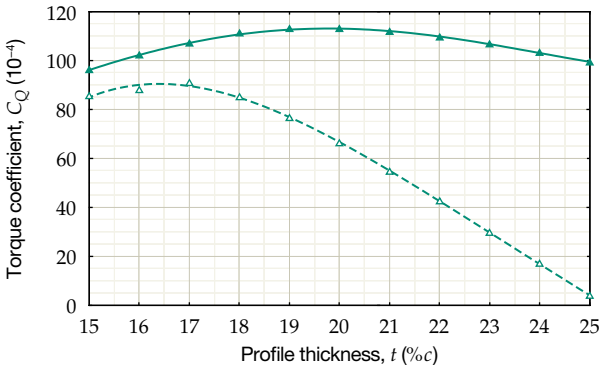

(d): Performance estimated for concept 1 for normal (▲) and turbulent flow (△) during nominal operation ($\mathrm{Re} = 350,000$, $\lambda = 4.0$, $U_\infty = 11$ m/s).

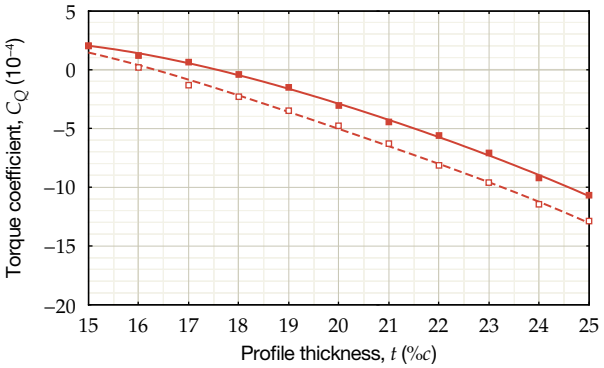

(e): Performance estimated for concept 2 for normal (■) and turbulent flow (□) at start-up ($\mathrm{Re} = 40,000$, $\lambda = 1.5$, $U_\infty = 3$ m/s).

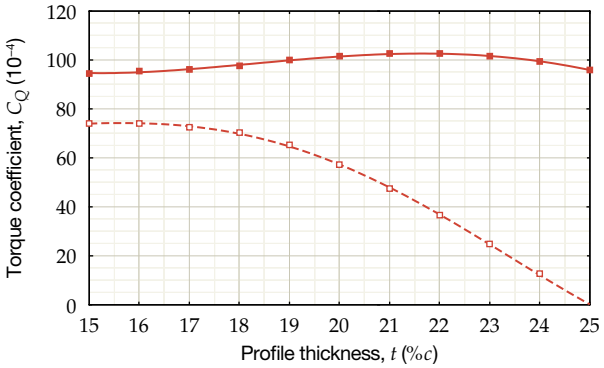

(f): Performance estimated for concept 2 for normal (■) and turbulent flow (□) during nominal operation ($\mathrm{Re} = 350,000$, $\lambda = 4.0$, $U_\infty = 11$ m/s).

Figure 10.3: Effect of profile thickness on the 2D static torque coefficient.

Reyolds-number aerodynamics, thinner is better in terms of performance to reduce the leading-edge suction peak. On the other hand, having sufficient thickness is important to ensure a strong and stable structure.

Because the angle of attack and wind speed vary so strongly for different tip speed ratios, it is inconvenient to judge the airfoil performance on aerodynamic force curves alone. A better measure would be to evaluate the 2D static torque coefficient through equa-

tion 5.21 and using the cyclic α and V distribution from the vortex panel model. Figures 10.3a through f show the results of scaling the thickness from 15%c to 25%c. The torque coefficient is evaluated for straightforward $N_{crit} = 9$ conditions and for turbulent conditions where $N_{crit} = 4$ and transition is fixed at $x = 5\%c$ (upper/concave surface) and $x = 10\%c$ (lower/convex surface). Since predicting C_Q at start-up conditions requires an estimate of the deep stall angle—a very tedious process at such low Reynolds numbers—a general trend is drawn through the points to smooth out errors[3].

[3] Still, it cannot be stressed enough that these predictions are made for conditions at which the accuracy is known to be very poor.

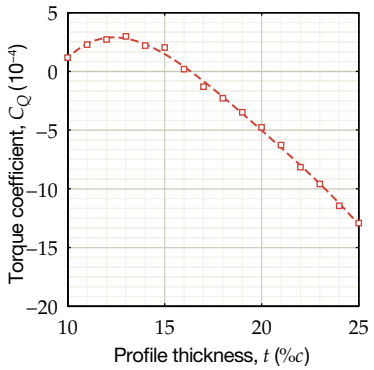

Figure 10.4: Performance estimated for concept 2 for turbulent flow at start-up conditions (Re = 40,000, $\lambda = 1.5$, $U_\infty = 3$ m/s).

Figure 10.3b confirms what was noted by Claessens (2006, p. 70) during the design of DU 06-W-200 – maximum performance is found for $t = 18\%c$, but upscaling to $t = 20\%c$ provides higher stiffness in turn for an acceptable loss. However, there is a substantial effect on start-up performance, likely caused by the formation of laminar separation bubbles. The results at start-up conditions affirm what can be expected from these low Reynolds numbers: very low thicknesses are required for an airfoil to be able to compensate for the drag of the post-stall region. Concept 2, which is optimized for start-up conditions, does not even find its optimum in the range $15\%c \leq t \leq 25\%c$, but rather at its original thickness of $t = 13.4\%c$ (see figure 10.4). This implies that, for this airfoil to start up successfully on lift, at least the structural requirement has to be dropped. Even so, it is interesting to pursue concept 2 further to find out how it performs. Furthermore, when looking at figure 10.3f it seems that increasing the thickness of concept 1 has its advantages; again at the expense of start-up. In this case, a thickness of 20%c is definitely feasible, making it a viable candidate to replace DU 06-W-200 for nominal operation.

10.2.3 Boundary layer trip

With the airfoils effectively operating upside down, the *concave side* is the suction side in the upwind rotor half and operates in a smoother flow ($15° \leq \theta \leq 135°$). The *convex side* is the suction side in the downwind half and operates in higher turbulence. To account for this, the trip locations at the concave and convex sides are predicted using $N_{crit} = 9$ and $N_{crit} = 4$, respectively.

The results of the RFOIL predictions are shown in figures 10.5c through f. Here, the 2D static torque coefficient is again evaluated using equation (5.21) and compared with the case of free transition. Clearly, forcing transition has some potential for improvement at the very low Reynolds numbers. For nominal operation, however, the benefits of tripping evidently do not outweigh the extra drag. This is especially true for the lower side, where the combination of the downwind turbulence and a higher Re already decrease bubble drag significantly.

For the flipped DU 06-W-200, the benefits of placing turbulators on the upper side near $x = 30 - 50\%c$ has likely to do with the occurrence of laminar separation bubbles at the S-tail. This aft curvature is convenient in the sense that it keeps the bubbles in place over a considerable range of angles. When considering a good trade-off be-

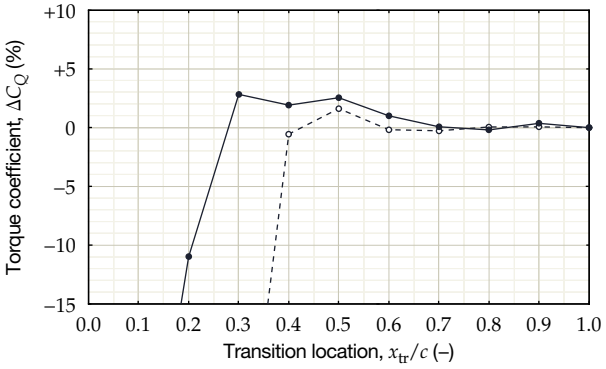

(a): Performance estimated for DU 06-W-200 (flipped) with transition forced at the upper (●) and lower side (○) at start-up (Re = 40,000, λ = 1.5, U_∞ = 3 m/s).

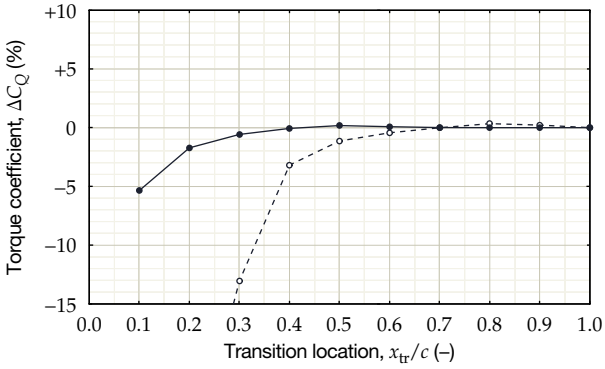

(b): Performance estimated for DU 06-W-200 (flipped) with transition forced at the upper (●) and lower side (○) during nominal operation (Re = 350,000, λ = 4.0, U_∞ = 11 m/s).

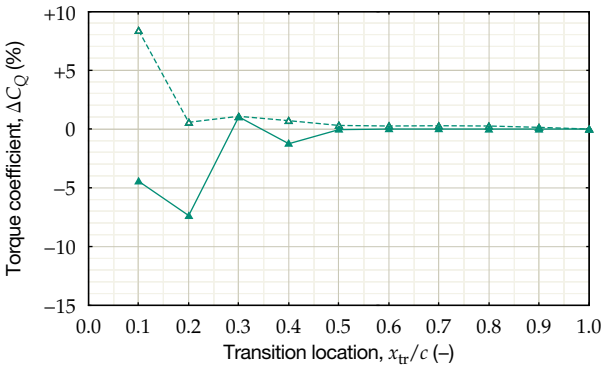

(c): Performance estimated for concept 1 with transition forced at the upper (▲) and lower side (△) at start-up (Re = 40,000, λ = 1.5, U_∞ = 3 m/s).

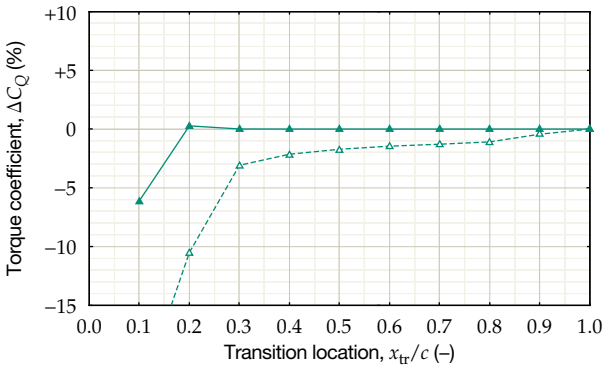

(d): Performance estimated for concept 1 with transition forced at the upper (▲) and lower side (△) during nominal operation (Re = 350,000, λ = 4.0, U_∞ = 11 m/s).

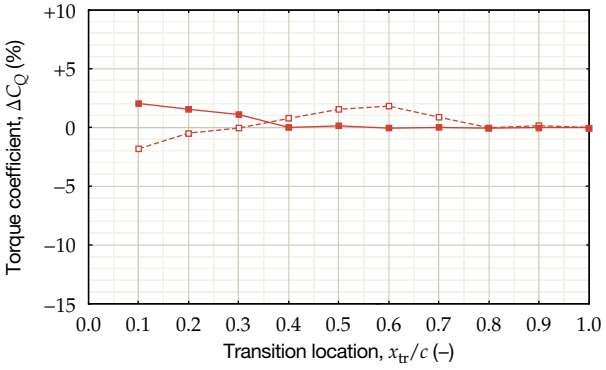

(e): Performance estimated for concept 2 with transition forced at the upper (■) and lower side (□) at start-up (Re = 40,000, λ = 1.5, U_∞ = 3 m/s).

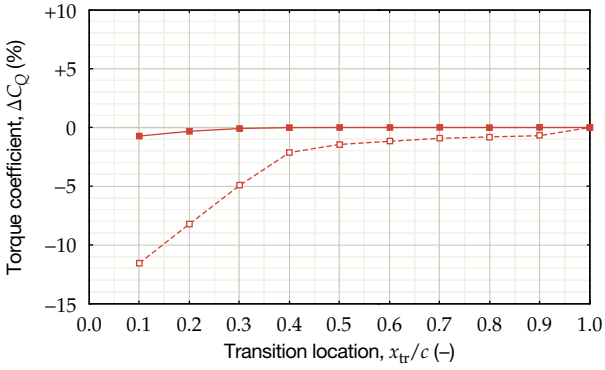

(f): Performance estimated for concept 2 with transition forced at the upper (■) and lower side (□) during nominal operation (Re = 350,000, λ = 4.0, U_∞ = 11 m/s).

Figure 10.5: Effect of trip location on the 2D static torque coefficient. The RFOIL predictions are made for the upper (concave) side at N_{crit} = 9 and the lower (convex) side at N_{crit} = 4.

tween starting and nominal operation, x = 30%c and x = 50%c seem to be good locations for the upper and lower side, respectively. The result is a substantial increase in C_l/C_d (see figure 10.6) which, in fact, allows it to compete with concept 2 at start-up.

For concept 1, tripping the lower surface at x = 10%c is definitely the most efficient for start-up, since the point of laminar separation remains relatively close to the leading-edge (see figures C.3 and C.4). Still, this is detrimental to the performance at λ = 4 which, in this

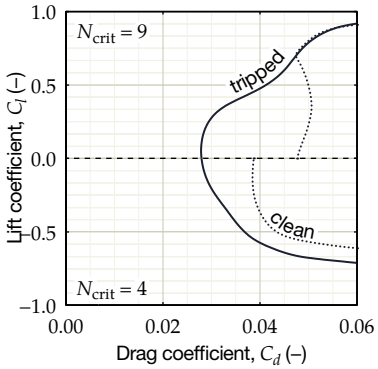

Figure 10.6: Gain in the lift-to-drag ratio of the flipped DU 06-W-200 at $\mathrm{Re} = 40,000$ as a result of boundary layer trip.

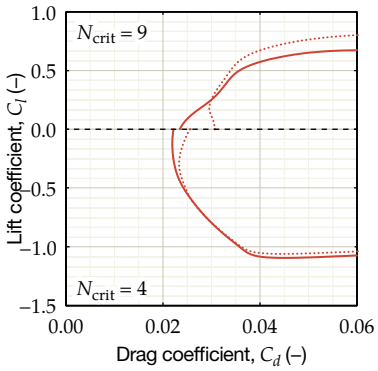

Figure 10.7: Gain in the lift-to-drag ratio of concept 2 at $\mathrm{Re} = 40,000$ as a result of boundary layer trip.

[4] **Although dynamic stall can definitely help with starting up, it becomes more of a nuisance at higher tip speed ratios where postponing stall is no longer important.**

[5] **Still, the real effects are not accurately reflected by the model since it relies on an inviscid wake and an empirical dynamic stall model.**

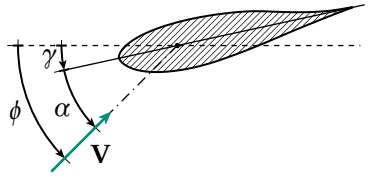

Figure 10.8: The flipped DU 06-W-200 airfoil set under a fixed pitch angle, γ.

case, is leading. Leaving transition free is therefore the best option for concept 1.

For concept 2, the start-up conditions are leading. In that case, there are some clear optimal locations to place turbulators; namely at the leading-edge for the upper surface and at $x = 60\%c$ for the lower surface. The gain in C_l/C_d can be seen in figure 10.7.

10.2.4 Fixed pitch

Setting the airfoil at a fixed pitch angle, γ (see figure 10.8), can be used to match the lift curve to the expected angle of attack variation and can help to avoid dynamic stall[4]. The angle of attack follows from

$$\alpha = \phi - \gamma, \tag{10.7}$$

where φ is the angle of inflow. The tangential force coefficient is then given by

$$C_t = C_l \sin\phi - C_d \cos\phi, \tag{10.8a}$$

$$C_n = C_l \cos\phi + C_d \sin\phi. \tag{10.8b}$$

When set correctly, a fixed pitch can also prevent combinations of positive ϕ and negative C_l, or vice versa, that arise from working with cambered airfoils. A good way to determine the optimal pitch angle for a large solidity rotor—where the blades are expected to move regularly in and out of stall—would be to find the trade-off between the increase in airfoil performance in attached flow conditions and the losses induced by stalling[5]. Positive values of γ will decrease the angle of attack and therefore move the airfoil away from stall.

The predicted power coefficients, shown in figures 10.9a through f, suggest that pitching out of dynamic stall can have a big positive impact on $C_{P_{\max}}$. However, the downside is that this is at the expense of starting. At start-up, the lower induction factors cause that the upwind half of the rotor is no longer favored over the downwind half. Instead, both halves play an important role in the generation of torque and a more symmetrical tangential force curve is desired. This becomes more clear when looking at the effect of a higher pitch angle on the tangential force curves; e.g. shown in figure 10.10. For small angle of attack variations, one can imagine that the loss in tangential force (marked red) is acceptable compared to the gain (marked green) as result of preventing stall. At lower λ and high α variations, this no longer the case as the airfoil will inevitably stall anyway. In that case, setting the blade under a pitch angle is only detrimental.

Even so, the improvement in $C_{P_{\max}}$ is so strong (modeling inaccuracies aside) that it is probably worth the loss in start-up performance. In that case it is the matter of finding a good balance between the two, and something in the order of $\gamma = 4 - 5°$ seems a good choice for all airfoils.

It is still interesting to continue with a configuration that aims for a passive start-up. At this point, the flipped DU 06-W-200 airfoil set at zero pitch seems to outperform concept 2 and would be a better candidate. This is most likely caused by the fact that the concept air-

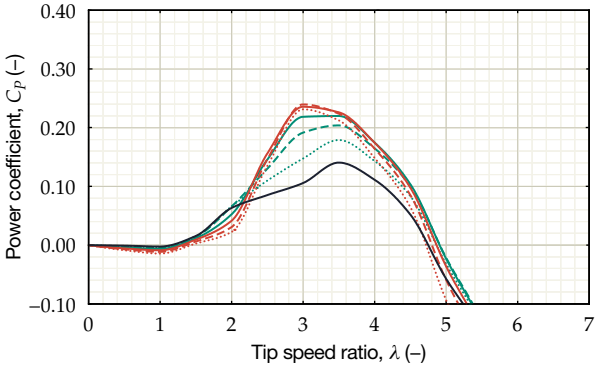

(a): Predicted power coefficient for the flipped DU 06-W-200 set at $\gamma = 0°$ (—), $+1°$ (····), $+2°$ (– –), $+3°$ (—), $+4°$ (—), $+5°$ (– –) and $+6°$ (····) at cut-in wind speed ($U_\infty = 3$ m/s).

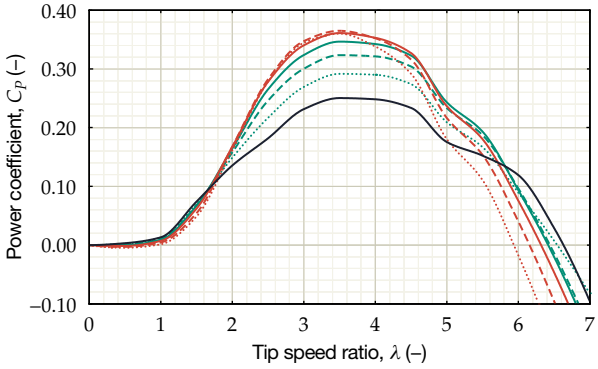

(b): Predicted power coefficient for the flipped DU 06-W-200 set at $\gamma = 0°$ (—), $+1°$ (····), $+2°$ (– –), $+3°$ (—), $+4°$ (—), $+5°$ (– –) and $+6°$ (····) at rated wind speed ($U_\infty = 11$ m/s).

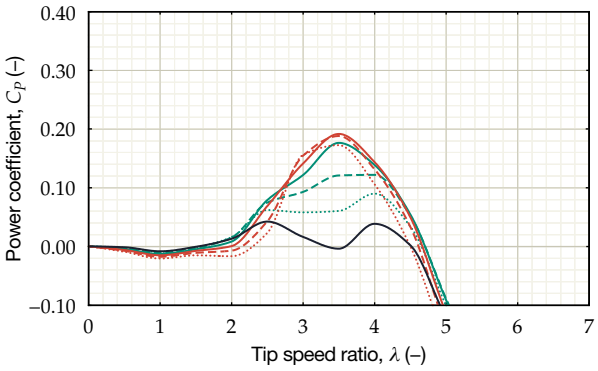

(c): Predicted power coefficient for concept 1 set at $\gamma = 0°$ (—), $+1°$ (····), $+2°$ (– –), $+3°$ (—), $+4°$ (—), $+5°$ (– –), $+6°$ (····) at cut-in wind speed ($U_\infty = 3$ m/s).

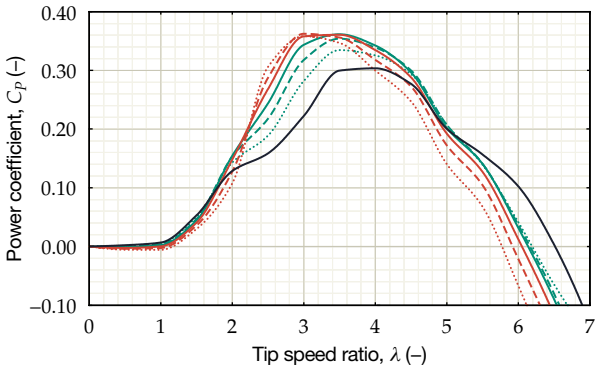

(d): Predicted power coefficient for concept 1 set at $\gamma = 0°$ (—), $+1°$ (····), $+2°$ (– –), $+3°$ (—), $+4°$ (—), $+5°$ (– –), $+6°$ (····) at rated wind speed ($U_\infty = 11$ m/s).

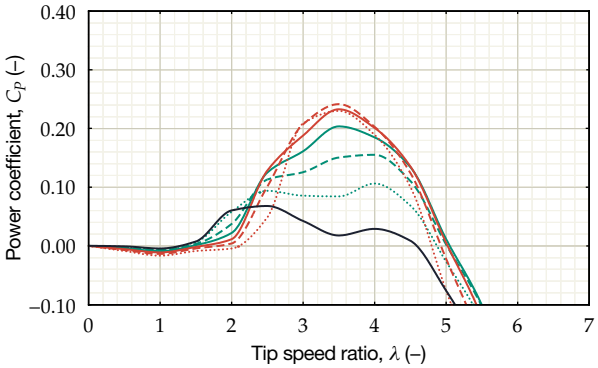

(e): Predicted power coefficient for concept 2 set at $\gamma = 0°$ (—), $+1°$ (····), $+2°$ (– –), $+3°$ (—), $+4°$ (—), $+5°$ (– –), $+6°$ (····) at cut-in wind speed ($U_\infty = 3$ m/s).

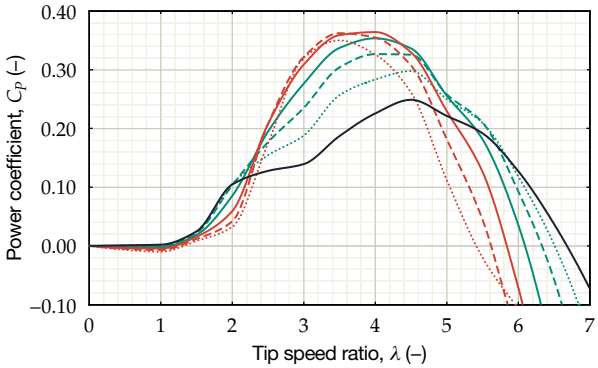

(f): Predicted power coefficient for concept 2 set at $\gamma = 0°$ (—), $+1°$ (····), $+2°$ (– –), $+3°$ (—), $+4°$ (—), $+5°$ (– –), $+6°$ (····) at rated wind speed ($U_\infty = 11$ m/s).

Figure 10.9: Effect of a fixed pitch angle on the turbine power coefficient; calculated in steps of $\Delta\lambda = 0.5$.

foil was optimized under turbulent conditions where the transition location was kept fixed under all circumstances. Keeping the transition location variable when airfoils are generated would ideally be better. Therefore, concept 2 is no longer pursued further.

10.2.5 Solidity

Raising the Reynolds numbers by increasing the chord length is not at all straightforward. As mentioned in section 8.1, higher rotor solidities cause the optimal tip speed ratios to decrease. For nominal

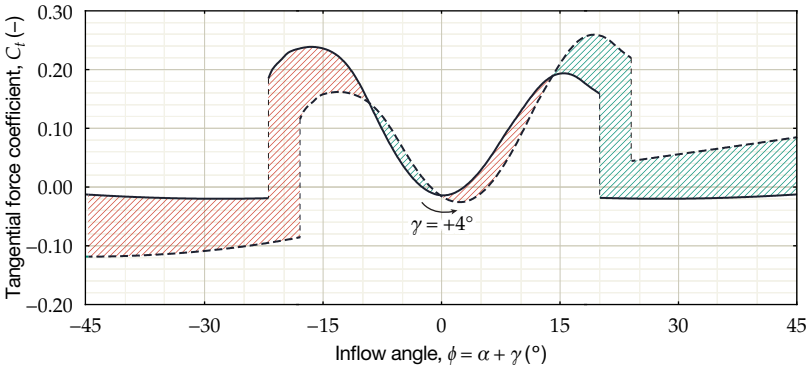

Figure 10.10: Effect of a +4° fixed pitch angle on the tangential force coefficient (Re = 300,000).

operation, the gain in Reynolds number due to a longer chord may therefore be negated by a lower blade speed. Furthermore, increasing solidity is limited by the static stall angles encountered during the rated tip speed ratio. Eventually, the benefits of having higher Reynolds numbers are overshadowed by increased flow curvature effects and dynamic stall ($\propto c/R$), although the latter can be avoided by setting the airfoils under a pitch angle.

Figures 10.11a through f show the effects of changing solidity on the turbine power coefficient. For U_∞ = 3 m/s, there are some advantages in increasing σ for the lower tip speed ratios, given that γ is set correctly. In this situation, raising the Reynolds numbers through the chord length often leads to improvement. For higher tip speed ratios, however, the Reynolds numbers remain in roughly the same order and the mutual differences are less pronounced. Furthermore, there seems to be quite a variation between the different solidities for each airfoil. Solidity has a big impact on Reynolds number, the apparent wind speeds and angle of attack variation and therefore it seems that—for VAWTs of this scale—it should ideally be included in the airfoil design process.

With a solidity of $\sigma > 0.200$, the flipped DU 06-W-200 set at $\gamma = 0°$ seems to accomplish a passive start-up – although just barely. Still, this is far from ideal for nominal operation where low values of σ are preferred to keep the blades from stalling. When the flipped DU 06-W-200 is set under $\gamma = +4°$ and with the eye on a balanced performance between start-up and nominal operation, $\sigma \approx 0.175$ would be best. A solidity of $\sigma = 0.150$ is most effective for concept 1 to yield a high $C_{P_{\max}}$.

10.2.6 Finalizing the designs

Some additional iterations in a narrower range of solidity yields the following design configurations:

- *Start-up*: flipped DU 06-W-200; tripped at $x = 30\%c$ (upper side) and $x = 50\%c$ (lower side); $\sigma = 0.220$; $\gamma = 0°$.
- *Balanced*: flipped DU 06-W-200; tripped at $x = 30\%c$ (upper side) and $x = 50\%c$ (lower side); $\sigma = 0.190$; $\gamma = 4°$.
- *Maximum power*: concept 1; clean; $\sigma = 0.160$; $\gamma = 4°$.

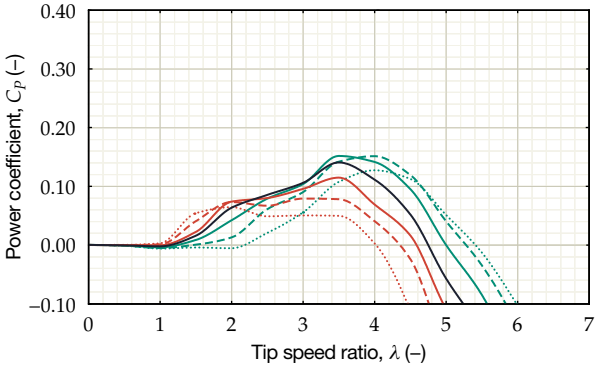

(a): Predicted power coefficient for the flipped DU 06-W-200 ($\gamma = 0°$) with a solidity of $\sigma = 0.100$ (····), 0.125 (– –), 0.150 (—), 0.175 (—), 0.200 (—), 0.225 (– –) and 0.250 (····) at cut-in wind speed ($U_\infty = 3$ m/s).

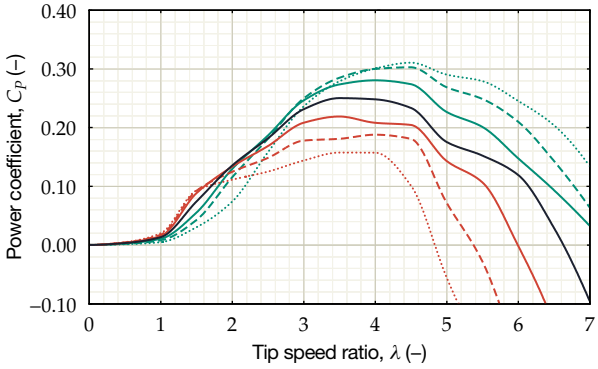

(b): Predicted power coefficient for the flipped DU 06-W-200 ($\gamma = 0°$) with a solidity of $\sigma = 0.100$ (····), 0.125 (– –), 0.150 (—), 0.175 (—), 0.200 (—), 0.225 (– –) and 0.250 (····) at rated wind speed ($U_\infty = 11$ m/s).

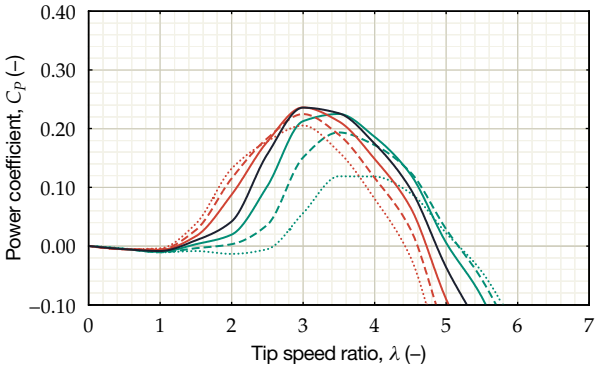

(c): Predicted power coefficient for the flipped DU 06-W-200 ($\gamma = +4°$) with a solidity of $\sigma = 0.100$ (····), 0.125 (– –), 0.150 (—), 0.175 (—), 0.200 (—), 0.225 (– –) and 0.250 (····) at cut-in wind speed ($U_\infty = 3$ m/s).

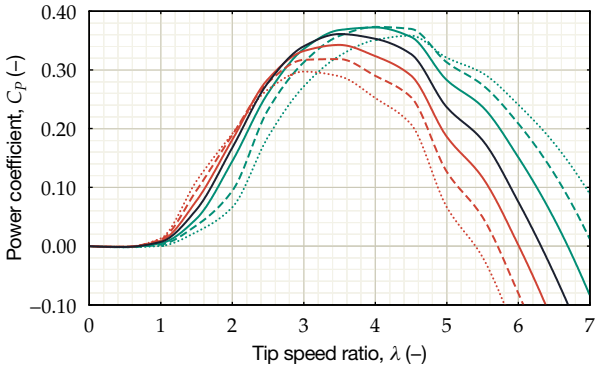

(d): Predicted power coefficient for the flipped DU 06-W-200 ($\gamma = +4°$) with a solidity of $\sigma = 0.100$ (····), 0.125 (– –), 0.150 (—), 0.175 (—), 0.200 (—), 0.225 (– –) and 0.250 (····) at rated wind speed ($U_\infty = 11$ m/s).

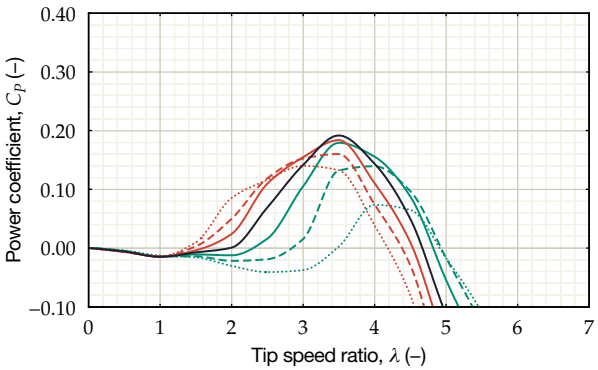

(e): Predicted power coefficient for concept 1 ($\gamma = +4°$) with a solidity of $\sigma = 0.100$ (····), 0.125 (– –), 0.150 (—), 0.175 (—), 0.200 (—), 0.225 (– –) and 0.250 (····) at cut-in wind speed ($U_\infty = 3$ m/s).

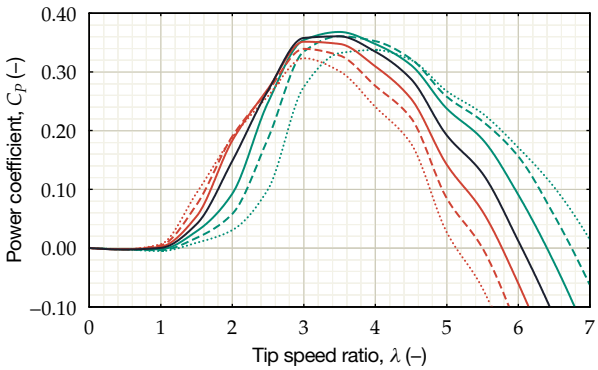

(f): Predicted power coefficient for concept 1 ($\gamma = +4°$) with a solidity of $\sigma = 0.100$ (····), 0.125 (– –), 0.150 (—), 0.175 (—), 0.200 (—), 0.225 (– –) and 0.250 (····) at rated wind speed ($U_\infty = 11$ m/s).

Figure 10.11: Effect of solidity on the turbine power coefficient; calculated in steps of $\Delta\lambda = 0.5$.

10.3 STRUTS

In section 9.3 it was concluded that struts with a hollow back are most likely not effective, considering the limits on the radius to which they can extend. The airfoil shape of the current struts does play a role in torque generation in the case of skewed flow, but this is not always guaranteed. Still, the current NACA 0018 profile is quite

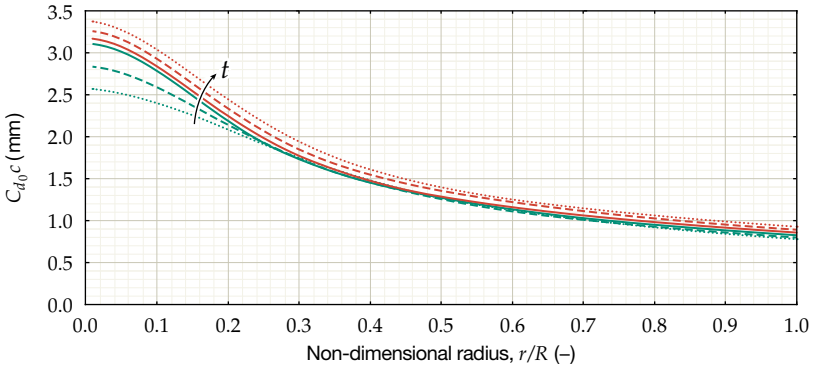

Figure 10.12: Drag of a symmetrical NACA 0010 (·····), 0012 (– –), 0014 (·····), 0016 (——), 0018 (– –) and 0020 (·····) with their chord lengths adapted to match the stiffness requirements ($\lambda = 4$, $U_\infty = 11$ m/s).

thick for the Reynolds numbers encountered by the arms and some drag reduction can easily be achieved here.

10.3.1 Airfoil and chord distribution

Going for thinner profiles means that the length of the profile has to be increased in order to compensate for the lower second moment of area, I_{xx}. Although this would seem to increase the term $C_{d_0}c$, the gain in Reynolds number can have a substantial effect on drag. Figure 10.12 shows the effect of different NACA 00XX sections on drag, taken into account the stiffness requirement. In this plot, the velocity distribution is assumed to be simply

$$V = U_\infty \left(\lambda \frac{r}{R} + \cos\theta \right). \tag{10.9}$$

As with the design of the main blades, the profile drag is evaluated at the root-mean-square Reynolds number.

Clearly, there is much to be gained by switching to thinner profiles, but it would be impractical to adopt very large chord lengths. Constraining the chord length to 120 mm, for instance, is a convenient measure to keep the hub connection unaltered. Minimizing the term $C_{d_0}c$ then yields the airfoil and chord distribution shown in figure 10.13[6]. The lower drag would mean a 7% reduction in counteracting torque at $\lambda = 4$ and $U_\infty = 11$ m/s. Evaluating at $\lambda = 1.5$ and $U_\infty = 3$ m/s, where Reynolds number effects are more pronounced, yields a reduction of 32%. In addition, the longer chords can aid in lift production in the case of skewed flow.

[6] **The thicknesses are evaluated in steps of $1\%c$. In real-life, the thickness can simply vary in a linear fashion from $18\%c$ at the hub to $10\%c$ at the blades.**

10.3.2 Joint area

In section 8.15, three strategies were discussed to decrease the interference drag at strut joints. Moving the joint towards the leading-edge is already not an attractive option since it will lead to large negative moments. The trade-off is then between the two remaining options: a bullet fairing or a simple root fairing. A bullet fairing is an effective option to separate the pressure fields of the blades and the struts, but is accompanied by heavy material use and a large wetted area. Since shockwaves are not a concern in this case[7], a simple root fairing would be a safer choice.

[7] **For aircraft T-tails, the trade-off is between the extra wetted area and wave drag.**

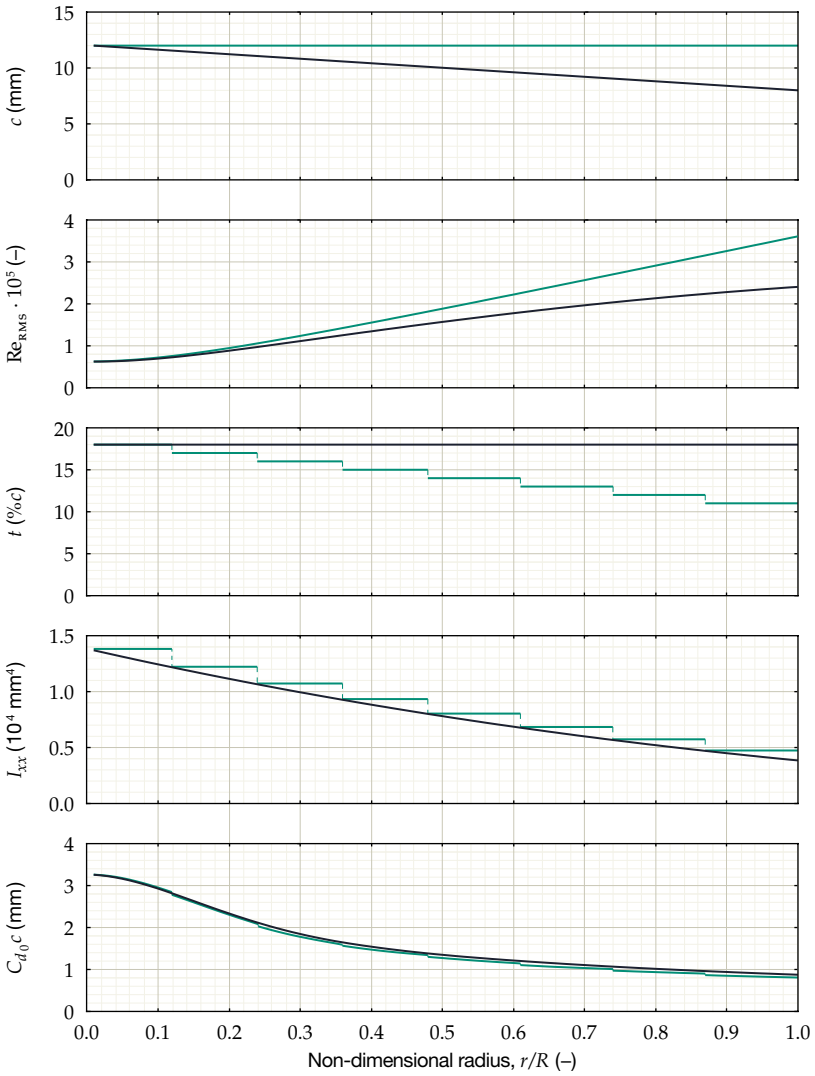

Figure 10.13: Comparison of the old strut (—) and the new concept (—) ($\lambda = 4$, $U_\infty = 11$ m/s).

11 Design proposals

During the design process it became clear that none of the generated airfoils succeeded in facilitating a passive start-up, while leaving the maximum power coefficient unchanged. Results from the model would indicate that a small VAWT operating on the verge of dynamic stall requires the design to be focused on avoiding critical angles of attack. Optimizing for start-up demands radical changes which force the rotor to operate far from optimal. The design process in the previous chapter led to three configurations: one optimized for start-up, one optimized for maximum power and one balanced between start-up and nominal operation.

This chapter presents the three design proposals in sections 11.1 through 11.3, followed by the struts in section 11.4.

11.1 Design for start-up

A start-up configuration was designed purely for the purpose of facilitating a passive start-up at the projected cut-in wind speed. It uses the original DU 06-W-200 airfoil, tripped at $x = 30\%c$ and $x = 50\%c$ on the upper and lower side, respectively. In order to boost the Reynolds numbers and the overall torque, the solidity had to be raised to $\sigma = 0.22$. The performance predictions at $U_\infty = 3$ m/s, shown in 11.4, suggest that this may indeed be possible. However, this is clearly at the cost of the maximum power coefficient. At higher λ, the high solidity and zero pitch angle cause the blades to stall often.

11.2 Balanced configuration

A balanced configuration was made by keeping the airfoil and trip locations from the previous set-up. The solidity and fixed pitch angle were adjusted to move the blades out of stall at the nominal tip speed ratio. This lowers the start-up performance, but also raises the peak power coefficient considerably.

Table 11.1: Characteristics for the configuration optimized for start-up.

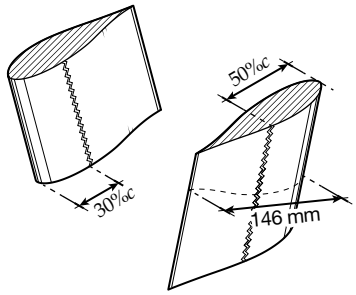

Figure 11.1: Geometry of the configuration optimized for start-up.

Operation		
Rotor speed (rpm)	Ω	382
Blade speed (m/s)	ΩR	44
Rated tip speed ratio (–)	λ	4.0
Rated power (kW)	P	0.93
Peak power coefficient (–)	$C_{P_{\max}}$	0.20
Geometry		
Airfoil		DU 06-W-200 (flipped)
Pitch angle (°)	γ	0
Fixed transition (inboard) (–)	x_{tr}/c	0.30
Fixed transition (outboard) (–)	x_{tr}/c	0.50
Blade chord (mm)	c	146
Blade aspect ratio (–)	AR	19.7
Rotor solidity (–)	σ	0.22
Blade arc (°)	ξ	60
Second moment of area (mm^4)	I_{xx}	$7.37 \cdot 10^4$
(τ = 3 mm)	I_{zz}	$1.15 \cdot 10^7$
	I_{xz}	$-6.04 \cdot 10^6$

Table 11.2: Characteristics for the balanced configuration.

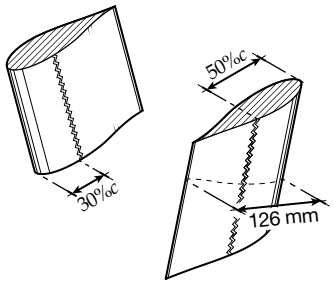

Figure 11.2: Geometry of the balanced configuration.

Operation		
Rotor speed (rpm)	Ω	334
Blade speed (m/s)	ΩR	39
Rated tip speed ratio (–)	λ	3.5
Rated power (kW)	P	1.68
Peak power coefficient (–)	$C_{P_{\max}}$	0.35
Geometry		
Airfoil		DU 06-W-200 (flipped)
Pitch angle (°)	γ	4
Fixed transition (inboard) (–)	x_{tr}/c	0.30
Fixed transition (outboard) (–)	x_{tr}/c	0.50
Blade chord (mm)	c	126
Blade aspect ratio (–)	AR	22.9
Rotor solidity (–)	σ	0.19
Blade arc (°)	ξ	60
Second moment of area (mm^4)	I_{xx}	$4.53 \cdot 10^4$
(τ = 3 mm)	I_{zz}	$6.37 \cdot 10^6$
	I_{xz}	$-3.08 \cdot 10^6$

Table 11.3: Characteristics for the configuration optimized for maximum power.

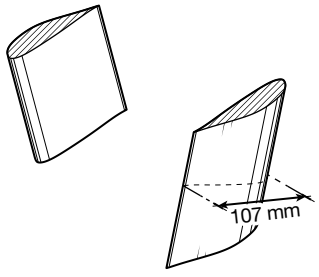

Figure 11.3: Geometry of the configuration optimized for maximum power.

Operation		
Rotor speed (rpm)	Ω	334
Blade speed (m/s)	ΩR	39
Rated tip speed ratio (–)	λ	3.5
Rated power (kW)	P	1.75
Peak power coefficient (–)	$C_{P_{\max}}$	0.37
Geometry		
Airfoil		concept 1
Pitch angle (°)	γ	4
Fixed transition (inboard) (–)	x_{tr}/c	–
Fixed transition (outboard) (–)	x_{tr}/c	–
Blade chord (mm)	c	107
Blade aspect ratio (–)	AR	27.1
Rotor solidity (–)	σ	0.16
Blade arc (°)	ξ	60
Second moment of area (mm^4)	I_{xx}	$2.50 \cdot 10^4$
(τ = 3 mm)	I_{zz}	$3.23 \cdot 10^6$
	I_{xz}	$-1.41 \cdot 10^6$

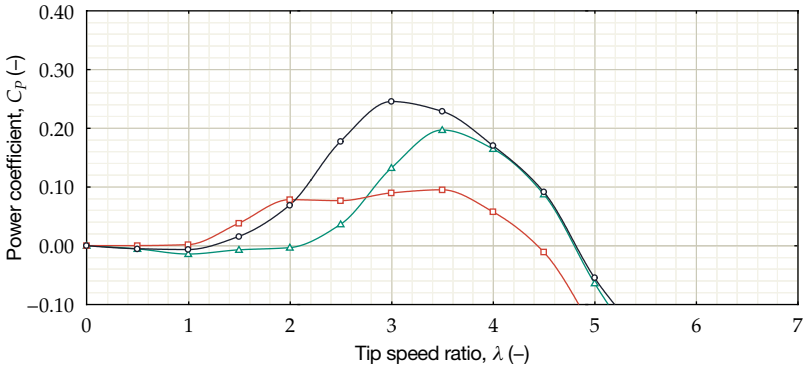

Figure 11.4: Predicted performance of the start-up (□), balanced (○) and maximum power (△) configurations at the cut-in wind speed of U_∞ = 3 m/s.

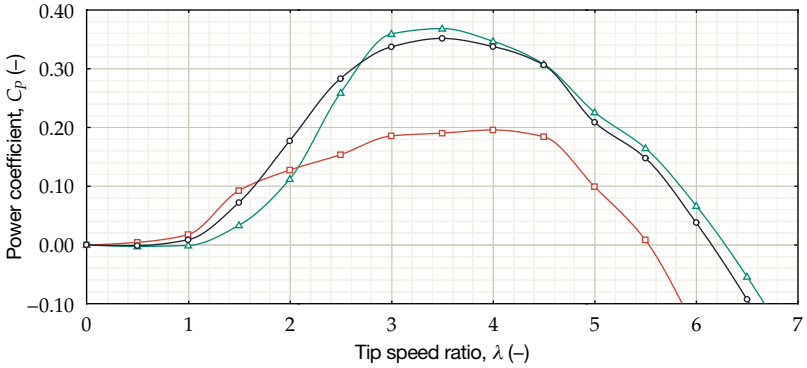

Figure 11.5: Predicted performance of the start-up (□), balanced (○) and maximum power (△) configurations at the rated wind speed of U_∞ = 11 m/s.

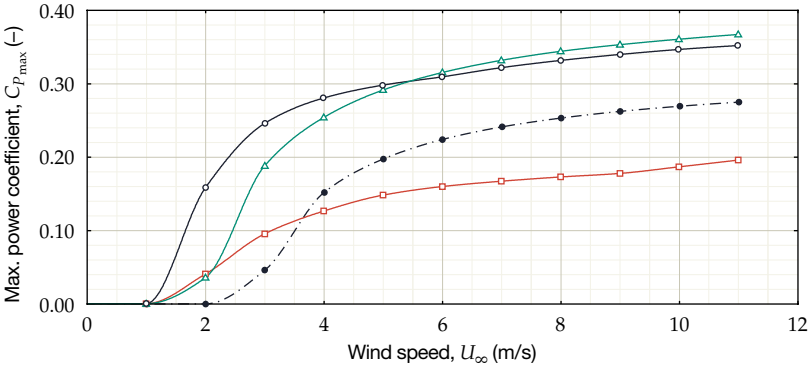

Figure 11.6: Predicted maximum power coefficients of the start-up (□), balanced (○) and maximum power (△) configurations; compared to the original rotor (•).

11.3 CONFIGURATION FOR MAXIMUM POWER

A third configuration was optimized for maximum power production only. This relies on a new airfoil concept which seems to be better suited for the conditions at the rated wind speed. The result is a power curve which shows a lot of improvement around the nominal tip speed ratio. However, this is at the cost of the performance at low U_∞ and λ.

11.4 STRUTS

The strut design[1], compared to the old geometry, is shown in figure 11.7. Because of the very low Reynolds numbers, there are significant drag reductions possible when switching to airfoils of lower

[1] Of course, a new iteration is needed when switching to a configuration with different structural requirements.

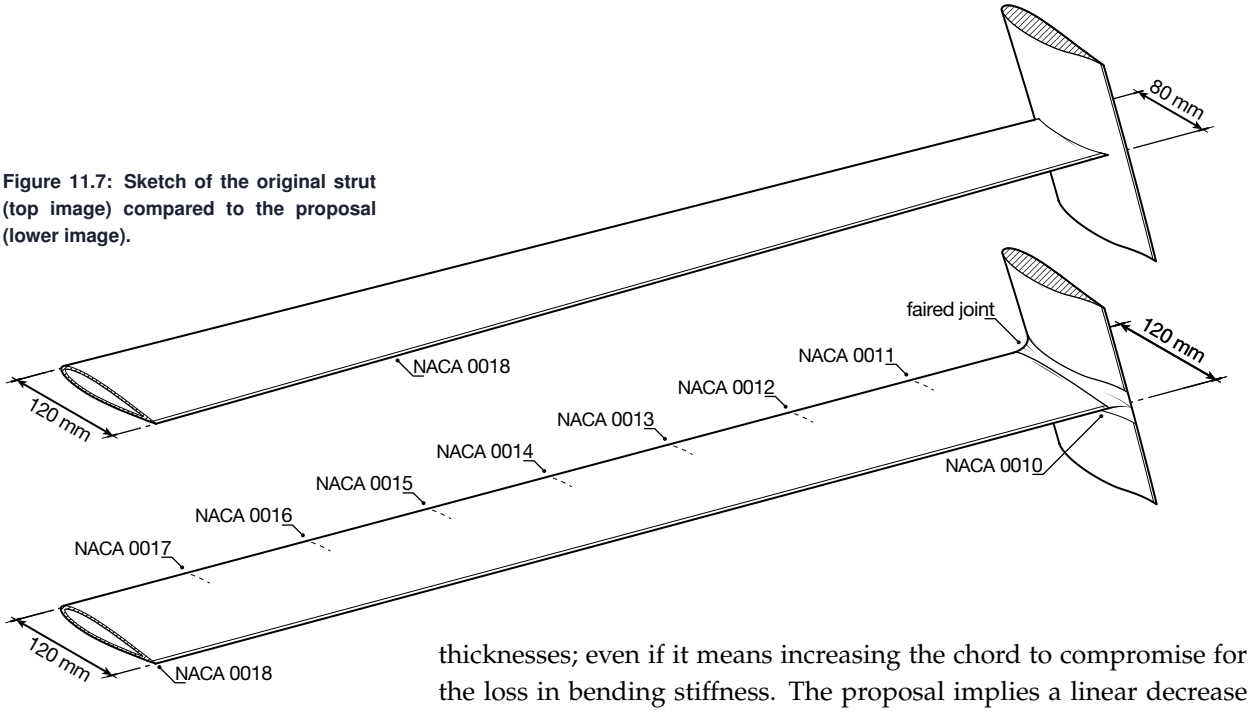

Figure 11.7: Sketch of the original strut (top image) compared to the proposal (lower image).

thicknesses; even if it means increasing the chord to compromise for the loss in bending stiffness. The proposal implies a linear decrease in thickness from 18%c to 10%c. Keeping the chord length constant from the root allows the second moment of area to remain constant.

The connection between the struts and blades ought to be faired to prevent the two pressure regions from creating very high suction peaks. Furthermore, some special attention should go out to possible stagnation points imposed by the struts on the blade surface.

Figures 11.8a and b show the impact of the strut geometry on performance, calculated with a simple drag model outlined in subsection 5.2.2. The effect on the power coefficient is not substantial, but it certainly benefits the rotor at low wind speeds and does not seem to harm $C_{P_{\max}}$ at U_∞ = 11 m/s. This is while the geometry remains at roughly the same level of complexity with respect to the original struts.

Figure 11.8: Drag reduction by altering the strut geometry; calculated in steps of $\Delta\lambda = 0.5$. The effect of joint fairings is not taken into account.

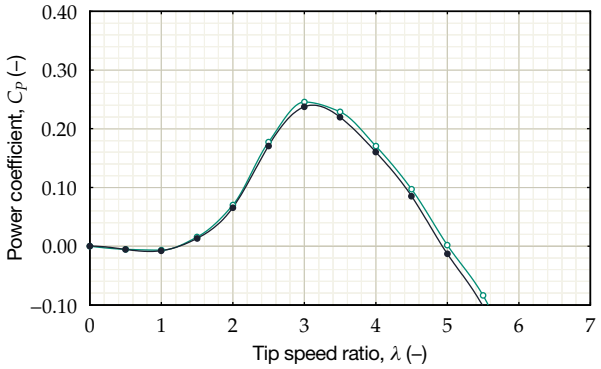

(a): Predicted power coefficient for the flipped DU 06-W-200 set at $\gamma = 4°$ fit with the original struts (•) and the design proposal (○) at the cut-in wind speed (U_∞ = 3 m/s).

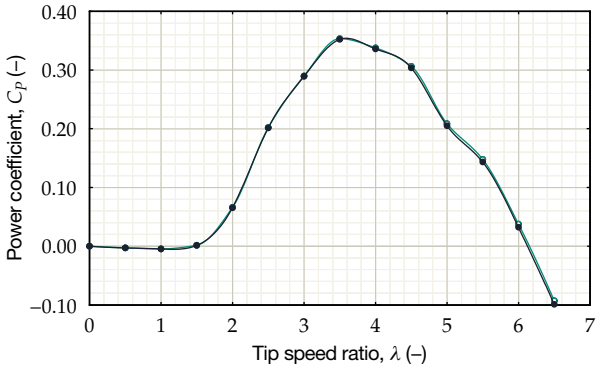

(b): Predicted power coefficient for the flipped DU 06-W-200 set at $\gamma = 4°$ fit with the original struts (•) and the design proposal (○) at the rated wind speed (U_∞ = 11 m/s).

12 Conclusions and recommendations

THE PURPOSE OF THIS MASTER PROJECT was to find and review strategies that could be used to enable a passive start-up for a small urban Darrieus rotor. The design case revolved around Turby – a small 1.6 kW, 2.20 m diameter VAWT with a projected cut-in wind speed of 3 m/s. First, a model was constructed that could mimic the behavior of Turby and help quantify some possible solutions. Next, a start-up analysis was performed to find out what prevents the device from accelerating to higher tip speed ratios. The following chapters then dealt with reviewing several subjects from literature and selecting the aspects that could be used for Turby. This eventually led to three design proposals.

First, the important points of this report are summarized in section 12.1. In addition, section 12.2 provides some recommendations for future study. After that, section 12.3 will add some final thoughts.

12.1 CONCLUSIONS

The major conclusions from this report can be found below.

12.1.1 Failure to start

When the wind speed allows it, a VAWT can accelerate from rest to a certain rated tip speed ratio. The combination of small scale, low wind speeds and low tip speed ratios, λ, has several implications.

- At low tip speed ratios, the angle of attack, α, fluctuates violently. As result, the airfoils are frequently pushed far beyond the point of stall (see 3.3.1).
- For $\lambda < 1$, blades sections may still experience tailwind, which enables a Darrieus rotor to partially operate on the drag difference between the advancing and retreating airfoils (see 3.3.1).

- For $\lambda \leq 2$, the angles of attack are so large that the airfoils mainly display flat plate behavior. The resulting tangential force, C_t, is predominantly negative for $\alpha \leq 45°$ (depending primarily on leading-edge geometry) and positive for $\alpha > 45°$. The deep stall angle therefore marks the beginning of a *post-stall region* of negative C_t (see 6.2.1).
- For $\lambda \approx 1.5$, the airfoils mainly reside inside this post-stall region (see 6.2.2).
- When the tangential force generated in attached flow conditions can no longer compensate for the drag of the stalled airfoils, it leads to a net negative torque. This manifests itself as a dip in the $C_Q - \lambda$ and $C_P - \lambda$ curves – often referred to as a *dead band* in literature (see 6.2.2).
- Combinations of small chords lengths and low apparent wind speeds will lead to low Reynolds numbers, well below 10^5. Performance degradation at these conditions will decrease C_l/C_d, lower the deep stall angle and widen the post-stall region, resulting in a more severe dead band (see 6.2.3).
- When modeling start-up, it is important to include the strong Reynolds number variations to account for performance degradation. For small VAWTS, it seems inaccurate to rely on the rated C_P for off-design conditions (see 6.2.3).

12.1.2 Solutions

Solutions for the start-up problem generally have to do with improving airfoil performance for Re $< 10^5$ or finding other ways of increasing the torque, apart from relying on lift. When looking for solutions, it often turns out that a configuration optimized for start-up is not ideal for the nominal tip speed ratio and rated wind speed – and vice versa. Chapter 8 discussed several possible strategies from literature, of which an overview can be found in section 8.17. Some of these topics had some extra attention and are worth mentioning again.

- Increasing the scale of a Darrieus VAWT will improve the performance of the blades inside the dead band and will have a positive effect on starting (see 7.2).
- Probably the most effective solution to solve the start-up problem is implementing a variable pitch system to give complete control over the angles of attack (see 8.14).
- Airfoil performance at start-up conditions is strongly dominated by laminar separation bubbles. A redesign will have to deal with this effectively (see 8.3, 8.8).
- Blade sweep decreases the lift according to the *independence principle* and can have an effect on the stalling characteristics. Setting the ideal sweep angle is a compromise between vibration levels and power output (see 9.1).

- A Savonius auxiliary rotor is a very effective way of allowing passive start-ups. However, there are some big disadvantages when it comes to adding drag devices. Most important is matching the tip speed ratios of the two devices. A Savonius machine finds is maximum C_Q at $\lambda = 0$ and its maximum C_P often at $\lambda \approx 0.7 - 0.8$. This is while the dead band of VAWTs generally resides in the range $0.5 \leq \lambda \leq 1.5$. Another issue arises when the nominal tip speed ratio is reached and the secondary device must be kept from braking the main rotor by imposing limits on the diameter or finding means to decouple it. In this case, combinations between Turby and a Savonius lead to inefficient designs, with the auxiliary device being too large compared to the primary rotor (see 9.2).
- A similar concept can be imagined where the support struts are hollowed out to create a drag differential. This did not turn out to be effective because of several reasons. First, creating enough surface area in the back of a profile will also tremendously increase the frontal drag coefficient. Second, hollow struts also suffer from limitations on the radius. Preventing braking at higher tip speed ratios will limit the hollow sections to the inboard part of the rotor where the generated torque is low. And third, it is hard to create enough surface area inside the rotor – especially when models do not tell anything about the impact on the wake (see 9.3.2).
- Struts can generate positive torque when the incoming flow is skewed, analogous to a propeller in yaw. However, it is hard to design for this because of the uncertainty of the skew angle and the unsteady nature of the flow. The amount of torque can be considered as a nice bonus, but is not game-changing (see 9.3.4).

12.1.3 Design proposal

In chapter 10, two airfoils were generated with a genetic algorithm to surpass the original DU 06-W-200 in start-up ($\lambda \approx 0.5 - 1.5$, $U_\infty = 3$ m/s) and nominal operation ($\lambda \approx 3.5 - 4.0$, $U_\infty = 11$ m/s). During this process, several things became clear.

- For every turbine configuration and operating condition, there is a different blade profile that performs best at that point. The circumstances at start-up and at the rated tip speed ratio are so different that it becomes very difficult to design a self-starting airfoil that upholds the structural requirement and still performs well at the maximum power point (see 10.1).
- A genetic algorithm is a suitable tool to design airfoils that have to satisfy many different requirements or have to operate in a wide range of conditions. However, the fitness functions did not take all the relevant aspects into account. At this small scale, the rotor solidity, σ, and pitch angle, γ, greatly affect the conditions in which the airfoils have to operate and should ideally be included in the optimization process (see 10.2.1).
- Airfoil performance at start-up is strongly dominated by laminar separation bubbles, and a well-placed boundary layer trip can of-

ten accomplish more than switching to a thinner airfoil. For very low Reynolds numbers, the location of fixed transition needs to be kept variable when generating geometries (see 10.2.2, 10.2.3).

- Two replacement airfoils for DU 06-W-200 were generated under turbulent conditions. One should increase $C_{P_{\max}}$ and was scaled to t = 20.0%c. Another airfoil was generated in an attempt to accomplish a passive start-up. For this design, the structural requirement had to be dropped, leading to a thickness of t = 13.4%c. However, it was eventually surpassed by a flipped DU 06-W-200 with tripping points placed at the right locations. This has to do with the previous point (see 10.2.2, 10.2.3).
- For high-solidity rotors operating close to the point of stall, setting the airfoils under a fixed pitch angle can greatly improve the power coefficient. However, this is at the cost of start-up performance (see 10.2.4).
- A configuration was optimized for start-up, using the flipped DU 06-W-200 airfoil, tripped at x = 30%c and x = 50%c on the inboard and outboard side, respectively. For self-starting to become feasible, it required a high solidity of σ = 0.22 and a zero pitch angle. Therefore, it suffered greatly from stall, which limited the power coefficient to 0.20 (see 11.1).
- A balanced configuration was designed, using the flipped DU 06-W-200 airfoil, tripped at x = 30%c and x = 50%c on the inboard and outboard side, respectively. It relied on a somewhat higher solidity than the baseline case (σ = 0.19), but has a fixed pitch angle of γ = 4° to avoid stall at high λ. It reached a peak power coefficient of 0.35 (see 11.2).
- A configuration was optimized for maximum power, using the replacement airfoil from the genetic algorithm. It has a lower solidity of σ = 0.16 and a pitch angle of γ = 4°. The peak power coefficient was estimated at $C_{P_{\max}}$ = 0.37, but also showed good improvement around the rated tip speed ratio and at wind speeds of $U_\infty \geq 6$ m/s (see 11.3).
- At the Reynolds numbers encountered by Turby, struts of a NACA 0012 cross-section will have lower drag than when using a NACA 0018 profile, even when it means increasing the chord length to compromise the lower bending stiffness (see 10.3).

12.2 RECOMMENDATIONS

To be able to model the start-up behavior of VAWTS, use was made of two important tools – a vortex panel method was used to extract the induction velocities, and viscous airfoil data was generated by RFOIL. The results of these tools were combined—with the possible intervention of a dynamic stall model—to make predictions of the turbine's performance. Several simplifications had to be adopted for this to work (see 5.3), which naturally leads to some recommendations for developing low λ models.

- For an accurate wake model, feedback is needed from the viscous effects of the blades; preferably including separation as result of (dynamic) stall (see 5.2.1).
- In this report, use has been made of a dynamic stall model developed by Gormont (1973), accompanied by the Massé-Berg modification (see Strickland, 1975; Massé, 1981). This is a semi-empirical model and is therefore not entirely reliable when used for other airfoils than the one it was tuned for (see 5.1.5). It relies on the use of static airfoil data and therefore also does not correctly account for the effects of pitch on the boundary layer. This stall region is an important part of the start-up problem and more accuracy is desired here.
- Closer collaboration is needed with experimental work to evaluate the effects of rapidly changing Reynolds numbers, the viscous wake, 3D stall effects over swept blades, influence of the support structure, etc.
- For the model used in this report, values of the turbulence intensity and N_{crit} were simply estimated in order to make a distinction between the upwind and downwind rotor halves. Of course, more accurate values can be found through better wake models or experiments.
- Using genetic algorithms is an effective way of designing airfoils for small VAWTS. When considering low Reynolds numbers, the transition location should be kept variable. Moreover, for airfoils that operate on the verge of dynamic stall, parameters like solidity and pitch angle should ideally be included in the design process.

12.3 SOME FINAL THOUGHTS

The goal of this project was to find solutions that allow Turby to achieve a passive start-up, while honoring the original design requirements and preventing a loss in total energy yield (see section 4.3). In retrospect, this is a complicated undertaking. During the course of this master project, it became clear that self-starting requires one or more of the design requirements to be dropped. Probably the most effective solutions are

- *Darrieus-Savonius hybrid*: adds a lot of torque but affects the aesthetics and increases the mass moment of inertia.
- *Variable pitch*: gives complete control of the angles of attack, but adds a lot of complexity and removes the indifference to wind direction.
- *Thin low-Reynolds-number airfoils*: greatly increase low-speed performance, but are unable to handle the loads at the rated speed.
- *High solidity rotor*: increase Reynolds numbers and torque at low λ, but causes the blades to enter stall regularly.

Eventually, the choice was made to do a redesign of the airfoils and set the solidity and pitch accordingly. Facilitating start-up required the configuration to be optimized for a range of angles of attack and Reynolds numbers that will hardly be encountered at the rated wind speed. Still, without a comparison to the actual real-life case, the depth of the dead band remains merely an estimation. This means that the first design proposal—optimized for start-up—is not guaranteed to be fully self-starting in real life.

Airfoils designed through a more thorough process might still achieve a good balance between start-up and nominal operation. Unfortunately, the optimization method that was used proved to be incomplete for low speed conditions and further improvement was not achieved within the timespan of this project. Including parameters such as solidity, pitch angle and trip location seems vital to achieve good results.

References

Agentschap NL (2011). Geluidregelgeving. Available at: http://windenergie.nl/154/geluidregelgeving [Accessed 14 November 2011].

Akwa, J. V., H. A. Vielmo, and A. P. Petry (2012). A review on the performance of Savonius wind turbines. *Renewable and Sustainable Energy Reviews 16*(5), 3054–3064. doi:10.1016/j.rser.2012.02.056.

Álvarez, J. C., J. Meseguer, E. Meseguer, and A. Pérez (2001). On the role of the alula in the steady flight of birds. *Ardeola 48*(2), 161–173.

Anderson, Jr., J. D. (1997). *A history of aerodynamics*. New York, NY: Cambridge University Press.

Baker, J. P., E. A. Mayda, and C. P. van Dam (2006). Experimental analysis of thick blunt trailing-edge wind turbine airfoils. *Journal of Solar Energy Engineering 128*(11), 422–431.

Baker, J. R. (1983). Features to aid or enable self starting of fixed pitch low solidity vertical axis wind turbines. *Journal of Wind Engineering and Industrial Aerodynamics 15*(1-3), 369–380. doi:10.1016/0167-6105(83)90206-4.

Bechert, D. W., M. Bruse, W. Hage, and R. Meyer (2000). Fluid mechanics of biological surfaces and their technological application. *Naturwissenschaften 87*(4), 157–171. doi:10.1007/s001140050696.

Berg, D. E. (1983). An improved double-multiple streamtube model for the Darrieus-type vertical axis wind turbine. In *Sixth Biennal Wind Energy Conference and Workshop*, Minneapolis, MN, pp. 231–233.

van den Berg, G. P. (2006). *The sound of high winds: the effect of atmospheric stability on wind turbine sound and microphone noise*. Ph. D. thesis, University of Groningen.

Bishop, K. (2006). The relationship between 3-d kinematics and gliding performance in the southern flying squirrel, Glaucomys volans. *Journal of Experimental Biology 209*(Pt 4), 689–701. doi:10.1242/jeb.02062.

Blackwell, B. F., R. E. Sheldahl, and L. V. Feltz (1977). Wind tunnel performance data for two- and three-bucket Savonius rotors. Technical Report SAND76-0131, Sandia Laboratories.

Burton, T., D. Sharpe, N. Jenkins, and E. Bossanyi (2001). *Wind energy handbook*. Chichester: John Wiley & Sons.

van Bussel, G. J. W., S. Mertens, H. Polinder, and H. F. A. Sidler (2004). TURBY®: concept and realisation of a small VAWT for the built environment. In *EAWE/EWEA Special Topic conference "The Science of making Torque from Wind"*, Delft, pp. 509–516.

Cace, J. and E. ter Horst (2007). Urban wind turbines: leidraad voor kleine windturbines in de bebouwde omgeving. Technical Report WINEUR, RenCom/HoriSun.

Carruthers, A. C., A. L. R. Thomas, and G. K. Taylor (2007). Automatic aeroelastic devices in the wings of a steppe eagle aquila nipalensis. *Journal of Experimental Biology 210*, 4136–4149. doi:10.1242/jeb.011197.

Claessens, M. C. (2006). The design and testing of airfoils for application in small vertical axis wind turbines. Master's thesis, Delft University of Technology.

Darrieus, G. J. M. (1931). Turbine having its rotating shaft transverse to the flow of the current. US Patent 1,835,018.

Davenport, A. G. (1960). Rationale for determining design wind velocities. *ASCE Journal of the Structural Division 86*(5), 39–68.

De Gregorio, F. and G. Fraioli (2008). Flow control on a high thickness airfoil by a trapped vortex cavity. In *International Symposium on Applications of Laser Techniques to Fluid Mechanics*, Lisbon, pp. 7–10.

Doyle, T., M. Gerritsen, and G. Iaccarino (2002). Towards sail-shape optimization of a modern clipper ship. In *Annual Research Briefs*, Center for Turbulence Research, NASA Ames/Stanford University, pp. 215–224.

Drela, M. (1988). Low-Reynolds-number airfoil design for the M.I.T. Daedalus prototype: a case study. *Journal of Aircraft 25*(8), 724–732.

Drela, M. (1989). XFOIL: An analysis and design system for low Reynolds number airfoils. In *Conference on Low Reynolds Number Airfoil Aerodynamics*, University of Notre Dame.

Drela, M. (1995). *XFOIL 6.5 user guide*. Cambridge, MA: Massachusetts Institute of Technology.

Finaish, F. and S. Witherspoon (1998). Aerodynamic performance of an airfoil with step-induced vortex for lift augmentation. *Journal of Aerospace Engineering 11*(1), 9–16.

Fujisawa, N. (1991). On the torque mechanism of Savonius rotors. *Journal of Wind Engineering and Industrial Aerodynamics 40*(3), 277–292. doi:10.1016/0167-6105(92)90380-S.

Fujisawa, N. and S. Shibuya (2001). Observations of dynamic stall on Darrieus wind turbine blades. *Journal of Wind Engineering and Industrial Aerodynamics 89*(2), 201–214. doi:10.1016/S0167-6105(00)00062-3.

Garrison, P. (2010). Technicalities: rules to fly by. Available at: http://www.flyingmag.com/transonic-area-rule/technicalities-rules-fly [Accessed 9 January 2012].

Gault, D. E. (1957). A collection of low-speed airfoil-section stalling characteristics with Reynolds number and airfoil geometry. Technical Report NACA-TN-3963, National Advisory Committee for Aeronautics.

Gavaldà, J., J. Massons, and F. Díaz (1990). Experimental study on a self-adapting Darrieus-Savonius wind machine. *Solar & Wind Technology 7*(4), 457–461. doi:10.1016/0741-983X(90)90030-6.

Gopalarathnam, A., B. A. Broughton, B. D. McGranahan, and M. S. Selig (2003). Design of low Reynolds number airfoils with trips. *Journal of Aircraft 40*(4), 768–775.

Gorlov, A. M. (1998). Development of the helical reaction hydraulic turbine. Technical Report DE-FG01-96EE 15669, US Department of Energy.

Gormont, R. E. (1973). An analytical model of unsteady aerodynamics and radial flow for application to helicopter rotors. Technical Report 72-67, U.S. Army Air Mobility Research and Development Laboratory.

Greitzer, E. M., C. S. Tan, and M. B. Graf (2004). *Internal flow: concepts and applications*. New York, NY: Cambridge University Press.

Gupta, R., A. Biswas, and K. K. Sharma (2008). Comparative study of a three-bucket Savonius rotor with a combined three-bucket SavoniusŰthree-bladed Darrieus rotor. *Renewable Energy 33*(9), 1974–1981. doi:10.1016/j.renene.2007.12.008.

Haydock, H. and J.-A. Arbon (2009). Study on energy performance of buildings. Technical Report IP/A/ITRE/ST/2008-10, European Parliament.

Healy, J. V. (1978). The influence of blade thickness on the output of vertical axis wind turbines. *Wind Engineering 2*(1), 1–9.

Hill, N., R. Dominy, G. Ingram, and J. Dominy (2009). Darrieus turbines: The physics of self-starting. *Proceedings of the Institution of Mechanical Engineers, Part A: Journal of Power and Energy 223*(1), 21–29. doi:10.1243/09576509JPE615.

Hirsch, H. and A. C. Mandal (1987). A cascade theory for the aerodynamic performance of Darrieus wind turbines. *Wind Engineering 11*(3), 164–75.

Hoerner, S. F. and H. V. Borst (1985). *Fluid-dynamic lift*. New York, NY: Mrs. Listelotte A. Hoerner.

Howe, M. S. (2007). Aerodynamic noise of a serrated trailing edge. *Journal of Fluids and Structures 5*(1), 33–45. doi:10.1016/0889-9746(91)80010-B.

Islam, M., D. S.-K. Ting, and A. Fartaj (2007a). Design of a special-purpose airfoil for smaller-capacity straight-bladed VAWT. *Wind Engineering 31*(6), 401–424. doi:10.1260/030952407784079780.

Islam, M., D. S.-K. Ting, and A. Fartaj (2007b). Desirable airfoil features for smaller-capacity straight-bladed VAWT. *Wind Engineering 31*(3), 165–196. doi:10.1260/030952407781998800.

Islam, M., D. S.-K. Ting, and A. Fartaj (2008). Aerodynamic models for Darrieus-type straight-bladed vertical axis wind turbines. *Renewable and Sustainable Energy Reviews 12*(4), 1087–1109. doi:10.1016/j.rser.2006.10.023.

Jacobs, E. N. and A. Sherman (1937). Airfoil characteristics as affected by variations of the Reynolds number. Technical Report 586, National Advisory Committee for Aeronautics.

Johnson, G. L. (2001). *Wind energy systems* (electronic ed.). Manhattan, KS.

Kamoji, M. A., S. B. Kedare, and S. V. Prabhu (2011). Experimental investigations on two and three stage modified Savonius rotor. *Wind Engineering 35*(4), 483–510. doi:10.1260/0309-524X.35.4.483.

Kerho, M., S. Hutcherson, R. F. Blackwelder, and R. H. Liebeck (1993). Vortex generators used to control laminar separation bubbles. *Journal of Aircraft 30*(3), 315–319.

Kirke, B. K. (1998). *Evaluation of self-starting vertical axis wind turbines for stand-alone applications*. Ph. D. thesis, Griffith University.

Kirke, B. K. and L. Lazauskas (1991). Enhancing the performance of vertical axis wind turbine using a simple variable pitch system. *Wind Engineering 15*(4).

Kline, R. L. (2011). KFm family of airfoils. [image online] Available at: http://upload.wikimedia.org/wikipedia/en/3/3c/KFm-Family-descriptions3.jpg [Accessed 6 December 2011].

Kline, R. L. and F. F. Fogleman (1972). Airfoil for aircraft. US Patent 3,706,430.

Larsen, H. C. (1975). Summary of a vortex theory for the cyclogiro. In *Proceedings of the 2nd US National Conferences on Wind Engineering Research*, Colorado State University.

Larsen, J. W. (2005). *Nonlinear dynamics of wind turbine wings*. Ph. D. thesis, Aalborg University.

Lasagna, D., R. Donelli, and F. D. G. Iuso (2011). Effects of a trapped vortex cell on a thick wing airfoil. *Experiments in Fluids 51*(5), 1369–1384. doi:10.1007/s00348-011-1160-9.

Lazauskas, L. (1992). Three pitch control systems for vertical axis wind turbines compared. *Wind Engineering 16*(5), 269–282.

Leishman, J. G. (2006). *Principles of helicopter aerodynamics* (2nd ed.). New York, NY: Cambridge University Press.

Li, Q. Y., S. L. Wu, F. B. Peng, and G. J. Li (1983). A study on aerodynamics of vertical-axis windmill with double blades. In *Solar World Congress: Proceedings of the 8th biennial congress of the International Solar Energy Society*, Perth, pp. 2360–2364.

Lin, J. C. (2002). Review of research on low-profile vortex generators to control boundary-layer separation. *Progress in Aerospace Sciences 38*(4-5), 389–420. doi:10.1016/S0376-0421(02)00010-6.

Lindenburg, C. (2003). Investigation into rotor blade aerodynamics. Technical Report ECN-C-03-025, Energy Research Centre of the Netherlands.

Liu, T., J. Montefort, W. Liou, and S. R. Pantula (2007). Lift enhancement by static extended trailing edge. *Journal of Aircraft 44*(6), 1939–1947. doi:10.2514/1.31995.

Lovins, A. B. (2002). *Small is profitable: The hidden economic benefits of making electrical resources the right size*. Snowmass, CO: Rocky Mountain Institute.

Lumsdaine, E., W. S. Johnson, L. M. Fletcher, and J. E. Peach (1974). Investigation of the Kline-Fogleman airfoil section for rotor blade applications. Technical Report NASA-CR-141282, National Aeronautics and Space Administration.

Mai, H., G. Dietz, W. Geißler, K. Richter, J. Bosbach, H. Richard, and K. de Groot (2008). Dynamic stall control by leading edge vortex generators. *Journal of the American Helicopter Society 53*(1), 26–36. doi:10.4050/JAHS.53.26.

Massé, B. (1981). Description de deux programmes d'ordinateur pour le calcul des performances et des charges aérodynamiques pour des éoliennes à axe vertical. Technical Report IREQ 2379.

Masson, C., C. Leclerc, and I. Paraschivoiu (1998). Appropriate dynamic-stall models for performance predictions of VAWTs with NLF blades. *International Journal of Rotating Machinery 4*(2), 129–139.

McGhee, R. J., G. Jones, and R. Jouty (1988). Performance characteristics from wind-tunnel tests of a low-Reynolds-number airfoil. In *26th AAIA Aerospace Sciences Meeting*, Reno, NV.

Mertens, S. (2006). *Wind energy in the built environment: concentrator effects of buildings*. Ph. D. thesis, Delft University of Technology.

Mertens, S., G. A. M. van Kuik, and G. J. W. van Bussel (2003). Performance of an H-Darrieus in the skewed flow on a roof. *Journal of Solar Energy Engineering 125*(4), 433–440. doi:10.1115/1.1629309.

Meseguer, J., S. Franchini, I. Pérez-Grande, and J. L. Sanz (2005). On the aerodynamics of leading-edge high-lift devices of avian wings. *Proceedings of the Institution of Mechanical Engineers, Part G: Journal of Aerospace Engineering 219*(1), 63–68. doi:10.1243/095441005X9067.

Mols, B. (2005). Turby - sustainable urban wind power from the roof top. *Delft Outlook 2005*(2), 18–22.

Morris, S. (1984). Fancy flights. *Omni 6*(7), 64.

Newman, B. G. and M. Païdoussis (1991). The stability of two-dimensional membranes in streaming flow. *Journal of Fluids and Structures 5*(4), 443–454. doi:10.1016/0889-9746(91)90437-T.

Nørkær Sørensen, J. (1999). VISCWIND: Viscous effects on wind turbine blades, final report on the JOR3-CT95-0007, Joule III project. Technical Report ET-AFM-9902, Technical University of Denmark.

de Oliveira, G. (2011). A novel approach to wind turbine airfoil design with boundary layer suction. Master's thesis, Delft University of Technology.

Olsman, W. F. J. and T. Colonius (2011). Numerical simulation of flow over an airfoil with a cavity. *AAIA Journal 49*(1), 143–149.

Pandey, M. M., K. P. Pandey, and T. P. Ojha (1988). Aerodynamic characteristics of cambered steel plates in relation to their use in wind energy conversion systems. *Wind Engineering 12*(2), 90–104.

Panek, E. (1993). Effects of structural elements on vertical axis wind turbine power production. Master's thesis, San Jose State University.

Paraschivoiu, I. (1981). Double multiple streamtube model for Darrieus wind turbines. In *Second DOE/NASA wind turbines dynamics workshop, NASA CP-2186*, Cleveland, OH, pp. 19–25.

Paraschivoiu, I. (2002). *Wind turbine design: with emphasis on the Darrieus concept*. Montreal: Polytechnic International Press.

Paraschivoiu, I., O. Trifu, and F. Saeed (2009). H-Darrieus wind turbine with blade pitch control. *International Journal of Rotating Machinery 2009*, 1–7.

Purser, P. E. and M. L. Spearman (1951). Wind-tunnel tests at low speed of swept and yawed wings having various plan forms. Technical Report NACA-TN-2445, National Advisory Committee for Aeronautics.

Roach, J. (2004). Owl's silent flight may inspire quiet aircraft tech. Available at: `http://news.nationalgeographic.com/news/2004/12/1217_041217_owl_feathers.html` [Accessed 17 November 2011].

Robert, J. and B. G. Newman (1979). Lift and drag of a sail aerofoil. *Wind Engineering 3*(1), 1–22.

Saeed, F., I. Paraschivoiu, O. Trifu, M. Hess, and C. Gabrys (2008). Inverse airfoil design method for low-speed straight-bladed Darrieus-type VAWT applications. In *7th World Wind Energy conference*, St. Lawrence College.

Saha, U., S. Thotla, and D. Maity (2008). Optimum design configuration of savonius rotor through wind tunnel experiments. *Journal of Wind Engineering and Industrial Aerodynamics 96*(8-9), 1359–1375. `doi:10.1016/j.jweia.2008.03.005`.

Schatz, M., T. Knacke, F. Thiele, R. Meyer, W. Hage, and D. W. Bechert (2004). Separation control by self-activated movable flaps. In *42th AAIA Aerospace Sciences Meeting & Exhibit*, Reno, NV.

Scheurich, F. and R. E. Brown (2011). Vertical-axis wind turbines in oblique flow: sensitivity to rotor geometry. In *EWEA Annual event*, Brussels.

Scheurich, F., T. M. Fletcher, and R. E. Brown (2010). The influence of blade curvature and helical blade twist on the performance of a vertical-axis wind turbine. In *29th ASME Wind Energy Symposium*, Orlando, FL.

Seki, K. (2005). Straight wing type wind and water turbine. US Patent 6,974,309.

Selig, M. S. (1995). S1210 (11.87%) and S1223 (11.93%) for R/C heavy lift/slow flight competition. Available at: `http://www.ae.illinois.edu/m-selig/ads/ref/s1210s1223_ref.html` [Accessed 15 November 2011].

Selig, M. S. (2003). Low Reynolds number airfoil design lecture notes. In *VKI Lecture Series*, von Karman Institute for Fluid Dynamics.

Selig, M. S., J. F. Donovan, and D. B. Fraser (1989). *Airfoils at low speeds*. Virginia Beach, VA: H. A. Stokely.

Selig, M. S. and B. D. McGranahan (2004). Wind tunnel aerodynamic tests of six airfoils for use on small wind turbines. *Journal of Solar Energy Engineering 126*(4), 986–1002. doi:10.1115/1.1793208.

Shyy, W., M. Berg, and D. Ljungqvist (1999). Flapping and flexible wings for biological and micro air vehicles. *Progress in Aerospace Sciences 35*(5), 455–505. doi:10.1016/S0376-0421(98)00016-5.

Simão Ferreira, C. J. (2009). *The near wake of the VAWT: 2D and 3D views of the VAWT aerodynamics*. Ph. D. thesis, Delft University of Technology.

Simão Ferreira, C. J., K. Dixon, C. Hofemann, G. A. M. van Kuik, and G. J. W. van Bussel (2009). The VAWT in skew: stereo-PIV and vortex modeling. In *47th AIAA Aerospace Sciences Meeting*, Orlando, FL.

Simão Ferreira, C. J., G. A. M. van Kuik, G. J. W. van Bussel, and F. Scarano (2009). Visualization by PIV of dynamic stall on a vertical axis wind turbine. *Experiments in Fluids 46*(1), 97–108. doi:10.1007/s00348-008-0543-z.

St. Hilaire, A. O. and F. O. Carta (1979). The influence of sweep on the aerodynamic loading of an oscillating naca 0012 airfoil, Vol. 2 - Data report. Technical Report NASA CR 145350, National Aeronautics and Space Administration.

Standish, K. J. and C. P. van Dam (2003). Aerodynamic analysis of blunt trailing edge airfoils. *Journal of Solar Energy Engineering 125*(4), 479–487.

Stankovic, S., N. A. Campbell, and A. Harries (2009). *Urban wind energy*. London: Earthscan.

Strickland, J. H. (1975). The Darrieus turbine: a performance prediction model using multiple streamtubes. Technical Report SAND75-0431, Sandia Laboratories.

Swartz, S. M., J. Iriarte-Diaz, D. K. Riskin, A. Song, X. Tian, D. J. Willis, and K. S. Breuer (2007). Wing structure and the aerodynamic basis of flight in bats. In *45th AIAA Aerospace Sciences Meeting*, Reno, NV.

Timmer, W. (2010). Aerodynamic characteristics of wind turbine blade airfoils at high angles-of-attack. In *The Science of Making Torque from Wind*, Crete, pp. 71–78.

Timmer, W. A. (2008). Two-dimensional low-Reynolds number wind tunnel results for airfoil NACA 0018. *Wind Engineering 32*(6), 525–537. doi:10.1260/030952408787548848.

Timmer, W. A. and R. P. J. O. M. van Rooij (2001). Some aspects of high angle-of-attack flow on airfoils for wind turbine application. In *European Wind Energy Conference and Exhibition (EWEC)*, Copenhagen.

Timmer, W. A. and R. P. J. O. M. van Rooij (2003). Summary of the Delft University wind turbine dedicated airfoils. *Journal of Solar Energy Engineering 125*, 488–496.

de Vries, O. (1979). Fluid dynamic aspects of wind energy conversion. Technical Report AGARD-AG-243, Advisory Group for Aerospace Research & Development.

Wakui, T., Y. Tanzawa, T. Hashizume, and T. Nagao (2005). Hybrid configuration of Darrieus and Savonius rotors for stand-alone wind turbine-generator systems. *Electrical Engineering in Japan 150*(4), 13–22. doi:10.1002/eej.20071.

Waltham, M. R. (1984). The pivotted leading edge sailwing turbine. In *Proceedings of the 6th BWEA Wind Energy Conference*, University of Reading, pp. 324–333.

White, F. M. (2004). *Fluid Mechanics* (6th ed.). New York, NY: McGraw-Hill.

Wieringa, J. (1980). Representativeness of wind observations at airports. *Bulletin American Meteorological Society 61*(9), 962–971. doi:10.1175/1520-0477(1980)061<0962:ROWOAA>2.0.CO;2.

Worasinchai, S., G. Ingram, and R. Dominy (2011). A low-Reynolds-number, high-angle-of-attack investigation of wind turbine aerofoils. *Proceedings of the Institution of Mechanical Engineers, Part A: Journal of Power and Energy 225*(6), 748–763. doi:10.1177/0957650911405411.

Predictions at low Reynolds numbers

A

The following pages show how RFOIL predictions at various Reynolds numbers hold against real-life wind tunnel data. The data sets used are summarized in table A.1.

Author	Airfoil	Facility	Turb. level
Gopalarathnam et al. (2003)	SA7026	Subsonic wind tunnel, University of Illinois	0.06–0.12%
McGhee et al. (1988)	Eppler 387	Low-turbulence pressure tunnel, NASA Langley	0.06–0.16%
Selig et al. (1989)	NACA 2.5411-PT	3 x 4 ft. smoke tunnel, Princeton University	0.01–0.06% *
Selig and McGranahan (2004)	FX 63-137	Subsonic wind tunnel, University of Illinois	0.06–0.12%
Timmer (2008)	NACA 0018	Low-speed wind tunnel, Delft University of Tech.	0.02–0.07%

* Corresponds to frequencies of > 1 Hz

Table A.1: Background data of the wind tunnel measurements depicted in the figures on the following pages.

Figure A.1: Wind tunnel data compared to RFOIL predictions at a range of Reynolds numbers.

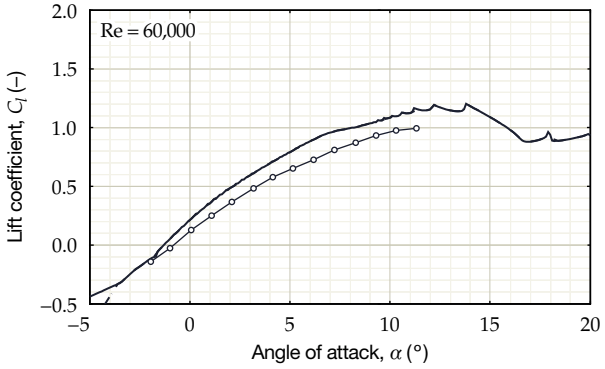

(a): Measurements of NACA 2.5411-PT (○), compared to RFOIL predictions at N_{crit} = 9 (– –) and 12 (—) at Re = 60,000.

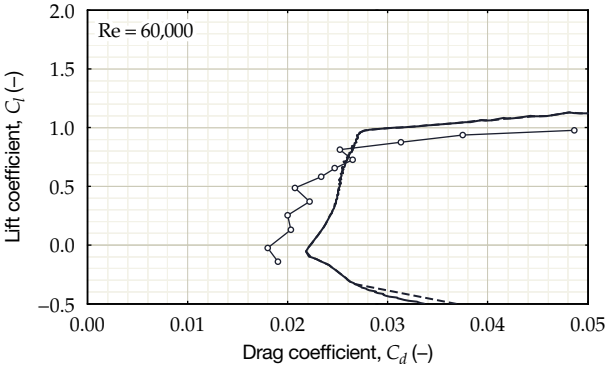

(b): Measurements of NACA 2.5411-PT (○), compared to RFOIL predictions at N_{crit} = 9 (– –) and 12 (—) at Re = 60,000.

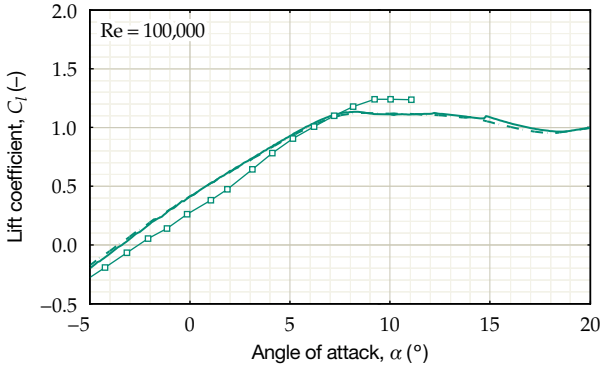

(c): Measurements of SA7026 (□), compared to RFOIL predictions at N_{crit} = 9 (– –) and 12 (—) at Re = 100,000.

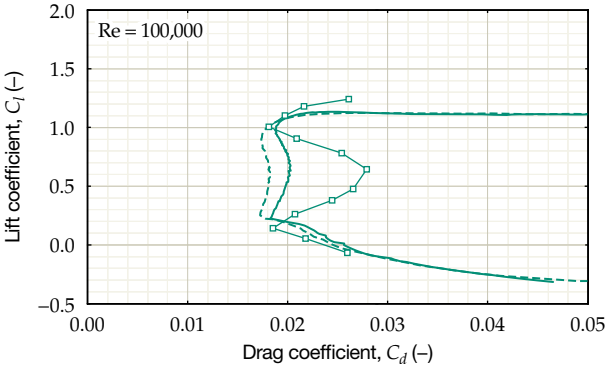

(d): Measurements of SA7026 (□), compared to RFOIL predictions at N_{crit} = 9 (– –) and 12 (—) at Re = 100,000.

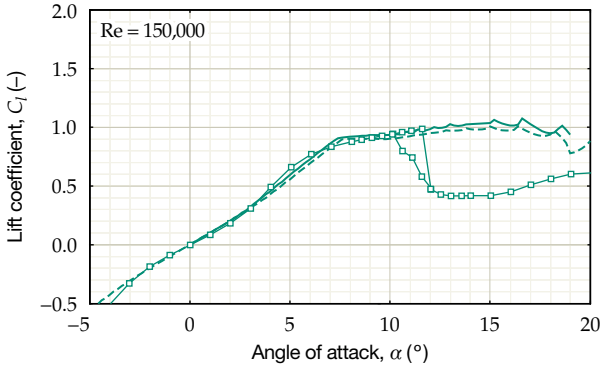

(e): Measurements of NACA 0018 (□), compared to RFOIL predictions at N_{crit} = 9 (– –) and 12 (—) at Re = 150,000.

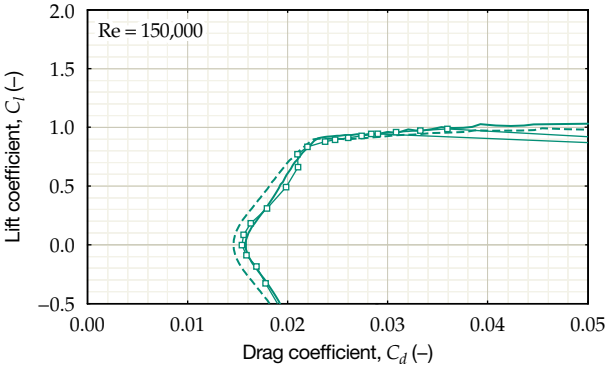

(f): Measurements of NACA 0018 (□), compared to RFOIL predictions at N_{crit} = 9 (– –) and 12 (—) at Re = 150,000.

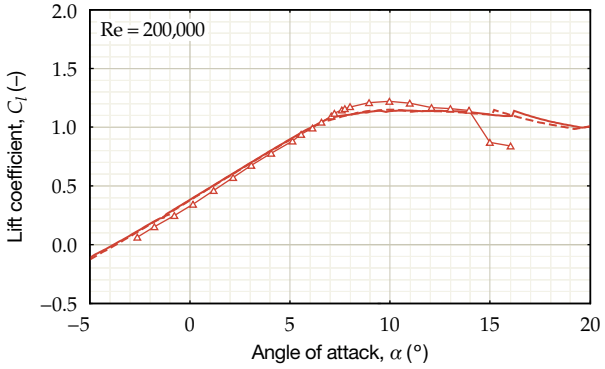

(g): Measurements of Eppler 387 (△), compared to RFOIL predictions at N_{crit} = 9 (– –) and 12 (—) at Re = 200,000.

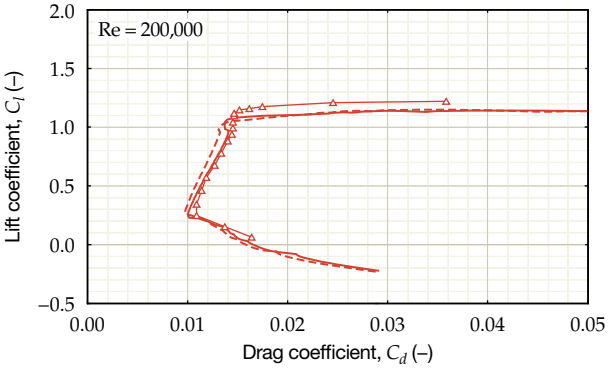

(h): Measurements of Eppler 387 (△), compared to RFOIL predictions at N_{crit} = 9 (– –) and 12 (—) at Re = 200,000.

Figure A.1: Wind tunnel data compared to RFOIL predictions at a range of Reynolds numbers (*continued*).

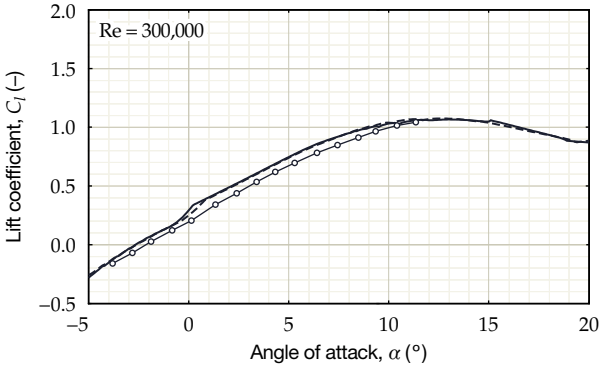

(i): Measurements of NACA 2.5411-PT (○), compared to RFOIL predictions at N_{crit} = 9 (– –) and 12 (—) at Re = 300,000.

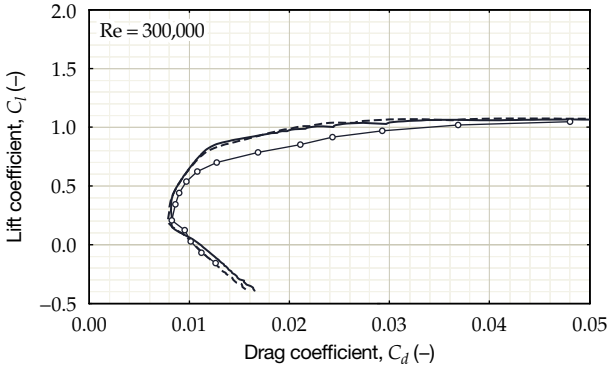

(j): Measurements of NACA 2.5411-PT (○), compared to RFOIL predictions at N_{crit} = 9 (– –) and 12 (—) at Re = 300,000.

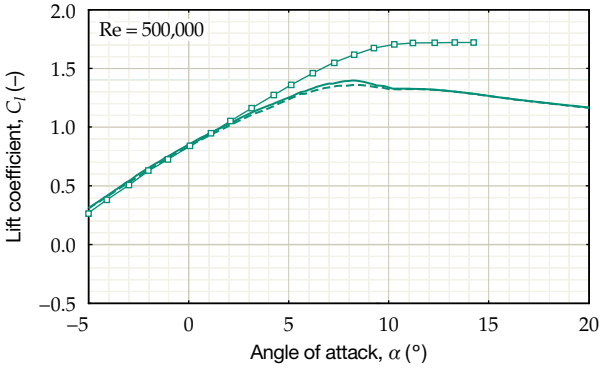

(k): Measurements of FX 63-137 (□), compared to RFOIL predictions at N_{crit} = 9 (– –) and 12 (—) at Re = 500,000.

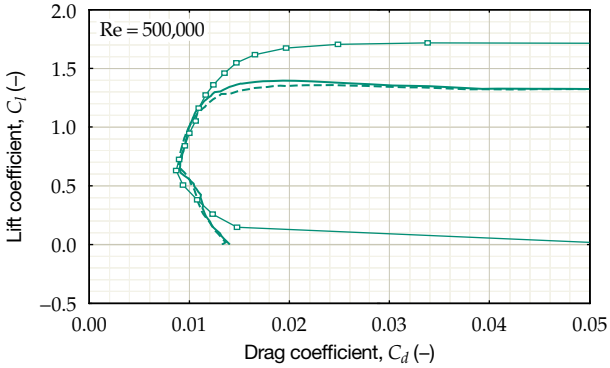

(l): Measurements of FX 63-137 (□), compared to RFOIL predictions at N_{crit} = 9 (– –) and 12 (—) at Re = 500,000.

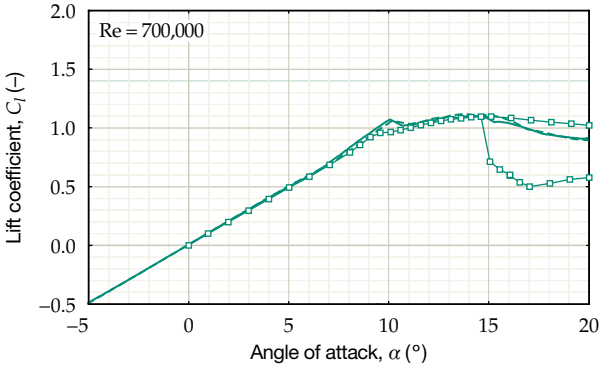

(m): Measurements of NACA 0018 (□), compared to RFOIL predictions at N_{crit} = 9 (– –) and 12 (—) at Re = 700,000.

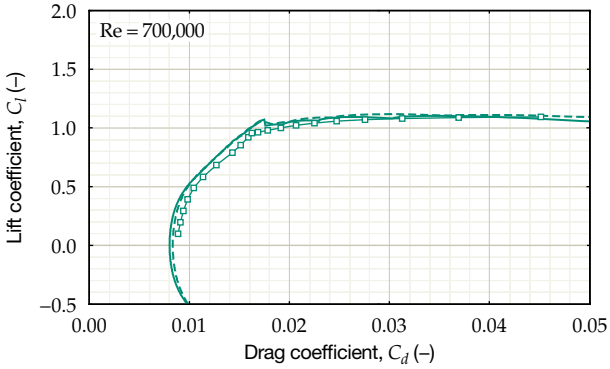

(n): Measurements of NACA 0018 (□), compared to RFOIL predictions at N_{crit} = 9 (– –) and 12 (—) at Re = 700,000.

B

Determining airfoil stiffness

In order to make the trade-off between aerodynamic performance at low Reynolds numbers and the bending stiffness, the second moment of area has to be determined. This appendix shows how an approximation can be made from airfoil coordinate files using a polygon method.

B.1 AIRFOIL POLYGON

The geometry of an airfoil as it is fed into RFOIL or the vortex panel model is described by an airfoil coordinate file. This consists of the vertex positions $\{x_i, z_i\}$ that enclose the outer shape. These are ordered counter-clockwise, starting at the trailing-edge.

A second polygon can then be added by subtracting the skin thickness, τ to define the inner cavity (see figure B.1). First, the length of an outer panel is given by

$$\Delta l = \sqrt{(x_{i+1} - x_i)^2 + (z_{i+1} - z_i)^2}. \tag{B.1}$$

Moreover, the angle ϑ that the panel makes with the x-axis is given by

$$\vartheta = \arcsin\left(\frac{z_{i+1} - z_i}{\sqrt{(x_{i+1} - x_i)^2 + (z_{i+1} - z_i)^2}}\right). \tag{B.2}$$

The vertices of the inner polygon are then determined by subtracting

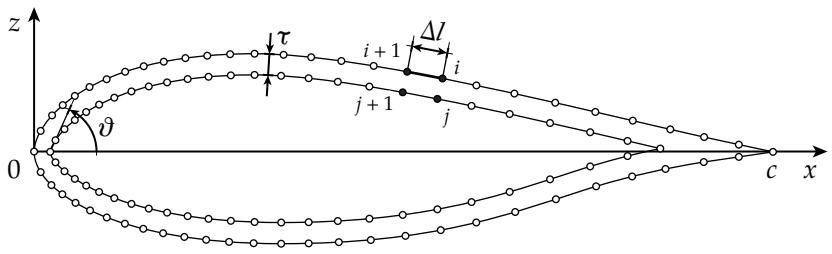

Figure B.1: Two polygons that enclose the cross-sectional area of an airfoil with skin thickness τ.

the skin thickness according to

$$x_j = \begin{cases} x_i - \frac{\tau}{c}\sin\vartheta, & z_i \geq 0,\ z_j \geq 0, \\ x_i - \frac{\tau}{c}\sin\vartheta, & z_i < 0,\ z_j \leq 0, \end{cases} \tag{B.3a}$$

$$z_j = \begin{cases} z_i - \frac{\tau}{c}\cos\vartheta, & z_i \geq 0,\ z_j \geq 0, \\ z_i + \frac{\tau}{c}\cos\vartheta, & z_i < 0,\ z_j \leq 0. \end{cases} \tag{B.3b}$$

B.2 SECOND MOMENT OF AREA

The second moment of area is given by

$$I_{xx} = \iint_A z^2\,dx\,dy, \tag{B.4a}$$

$$I_{zz} = \iint_A x^2\,dx\,dy, \tag{B.4b}$$

$$I_{xz} = \iint_A xz\,dx\,dy. \tag{B.4c}$$

Since moments can be subtracted from each other in a straightforward fashion, the inner polygon can be easily cut from the outer contour. The area of the cross-section—which is a good measure for the spanwise mass distribution—can then be calculated by

$$A = \tfrac{1}{2}\sum_{i=1}^{m-1}\left(x_i z_{i+1} - x_{i+1} z_i\right) - \tfrac{1}{2}\sum_{j=1}^{n-1}\left(x_j z_{j+1} - x_{j+1} z_j\right). \tag{B.5}$$

For the two polygons, equations (B.4a) through (B.4c) can be rewritten as

$$\begin{aligned} I_{xx} =& \tfrac{1}{12}c^4\sum_{i=1}^{m-1}\left(z_i^2 + z_i z_{i+1} + z_{i+1}^2\right)\left(x_i z_{i+1} - x_{i+1} z_i\right) \\ &- \tfrac{1}{12}c^4\sum_{j=1}^{n-1}\left(z_j^2 + z_j z_{j+1} + z_{j+1}^2\right)\left(x_j z_{j+1} - x_{j+1} z_j\right), \end{aligned} \tag{B.6a}$$

$$\begin{aligned} I_{zz} =& \tfrac{1}{12}c^4\sum_{i=1}^{m-1}\left(x_i^2 + x_i x_{i+1} + x_{i+1}^2\right)\left(x_i z_{i+1} - x_{i+1} z_i\right) \\ &- \tfrac{1}{12}c\sum_{j=1}^{n-1}\left(x_j^2 + x_j z_{j+1} + x_{j+1}^2\right)\left(x_j z_{j+1} - x_{j+1} z_j\right), \end{aligned} \tag{B.6b}$$

$$\begin{aligned} I_{xz} =& \tfrac{1}{24}c\sum_{i=1}^{m-1}\left(x_i z_{i+1} + 2x_i z_i + 2x_{i+1} z_{i+1} + x_{i+1} z_i\right)\left(x_i z_{i+1} - x_{i+1} z_i\right) \\ &- \tfrac{1}{24}c^4\sum_{j=1}^{n-1}\left(x_j z_{j+1} + 2j_i z_j + 2x_{j+1} z_{j+1} + x_{j+1} z_j\right)\left(x_j z_{j+1} - x_{j+1} z_j\right). \end{aligned} \tag{B.6c}$$

Concept airfoils

C

The following pages show two airfoils that have been generated by the genetic algorithm discussed in section 10.2.1, compared to the flipped DU 06-W-200 airfoil (—). The torque coefficient, C_Q, is obtained by evaluating equation (5.21) at $\lambda = 4$ and $U_\infty = 11$ m/s for one 2D blade section. The aerodynamic force curves are generated in clean conditions for both Re = 40,000 and 350,000 to represent start-up conditions and nominal operation, respectively.

In addition, the force curves contain thin lines that represent the 'raw' RFOIL data, as well as thick lines where the data has been smoothed using a Gaussian function over a 3° interval. The spread of the data points near stall clearly shows that the accuracy at Re $< 10^5$ leaves much to be desired.

Figure C.1: Airfoil concept 1.

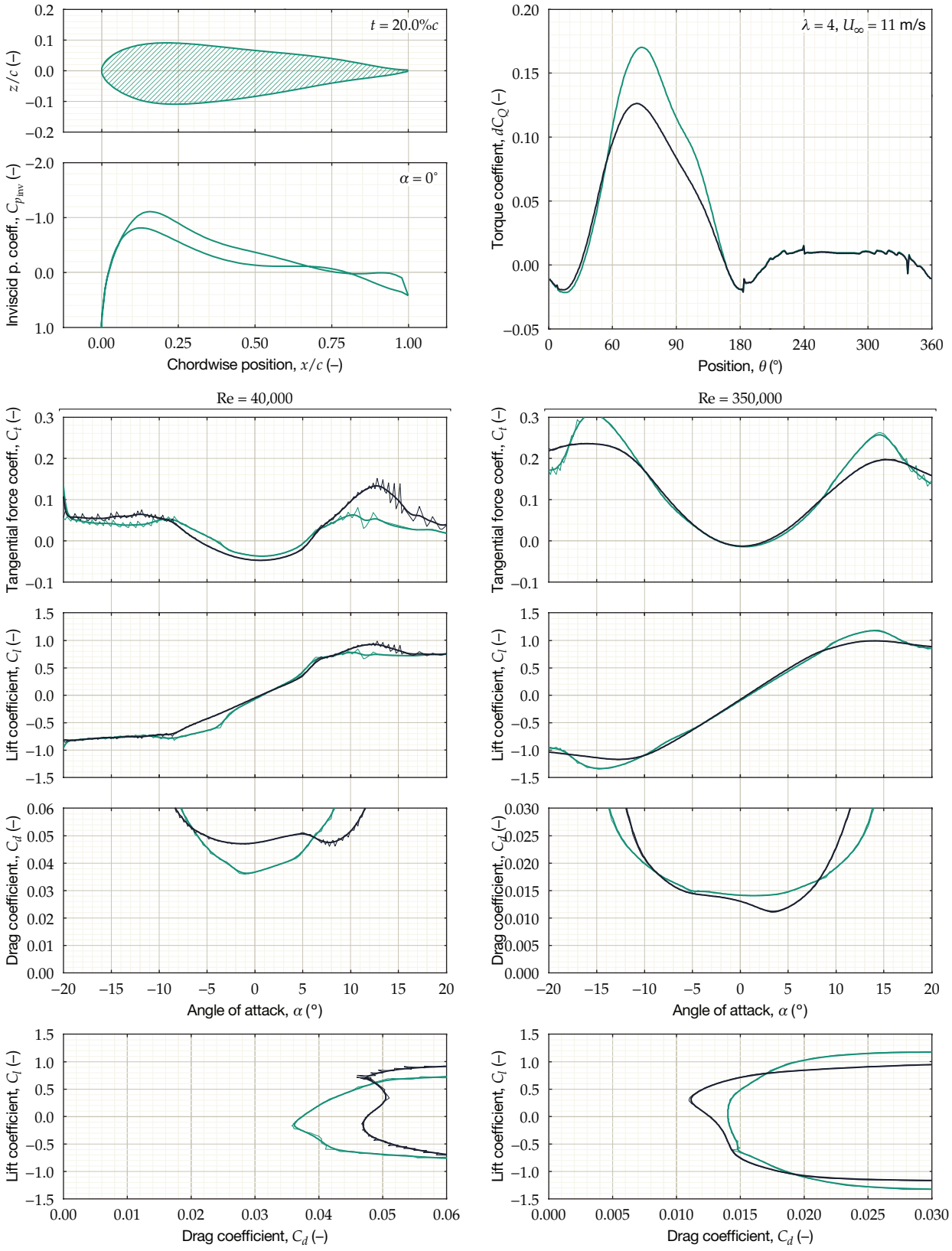

Figure C.2: Airfoil concept 2.

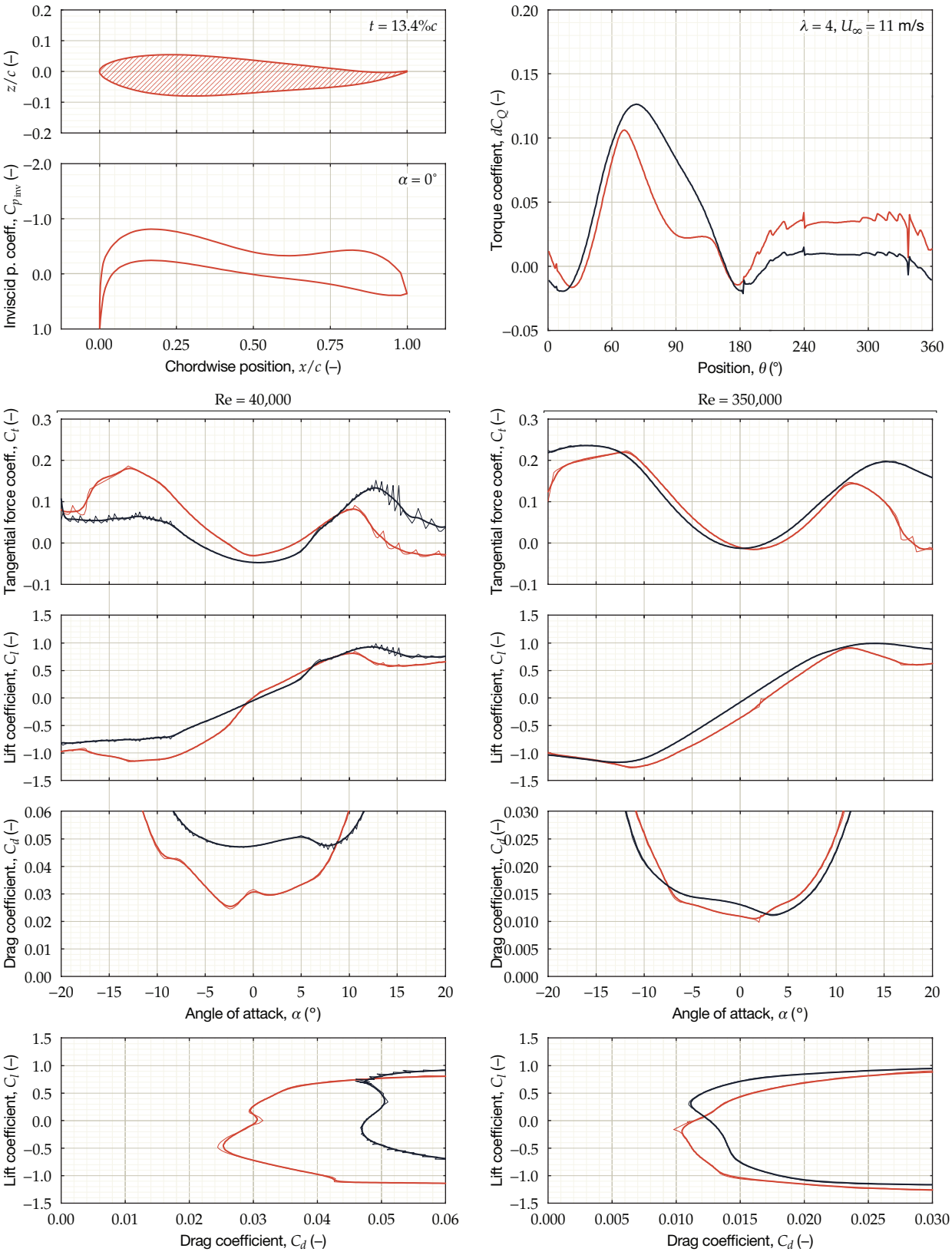

Figure C.3: Airfoil concept pressure distributions at $N_{crit} = 9$ (—, —, —) and $N_{crit} = 4$ (·····, ·····, ·····); Re = 40,000.

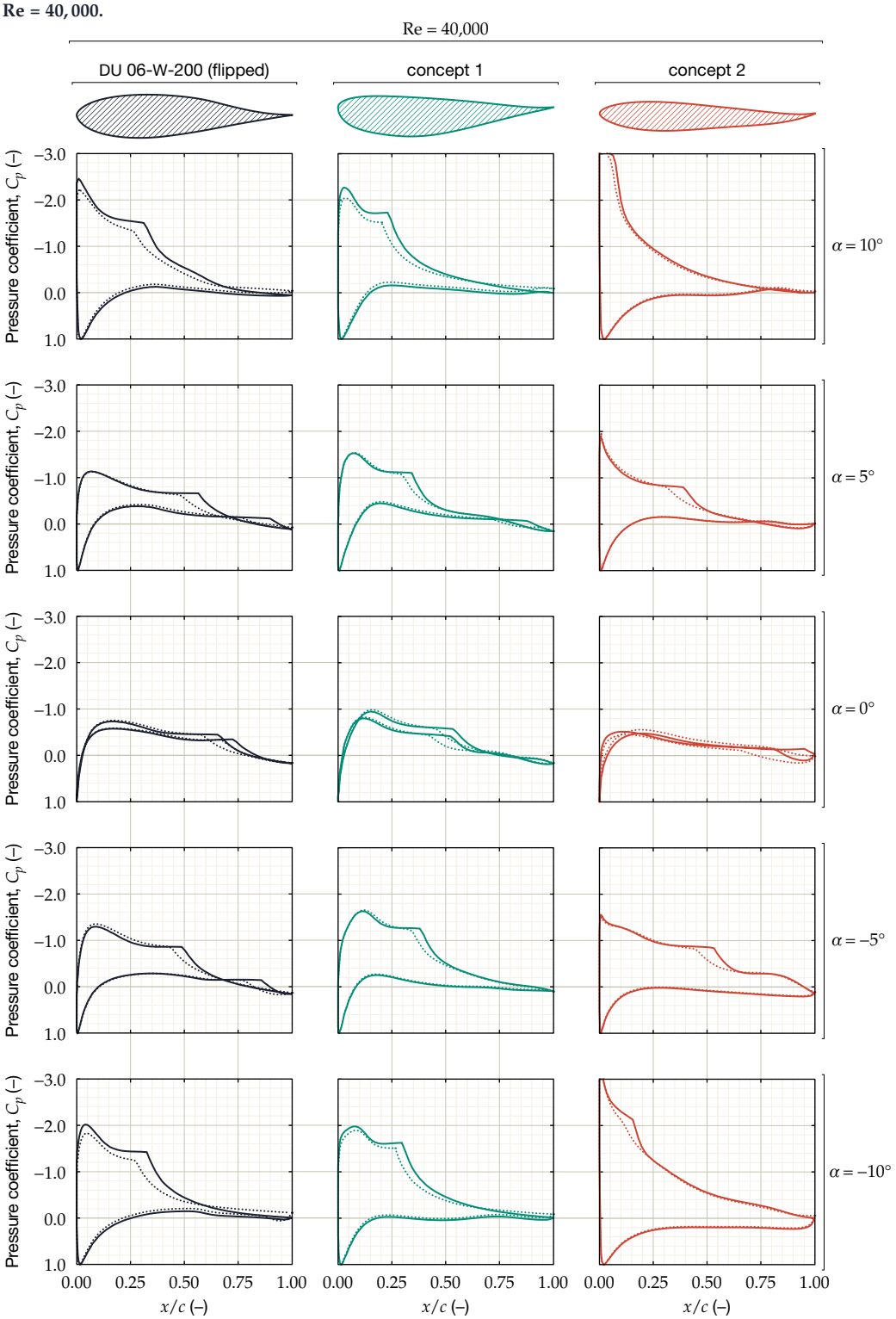

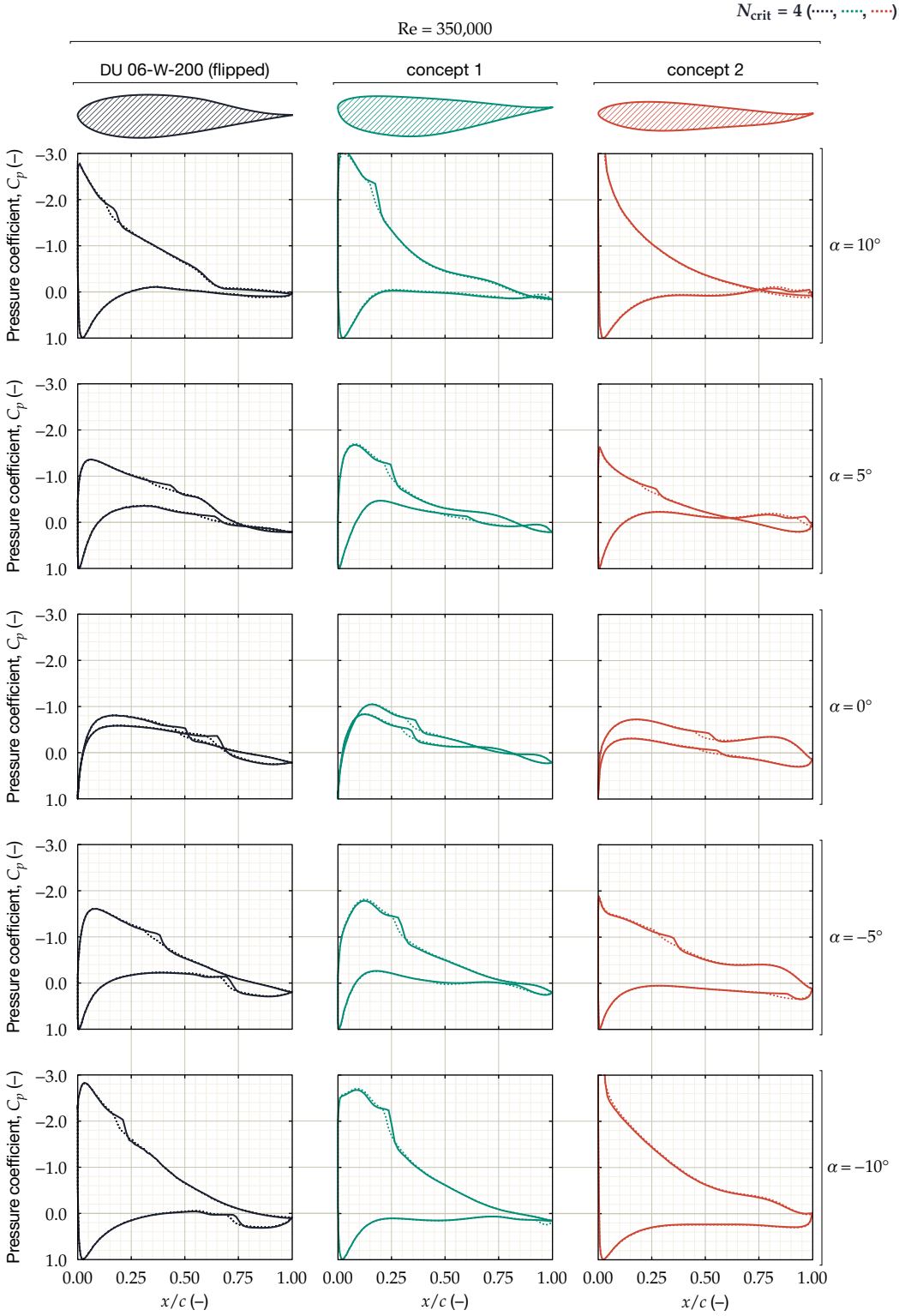

Figure C.4: Airfoil concept pressure distributions at N_{crit} = 9 (—, —, —) and N_{crit} = 4 (·····, ·····, ·····); Re = 350,000.

Airfoil coordinates

D

The following pages contain the airfoil coordinates for DU 06-W-200 (unflipped) and the two concepts treated in chapter 10.

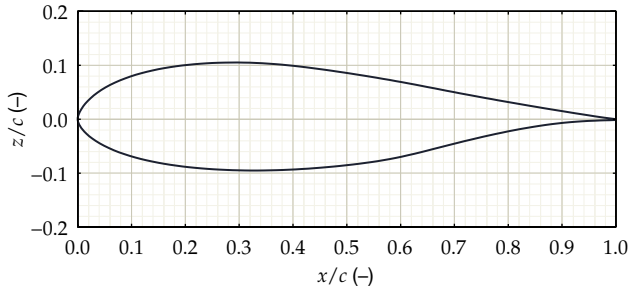

Table D.1: Coordinates of DU 06-W-200.

x/c	z/c	x/c	z/c	x/c	z/c	x/c	z/c
1.00000	-0.00075	0.32646	0.10338	0.00003	-0.00127	0.36458	-0.09366
0.99367	0.00013	0.31336	0.10375	0.00028	-0.00281	0.37813	-0.09326
0.98343	0.00150	0.30030	0.10396	0.00068	-0.00439	0.39168	-0.09272
0.97233	0.00309	0.28726	0.10397	0.00120	-0.00600	0.40526	-0.09206
0.96043	0.00488	0.27424	0.10382	0.00186	-0.00764	0.41886	-0.09128
0.94787	0.00683	0.26128	0.10348	0.00265	-0.00931	0.43247	-0.09039
0.93480	0.00891	0.24838	0.10296	0.00355	-0.01103	0.44610	-0.08938
0.92134	0.01109	0.23556	0.10225	0.00458	-0.01279	0.45972	-0.08827
0.90762	0.01332	0.22283	0.10135	0.00574	-0.01459	0.47333	-0.08705
0.89373	0.01559	0.21021	0.10026	0.00705	-0.01644	0.48691	-0.08573
0.87972	0.01790	0.19773	0.09896	0.00851	-0.01835	0.50045	-0.08432
0.86567	0.02022	0.18540	0.09746	0.01013	-0.02030	0.51391	-0.08281
0.85160	0.02256	0.17327	0.09575	0.01194	-0.02231	0.52726	-0.08119
0.83753	0.02492	0.16135	0.09381	0.01396	-0.02438	0.54050	-0.07944
0.82346	0.02731	0.14966	0.09166	0.01619	-0.02651	0.55359	-0.07756
0.80943	0.02972	0.13826	0.08928	0.01866	-0.02873	0.56656	-0.07551
0.79539	0.03215	0.12718	0.08671	0.02139	-0.03103	0.57945	-0.07325
0.78135	0.03461	0.11647	0.08391	0.02443	-0.03342	0.59232	-0.07079
0.76730	0.03710	0.10617	0.08093	0.02781	-0.03590	0.60522	-0.06810
0.75325	0.03962	0.09635	0.07778	0.03157	-0.03848	0.61822	-0.06521
0.73921	0.04218	0.08705	0.07447	0.03575	-0.04116	0.63132	-0.06213
0.72518	0.04477	0.07831	0.07104	0.04040	-0.04394	0.64459	-0.05886
0.71116	0.04739	0.07018	0.06755	0.04559	-0.04681	0.65803	-0.05548
0.69718	0.05003	0.06267	0.06400	0.05135	-0.04977	0.67161	-0.05202
0.68324	0.05267	0.05578	0.06045	0.05774	-0.05281	0.68524	-0.04857
0.66931	0.05533	0.04951	0.05694	0.06479	-0.05589	0.69888	-0.04515
0.65534	0.05799	0.04384	0.05348	0.07252	-0.05900	0.71249	-0.04178
0.64134	0.06066	0.03874	0.05011	0.08093	-0.06209	0.72604	-0.03850
0.62736	0.06329	0.03415	0.04683	0.09000	-0.06515	0.73956	-0.03531
0.61340	0.06588	0.03004	0.04367	0.09968	-0.06812	0.75304	-0.03224
0.59949	0.06842	0.02636	0.04062	0.10994	-0.07098	0.76648	-0.02924
0.58559	0.07089	0.02306	0.03768	0.12068	-0.07369	0.77988	-0.02637
0.57170	0.07329	0.02012	0.03487	0.13187	-0.07624	0.79326	-0.02360
0.55781	0.07564	0.01749	0.03216	0.14345	-0.07862	0.80657	-0.02095
0.54393	0.07792	0.01514	0.02956	0.15534	-0.08083	0.81982	-0.01845
0.53004	0.08015	0.01303	0.02707	0.16749	-0.08286	0.83302	-0.01609
0.51613	0.08231	0.01114	0.02467	0.17987	-0.08470	0.84617	-0.01389
0.50220	0.08443	0.00945	0.02237	0.19244	-0.08635	0.85925	-0.01184
0.48827	0.08650	0.00793	0.02017	0.20518	-0.08785	0.87226	-0.00998
0.47437	0.08851	0.00657	0.01805	0.21806	-0.08914	0.88519	-0.00829
0.46051	0.09045	0.00535	0.01600	0.23106	-0.09030	0.89806	-0.00680
0.44670	0.09233	0.00429	0.01402	0.24416	-0.09129	0.91086	-0.00551
0.43299	0.09411	0.00336	0.01211	0.25735	-0.09212	0.92357	-0.00441
0.41937	0.09579	0.00256	0.01025	0.27060	-0.09281	0.93618	-0.00351
0.40585	0.09735	0.00188	0.00845	0.28391	-0.09335	0.94862	-0.00279
0.39242	0.09877	0.00127	0.00671	0.29727	-0.09374	0.96078	-0.00221
0.37909	0.10005	0.00075	0.00504	0.31067	-0.09400	0.97246	-0.00171
0.36585	0.10116	0.00037	0.00340	0.32411	-0.09412	0.98344	-0.00134
0.35268	0.10208	0.00013	0.00180	0.33757	-0.09410	0.99363	-0.00103
0.33956	0.10283	0.00000	0.00026	0.35106	-0.09395	1.00000	-0.00075

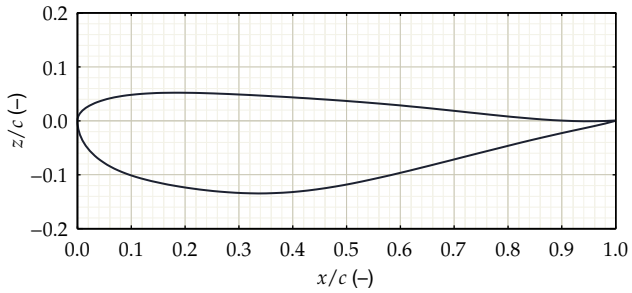

Table D.2: Coordinates of concept 1.

x/c	z/c	x/c	z/c	x/c	z/c	x/c	z/c
1.00000	-0.00202	0.21117	0.08873	0.00006	-0.00410	0.23361	-0.11152
0.99304	-0.00168	0.19921	0.08862	0.00025	-0.00615	0.24612	-0.11152
0.98228	-0.00095	0.18776	0.08831	0.00056	-0.00823	0.25908	-0.11130
0.97109	0.00007	0.17681	0.08780	0.00100	-0.01032	0.27250	-0.11084
0.95942	0.00138	0.16637	0.08710	0.00157	-0.01244	0.28637	-0.11017
0.94724	0.00298	0.15640	0.08621	0.00227	-0.01457	0.30069	-0.10930
0.93451	0.00487	0.14692	0.08516	0.00310	-0.01671	0.31544	-0.10822
0.92120	0.00703	0.13789	0.08396	0.00405	-0.01887	0.33060	-0.10697
0.90728	0.00946	0.12931	0.08261	0.00514	-0.02103	0.34614	-0.10554
0.89275	0.01212	0.12117	0.08113	0.00635	-0.02320	0.36202	-0.10395
0.87762	0.01498	0.11344	0.07953	0.00769	-0.02538	0.37819	-0.10223
0.86197	0.01798	0.10611	0.07783	0.00915	-0.02757	0.39462	-0.10037
0.84594	0.02105	0.09917	0.07605	0.01073	-0.02978	0.41124	-0.09839
0.82970	0.02411	0.09260	0.07418	0.01244	-0.03200	0.42803	-0.09631
0.81335	0.02711	0.08638	0.07225	0.01428	-0.03423	0.44495	-0.09411
0.79696	0.03000	0.08050	0.07026	0.01626	-0.03649	0.46195	-0.09182
0.78055	0.03277	0.07493	0.06823	0.01836	-0.03876	0.47902	-0.08942
0.76411	0.03540	0.06967	0.06616	0.02061	-0.04107	0.49615	-0.08693
0.74762	0.03788	0.06470	0.06405	0.02299	-0.04339	0.51333	-0.08433
0.73106	0.04023	0.05999	0.06193	0.02553	-0.04575	0.53056	-0.08163
0.71440	0.04244	0.05554	0.05979	0.02823	-0.04814	0.54785	-0.07883
0.69759	0.04452	0.05134	0.05764	0.03109	-0.05056	0.56521	-0.07592
0.68062	0.04650	0.04736	0.05548	0.03412	-0.05302	0.58266	-0.07292
0.66345	0.04839	0.04360	0.05331	0.03734	-0.05551	0.60019	-0.06983
0.64607	0.05019	0.04005	0.05114	0.04075	-0.05804	0.61782	-0.06665
0.62848	0.05194	0.03669	0.04898	0.04436	-0.06061	0.63554	-0.06342
0.61067	0.05365	0.03352	0.04681	0.04819	-0.06321	0.65331	-0.06014
0.59268	0.05534	0.03052	0.04465	0.05225	-0.06584	0.67108	-0.05685
0.57455	0.05702	0.02769	0.04249	0.05655	-0.06850	0.68876	-0.05360
0.55635	0.05871	0.02502	0.04033	0.06111	-0.07119	0.70631	-0.05040
0.53813	0.06042	0.02251	0.03818	0.06593	-0.07389	0.72371	-0.04730
0.51994	0.06215	0.02014	0.03603	0.07103	-0.07661	0.74095	-0.04430
0.50176	0.06392	0.01792	0.03388	0.07643	-0.07933	0.75804	-0.04141
0.48362	0.06574	0.01583	0.03174	0.08213	-0.08203	0.77502	-0.03865
0.46550	0.06759	0.01388	0.02959	0.08815	-0.08472	0.79189	-0.03602
0.44741	0.06948	0.01206	0.02745	0.09450	-0.08737	0.80869	-0.03351
0.42936	0.07140	0.01037	0.02531	0.10118	-0.08996	0.82541	-0.03111
0.41139	0.07334	0.00881	0.02317	0.10821	-0.09249	0.84203	-0.02881
0.39357	0.07526	0.00738	0.02103	0.11559	-0.09493	0.85850	-0.02660
0.37599	0.07714	0.00608	0.01889	0.12333	-0.09726	0.87471	-0.02445
0.35872	0.07895	0.00490	0.01675	0.13143	-0.09947	0.89051	-0.02234
0.34183	0.08067	0.00385	0.01461	0.13989	-0.10154	0.90572	-0.02025
0.32536	0.08227	0.00292	0.01247	0.14873	-0.10345	0.92027	-0.01814
0.30933	0.08373	0.00213	0.01034	0.15795	-0.10518	0.93410	-0.01600
0.29379	0.08503	0.00146	0.00822	0.16754	-0.10673	0.94723	-0.01378
0.27873	0.08615	0.00092	0.00611	0.17753	-0.10808	0.95968	-0.01147
0.26419	0.08707	0.00051	0.00402	0.18792	-0.10921	0.97147	-0.00906
0.25015	0.08780	0.00022	0.00195	0.19871	-0.11013	0.98264	-0.00652
0.23664	0.08832	0.00005	-0.00009	0.20991	-0.11083	0.99323	-0.00386
0.22364	0.08864	0.00000	-0.00209	0.22154	-0.11129	1.00000	-0.00202

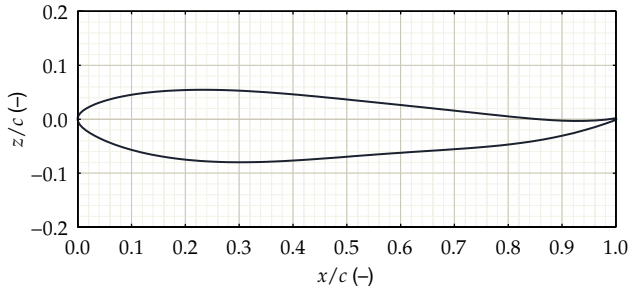

Table D.3: Coordinates of concept 2.

x/c	z/c	x/c	z/c	x/c	z/c	x/c	z/c
1.00000	-0.00143	0.38014	0.04594	0.00013	-0.00331	0.40367	-0.07836
0.99506	-0.00212	0.36724	0.04695	0.00042	-0.00480	0.41656	-0.07756
0.98698	-0.00311	0.35438	0.04790	0.00089	-0.00633	0.42952	-0.07670
0.97810	-0.00400	0.34157	0.04878	0.00154	-0.00787	0.44255	-0.07579
0.96851	-0.00476	0.32881	0.04959	0.00237	-0.00943	0.45564	-0.07484
0.95837	-0.00533	0.31609	0.05031	0.00338	-0.01101	0.46879	-0.07386
0.94780	-0.00571	0.30341	0.05096	0.00458	-0.01261	0.48200	-0.07285
0.93687	-0.00588	0.29079	0.05151	0.00597	-0.01424	0.49526	-0.07183
0.92564	-0.00585	0.27822	0.05197	0.00757	-0.01591	0.50854	-0.07080
0.91417	-0.00562	0.26569	0.05233	0.00939	-0.01763	0.52181	-0.06978
0.90247	-0.00521	0.25322	0.05258	0.01146	-0.01942	0.53507	-0.06877
0.89057	-0.00462	0.24081	0.05272	0.01382	-0.02130	0.54830	-0.06777
0.87848	-0.00389	0.22846	0.05275	0.01650	-0.02327	0.56152	-0.06679
0.86623	-0.00301	0.21618	0.05264	0.01956	-0.02536	0.57473	-0.06583
0.85381	-0.00201	0.20397	0.05241	0.02306	-0.02759	0.58793	-0.06489
0.84124	-0.00091	0.19184	0.05204	0.02709	-0.02998	0.60114	-0.06397
0.82854	0.00028	0.17980	0.05153	0.03172	-0.03255	0.61436	-0.06308
0.81571	0.00154	0.16786	0.05087	0.03704	-0.03531	0.62761	-0.06219
0.80278	0.00286	0.15604	0.05005	0.04312	-0.03826	0.64087	-0.06132
0.78975	0.00423	0.14435	0.04908	0.05000	-0.04135	0.65416	-0.06046
0.77665	0.00563	0.13283	0.04793	0.05767	-0.04456	0.66743	-0.05959
0.76347	0.00705	0.12149	0.04661	0.06607	-0.04781	0.68067	-0.05872
0.75025	0.00849	0.11040	0.04512	0.07509	-0.05103	0.69384	-0.05784
0.73699	0.00993	0.09960	0.04345	0.08463	-0.05418	0.70693	-0.05694
0.72372	0.01137	0.08917	0.04162	0.09459	-0.05719	0.71993	-0.05600
0.71044	0.01281	0.07921	0.03964	0.10488	-0.06004	0.73284	-0.05502
0.69717	0.01424	0.06983	0.03754	0.11545	-0.06271	0.74566	-0.05399
0.68391	0.01566	0.06113	0.03537	0.12624	-0.06520	0.75837	-0.05290
0.67064	0.01707	0.05322	0.03316	0.13722	-0.06750	0.77098	-0.05172
0.65737	0.01848	0.04612	0.03098	0.14837	-0.06961	0.78349	-0.05047
0.64410	0.01987	0.03984	0.02884	0.15966	-0.07153	0.79590	-0.04911
0.63082	0.02127	0.03433	0.02678	0.17109	-0.07327	0.80821	-0.04766
0.61753	0.02265	0.02951	0.02480	0.18264	-0.07483	0.82042	-0.04608
0.60424	0.02404	0.02530	0.02292	0.19429	-0.07621	0.83253	-0.04439
0.59094	0.02542	0.02161	0.02112	0.20605	-0.07743	0.84455	-0.04256
0.57764	0.02679	0.01837	0.01939	0.21789	-0.07849	0.85648	-0.04059
0.56434	0.02817	0.01551	0.01772	0.22982	-0.07938	0.86832	-0.03848
0.55105	0.02954	0.01299	0.01611	0.24182	-0.08013	0.88007	-0.03621
0.53776	0.03090	0.01075	0.01454	0.25389	-0.08073	0.89172	-0.03379
0.52448	0.03227	0.00877	0.01300	0.26604	-0.08118	0.90328	-0.03121
0.51122	0.03362	0.00701	0.01148	0.27824	-0.08150	0.91473	-0.02847
0.49797	0.03496	0.00547	0.00998	0.29051	-0.08168	0.92606	-0.02557
0.48475	0.03629	0.00413	0.00848	0.30284	-0.08174	0.93724	-0.02251
0.47156	0.03760	0.00297	0.00699	0.31523	-0.08167	0.94819	-0.01933
0.45839	0.03889	0.00201	0.00549	0.32768	-0.08149	0.95883	-0.01604
0.44526	0.04016	0.00123	0.00399	0.34019	-0.08121	0.96906	-0.01271
0.43215	0.04140	0.00064	0.00249	0.35276	-0.08081	0.97869	-0.00939
0.41909	0.04260	0.00024	0.00100	0.36539	-0.08033	0.98747	-0.00622
0.40607	0.04376	0.00003	-0.00045	0.37809	-0.07975	0.99529	-0.00326
0.39308	0.04488	0.00000	-0.00187	0.39085	-0.07909	1.00000	-0.00143